



НАЦИОНАЛЬНЫЙ ИССЛЕДОВАТЕЛЬСКИЙ ЦЕНТР  
«КУРЧАТОВСКИЙ ИНСТИТУТ»  
Петербургский институт ядерной физики им. Б. П. Константинова  
Национального исследовательского центра «Курчатовский институт»



# ФИЗИКА АТОМНОГО ЯДРА И ЭЛЕМЕНТАРНЫХ ЧАСТИЦ ТЕОРЕТИЧЕСКАЯ ФИЗИКА

---

ГАТЧИНА  
2024



МАТЕРИАЛЫ LIV И LV  
ЗИМНИХ ШКОЛ ПИЯФ



НАЦИОНАЛЬНЫЙ ИССЛЕДОВАТЕЛЬСКИЙ ЦЕНТР  
«КУРЧАТОВСКИЙ ИНСТИТУТ»

Петербургский институт ядерной физики им. Б. П. Константинова  
Национального исследовательского центра «Курчатовский институт»



# ФИЗИКА АТОМНОГО ЯДРА И ЭЛЕМЕНТАРНЫХ ЧАСТИЦ ТЕОРЕТИЧЕСКАЯ ФИЗИКА

---

МАТЕРИАЛЫ LIV И LV ЗИМНИХ ШКОЛ ПИЯФ

Гатчина  
2024

УДК 539; 53.01

Данный сборник содержит избранные лекции тематических Школ по физике атомного ядра и элементарных частиц и Школ по теоретической физике, проведенных в рамках LIV и LV Зимних школ ПИЯФ.

*LIV и LV Зимние школы ПИЯФ были проведены при поддержке  
Федерального государственного бюджетного учреждения  
«Петербургский институт ядерной физики им. Б. П. Константинова  
Национального исследовательского центра «Курчатовский институт»*

ФИЗИКА АТОМНОГО ЯДРА И ЭЛЕМЕНТАРНЫХ ЧАСТИЦ.

ТЕОРЕТИЧЕСКАЯ ФИЗИКА

(Материалы LIV и LV Зимних школ ПИЯФ)

Издательство НИЦ «Курчатовский институт» – ПИЯФ,

Гатчина, 2024. – 212 с.

ISBN 978-5-86763-2

© НИЦ «Курчатовский институт» – ПИЯФ, 2024

## ПРЕДИСЛОВИЕ

За свою уже более полувековую историю Зимние Школы по физике стали важнейшим элементом научной жизни Петербургского института ядерной физики (ПИЯФ). Являясь одним из самых продолжительных периодических мероприятий в мире в области фундаментальных наук, Зимние Школы внесли важный вклад в развитие физических наук в СССР и России. Высочайший уровень дискуссий на Школе в 1960-80-х г. задавал выдающийся физик и неординарная личность, руководитель отдела теоретической физики член-корреспондент АН СССР В.Н. Грибов, в то время один из лидеров мировой теоретической физики элементарных частиц, создавший одну из самых ярких научных школ. Это способствовало тому, что многие физики страны стремились попасть на Зимние Школы Физико-Технического Института им. А.Ф. Иоффе (ФТИ АН СССР), затем с 1971 г. на Зимние Школы Ленинградского Института Ядерной Физики им. Б.П. Константинова (ЛИЯФ АН СССР), чтобы обсудить свои работы с В.Н. Грибовым, А.А. Ансельмом, Л.Н. Липатовым и другими сотрудниками теоретического отдела и присутствовать при зарождении новых идей и направлений. Зимние Школы ПИЯФ с успехом продолжают сложившиеся традиции.

LIV Зимняя Школа ПИЯФ была проведена в загородном центре отдыха «Райвола», в пос. Рощино, вблизи Санкт-Петербурга, с 10 по 15 марта 2020 г., а LV Зимняя Школа в Оздоровительном объединении «Зеленый Бор» ЦБ России, г. Луга Ленинградской обл., с 13 по 18 марта 2023 г. Как всегда, в рамках общей Школы ПИЯФ проводились различные тематические Школы: Физика ядра и элементарных частиц, Теоретическая физика, Атомная физика, Физика и техника реакторов, Ядерная медицина и ускорительная физика.

Данный сборник предназначен для студентов старших курсов и аспирантов, начинающих исследователей и широкого круга специалистов, как теоретиков, так и экспериментаторов.

Виктор Т. Ким

Сопредседатель оргкомитета Зимней Школы ПИЯФ

## FOREWORD

Over their more than half-century history, the Winter Schools in Physics have become the most important element of the scientific life of the Petersburg Institute of Nuclear Physics (NRC Kurchatov Institute – PNPI). As one of the longest-running periodic events in the world in the field of fundamental sciences, the Winter Schools made an important contribution to the development of the physical sciences in the USSR and Russia. The highest level of discussions at the School in the 1960-80s was set by the outstanding physicist and extraordinary personality, head of the department of theoretical physics, corresponding member of the USSR Academy of Sciences V.N. Gribov, at that time one of the leaders of the world theoretical physics of elementary particles, who created one of the most brilliant scientific schools. This contributed to the fact that many physicists in the country sought to attend the Winter Schools of the Physico-Technical Institute named after A.F. Ioffe (PTI AS USSR), then from 1971 to the Winter Schools of the Leningrad Institute of Nuclear Physics named after B.P. Konstantinov (LNPI AS USSR) to discuss their works with V.N. Gribov, A.A. Anselm, L.N. Lipatov and other staff members of the theoretical department and to participate at the emergence of new ideas and trends. PNPI Winter Schools successfully continue the established traditions.

The LIVth PNPI Winter School was held at the “Raivola” recreation center, in Roshchino, near St. Petersburg, from March 10 to 15, 2020, and the LVth Winter School at the “Zeleny Bor” health-recreation center of the Central Bank of Russia, Luga of Leningrad region, from March 13 to 18, 2023. As always, within the framework of the general PNPI School, various topical Schools were held: Physics of Nuclei and Elementary Particles, Theoretical Physics, Atomic Physics, Physics and Reactor Technics, Nuclear Medicine and Accelerator Physics.

These Proceedings are intended for senior and graduate students, young researchers and a wide range of specialists, both theorists and experimentalists.

Victor T. Kim

Co-Chair of the PNPI Winter School Organizing Committee

# ON LANDAU–KHALATNIKOV–FRADKIN TRANSFORMATION IN QED

Anatoly V. Kotikov  
Bogoliubov Laboratory of Theoretical Physics,  
Joint Institute for Nuclear Research, Dubna

Abstract

We present the results of studies of the gauge dependence of the massless fermion propagator in QED in the framework of dimensional regularization. The results were obtained using the Landau–Khalatnikov–Fradkin transformation between massless charged particle propagators interacting with gauge fields in two different gauges. In the  $d = 4 - 2\varepsilon$  case, we present the exact results obtained in [1], which relate the hatted and standard  $\zeta$  values and are valid in all orders of perturbation theory. In three-dimensional quenched QED assuming the finiteness of the perturbative expansion coefficients, it was shown in [2] that exactly for  $d = 3$  all odd perturbative coefficients, starting from the third order, must be equal to zero in any gauge. To test this, in Ref. [3] we calculated three- and four-loop corrections to the massless fermionic propagator. Three-loop corrections are finite and gauge-invariant, while four-loop corrections have singularities.

# О ПРЕОБРАЗОВАНИИ ЛАНДАУ–ХАЛАТНИКОВА–ФРАДКИНА В КЭД

Анатолий В. Котиков

Лаборатория теоретической физики им. Боголюбова,  
Объединенный институт ядерных исследований, Дубна

## Аннотация

Представлены результаты исследования калибровочной зависимости безмассового фермионного пропагатора в КЭД в рамках размерной регуляризации. Результаты были получены с помощью преобразования Ландау–Халатникова–Фрадкина между пропагаторами безмассовых заряженных частиц, взаимодействующими с калибровочными полями в двух разных калибровках. В случае  $d = 4 - 2\epsilon$  мы представляем точные результаты, полученные в [1], которые связывают стандартные  $\zeta$ -функции и  $\zeta$ -функции со шляпкой и справедливы во всех порядках теории возмущений. В трехмерной замороженной КЭД в предположении конечности коэффициентов пертурбативного разложения, в [2] показано, что при  $d = 3$  все нечетные пертурбативные коэффициенты, начиная с третьего порядка, должны быть равны нулю в любой калибровке. Чтобы проверить это, в [3] мы рассчитали трех- и четырехпетлевые поправки к безмассовому фермионному пропагатору. Трехпетлевые поправки конечны и калибровочно-инвариантны, а четырехпетлевые поправки содержат сингулярности.

# 1 Introduction

The Landau–Khalatnikov–Fradkin transformation (LKFT) [4, 5] elegantly links the QED fermion propagator in two different gauges (and similarly for the fermion-photon vertex but it is beyond the present consideration). This transformation has a simple form in representing a coordinate space and allows us to compute Green functions in an arbitrary covariant gauge if we know their value at any particular gauge.

Here we show the LKFT applications around three and four dimensions in the framework of dimensional regularization.

In the case of the usual four-dimensional QED (QED<sub>4</sub>) let us consider the multiloop structure of propagator-type functions. It was recently noticed that contributions for various massless Euclidean physical quantities proportional to even values of the  $\zeta$  function,  $\zeta_{2n}$ , mysteriously often cancel out (see, *e.g.*, [6–13]). Such puzzling facts have recently given rise to the "absence of  $\pi$  theorem". The latter is based on [14, 15] observation that  $\varepsilon$ -dependent transformation of  $\zeta$  values:

$$\hat{\zeta}_3 \equiv \zeta_3 + \frac{3\varepsilon}{2}\zeta_4 - \frac{5\varepsilon^3}{2}\zeta_6, \quad \hat{\zeta}_5 \equiv \zeta_5 + \frac{5\varepsilon}{2}\zeta_6, \quad \hat{\zeta}_7 \equiv \zeta_7, \quad (1)$$

eliminates even zetas. The reason for the appearance of the hatted  $\zeta$ -values is not clear and requires additional investigations.

A generalization (1) is available in Refs. [16–19]. The results (1) and their generalizations make it possible to predict the terms  $\sim \pi^{2n}$  in higher orders of perturbation theory (PT) (see their estimate in [16–20]). Also note that [16–19] results contain multi-zeta values, which are beyond the scope of this paper.

Here we consider the LKFT results obtained in [1] (see also [21, 22]) to study the general properties of the PT expansion of the fermion propagator. We show how transformation naturally reveals the existence of the hatted transcendental basis. Moreover, this allows the results shown in (1) to be extended to any  $\varepsilon$  order.

Quantum electrodynamics in three space-time dimensions of (QED<sub>3</sub>) with  $N$  flavors of four-component massless Dirac fermions has been under continuous study for the past forty years as a useful field-theoretical model. QED<sub>3</sub> served as a toy model for exploring several key problems in quantum field theory, such as infrared singularities in low-dimensional massless particle theories, coupling constant nonanalyticity within PT, dynamic symmetry breaking and fermion mass generation, phase transition and the relationship between chiral symmetry breaking and confinement.

Moreover, QED<sub>3</sub> has found many applications also in condensed matter physics, in particular, in superconductivity with high  $T_c$  [23–25], in planar antiferromagnets [26], as well as in studies of graphene [27], where excitations of quasiparticles have linear dispersion at low energies and are described by the massless Dirac equation in 2 + 1 dimensions (see reviews on graphene studies in [28–31]).

Massless QED<sub>3</sub> plays an important role in investigating the problems of dynamic symmetry breaking and fermion mass generation in gauge theories. The main question that has been debated for a long time is whether there is a critical fermion flavor number,  $N_{cr}$ , where the separation of the chiral symmetric phase and the phase with broken chiral symmetry occurs (see [32–48]). Analytical studies of chiral symmetry breaking and mass generation in QED<sub>3</sub> are usually based on the use of the Schwinger–Dyson equations with some ansatzes for the full fermion-photon vertex.

In the recent paper [2], we studied the gauge-covariance of the massless fermion propagator in quenched QED<sub>3</sub> in a covariant gauge. We recall here that the quenched limit of QED is the approximation in which we can neglect the effects of closed fermion loops. This approximation arose in the study of the lattice representation of QED<sub>4</sub> (see [49–52]), which showed that a reasonable estimate of the hadron spectrum can be obtained by eliminating all internal quark loops. Moreover, the quenching approximation in QED<sub>4</sub> is now used to include QED effects in lattice QCD calculations (see the recent paper [53] and discussions therein).

Immediately after its introduction in the study of the lattice representation QED<sub>4</sub>, the quenched approximation in QED<sub>4</sub> was also used in Refs. [54–60] within the framework of the formalism based on the study of the Schwinger–Dyson equations.

In Ref. [2], following [1, 60, 61] we applied dimensional regularization and studied the LKFT self-consistency in quenched QED<sub>3</sub> in a covariant gauge. Analysis of [2] led to the conclusion that in exactly three dimensions,  $d = 3$ , all odd perturbative coefficients, starting from the third order, must be equal to zero in any gauge if QED<sub>3</sub> does not have (infrared) singularities, as discussed in [62–64]. To test this, in Ref. [3] we calculated the three- and four-loop orders and found that the three-loop corrections are finite and gauge-invariant, while the four-loop corrections have singularities.

## 2 LKFT in $x$ space with $d = 4 - 2\varepsilon$

Further, we will consider QED in the Euclidean space of dimension  $d$  (in the first two sections  $d = 4 - 2\varepsilon$ ). The general form of the fermion propagator in the momentum and  $x$ -space representations,  $S_F(p, \xi)$  and  $S_F(x, \xi)$ , in some gauge  $\xi$  is as follows:

$$S_F(p, \xi) = \frac{i}{\hat{p}} P(p, \xi), \quad S_F(x, \xi) = \hat{x} X(x, \xi), \quad (2)$$

where the tensor structure is distinguished by the factors  $\hat{p}$  and  $\hat{x}$  containing the  $\gamma$ -Dirac matrices. The two representations,  $S_F(x, \xi)$  and  $S_F(p, \xi)$ , are related by a Fourier transform, which is defined as:

$$S_F(p, \xi) = \int \frac{d^d x}{(2\pi)^{d/2}} e^{ipx} S_F(x, \xi), \quad S_F(x, \xi) = \int \frac{d^d p}{(2\pi)^{d/2}} e^{-ipx} S_F(p, \xi). \quad (3)$$

The famous LKFT very simply relates the fermionic propagator in two different gauges, *e.g.*,  $\xi$  and  $\eta$ . In dimensional regularization, it looks like this [1]:

$$S_F(x, \xi) = S_F(x, \eta) e^{iD(x)}, \quad D(x) = -ie^2 \Delta \mu^{2\varepsilon} \int \frac{d^d q}{(2\pi)^d} \frac{e^{-iqx}}{q^4}, \quad \Delta = \xi - \eta. \quad (4)$$

Now we can proceed to the calculation of  $D(x)$ . To do this, you can use the following simple formulas for the Fourier transform of massless propagators (see, *e.g.*, [65]):

$$\int d^d x \frac{e^{ipx}}{x^{2\alpha}} = \frac{2^{2\tilde{\alpha}} \pi^{d/2} a_0(\alpha)}{p^{2\tilde{\alpha}}}, \quad \int d^d p \frac{e^{-ipx}}{p^{2\alpha}} = \frac{2^{2\tilde{\alpha}} \pi^{d/2} a_0(\alpha)}{x^{2\tilde{\alpha}}},$$

$$a_n(\alpha) = \frac{\Gamma(d/2 - \alpha + n)}{\Gamma(\alpha)}. \quad (5)$$

This gives:

$$D(x) = \frac{i \Delta A}{\varepsilon} \Gamma(1 - \varepsilon) (\pi \mu^2 x^2)^\varepsilon, \quad A = \frac{\alpha_{\text{em}}}{4\pi} = \frac{e^2}{(4\pi)^2}. \quad (6)$$

## 3 LKFT in momentum space with $d = 4 - 2\varepsilon$

Suppose that for some gauge parameter  $\eta$  the fermionic propagator  $S_F(p, \eta)$  with external momentum  $p$  has the form (2) with  $P(p, \eta)$  as:

$$P(p, \eta) = \sum_{m=0}^{\infty} a_m(\eta) A^m \left( \frac{\tilde{\mu}^2}{p^2} \right)^{m\varepsilon}, \quad \tilde{\mu}^2 = 4\pi\mu^2, \quad (7)$$

where  $a_m(\eta)$  are the coefficients of the loop expansion of the propagator, and  $\tilde{\mu}$  is the renormalization scale, which lies somewhere between the MS-scale  $\mu$  and the  $\overline{\text{MS}}$ -scale  $\bar{\mu}$ .

Using the Fourier transform (5), we have

$$\int \frac{d^d q}{(2\pi)^d} \frac{e^{-iqx}}{(q^2)^\alpha} q_\mu = \left( \frac{i \partial}{\partial x_\mu} \right) \int \frac{d^d q}{(2\pi)^d} \frac{e^{-iqx}}{(q^2)^\alpha} = \frac{1}{(4\pi)^{d/2}} \frac{2^{2\tilde{\alpha}+1} a_1(\alpha) x_\mu}{i (x^2)^{\tilde{\alpha}+1}}. \quad (8)$$

Then, using (3), we obtain that:

$$S_F(x, \eta) = \frac{2^{d-1} \hat{x}}{(4\pi x^2)^{d/2}} \sum_{m=0}^{\infty} b_m(\eta) A^m (\pi \mu^2 x^2)^{m\varepsilon}, \quad b_m(\eta) = a_m(\eta) \frac{\Gamma(d/2 - m\varepsilon)}{\Gamma(1 + m\varepsilon)}. \quad (9)$$

With the help of (9) together with an expansion of the LKFT exponent, we have

$$S_F(x, \xi) = \frac{2^{d-1} \hat{x}}{(4\pi x^2)^{d/2}} \sum_{m=0}^{\infty} b_m(\eta) A^m (\pi \mu^2 x^2)^{m\varepsilon} \sum_{l=0}^{\infty} \left( -\frac{A\Delta}{\varepsilon} \right)^l \frac{\Gamma^l(1-\varepsilon)}{l!} (\pi \mu^2 x^2)^{l\varepsilon}. \quad (10)$$

Factorizing all  $x$ -dependence yields:

$$S_F(x, \xi) = \frac{2^{d-1} \hat{x}}{(4\pi x^2)^{d/2}} \sum_{p=0}^{\infty} b_p(\xi) A^p (\pi \mu^2 x^2)^{p\varepsilon},$$

$$b_p(\xi) = \sum_{m=0}^p \frac{b_m(\eta)}{(p-m)!} \left( -\frac{\Delta}{\varepsilon} \right)^{p-m} \Gamma^{p-m}(1-\varepsilon). \quad (11)$$

Hence, taking the correspondence between the results for propagators  $P(p, \eta)$  and  $S_F(x, \eta)$  in (7) and (9), respectively, together with the result (11) for  $S_F(x, \eta)$ , we have for  $P(p, \xi)$ :

$$P(p, \xi) = \sum_{m=0}^{\infty} a_m(\xi) A^m \left( \frac{\tilde{\mu}^2}{p^2} \right)^{m\varepsilon}, \quad (12)$$

where

$$a_m(\xi) = b_m(\xi) \frac{\Gamma(1 + m\varepsilon)}{\Gamma(d/2 - m\varepsilon)} \quad (13)$$

$$= \sum_{l=0}^m \frac{a_l(\eta)}{(m-l)!} \frac{\Gamma(d/2 - l\varepsilon)\Gamma(1 + m\varepsilon)}{\Gamma(1 + l\varepsilon)\Gamma(d/2 - m\varepsilon)} \left( -\frac{\Delta}{\varepsilon} \right)^{m-l} \Gamma^{m-l}(1-\varepsilon).$$

In this way, we have derived the expression of  $a_m(\xi)$  using a simple expansion of the LKFT exponent in  $x$  space. From this LKFT representation, we see that the magnitude  $a_m(\xi)$  is determined by  $a_l(\eta)$  with  $0 \leq l \leq m$ .

Very often, however, the subject of the study is not the magnitude  $a_m(\xi)$  but the  $p$ - and  $\Delta$ -dependencies of each magnitude  $a_l(\eta)$  as it evolves from the  $\eta$  to the  $\xi$  gauge. The corresponding result for the  $p$ - and  $\Delta$ -dependencies of  $\hat{a}_m(\xi, p)$  can be obtained interchanging the order of the sums in the r.h.s. of (12). Performing such interchange yields:

$$P(p, \xi) = \sum_{m=0}^{\infty} \hat{a}_m(\xi, p) A^m \left( \frac{\tilde{\mu}^2}{p^2} \right)^{m\varepsilon}, \quad (14)$$

where

$$\hat{a}_m(\xi, p) = a_m(\eta) \sum_{l=0}^{\infty} \frac{\Gamma(d/2 - m\varepsilon)\Gamma(1 + (l+m)\varepsilon)}{\Gamma(1 + m\varepsilon)\Gamma(d/2 - (l+m)\varepsilon)} \left( \frac{A\Delta}{\varepsilon} \right)^l \frac{\Gamma^l(1 - \varepsilon)}{l!} \left( \frac{\tilde{\mu}^2}{p^2} \right)^{l\varepsilon}. \quad (15)$$

### 3.1 Scale fixing

Following [1], we consider only the case of so-called MS-like schemes. In such schemes, we need to fix some terms resulting from the application of dimensional regularization. This procedure will be called *scale fixing* and will play a decisive role in our analysis.

It is well known that when calculating two-point massless diagrams, the final results do not contain  $\zeta_2$ .<sup>1</sup> Therefore, it is convenient to choose a certain scale in which  $\zeta_2$  disappears already at intermediate steps of the calculations. To do this, in [1] we also introduced a new scale based on the old calculations of massless diagrams, performed by Vladimirov who added (see [69]) an additional factor  $\Gamma(1 - \varepsilon)$  to the contribution of each loop. This corresponds to adding the factor  $\Gamma^{-1}(1 - \varepsilon)$  to the corresponding scale. In [1] we called this scale the *minimal Vladimirov* scale, or the MV-scale, and gave the following definition:

$$\mu_{\text{MV}}^{2\varepsilon} = \frac{\tilde{\mu}^{2\varepsilon}}{\Gamma(1 - \varepsilon)}. \quad (16)$$

---

<sup>1</sup>Strictly speaking,  $\zeta_2$  may appear in some formulas, such as the sum rules in deep inelastic scattering. They come from analytic continuation [66–68] but we will not consider this case in this paper.

In the scale, we can rewrite the result (15) in the following general form:

$$\hat{a}_m(\xi, p) = a_m(\eta) \sum_{l=0}^{\infty} \frac{1 - (m+1)\varepsilon}{1 - (m+l+1)\varepsilon} \Phi_{\text{MV}}(m, l, \varepsilon) \frac{(\Delta A)^l}{(-\varepsilon)^{l!}} \left( \frac{\mu_{\text{MV}}^2}{p^2} \right)^{l\varepsilon}, \quad (17)$$

where

$$\Phi_{\text{MV}}(m, l, \varepsilon) = \frac{\Gamma(1 - (m+1)\varepsilon)\Gamma(1 + (m+l)\varepsilon)\Gamma^{2l}(1 - \varepsilon)}{\Gamma(1 + m\varepsilon)\Gamma(1 - (m+l+1)\varepsilon)}. \quad (18)$$

The factor  $(1 - (m+1)\varepsilon)/(1 - (m+l+1)\varepsilon)$  was specially extracted from  $\Phi_{\text{MV}}(m, l, \varepsilon)$ , to insure the same transcendental level, *i.e.*, the same value  $s$  for  $\zeta_s$  for each order of the  $\varepsilon$  expansion  $\Phi_{\text{MV}}(m, l, \varepsilon)$  (see below).

### 3.2 MV scale

The  $\Gamma$  function  $\Gamma(1 + \beta\varepsilon)$  has the following expansion:

$$\Gamma(1 + \beta\varepsilon) = \exp \left[ -\gamma\beta\varepsilon + \sum_{s=2}^{\infty} (-1)^s \eta_s \beta^s \varepsilon^s \right], \quad \eta_s = \frac{\zeta_s}{s}. \quad (19)$$

Substituting Eq. (19) in Eq. (18), we obtain for the factor  $\Phi_{\text{MV}}(m, l, \varepsilon)$ :

$$\Phi_{\text{MV}}(m, l, \varepsilon) = \exp \left[ \sum_{s=2}^{\infty} \eta_s p_s(m, l) \varepsilon^s \right], \quad (20)$$

where

$$p_s(m, l) = (m+1)^s - (m+l+1)^s + 2l + (-1)^s \left\{ (m+l)^s - m^s \right\}, \quad (21)$$

and, as expected by the MV scale, we have  $p_1(m, l) = 0, p_2(m, l) = 0$ .

As can be seen from the Eq. (20),  $\Phi_{\text{MV}}(m, l, \varepsilon)$  contains the values of the  $\zeta_s$  function of a given weight (or transcendental level)  $s$  in the factor  $\varepsilon^s$ . This property severely limits the coefficients of the  $\varepsilon$  series, which simplifies our analysis. It resembles the one found earlier in Ref. [70]. When used wisely, this property sometimes allows you to get results without any calculations (as in Ref. [71–74]). In other cases, this simplifies the structure of the results, which can then be very easily predicted in the form of some ansatz (see Refs. [75–81]).

### 3.3 Solution of the recurrence relations

Now let us focus on the polynomial  $p_s(m, l)$  in Eq. (21), which can be conveniently divided into even and odd values of  $s$ . Then we see that the following recursive relations hold:

$$p_{2k} = p_{2k-1} + Lp_{2k-2} + p_3, \quad p_{2k-1} = p_{2k-2} + Lp_{2k-3} + p_3, \quad L = l(l+1). \quad (22)$$

For the MV scheme, these relations depend only on  $L$ , which leads to strong simplifications.

Taking the results for  $p_{2k}$  in the following form

$$p_{2k} = \sum_{s=2}^k p_{2s-1} C_{2k,2s-1} = \sum_{m=1}^{k-1} p_{2k-2m+1} C_{2k,2k-2m+1}, \quad (23)$$

one can determine the exact  $k$  dependency  $C_{2k,2s-1}$ , which has the following structure:

$$C_{2k,2k-2m+1} = b_{2m-1} \frac{(2k)!}{(2m-1)!(2k-2m+1)!}, \quad b_{2m-1} = \frac{(2^{2m}-1)}{m} B_{2m}, \quad (24)$$

where  $B_m$  are the well-known Bernoulli numbers.

### 3.4 Hatted $\zeta$ values

At this point it is convenient to represent the exponent argument in the r.h.s. of (20) as follows:

$$\sum_{s=3}^{\infty} \eta_s p_s \varepsilon^s = \sum_{k=2}^{\infty} \eta_{2k} p_{2k} \varepsilon^{2k} + \sum_{k=2}^{\infty} \eta_{2k-1} p_{2k-1} \varepsilon^{2k-1}. \quad (25)$$

Using Eq. (23) the first term in the r.h.s. of Eq. (25) can be expressed as:

$$\sum_{k=2}^{\infty} \eta_{2k} p_{2k} \varepsilon^{2k} = \sum_{k=2}^{\infty} \eta_{2k} \varepsilon^{2k} \sum_{s=2}^k p_{2s-1} C_{2k,2s-1} = \sum_{s=2}^{\infty} p_{2s-1} \sum_{k=s}^{\infty} \eta_{2k} C_{2k,2s-1} \varepsilon^{2k}. \quad (26)$$

Then, Eq. (25) can be written as  $\sum_{s=2}^{\infty} \hat{\eta}_{2s-1} p_{2s-1} \varepsilon^{2s-1}$ , where

$$\begin{aligned} \hat{\eta}_{2s-1} &= \eta_{2s-1} + \sum_{k=s}^{\infty} \eta_{2k} C_{2k,2s-1} \varepsilon^{2(k-s)+1}, \\ C_{2k,2s-1} &= b_{2k-2s+1} \frac{(2k)!}{(2s-1)!(2k-2s+1)!}. \end{aligned} \quad (27)$$

and, correspondently, for  $\zeta_s = s\eta_s$  (see Eq. (19))

$$\hat{\zeta}_{2s-1} = \zeta_{2s-1} + \sum_{k=s}^{\infty} \zeta_{2k} \hat{C}_{2k,2s-1} \varepsilon^{2(k-s)+1} \quad (28)$$

with

$$\hat{C}_{2k,2s-1} = \frac{2s-1}{2k} C_{2k,2s-1} = b_{2k-2s+1} \frac{(2k-1)!}{(2s-2)!(2k-2s+1)!}. \quad (29)$$

Together with (29) and (24), Eq. (28) provides an exact expression for the hatted  $\zeta$  values in terms of standard  $\zeta$ , which is holds for all orders of  $\varepsilon$  expansion.

## 4 LKFT with $d = 3 - 2\varepsilon$

In Sections 4 and 5, we will consider a Euclidean space of dimension  $d = 3 - 2\varepsilon$ . The general form of the fermionic propagators  $S_F(p, \xi)$  and  $S_F(x, \xi)$  in some gauge  $\xi$  is shown in Eq.(2).

As in Eq.(7), the fermion propagator can be represented in the form

$$P(p, \eta) = \sum_{m=0}^{\infty} a_m(\eta) B^m \left( \frac{\bar{\mu}^2}{p^2} \right)^{m\varepsilon}, \quad B = \frac{\alpha}{2\sqrt{\pi} p}, \quad (30)$$

where  $\bar{\mu}$  is the  $\overline{MS}$  scale.

Repeating the evaluation done in Eqs. (8)–(14) with the replacement  $\varepsilon \rightarrow 1/2 + \varepsilon$  and  $A \rightarrow B$ , we obtain the results

$$P(p, \xi) = \sum_{m=0}^{\infty} a_m(\xi) B^m \left( \frac{\tilde{\mu}^2}{p^2} \right)^{m\varepsilon}, \quad (31)$$

where

$$a_k(\xi) = \sum_{m=0}^k (-2\Delta)^{k-m} a_m(\eta) \hat{\Phi}(m, k, \varepsilon) \phi(k-m, \varepsilon) \quad (32)$$

and

$$\begin{aligned} \hat{\Phi}(m, k, \varepsilon) &= \frac{\Gamma(3/2 - m/2 - (m+1)\varepsilon)\Gamma(1 + k/2 + k\varepsilon)}{\Gamma(1 + m/2 + m\varepsilon)\Gamma(3/2 - k/2 - (k+1)\varepsilon)}, \\ \phi(l, \varepsilon) &= \frac{\Gamma^l(1/2 - \varepsilon)}{l!(1 + 2\varepsilon)^l \Gamma^l(1 + \varepsilon)}. \end{aligned} \quad (33)$$

Now consider  $a_m(\xi)$  with  $m \leq 4$ :

$$\begin{aligned}
a_0(\xi) &= a_0(\eta) = 1, \quad a_1(\xi) = a_1(\eta) - \frac{\pi}{2} \delta \left(1 + 2\varepsilon(l_2 - 1)\right) a_0(\eta), \quad (\delta = \sqrt{\pi}\Delta), \\
a_2(\xi) &= a_2(\eta) - \frac{4}{\pi} \delta \left(1 - 2\varepsilon(l_2 + 1)\right) a_1(\eta) + \delta^2 \left(1 - 4\varepsilon\right) a_0(\eta), \\
a_3(\xi) &= a_3(\eta) + 6\pi\varepsilon \delta a_2(\eta) - 12\varepsilon \delta^2 a_1(\eta) + 2\pi\varepsilon \delta^3 a_0(\eta), \\
a_4(\xi) &= a_4(\eta) - \frac{2\delta}{3\pi\varepsilon} \left(1 + 2\varepsilon(3 - l_2)\right) a_3(\eta) - 2\delta^2 a_2(\eta) + \frac{8\delta^3}{3\pi} a_1(\eta) - \frac{\delta^4}{3} a_0(\eta).
\end{aligned} \tag{34}$$

Setting  $\eta = 0$ , i.e. choosing the initial Landau gauge, we can represent the results (35) for  $a_m(\xi)$  in the form

$$a_m(\xi) = a_m(0) + \xi \tilde{a}_m(\xi) \tag{35}$$

and verify that our results for  $\tilde{a}_m(\xi)$  are completely determined by  $a_l(0)$ , ( $l < m$ ), i.e. coefficients of lower orders in accordance with the LKF transformation.

It is clearly seen in (35) that, starting from the third, the contributions of odd orders to even ones are accompanied by singularities  $\varepsilon^{-1}$ . In turn, the even orders contribute to the odd ones, starting from the third,  $\sim \varepsilon$ . Assuming the perturbative finiteness of the massless quenched QED<sub>3</sub> [62–64] and the existence of a finite limit at  $\varepsilon \rightarrow 0$ , we showed in [2] that exactly in  $d = 3$  all odd PT terms except  $a_1$  must be equal to zero in any gauge. This required verification, and in Ref. [3] we calculated the three- and four-loop corrections shown in the next section.

## 5 Fermion propagator: three- and four-loop coefficients

For the calculations, it is convenient to use

$$P(p, \xi) = \frac{1}{1 - \sigma(p, \xi)}, \tag{36}$$

where the 1PI-part  $\sigma(p, \xi)$  can be represented (similarly to (30)) as

$$\sigma(p, \xi) = \sum_{m=1}^{\infty} \sigma_m(\xi) B^m \left( \frac{\bar{\mu}^2}{p^2} \right)^{m\varepsilon}. \tag{37}$$

Some details of the calculations can be found in [3]. Here we present the results for  $\sigma_m(\xi)$ , which can be represented in the form similar to (35):

$$\sigma_m(\xi) = \sigma_m(0) + \xi \tilde{\sigma}_m(\xi). \tag{38}$$

Taking into account the first two orders of the  $\varepsilon$  expansion, we have for  $\sigma_m(0)$

$$\begin{aligned}\sigma_1(0) &= 0; \quad \sigma_2(0) = \pi \left[ \frac{3\pi^2}{4} - 7 - \left( (1 - 3l_2)\pi^2 + 12 \right) \varepsilon \right], \\ \sigma_3(0) &= \pi^{5/2} \left[ \frac{43\pi^2}{4} - 105 + \varepsilon \left\{ 2 \left( 185 - 105l_2 + 137\zeta_3 \right) - \frac{\pi^2}{6} \left( 451 - 171l_2 \right) \right\} \right], \\ \sigma_4(0) &= \pi^2 \left[ \left( \frac{43}{6}\pi^2 - 70 \right) \frac{1}{\varepsilon} + \bar{\sigma}_4 + \frac{5954}{3} + \frac{173}{18}\pi^2 - \frac{513}{10}\pi^4 \right],\end{aligned}\quad (39)$$

where  $\bar{\sigma}_4$  contains the most complicated part

$$\bar{\sigma}_4 = 209l_2^4 + 5016a_4 + 4264\text{Cl}_4(\pi/2) + \left( \frac{533}{3}\text{C} - 930l_2 \right) \pi^2 + \frac{2078}{3}\zeta_3, \quad (40)$$

and

$$l_2 = \ln 2, \quad a_4 = \text{Li}_4(1/2), \quad \zeta_n = \text{Li}_n(1), \quad (41)$$

C is Catalan,  $\text{Li}_n$  are polylogarithms and  $\text{Cl}_4$  is Clausen number.

With the same accuracy, we have for the coefficients  $\tilde{\sigma}_m(\xi)$

$$\begin{aligned}\tilde{\sigma}_1(\xi) &= -\frac{\pi^{3/2}}{2} \left( 1 - 2(1 - l_2)\varepsilon \right), \quad \tilde{\sigma}_2(\xi) = \pi \xi \left[ 1 - \frac{\pi^2}{4} - \left( 4 - (1 - l_2)\pi^2 \right) \varepsilon \right], \\ \tilde{\sigma}_3(\xi) &= \pi^{5/2} \left[ \frac{3\pi^2}{4} - 7 + \left( 1 - \frac{\pi^2}{8} \right) \xi^2 + \varepsilon \left\{ -40 - 14l_2 + \frac{\pi^2}{2} (4 + 9l_2) \right. \right. \\ &\quad \left. \left. + \left( 2l_2 - 4 + \frac{3\pi^2}{4} (1 - l_2) \right) \xi^2 \right\} \right]; \\ \tilde{\sigma}_4(\xi) &= \pi^2 \left[ \left( 70 - \frac{43\pi^2}{6} \right) \frac{1}{\varepsilon} + \frac{520}{3} - \frac{\pi^2}{9} (881 + 42l_2) + \frac{129\pi^4}{27} - \frac{548}{3}\zeta_3 \right. \\ &\quad \left. + \xi \left( 28 - \frac{33\pi^2}{4} + \frac{9\pi^4}{16} \right) + \xi^3 \left( -\frac{4}{3} + \frac{3\pi^2}{4} - \frac{\pi^4}{16} \right) \right].\end{aligned}\quad (42)$$

Note that the finite parts of the coefficients  $\sigma_1(\xi)$  and  $\sigma_2(\xi)$  coincide with the corresponding ones in Ref. [82]. So, we see that

$$\sigma_4(\xi) = \pi^2 \left( \frac{43}{6}\pi^2 - 70 \right) \frac{(1 - \xi)}{\varepsilon} + O(\varepsilon^0), \quad (43)$$

i.e. the four-loop results are finite in Feynman gauge.

## 5.1 $a_m(\xi)$

The coefficients  $a_m(\xi)$  and  $\sigma_m(\xi)$  are related each other as

$$a_1 = \sigma_1, \quad a_2 = \sigma_2 + \sigma_1^2, \quad a_3 = \sigma_3 + 2\sigma_2\sigma_1 + \sigma_1^3, \quad a_4 = \sigma_4 + 2\sigma_3\sigma_1 + \sigma_2^2 + 3\sigma_2\sigma_1^2 + \sigma_1^4. \quad (44)$$

Since  $\sigma_1(\xi) \sim \xi$ , we see in (44) that  $a_i(0) = \sigma_i(0)$  for  $i \leq 3$  and thus so  $a_i(0)$  with  $i \leq 3$  can be found in Eq. (39). According to (44) we have for  $a_4(0)$ :

$$a_4(0) = \sigma_4(0) + \pi^2 \left( \frac{3\pi^2}{4} - 7 \right)^2 = \pi^2 \left[ \left( \frac{43}{6}\pi^2 - 70 \right) \frac{1}{\varepsilon} + \bar{\sigma}_4 + \frac{6101}{3} - \frac{8}{9}\pi^2 - \frac{4059}{80}\pi^4 \right]. \quad (45)$$

With the same accuracy, we have for the coefficients  $\tilde{a}_m(\xi)$

$$\begin{aligned} \tilde{a}_1(\xi) &= \tilde{\sigma}_1(\xi) = -\frac{\pi^{3/2}}{2} \left( 1 - 2(1 - l_2)\varepsilon \right), \quad \tilde{a}_2(\xi) = \pi \xi \left( 1 - 4\varepsilon \right), \\ \tilde{a}_3(\xi) &= \pi^{5/2} \varepsilon \left( \frac{43\pi^2}{4} - 105 + 2\xi^2 \right), \\ \tilde{a}_4(\xi) &= \frac{\pi^2}{3} \left[ \left( 210 - \frac{43\pi^2}{2} \right) \frac{1}{\varepsilon} + 520 + \frac{2\pi^2}{3} (32 - 21l_2) - 548\zeta_3 + 6\xi \left( 7 - \frac{3\pi^2}{4} \right) - \xi^3 \right]. \end{aligned} \quad (46)$$

Note that the finite parts of the coefficients  $a_1(\xi)$  and  $a_2(\xi)$  coincide with the corresponding ones in [83–85] (see also the Ref. [2] and discussions therein).

We see that the coefficients  $\tilde{a}_m(\xi)$  ( $m = 2, 3, 4$ ) have a simpler form than the corresponding coefficients  $\tilde{\sigma}_m(\xi)$ . Moreover, as in the case of  $\sigma_4(\xi)$ , we also see that

$$a_4(\xi) = \sigma_4(\xi) + O(\varepsilon^0) = \pi^2 \left( \frac{43}{6}\pi^2 - 70 \right) (1 - \xi) \frac{1}{\varepsilon} + O(\varepsilon^0), \quad (47)$$

i.e. the four-loop results are finite in Feynman gauge.

## 6 Conclusion

In the framework of QED<sub>4</sub>, based on the LKFT results (17) for the fermionic propagator, we have shown the specific recurrence relations (22) found in [1] between even and odd values of the polynomial associated with a uniformly transcendental factor  $\Phi_{\text{MV}}(m, l, \varepsilon)$  (18). These relations are simple in the MV scheme introduced in (16). So, they terms of hatted  $\zeta$  values and thus lead to Eq. (28) relating the hatted and standard  $\zeta$  values for all PT orders. The

coefficients in Eq. (28) are expressed in terms of the well-known Bernoulli numbers,  $B_{2m}$  (see (29) and (24)).

These results impose constraints on the results of multi-loop calculations in any PT order, which have already been used in the recent paper [20]. However, the reason for the appearance of hatted  $\zeta$  values, i.e. the appearance of even  $\zeta$ -values along with additional  $\varepsilon$  powers is not clear and requires additional explanation.

In the case of QED<sub>3</sub>, in our recent paper [2] (see also [86]) we studied the LKFT for the massless fermionic propagator in the quenched approximation. Studying this transformation in dimensional regularization, we found that the contributions of odd orders, starting from the third, to even ones, are accompanied by singularities that look like  $\varepsilon^{-1}$  in dimensional regularization. In turn, the even orders produce contributions to the odd ones, starting from the third,  $\sim \varepsilon$ .

Following the arguments in favor of the perturbative finiteness of the massless quenched QED<sub>3</sub> [62–64] and assuming the existence of a finite limit at  $\varepsilon \rightarrow 0$ , in [2] we have shown exactly in  $d = 3$  that *all odd terms of  $a_{2t+1}(\xi)$  in perturbation theory except  $a_1$  must be exactly zero in any gauge.*

This statement was very strong and needed verification, which was done exactly in Ref. [3]. We calculated three- and four-loop corrections, i.e. terms  $a_3(\xi)$  and  $a_4(\xi)$ , directly in the PT framework. We found that  $a_3(\xi)$  is finite and gauge independent when  $\varepsilon \rightarrow 0$ . The coefficient  $a_4(\xi)$  has singularities, which violates the status of the infrared perturbative finiteness of the massless quenched QED<sub>3</sub>.

Moreover, in Ref. [3] we found that the singularities contributing to the coefficient  $a_4(\xi)$ ,  $\sim (1 - \xi)$  and thus  $a_4(\xi)$  is finite in the Feynman gauge. The reason for this effect is not clear and more research is needed to elucidate it.

Author thanks the Organizing Committee of the LV PNPI Winter School for the invitation.

# References

- [1] A. V. Kotikov and S. Teber, Phys. Rev. D **100**, 105017 (2019), arXiv:1906.10930 [hep-th].
- [2] V. P. Gusynin, A. V. Kotikov, and S. Teber, Phys. Rev. D **102**, 025013 (2020), arXiv:2006.09315 [hep-th].
- [3] A. F. Pikelner, V. P. Gusynin, A. V. Kotikov, and S. Teber, Phys. Rev. D **102**, 105012 (2020), arXiv:2008.09400 [hep-th].
- [4] L. D. Landau and I. M. Khalatnikov, Zh. Eksp. Teor. Fiz. **29**, 89 (1955).
- [5] E. S. Fradkin, Zh. Eksp. Teor. Fiz. **29**, 258 (1955).
- [6] P. A. Baikov, K. G. Chetyrkin, and J. H. Kühn, Phys. Rev. Lett. **118**, 082002 (2017), arXiv:1606.08659 [hep-ph].
- [7] K. G. Chetyrkin, G. Falcioni, F. Herzog, and J. A. M. Vermaseren, JHEP **10**, 179 (2017), arXiv:1709.08541 [hep-ph], [Addendum: JHEP 12, 006 (2017)].
- [8] F. Herzog, B. Ruijl, T. Ueda, J. A. M. Vermaseren, and A. Vogt, JHEP **02**, 090 (2017), arXiv:1701.01404 [hep-ph].
- [9] B. Ruijl, F. Herzog, T. Ueda, J. A. M. Vermaseren, and A. Vogt, PoS **RADCOR2017**, 011 (2018), arXiv:1801.06084 [hep-ph].
- [10] J. Davies and A. Vogt, Phys. Lett. B **776**, 189 (2018), arXiv:1711.05267 [hep-ph].
- [11] S. Moch, B. Ruijl, T. Ueda, J. A. M. Vermaseren, and A. Vogt, Phys. Lett. B **782**, 627 (2018), arXiv:1805.09638 [hep-ph].
- [12] A. Vogt *et al.*, PoS **LL2018**, 050 (2018), arXiv:1808.08981 [hep-ph].
- [13] F. Herzog *et al.*, Phys. Lett. B **790**, 436 (2019), arXiv:1812.11818 [hep-ph].
- [14] D. J. Broadhurst, (1999), arXiv:hep-th/9909185.
- [15] P. A. Baikov and K. G. Chetyrkin, Nucl. Phys. B **837**, 186 (2010), arXiv:1004.1153 [hep-ph].
- [16] P. A. Baikov and K. G. Chetyrkin, JHEP **06**, 141 (2018), arXiv:1804.10088 [hep-ph].

- [17] A. Georgoudis *et al.*, JHEP **09**, 098 (2021), arXiv:2104.08272 [hep-ph].
- [18] A. Georgoudis, V. Goncalves, E. Panzer, and R. Pereira, (2018), arXiv:1802.00803 [hep-th].
- [19] P. A. Baikov and K. G. Chetyrkin, JHEP **10**, 190 (2019), arXiv:1908.03012 [hep-ph].
- [20] G. Falcioni, F. Herzog, S. Moch, and A. Vogt, Phys. Lett. B **842**, 137944 (2023), arXiv:2302.07593 [hep-ph].
- [21] A. V. Kotikov and S. Teber, Phys. Part. Nucl. **51**, 562 (2020), arXiv:1912.10957 [hep-th].
- [22] A. V. Kotikov and S. Teber, Phys. Atom. Nucl. **84**, 105 (2021), arXiv:2101.06952 [hep-th].
- [23] N. Dorey and N. E. Mavromatos, Nucl. Phys. B **386**, 614 (1992).
- [24] M. Franz and Z. Tesanovic, Phys. Rev. Lett. **87**, 257003 (2001), arXiv:cond-mat/0012445.
- [25] I. F. Herbut, Phys. Rev. B **66**, 094504 (2002), arXiv:cond-mat/0202491.
- [26] K. Farakos, G. Koutsoumbas, and N. E. Mavromatos, Int. J. Mod. Phys. B **12**, 2475 (1998), arXiv:cond-mat/9805402.
- [27] G. W. Semenoff, Phys. Rev. Lett. **53**, 2449 (1984).
- [28] V. P. Gusynin, S. G. Sharapov, and J. P. Carbotte, Int. J. Mod. Phys. B **21**, 4611 (2007), arXiv:0706.3016 [cond-mat.mes-hall].
- [29] A. H. Castro Neto, F. Guinea, N. M. R. Peres, K. S. Novoselov, and A. K. Geim, Rev. Mod. Phys. **81**, 109 (2009), arXiv:0709.1163 [cond-mat.other].
- [30] V. N. Kotov, B. Uchoa, V. M. Pereira, A. H. C. Neto, and F. Guinea, Rev. Mod. Phys. **84**, 1067 (2012), arXiv:1012.3484 [cond-mat.str-el].
- [31] S. Teber, *Field theoretic study of electron-electron interaction effects in Dirac liquids*, PhD thesis, Paris, LPTHE, 2017, arXiv:1810.08428 [cond-mat.mes-hall].
- [32] T. W. Appelquist, M. J. Bowick, D. Karabali, and L. C. R. Wijewardhana, Phys. Rev. D **33**, 3704 (1986).

- [33] T. Appelquist, D. Nash, and L. C. R. Wijewardhana, *Phys. Rev. Lett.* **60**, 2575 (1988).
- [34] R. D. Pisarski, *Phys. Rev. D* **29**, 2423 (1984).
- [35] D. Nash, *Phys. Rev. Lett.* **62**, 3024 (1989).
- [36] A. V. Kotikov, *JETP Lett.* **58**, 731 (1993).
- [37] A. V. Kotikov, *Phys. Atom. Nucl.* **75**, 890 (2012), arXiv:1104.3888 [hep-ph].
- [38] D. Atkinson, P. W. Johnson, and P. Maris, *Phys. Rev. D* **42**, 602 (1990).
- [39] M. R. Pennington and D. Walsh, *Phys. Lett. B* **253**, 246 (1991).
- [40] V. P. Gusynin, A. H. Hams, and M. Reenders, *Phys. Rev. D* **53**, 2227 (1996), arXiv:hep-ph/9509380.
- [41] V. P. Gusynin and M. Reenders, *Phys. Rev. D* **68**, 025017 (2003), arXiv:hep-ph/0304302.
- [42] P. Maris, *Phys. Rev. D* **54**, 4049 (1996), arXiv:hep-ph/9606214.
- [43] C. S. Fischer, R. Alkofer, T. Dahm, and P. Maris, *Phys. Rev. D* **70**, 073007 (2004), arXiv:hep-ph/0407104.
- [44] V. P. Gusynin and P. K. Pyatkovskiy, *Phys. Rev. D* **94**, 125009 (2016), arXiv:1607.08582 [hep-ph].
- [45] A. V. Kotikov, V. I. Shilin, and S. Teber, *Phys. Rev. D* **94**, 056009 (2016), arXiv:1605.01911 [hep-th], [Erratum: *Phys.Rev.D* 99, 119901 (2019)].
- [46] A. V. Kotikov and S. Teber, *Phys. Rev. D* **94**, 114011 (2016), arXiv:1902.03790 [hep-th], [Addendum: *Phys.Rev.D* 99, 059902 (2019)].
- [47] A. V. Kotikov and S. Teber, *Particles* **3**, 345 (2020).
- [48] N. Karthik and R. Narayanan, *Phys. Rev. D* **100**, 054514 (2019), arXiv:1908.05500 [hep-lat].
- [49] E. Marinari, G. Parisi, and C. Rebbi, *Nucl. Phys. B* **190**, 734 (1981).
- [50] F. Fucito, E. Marinari, G. Parisi, and C. Rebbi, *Nucl. Phys. B* **180**, 369 (1981).

- [51] E. Marinari, G. Parisi, and C. Rebbi, Phys. Rev. Lett. **47**, 1795 (1981).
- [52] H. Hamber and G. Parisi, Phys. Rev. Lett. **47**, 1792 (1981).
- [53] D. Hatton *et al.*, (HPQCD Collaboration), Phys. Rev. D **102**, 054511 (2020), arXiv:2005.01845 [hep-lat].
- [54] P. I. Fomin, V. P. Gusynin, V. A. Miransky, and Y. A. Sitenko, Riv. Nuovo Cim. **6N5**, 1 (1983).
- [55] V. A. Miransky, *Dynamical symmetry breaking in quantum field theories* (, 1994).
- [56] C. N. Leung, S. T. Love, and W. A. Bardeen, Nucl. Phys. B **273**, 649 (1986).
- [57] C. N. Leung, S. T. Love, and W. A. Bardeen, Nucl. Phys. B **323**, 493 (1989).
- [58] B. Holdom, Phys. Rev. Lett. **62**, 997 (1989).
- [59] U. Mahanta, Phys. Lett. B **225**, 181 (1989).
- [60] V. P. Gusynin, A. W. Schreiber, T. Sizer, and A. G. Williams, Phys. Rev. D **60**, 065007 (1999), arXiv:hep-th/9811184.
- [61] A. James, A. V. Kotikov, and S. Teber, Phys. Rev. D **101**, 045011 (2020), arXiv:1912.05982 [hep-th].
- [62] R. Jackiw and S. Templeton, Phys. Rev. D **23**, 2291 (1981).
- [63] O. M. Del Cima, D. H. T. Franco, and O. Piguet, Phys. Rev. D **89**, 065001 (2014), arXiv:1310.3541 [hep-th].
- [64] N. Karthik and R. Narayanan, Phys. Rev. D **96**, 054509 (2017), arXiv:1705.11143 [hep-th].
- [65] A. V. Kotikov and S. Teber, Phys. Part. Nucl. **50**, 1 (2019), arXiv:1805.05109 [hep-th].
- [66] A. V. Kotikov and V. N. Velizhanin, (2005), arXiv:hep-ph/0501274.
- [67] D. I. Kazakov and A. V. Kotikov, Nucl. Phys. B **307**, 721 (1988), [Erratum: Nucl.Phys.B 345, 299 (1990)].

- [68] A. V. Kotikov, Phys. Atom. Nucl. **57**, 133 (1994).
- [69] A. A. Vladimirov, Theor. Math. Phys. **43**, 417 (1980).
- [70] A. V. Kotikov and L. N. Lipatov, Nucl. Phys. B **582**, 19 (2000), arXiv:hep-ph/0004008.
- [71] A. V. Kotikov and L. N. Lipatov, Nucl. Phys. B **661**, 19 (2003), arXiv:hep-ph/0208220, [Erratum: Nucl.Phys.B 685, 405–407 (2004)].
- [72] A. V. Kotikov and L. N. Lipatov, DGLAP and BFKL evolution equations in the N=4 supersymmetric gauge theory, in *35th Annual Winter School on Nuclear and Particle Physics*, 2001, arXiv:hep-ph/0112346.
- [73] A. V. Kotikov, L. N. Lipatov, A. I. Onishchenko, and V. N. Velizhanin, Phys. Lett. B **595**, 521 (2004), arXiv:hep-th/0404092, [Erratum: Phys.Lett.B 632, 754–756 (2006)].
- [74] L. Bianchi, V. Forini, and A. V. Kotikov, Phys. Lett. B **725**, 394 (2013), arXiv:1304.7252 [hep-th].
- [75] J. Fleischer, A. V. Kotikov, and O. L. Veretin, Nucl. Phys. B **547**, 343 (1999), arXiv:hep-ph/9808242.
- [76] A. V. Kotikov, Differential Equations and Feynman Integrals, in *Antidifferentiation and the Calculation of Feynman Amplitudes*, 2021, arXiv:2102.07424 [hep-ph].
- [77] A. V. Kotikov, L. N. Lipatov, A. Rej, M. Staudacher, and V. N. Velizhanin, J. Stat. Mech. **0710**, P10003 (2007), arXiv:0704.3586 [hep-th].
- [78] Z. Bajnok, R. A. Janik, and T. Lukowski, Nucl. Phys. B **816**, 376 (2009), arXiv:0811.4448 [hep-th].
- [79] T. Lukowski, A. Rej, and V. N. Velizhanin, Nucl. Phys. B **831**, 105 (2010), arXiv:0912.1624 [hep-th].
- [80] C. Marboe, V. Velizhanin, and D. Volin, JHEP **07**, 084 (2015), arXiv:1412.4762 [hep-th].
- [81] C. Marboe and V. Velizhanin, JHEP **11**, 013 (2016), arXiv:1607.06047 [hep-th].

- [82] A. V. Kotikov and S. Teber, Phys. Rev. D **89**, 065038 (2014), arXiv:1312.2430 [hep-ph].
- [83] A. Bashir, A. Kizilersu, and M. R. Pennington, Phys. Rev. D **62**, 085002 (2000), arXiv:hep-th/0010210.
- [84] A. Bashir, Phys. Lett. B **491**, 280 (2000), arXiv:hep-th/0011022.
- [85] A. Bashir and A. Raya, Phys. Rev. D **66**, 105005 (2002), arXiv:hep-ph/0206277.
- [86] A. V. Kotikov, On Landau-Khalatnikov-Fradkin transformation in quenched QED3, 2023, arXiv:2305.17775 [hep-th].

# GENERALIZATION OF SUDAKOV FORM FACTOR FOR SKEWED REGIME

Victor T. Kim<sup>1,2</sup>, Grigorii B. Pivovarov<sup>3</sup>

<sup>1</sup> Petersburg Nuclear Physics Institute of NRC “KI”, Gatchina

<sup>2</sup> Peter the Great St. Petersburg Polytechnic University,  
St. Petersburg

<sup>3</sup> Institute for Nuclear Research RAS, Moscow

## Abstract

On the example of massless QED we study an asymptotic of the vertex when only one of the two virtualities of the external fermions is sent to zero. We call this regime the skewed Sudakov regime. We consider the problem in the one loop approximation and then in all orders. First, we show that the asymptotic is described with a single form factor, for which we derive a linear evolution equation. The linear operator involved in this equation has a discrete spectrum. Its eigenfunctions and eigenvalues are found. The spectrum is a shifted sequence of harmonic numbers. With the spectrum found, we represent the expansion of the asymptotic in the fine structure constant in terms of multiple polylogarithms. Using this representation, the exponentiation of the doubly logarithmic corrections of the Sudakov form factor is recovered. It is pointed out that the form factor of the skewed Sudakov regime is growing with the virtuality of a fermion decreasing at a fixed virtuality of another fermion.

# ОБОБЩЕНИЕ СУДАКОВСКОГО ФОРМФАКТОРА НА АСИММЕТРИЧНЫЙ РЕЖИМ

Виктор Т. Ким<sup>1,2</sup>, Григорий Б. Пивоваров<sup>3</sup>

<sup>1</sup> Петербургский институт ядерной физики НИЦ «КИ», Гатчина

<sup>2</sup> Санкт-Петербургский политехнический университет Петра Великого, Санкт-Петербург

<sup>3</sup> Институт ядерных исследований РАН, Москва

## Аннотация

На примере безмассовой КЭД изучается асимптотика вершины при только одна из двух виртуальностей внешних фермионов стремится к нулю. Мы называем этот режим асимметричным режимом Судакова. Проблема рассматривается сначала в однопетлевом приближении, а затем во всех порядках. Сначала мы покажем, что асимптотика описывается единственным форм-фактором, для которого мы получаем уравнение для линейной эволюции. Линейный оператор, входящий в это уравнение, имеет дискретный спектр. Найдены его собственные функции и собственные значения. Спектр представляет собой сдвинутую последовательность гармонических чисел. С найденным спектром мы представляем разложение асимптотики по постоянной тонкой структуре в терминах кратных полилогарифмов. Используя это представление, мы воспроизводим экспоненциацию дважды-логарифмических поправок форм-фактора Судакова. Показано, что форм-фактор Судакова в асимметричном режиме растет с уменьшением виртуальности фермиона при фиксированной виртуальности другого фермиона.

# 1 Introduction

In the textbooks (see, e.g., [1]) perturbative corrections proportional to powers of a product of two logarithms of kinematic invariants are related to the infrared divergences. It is also pointed out in the textbooks that it was V. V. Sudakov who discovered these corrections [2]. If a curious student checks the original paper, she/he discovers that infrared divergences are not mentioned at all. The reason for this is that Sudakov considered not a physical phenomenon but a technical problem of describing the amplitudes of massless QED near the zero virtualities of the fermions.

While the treatment of the infrared divergences is still under active scrutiny [3], the technical problem considered by Sudakov is well understood. In this lecture we want to generalize and simplify the treatment of Sudakov, leaving a tougher problem of considering infrared divergences aside. Namely, we will consider a three-point amplitude of massless QED at a small virtuality of a fermion. This problem differs the one considered by Sudakov, because we do not require the virtuality of the second fermion to be small. Obviously, the classic result of Sudakov should be recovered in our treatment, because one can send the second virtuality to zero at the end of the day. We will call the regime when only one of the fermion virtualities is sent to zero the *skewed Sudakov regime*, because there will be no symmetry between the fermions in our treatment.

The purpose in this lecture is to consider in the beginning the skewed Sudakov regime in the one loop approximation and to develop a method to be applied to the problem in all orders later.

A preliminary question we are to answer is what should be the quantity we will study. Sudakov studied the irreducible three point amplitude. Should we do the same? This is not immediately evident because the case we consider differs the one considered by Sudakov. In particular, one could include self-energy corrections to one or several legs of the amplitude under consideration. The choice we take is to include the self-energy corrections to the fermion leg of small virtuality. If the renormalization scale is chosen to be equal to the small virtuality, the ratio of the self-energy correction to the small virtuality does not depend on the small virtuality. On the other hand, such an amplitude—the three-point amplitude with the self energy corrections included in a fermion leg—does not contain ultraviolet divergences because of the Ward-Takahashi identity between the renormalization constants. These observations explain our choice.

In the next section we introduce our notations, give the classic result of

Sudakov in the notations introduced, and our generalization. After that, we sketch the derivation of the generalization in the one loop approximation and then in all orders.

The lecture is based on papers [4] and [5].

## 2 Notations and Results for One-Loop Order

Let  $\Gamma_\mu(p, p')$  be the three-point amplitude of massless QED, where  $p, p'$  are the momenta of incoming and outgoing fermion respectively. Self-energy corrections are included in the  $p$ -leg, and the factor  $ie$  excluded. Neglecting powers of the coupling  $e$  one has  $\Gamma_\mu(p, p') \approx \gamma_\mu$ .

To avoid infrared problems, we require  $p^2 < 0$ ,  $p'^2 < 0$ , and  $(p - p')^2 < 0$ . We will use two variables

$$x = \frac{-p^2}{2pp'}, \quad y = \frac{-p'^2}{2pp'}. \quad (1)$$

In terms of these variables, Sudakov regime is the regime when both  $x$  and  $y$  are small and positive. The Sudakov result is that in the Sudakov regime one has

$$\Gamma_\mu(p, p') \approx \gamma_\mu \left( 1 - \frac{\alpha}{2\pi} \log(x) \log(y) + \dots \right), \quad (2)$$

where  $\alpha = e^2/(4\pi)$  is the fine structure constant.

In the skewed Sudakov regime, only one of the variables  $x, y$  is small, while the second variable is not restricted. For definiteness, we consider the regime when  $x \rightarrow +0$ . The generalization of (2) for this regime reads

$$\begin{aligned} \Gamma_\mu(p, p') \approx & \gamma_\mu \left( 1 - \frac{\alpha}{2\pi} \log(x) \left[ \frac{3}{2} + (1+y) \log\left(\frac{y}{1+y}\right) \right] + \dots \right) + \\ & + \frac{\alpha}{2\pi} \log(x) \frac{p_\mu p'^\mu}{pp'} \left[ 1 + (1+y) \log\left(\frac{y}{1+y}\right) \right] + \dots \end{aligned} \quad (3)$$

To check that this agrees with (2) one needs to realize that  $p'^\mu$  is the leftmost position is small at  $p'^2 \rightarrow 0$ , neglect the second line in (3), and send  $y \rightarrow 0$  in the first line.

Our aim in the next two sections is to derive (3). The first step to this end is to give an integral representation of  $\Gamma_\mu^{(1)}(p, p')$ , which is the one-loop contribution to  $\Gamma_\mu(p, p')$ .

### 3 An Integral Representation for the One-Loop Correction

The one-loop correction  $\Gamma_\mu^{(1)}(p, p')$  is a sum of two diagrams. Namely, of the self-energy correction to the  $p$ -line, and of the 1PI (triangle) diagram. The sum can be represented as an integral over loop momentum, for which we take the momentum  $k$  of the incoming fermion after emission of the loop photon:

$$\Gamma_\mu^{(1)}(p, p') = -e^2 \int \frac{d^4k}{(2\pi)^4} \Gamma_{\mu\nu}^{(0)}(k, p'; p - k) \frac{\not{k}}{k^2} \gamma_\rho (iD^{\rho\nu}(p - k)), \quad (4)$$

where  $D^{\rho\nu}(k - p)$  is the photon propagator (we use arbitrary covariant gauge), and  $\Gamma_{\mu\nu}^{(0)}(k, p'; p - k)$  is the connected tree amplitude of absorption of two photons by a fermion divided by  $(ie)^2$ :

$$\Gamma_{\mu\nu}^{(0)}(k, p'; l) = \gamma_\mu \frac{i\not{k} + i\not{l}}{(k + l)^2} \gamma_\nu + \gamma_\nu \frac{i\not{p}' - i\not{l}}{(p' - l)^2} \gamma_\mu. \quad (5)$$

The first term generates the self-energy correction in (4), and the second, the triangle diagram. Using, for example, dimensional regularization, one checks that ultraviolet divergences of these two contributions cancel against each other, and one does not regularise the integral in (4) in any way, because it converges. The  $i\epsilon$ -prescription is used to define the integral at  $k^2 = 0$ ,  $(p - k)^2 = 0$ , and  $(p' - p + k)^2 = 0$ .

We now change the integration variables in (4). The loop momentum  $k$  is decomposed into longitudinal and transverse components,  $k = k_\parallel + k_\perp$ , where  $k_\parallel$  is a linear combination of  $p$  and  $p'$ , and  $pk_\perp = p'k_\perp = 0$ . These conditions imply that  $k_\perp$  is a two-dimensional euclidean vector,  $k_\perp^2 < 0$ . Using polar coordinates for the transverse components  $k_\perp = (k_1, k_2)$  one has

$$2dk^4 = d^2k_\parallel (\theta(\phi)\theta(2\pi - \phi)d\phi) dk_\perp^2 \theta(-k_\perp^2), \quad (6)$$

where the components are related to the polar angle,  $k_1 = \cos(\phi)\sqrt{-k_\perp^2}$ ,  $k_2 = \sin(\phi)\sqrt{-k_\perp^2}$ .

Next we notice that one can do the following replacement in (27) if it is used in (4):

$$\theta(-k_\perp^2) \rightarrow \theta(-k_\perp^2) - \theta(k_\parallel^2). \quad (7)$$

This is the case because the second term gives exactly zero if substituted in (4) due to the  $i\epsilon$ -prescription.

Furthermore, one easily checks that

$$\theta(-k_{\perp}^2) - \theta(k_{\parallel}^2) = -\frac{k_{\parallel}^2}{|k_{\parallel}^2|} \theta(\nu) \theta(1 - \nu), \quad (8)$$

where we have introduced a new variable, which we will call *the inclination* of the fermion with momentum  $k$ :

$$\nu \equiv \frac{k_{\parallel}^2}{k^2}. \quad (9)$$

This variable is in one-to-one correspondence with  $k_{\perp}^2$ :

$$k_{\perp}^2 = k_{\parallel}^2(1/\nu - 1). \quad (10)$$

We see that one can replace the integral over  $d^4k$  in (4) with integrations over the polar angle, the inclination, and the integral over the longitudinal momentum:

$$\begin{aligned} \Gamma_{\mu}^{(1)}(p, p') &= \frac{\alpha}{2\pi} \int_0^{2\pi} \frac{d\phi}{2\pi} \int_0^1 d\nu \int \frac{d^2k_{\parallel}}{2\pi} \frac{\Gamma_{\mu\nu}^{(0)}(k, p'; p - k) \not{k} \gamma_{\rho}}{(k_{\parallel} - \nu p)^2 + p^2 \nu(1 - \nu) + i\epsilon} \times \\ &\quad \times (i(p - k)^2 D^{\rho\nu}(p - k)). \end{aligned} \quad (11)$$

We stress that no approximation is used in the above transformations of (4) into (11). It is tacitly assumed in (11) that  $k$  is expressed in terms of the integration variables. Another point to contemplate is that the components of  $k_{\perp}$  are purely imaginary in this expression if  $k_{\parallel}^2 > 0$ .

Next we will use the integral representation (11) to consider the limit  $p^2 \rightarrow 0$ . Along the way we will explain why  $\nu$  has the name inclination.

## 4 The Limit at the One-Loop

The denominator in (11) vanishes at  $k_{\parallel} = \nu p, p^2 = 0$ . Because of this, the leading contribution to the integral in the limit  $p^2 \rightarrow 0$  comes from a vicinity of the point  $k_{\parallel} = \nu p$ . This explains the name inclination: at  $p^2 \rightarrow 0$  the fermion is “inclined” to keep the fraction  $\nu$  of the initial momentum  $p$  after the emission of the photon. Also, in the leading approximation one can restrict the integration in  $k_{\parallel}$  to a vicinity  $V$  of the point  $k_{\parallel} = \nu p$ .

Next we notice that the contribution related to the longitudinal part of the photon propagator has a finite limit at  $p^2 \rightarrow 0$ . Because of this, in (11) we can do the replacement  $(i(p - k)^2 D^{\rho\nu}(p - k)) \rightarrow g^{\nu\rho}$  in the leading approximation.

Furthermore,  $\not{p}$  in the rightmost position is small when  $p^2 \rightarrow 0$ . In view of this the numerator of (11) can be approximated as follows:

$$\begin{aligned}\Gamma_{\mu\nu}^{(0)}(k, p'; p - k) \not{k} \gamma^\nu &\approx 2i\nu \left[ \gamma_\mu + \frac{2pp' \gamma_\mu - 2\not{p}' p_\mu}{p'^2 - 2pp'(1 - \nu)} \right] \\ &= 2i\nu \left[ \left(1 - \frac{1}{1 + y - \nu}\right) \gamma_\mu + \frac{1}{1 + y - \nu} \frac{\not{p}' p_\mu}{p' p} \right].\end{aligned}\quad (12)$$

The dependence on  $k_{\parallel}$  remains only in the denominator. The integration of the denominator can be removed with the approximate equality

$$\int_V \frac{id^2 k_{\parallel} / \pi}{(k_{\parallel} - \nu p)^2 + p^2 \nu (1 - \nu)} \approx -\log(x).\quad (13)$$

As a result, one obtains

$$\Gamma_\mu^{(1)}(p, p') \approx -\frac{\alpha}{2\pi} \log(x) \int_0^1 d\nu \left[ \left(1 - \frac{1}{1 + y - \nu}\right) \gamma_\mu + \frac{1}{1 + y - \nu} \frac{\not{p}' p_\mu}{p' p} \right] \nu,\quad (14)$$

which implies (3).

We have given above a generalization of the classic result of Sudakov [2] to a wider kinematical range. Of course, Sudakov obtained not only the one-loop result but gave his approximate expressions at any number of loops, and was able to resum them into his famous form-factor. In our view, our derivation is simpler than the one-loop part of [2].

Now we will try to do the above exercise in all orders, and to resum the expressions into form factor(s).

## 5 Skewed Sudakov Regime in All Orders

We start with recalling again the classical result of Ref. [2] with the introduced notations earlier. Let  $\Gamma_\mu(p, p')$  be a connected three-point amplitude of massless QED renormalized with minimal subtractions. Here  $p$  and  $p'$  are the momenta of the incoming and outgoing fermion respectively. We use namely a *connected* amplitude because it will be technically important for our consideration to include self-energy corrections to one of the external fermion legs of  $\Gamma_\mu(p, p')$ . We also exclude again the overall factor  $ie$  from the definition of  $\Gamma_\mu(p, p')$ . Due to this, the expansion of  $\Gamma_\mu(p, p')$  in the coupling starts with Dirac gamma matrix,  $\Gamma_\mu(p, p') = \gamma_\mu + \dots$

To avoid infrared problems, one considers  $\Gamma_\mu(p, p')$  at negative virtualities of the external fermions,  $p^2 < 0, p'^2 < 0$ , and of the external photon,  $(p' -$

$p)^2 < 0$ . The results of [2] are for the kinematics when, on top of the above restrictions, the Minkowski product of the fermion momenta satisfies the inequality preventing Wick rotation,  $(pp')^2 > p^2p'^2$ . These conditions combined imply that if  $|p^2|$  and  $|p'^2|$  are small with respect to  $|(p-p')^2|$ ,  $pp' > 0$ . We will use two positive variables to describe this kinematics:

$$x = \frac{-p^2}{2pp'} > 0, y = \frac{-p'^2}{2pp'} > 0. \quad (15)$$

We repeat here again Sudakov result of Ref. [2] Eq. (2) in our notations:

$$\Gamma_\mu(p, p') \approx \gamma_\mu \exp\left(-\frac{\alpha}{2\pi} \log(x) \log(y)\right), \quad (16)$$

where the approximate equality holds when both  $|p^2|$  and  $|p'^2|$  are small with respect to  $|(p' - p)^2|$ , and their ratio is of order unity. Also,  $\alpha$  is the QED fine structure constant normalized at any of the small virtualities.

In what follows we derive a generalization of the approximation (16) valid in a wider region where the magnitude of only one of the two fermion virtualities is small with respect to the magnitude of the virtuality of the photon. Because the symmetry between the two fermion virtualities present in the Sudakov regime is lost for this generalization, we call this generalized regime the *skewed* Sudakov regime. For definiteness, we consider the kinematics with  $|p^2|$  small with respect to the magnitude of the photon virtuality, and no restrictions on  $|p'^2|$  is present. All the considerations can be repeated with the obvious changes for the case when  $|p'^2|$  is small instead of  $|p^2|$ .

After the external fermion with small virtuality magnitude is specified, we can also specify the external fermion leg of  $\Gamma_\mu(p, p')$  with self-energy corrections included—it is the leg of small virtuality. Also, as before, the fine structure constant in the subsequent formulas is normalized at the small virtuality.

To write down the generalization of the approximation (2) we introduce the following variables:

$$t = -\frac{\alpha \log(x)}{2\pi} > 0, z = \frac{1}{1+y}. \quad (17)$$

Notice that  $0 < z < 1$ , and, in the Sudakov regime  $z \rightarrow 1$  from the left. With these variables the approximation valid in the skewed Sudakov regime reads

$$\Gamma_\mu(p, p') \approx \gamma_\mu F(t, z) + \frac{p_\mu \not{p}'}{pp'} [e^{t/2} - F(t, z)], \quad (18)$$

where the form factor  $F(t, z)$  is as follows:

$$F(t, z) = e^{3t/2} \sum_{n=0}^{\infty} e^{-tH_{n+1}} z^n (1-z). \quad (19)$$

Here  $H_{n+1}$  are the harmonic numbers,

$$H_k = \sum_{i=1}^k \frac{1}{i}. \quad (20)$$

We point out that the series in the right hand side of Eq. (19) converges at  $|z| < 1$ , and to recover the approximation (2) one has to send  $z \rightarrow 1$ , where the convergence fails.

To overcome this difficulty, we derive from Eq. (19) the following representation:

$$F(t, z) = e^{3t/2} \left[ 1 + \frac{1}{z} \sum_{\underline{s}} \frac{(-t)^{|\underline{s}|}}{\underline{s}!} Li_{\underline{s}}(z) \right], \quad (21)$$

where the sum runs over strings of positive integers of arbitrary depth  $d$ ,  $\underline{s} = (s_1, s_2, \dots, s_d)$ ;  $|\underline{s}|$  denotes the weight of the string,

$$|\underline{s}| = \sum_{i=1}^d s_i,$$

and the factorial of the string is the product of the factorials,

$$\underline{s}! = \prod_{i=1}^d s_i!$$

The key ingredient of the representation (21) is the so called multiple polylogarithm  $Li_{\underline{s}}(z)$ . See, e. g., Ref. [6] for an introductory exposition of these functions, and Refs. [7,8] for their recent applications to Feynman integrals.

Using the properties of multiple polylogarithms discussed in Ref. [6] one can single out the terms of the sum of Eq. (21) most singular in the limit  $z \rightarrow 1$ . By ‘‘most singular’’ we mean that each power of  $t$  is compensated by a power of  $\log(1 - z)$ . These are the terms with the strings  $\underline{s}$  consisting of units,  $\underline{s}_d = (1, \dots, 1)$ , with the unit repeated  $d = |\underline{s}|$  times. Explicitly,

$$Li_{\underline{s}_d}(z) = (-\log(1 - z))^d / d! \approx (-\log(y))^d / d! \quad (22)$$

Using this and taking into account that  $p''$  is small in the Sudakov regime, one reproduces approximation (2) from approximation (18).

On the other hand, at fixed  $z < 1$  and large  $t$  one picks up the infinitely growing term in Eq. (19) and obtains the following approximation valid at  $x \rightarrow +0$  and  $y > 0$  fixed:

$$\Gamma_{\mu}(p, p') \approx \frac{y}{(1 + y)x^{\alpha/(4\pi)}} \left[ \gamma_{\mu} + 2 \frac{p_{\mu} p'}{-p^2} \right]. \quad (23)$$

We conclude that Eqs. (18) and (19) give a unified description for qualitatively different asymptotics of the vertex, one of which coincides with the known Sudakov asymptotic.

The validity of approximation (18), (19), and the representation (21) are our main results. In the rest of the lecture we sketch the way these results are derived.

## 6 Schwinger-Dyson Equation and the Inclination Variable

The vertex  $\Gamma_\mu(p, p')$  coincides with its bare counterpart because its renormalization constant  $Z_\Gamma = 1$  due to Ward identities between the renormalization constants of QED. With this observation one can derive the following Schwinger-Dyson equation for the vertex:

$$\Gamma_\mu(p, p') = \gamma_\mu - \alpha \int \frac{2d^4k}{(2\pi)^3} \Gamma_{\mu\lambda}(k, p'; p - k) \frac{\not{k}\gamma_\rho}{k^2} (iD^{\lambda\rho}(p - k)). \quad (24)$$

Here  $\Gamma_{\mu\nu}(k, p'; p - k)$  is a renormalized connected four point amplitude with  $k$  and  $p'$  denoting the momenta of incoming and outgoing fermion, and  $p - k$  is the incoming momentum of a photon with Lorentz index  $\nu$ . Self-energy corrections are included in its  $k$ -leg, and the amplitude is divided by  $(ie)^2$ . Its expansion in the coupling starts as follows:

$$\Gamma_{\mu\nu}(k, p'; l) = \gamma_\nu \frac{i}{\not{p}' - \not{l}} \gamma_\mu + \gamma_\mu \frac{i}{\not{k} + \not{l}} \gamma_\nu + \dots \quad (25)$$

Another ingredient in Eq. (24) is the full photon propagator  $D^{\nu\rho}(p - k)$ . We use an arbitrary covariant gauge to define it.

Notice that the integration in the right hand side of Eq. (24) is ultraviolet (UV) finite. This is because the UV divergences originating from various contributions to the four point amplitude under the integral cancel against each other due to gauge invariance. For example, in the one loop approximation, the first term in the right hand side of Eq. (25) produces an 1PI contribution to the vertex, while the second, the self energy correction to the  $p$ -leg, and their sum is UV finite. We conclude that there is no need to regularize the integration in any way.

Next we change the integration variables. A first step in this direction is to decompose  $k$  into transverse and longitudinal parts, the longitudinal part is a

linear combination of the external momenta  $p$  and  $p'$ , and the transverse part has zero Minkowski products with them:

$$\begin{aligned} k &= k_{\perp} + k_{\parallel}, \\ k_{\parallel} &= \alpha p + \beta p', p k_{\perp} = 0, p' k_{\perp} = 0. \end{aligned} \quad (26)$$

Because of the above condition  $(pp')^2 > p^2 p'^2$ ,  $k_{\perp}$  is necessarily euclidean, and we represent the measure of integration from Eq. (24) in the polar coordinates:

$$2d^4 k \rightarrow d^2 k_{\parallel} (\theta(\phi) \theta(2\pi - \phi) d\phi) dk_{\perp}^2 \theta(-k_{\perp}^2), \quad (27)$$

where the transverse components are

$$k_1 = \cos(\phi) \sqrt{-k_{\perp}^2}, k_2 = \sin(\phi) \sqrt{-k_{\perp}^2}. \quad (28)$$

Next we observe that if there were no restriction on the sign of  $k_{\perp}^2$  in the last factor of Eq. (27), the integral in Eq. (24) would vanish. This happens because of the analytic properties of the integrand. In the one loop approximation this is evident from the explicit form of Eq. (25), and is less evident but true in any order of the perturbation theory. One can check it using Feynman parameters, and general properties of Symanzik polynomials [9]. Taking this observation into account, we replace the last factor in Eq. (27) as follows:

$$\theta(-k_{\perp}^2) \rightarrow \theta(-k_{\perp}^2) - \theta(k_{\parallel}^2). \quad (29)$$

We stress that this substitution of the measure does not change the right hand side of Eq. (24). Furthermore, the difference of theta functions can be represented as follows:

$$\theta(-k_{\perp}^2) - \theta(k_{\parallel}^2) = -\frac{k_{\parallel}^2}{|k_{\parallel}^2|} \theta(\nu) \theta(1 - \nu), \quad (30)$$

where we introduced a new variable  $\nu$ , which we will call the *inclination* of the fermion with momentum  $k$ :

$$\nu \equiv \frac{k_{\parallel}^2}{k^2}. \quad (31)$$

This variable is in one-to-one correspondence with  $k_{\perp}^2$ :

$$k_{\perp}^2 = k_{\parallel}^2 (1/\nu - 1). \quad (32)$$

Notice that when  $k_{\parallel}^2 > 0$ , and  $0 < \nu < 1$ , the components of  $k_{\perp}$  are purely imaginary. We say that using inclination leads one to consider *doubly virtual*

particles, by which we mean particles not only away from the mass shell, but also with imaginary momentum components.

The last step in the transformation of the integration measure which we need is to replace the variable  $k_{\perp}^2$  with the inclination variable:

$$dk_{\perp}^2 = |k_{\parallel}^2| d\nu/\nu^2. \quad (33)$$

We conclude that Schwinger-Dyson equation (24) can be rewritten as follows:

$$\Gamma_{\mu}(p, p') = \gamma_{\mu} + \frac{\alpha}{2\pi} \int_0^{2\pi} \frac{d\phi}{2\pi} \int_0^1 d\nu \int \frac{d^2 k_{\parallel}}{2\pi}. \quad (34)$$

$$\cdot \frac{\Gamma_{\mu\lambda}(k, p'; p - k)}{(k_{\parallel} - \nu p)^2 + p^2 \nu(1 - \nu) + i\epsilon} (i(p - k)^2 D^{\lambda\rho}(p - k)) \not{k} \gamma_{\rho}.$$

It is tacitly assumed in this formula that the transverse components of  $k$  are expressed in terms of the integration variables, for which one uses Eqs. (28) and (32). As mentioned above, integration over the inclination implies integration over the momentum of the doubly virtual particle.

The form of Eq. (34) explains the origin of the name ‘‘inclination’’ for the variable  $\nu$ : at  $p^2 \rightarrow 0$  a vicinity of the point  $k_{\parallel} = \nu p$  gives a dominant contribution to the integral. So, one can say that  $\nu$  is a fraction of the original momentum which the fermion is inclined to keep after emitting a photon.

In the next Section we expound on this, and see how restricting the integration to a vicinity of the point  $k_{\parallel} = \nu p$  allows one to truncate the Schwinger-Dyson equation (34) to a closed equation for the vertex.

## 7 Truncation of the Schwinger-Dyson Equation

First we point out that if  $k_{\parallel} = \nu p$ , Eq. (32) implies that  $k_{\perp} \rightarrow 0$  when  $p^2 \rightarrow 0$ . Therefore, in the leading approximation  $k_{\perp}$  can be set to zero in the right hand side of Eq. (34) and the integration in the angle  $\phi$  removed. Second, the factor  $\not{k} \gamma_{\rho}$  can be replaced as follows:

$$\not{k} \gamma_{\rho} \rightarrow 2\nu(p - k)_{\rho}/(1 - \nu), \quad (35)$$

because  $\not{k} \gamma_{\rho} = 2\nu p_{\rho} - \gamma_{\rho} \not{p}$  at  $k = \nu p$ , and  $\not{p} \approx 0$  in the rightest position.

Next simplification which one can make near the point  $k_{\parallel} = \nu p$  is available if the dimensional regularization unit of mass  $\mu^2$  normalizing the renormalized fine structure constant is taken to be equal to  $-p^2$ . In this case the vacuum

polarization involved in the photon propagator may be set to zero, because it depends on  $\log(-p^2/\mu^2) = 0$ . This means that photon propagator in Eq. (34) can be replaced with the free one.

The last simplification which we make is removing the longitudinal part of the free photon propagator. We can do it in the leading approximation, because the longitudinal part does not give a contribution logarithmic in  $-p^2$ .

After these replacements, Schwinger-Dyson equation (34) takes the following form:

$$\Gamma_\mu(p, p') \approx \gamma_\mu + \frac{\alpha}{2\pi} \int_0^1 \frac{\nu d\nu}{1-\nu} \int_V \frac{d^2 k_\parallel}{\pi} \frac{(p-k_\parallel)^\rho \Gamma_{\mu\rho}(k_\parallel, p'; p-k_\parallel)}{(k_\parallel - \nu p)^2 + p^2 \nu(1-\nu) + i\epsilon}. \quad (36)$$

Notice that the integration in  $k_\parallel$  is now restricted to a vicinity  $V$  of the point  $k_\parallel = \nu p$ . The approximate equality means that only the leading contribution at  $p^2 \rightarrow 0$  is kept in the right hand side.

Now we can use Ward-Takahashi identity for the four-point amplitude featuring Eq. (36). For this particular connected amplitude it reads

$$(p-k_\parallel)^\rho \Gamma_{\mu\rho}(k_\parallel, p'; p-k_\parallel) = -i \left[ \Gamma_\mu(p, p') \frac{\not{p} \not{k}_\parallel}{p^2} - S^{-1}(p') S(p' - (p-k_\parallel)) \Gamma_\mu(k, p' - (p-k_\parallel)) \right], \quad (37)$$

where  $S(l)$  denotes the full fermion propagator depending on momentum  $l$ . In the leading approximation, the full propagators can be replaced with the free propagators, because the dependence on the normalization point cancels in the ratio of the propagators. Finally, setting  $k_\parallel = \nu p$  and neglecting  $p^2$  where possible, we obtain after a simple rearrangement of the terms the form of the Ward-Takahashi identity we will use:

$$(p-k_\parallel)^\rho \Gamma_{\mu\rho}(k_\parallel, p'; p-k_\parallel) \approx -i \left[ \Gamma_\mu(p, p') \nu - \Gamma_\mu(k_\parallel, p' - p(1-\nu)) + \frac{(1-\nu) \not{p} \not{p}'}{(2pp')(y+1-\nu)} \Gamma_\mu(k_\parallel, p' - p(1-\nu)) \right]. \quad (38)$$

We recall that  $y = -p'^2/(2pp')$ . Notice that  $k_\parallel$  is not replaced with  $\nu p$  in the first argument of  $\Gamma_\mu$ . This is because at  $p^2 = 0$  such a replacement would give infinity.

Substituting Eq. (38) into Eq. (36) gives the truncation of Schwinger-Dyson equation we aimed at:

$$\Gamma_\mu(p, p') \approx \gamma_\mu - \frac{\alpha}{2\pi} \int_0^1 \frac{\nu d\nu}{1-\nu} \int_V \frac{id^2 k_\parallel / \pi}{(k_\parallel - \nu p)^2 + p^2 \nu(1-\nu) + i\epsilon} \\ \times [\Gamma_\mu(p, p')\nu - \Gamma_\mu(k_\parallel, p' - p(1-\nu)) + \frac{(1-\nu)\cancel{p}p'}{(2pp')(y+1-\nu)} \Gamma_\mu(k_\parallel, p' - p(1-\nu))]. \quad (39)$$

This equation can be used to generate iteratively the expansion in  $\alpha$  of the vertex  $\Gamma_\mu$  starting from the initial term  $\gamma_\mu$ . This is the subject of the next section.

## 8 The Form Factor of the Skewed Sudakov Regime

To compute the first correction in the perturbative expansion of the vertex, one takes the second term in the right hand side of Eq. (39) and makes in it the substitution  $\Gamma_\mu \rightarrow \gamma_\mu$  regardless of the arguments of  $\Gamma_\mu$ . One keeps in the integrals only the leading terms at  $p^2 \rightarrow 0$ . The outcome of this exercise is as follows:

$$\Gamma_\mu^{(1)}(p, p') \approx \gamma_\mu [t \int_0^1 d\nu (\nu - \frac{\nu z}{1-\nu z})] + \frac{p_\mu \cancel{p}'}{pp'} [t \int_0^1 d\nu \frac{\nu z}{1-\nu z}], \quad (40)$$

where the first correction is in the left hand side, and the variables  $t, z$  were defined in Eq. (17). A relation useful in checking this reads

$$\frac{\alpha}{2\pi} \int_V \frac{id^2 k_\parallel / \pi}{(k_\parallel - \nu p)^2 + p^2 \nu(1-\nu) + i\epsilon} \approx t. \quad (41)$$

With the first correction known, one can use it to obtain the second one, and so on. A minor complication is that the integration in  $k_\parallel$  requires the knowledge of  $\Gamma_\mu(k_\parallel, p' - p(1-\nu))$  at small  $k_\parallel^2$  of any sign, and Eq. (40) gives it only for  $k_\parallel^2 < 0$ . As follows from the derivation of Eq. (40), it can be extended to positive small virtuality of the incoming fermion by making the replacement  $\log(x) \rightarrow \log(|x|)$  in Eq. (17). Apart of this clarification, one also needs in this computation the following generalization of Eq. (41):

$$\frac{\alpha^{(n+1)}}{(2\pi)^{(n+1)} n!} \int_V \frac{\log^n (|2pp'/k_\parallel^2|) id^2 k_\parallel / \pi}{(k_\parallel - \nu p)^2 + p^2 \nu(1-\nu) + i\epsilon} \approx \frac{t^{(n+1)}}{(n+1)!}, \quad (42)$$

where  $n$  is any integer.

The outcome of the approximate computation of the perturbative corrections outlined above can be summarized as follows. First, no new tensor structures appear in the vertex apart of the ones already present in the leading correction of Eq. (40):

$$\Gamma_\mu(p, p') \approx \gamma_\mu F(t, z) + \frac{p_\mu p'^\mu}{pp'} \Phi(t, z). \quad (43)$$

Second, the form factors satisfy the following evolution equations:

$$\frac{\partial F(t, z)}{\partial t} = \frac{1}{2} F(t, z) - \int_0^1 d\nu \left[ \frac{\nu(F(t, z) - F(t, \nu z))}{1 - \nu} + \frac{\nu z F(t, \nu z)}{1 - \nu z} \right], \quad F(0, z) = 1, \quad (44)$$

$$\frac{\partial \Phi(t, z)}{\partial t} = \frac{1}{2} \Phi(t, z) - \int_0^1 d\nu \left[ \frac{\nu(\Phi(t, z) - \Phi(t, \nu z))}{1 - \nu} - \frac{\nu z F(t, \nu z)}{1 - \nu z} \right], \quad \Phi(0, z) = 0. \quad (45)$$

Next we notice that the sum of these equations yields a simpler equation, which can be solved:

$$F(t, z) + \Phi(t, z) = e^{t/2}.$$

We conclude that the vertex is approximated with a single form factor, Eq. (18), which satisfies the evolution equation (44).

## 9 Solving Evolution Equation for the Form Factor

Eq. (44) is a linear evolution equation of the form  $\dot{F} = \mathcal{O}F$ , where the linear operator  $\mathcal{O}$  acts on a function of  $z$ :

$$(\mathcal{O}\chi)(z) = \frac{\chi(z)}{2} - \int_0^1 d\nu \left[ \frac{\nu(\chi(z) - \chi(\nu z))}{1 - \nu} + \frac{\nu z \chi(\nu z)}{1 - \nu z} \right]. \quad (46)$$

One explicitly checks that  $\chi_n(z) = z^n(1 - z)$  are eigenfunctions of the operator  $\mathcal{O}$ :

$$\mathcal{O}\chi_n = \left( \frac{3}{2} - H_{n+1} \right) \chi_n, \quad (47)$$

and the initial condition for the form factor can be expanded in terms of these eigenfunctions:

$$F(0, z) = \sum_{n=0}^{\infty} \chi_n(z). \quad (48)$$

This implies Eq. (19).

Next we derive the representation (21) starting from Eq. (19). According to it, expansion of  $(e^{-3t/2}F(t, z) - 1)z \equiv \bar{F}(t, z)$  in powers of  $t$  is as follows:

$$S_k(z) = \frac{1}{k!} \sum_{n=1}^{\infty} H_n^k z^n (1-z), \quad \bar{F}(t, z) = \sum_{k=1}^{\infty} (-t)^k S_k(z) \quad (49)$$

Our task is to express  $S_k(z)$  in terms of multiple polylogarithms.

To complete the formulation of the task we give a definition of the multiple polylogarithms in terms of linear operators acting on a function of a single variable, which is equivalent to the standard definition in terms of the iterated integrals [?]. First we define two operators used in the definition:

$$\begin{aligned} (A\phi)(z) &= \int_0^z \frac{dz'}{z'} \phi(z'), \\ (E\phi)(z) &= \int_0^z \frac{dz'}{1-z'} \phi(z'). \end{aligned} \quad (50)$$

Here  $\phi(z)$  is a function on which the operators  $A$  and  $E$  act.

Next we define an operator labelled with a string of integers  $\underline{s} = (s_1, \dots, s_d)$ ,  $s_i > 0$ :

$$L_{\underline{s}} = A^{s_1-1} E A^{s_2-1} E \dots A^{s_d-1} E, \quad (51)$$

where  $d$  is the depth of the string  $\underline{s}$ .

With these notations a multiple polylogarithm is defined as follows:

$$Li_{\underline{s}}(z) = (L_{\underline{s}}u)(z), \quad (52)$$

where the operator  $L_{\underline{s}}$  acts on the function  $u(z) = 1$ .

We now return to transforming  $S_k(z)$ . Expansion of  $S_k(z)$  in powers of  $z$  reads

$$S_k(z) = \frac{z}{k!} + \sum_{n=2}^{\infty} z^n \frac{H_n^k - H_{n-1}^k}{k!}. \quad (53)$$

Since  $H_n = H_{n-1} + 1/n$ , one can expand its power in Eq. (53), and cancel the term  $H_{n-1}^k$  in the numerator. A straightforward regrouping of terms transforms thus Eq. (53) as follows:

$$S_k(z) = \frac{1}{k!} \sum_{n=1}^{\infty} \frac{z^n}{n^k} + \sum_{n=2}^{\infty} z^n \sum_{l=1}^{k-1} \frac{H_{n-1}^l}{n^{k-l} l! (k-l)!}, \quad (54)$$

where the second sum vanishes for  $k = 1$ .

Next we notice that  $Ax^n = x^n/n$ , and one can write the above expansion using the operators  $A$  and  $E$ :

$$S_k(z) = \frac{1}{k!} (A^{(k-1)}Eu)(z) + \sum_{l=1}^{k-1} \frac{1}{l!} A^l E S_{k-l}(z). \quad (55)$$

This gives a recursive definition of  $S_k(z)$  in terms of the operators  $A, E$  and function  $u$  starting with  $S_1(z) = (Eu)(z)$ .

At last, one proves by induction that this recursion yields the following expression for  $S_k(z)$

$$S_k(z) = \sum_{|\underline{s}|=k} \frac{1}{\underline{s}!} (L_{\underline{s}}u)(z), \quad (56)$$

which implies Eq. (21).

## 10 Summary

In this lecture we have given a generalization (18) of the Sudakov approximation (2) valid in a wider kinematic range. Considering the abundant literature (see, e.g., [10–14]) derived in various ways from Ref. [2] one may envisage a scientific program trying to give a skewed version to any result descending from Ref. [2].

Our subjective choice for the sequence of these possible generalizations is as follows: First, one may try to study the skewed asymptotic for non-abelian gauge theories [12], second, the subleading corrections [13], third, the phenomenology [14].

The idea of this consideration belongs to L. N. Lipatov, who passed away before the initial drafts of the papers [4, 5] were completed. His profound influence contributed substantially to our studies and, in particular, to this research. We are grateful to V. A. Matveev for fruitful collaboration and V. S. Fadin for useful discussions. We thank CERN Theory Department for the kind hospitality.

## References

- [1] M. E. Peskin and D. V. Schroeder, *An Introduction to quantum field theory* (Addison-Wesley, Reading, USA, 1995).
- [2] V. V. Sudakov, Sov. Phys. JETP **3**, 65 (1956).

- [3] A. Strominger, *Lectures on the Infrared Structure of Gravity and Gauge Theory* (, 2017), arXiv:1703.05448 [hep-th].
- [4] V. T. Kim and G. B. Pivovarov, *Phys. Part. Nucl. Lett.* **16**, 530 (2019).
- [5] V. T. Kim, V. A. Matveev, and G. B. Pivovarov, *Phys. Rev. D* **99**, 025016 (2019), arXiv:1812.07269 [hep-th].
- [6] M. Waldschmidt, Multiple Polylogarithms: An Introduction, in *Number Theory and Discrete Mathematics*, edited by A. K. Agarwal and et al., pp. 1–12, Basel, 2002, Birkhäuser.
- [7] S. Weinzierl, IRMA Lect. Math. Theor. Phys. **15**, 247 (2009), arXiv:0705.0900 [hep-ph].
- [8] C. Bogner and F. Brown, *PoS LL2012*, 053 (2012), arXiv:1209.6524 [hep-ph].
- [9] C. Bogner and S. Weinzierl, *Int. J. Mod. Phys. A* **25**, 2585 (2010), arXiv:1002.3458 [hep-ph].
- [10] A. H. Mueller, *Phys. Rev. D* **20**, 2037 (1979).
- [11] J. C. Collins, *Phys. Rev. D* **22**, 1478 (1980).
- [12] A. Sen, *Phys. Rev. D* **24**, 3281 (1981).
- [13] G. P. Korchemsky, *Phys. Lett. B* **220**, 629 (1989).
- [14] A. J. Larkoski, S. Marzani, and J. Thaler, *Phys. Rev. D* **91**, 111501 (2015), arXiv:1502.01719 [hep-ph].

## TWO PHOTON PHYSICS AT THE LHC

Mikhail I. Vysotsky

I. E. Tamm Department of Theoretical Physics,  
Lebedev Physical Institute, Moscow

Abstract

Lepton pair production in the annihilation of two photons at the LHC is considered.

## ДВУХФОТОННАЯ ФИЗИКА НА LHC

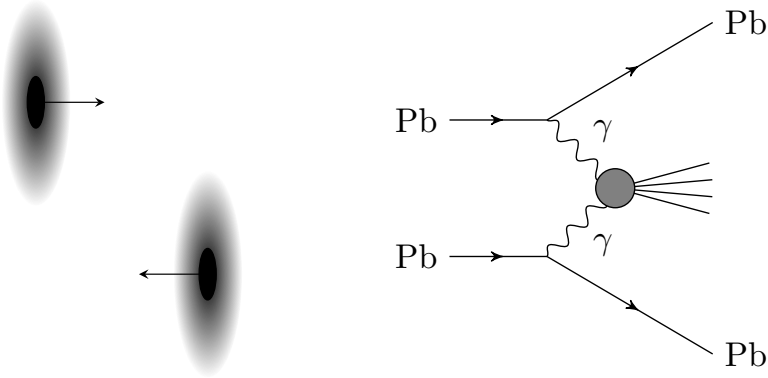
Михаил И. Высоцкий

Отдел Теоретической физики им. И.Е. Тамма,  
Институт физики им. Лебедева, Москва

Аннотация

Обсуждается рождение лептонных пар при аннигиляции двух фотонов на LHC.

LHC is pp (pN, NN) collider, so how we manage to discuss  $\gamma\gamma$  collisions at it? A bit of history is in order. Dirac wrote his equation in 1928 and Anderson discovered positrons in cosmic rays in 1932. A natural question arose: how to produce positrons in the laboratory? G. Breit and J.A. Wheeler calculated cross section of the reaction  $\gamma\gamma \rightarrow e^+e^-$  in 1934. However the problem is: how to produce the beams of photons? Almost the same time the paper of L. D. Landau, E. M. Lifshitz "Production of electrons and positrons by a collision of two particles." Phys. Zs. Sowjet 6, 244 (1934) was published which suggested solution of this problem.



In this way we are approaching what is called an equivalent photon approximation:

E. Fermi, *Über die Theorie des Stoßes zwischen Atomen und elektrisch geladenen Teilchen.* Z.Physik 29, 315 (1924);

C. F. V. Weizsacker, *Ausstrahlung bei Stoßen sehr schneller Elektronen.* Z.Physik 88, 612 (1934);

E. J. Williams, *Correlation of certain collision problems with radiation theory.* Kgl. Danske Vidensk. Selskab. Mat.-Fiz. Medd. 13, 4 (1935).

In some recent papers a reference to the paper by Landau and Lifshitz is added to the first three references on the subject of EPA.

An old review paper [1] contains detailed information on two photon particle production physics.

The results discussed in the present lecture were obtained in the papers [2-6].

The distribution of the photons which accompanied ultrarelativistic proton over energy  $\omega$  is given by

$$n(\omega)d\omega = \frac{2\alpha}{\pi} \ln\left(\frac{\hat{q}\gamma}{\omega}\right) \frac{d\omega}{\omega},$$

where  $\gamma$  is the proton  $\gamma$ -factor and  $\hat{q} \approx 200$  MeV originates from the proton formfactor. The cross section of muon pair production in the collision of equivalent photons is given by the following expression:

$$\sigma(pp(\gamma\gamma) \rightarrow pp\mu^+\mu^-) = \int_{m_\mu^2/\hat{q}\gamma}^{\hat{q}\gamma} d\omega_1 \int_{m_\mu^2/\omega_1}^{\hat{q}\gamma} d\omega_2 \sigma(\gamma\gamma \rightarrow \mu^+\mu^-) n(\omega_1) n(\omega_2).$$

It is convenient to change the integration variables from  $\omega_1$  and  $\omega_2$  to  $s = 4\omega_1\omega_2$  and  $x = \omega_1/\omega_2$ :

$$\begin{aligned} \sigma(pp(\gamma\gamma) \rightarrow pp\mu^+\mu^-) &= \int_{(2m_\mu)^2}^{(2\hat{q}\gamma)^2} ds \sigma(\gamma\gamma \rightarrow \mu^+\mu^-) \int_{s/(2\hat{q}\gamma)^2}^{(2\hat{q}\gamma)^2/s} \frac{dx}{8x} n\left(\sqrt{\frac{sx}{4}}\right) n\left(\sqrt{\frac{s}{4x}}\right) \\ &= \frac{\alpha^2}{2\pi^2} \int_{(2m_\mu)^2}^{(2\hat{q}\gamma)^2} \frac{ds}{s} \sigma(\gamma\gamma \rightarrow \mu^+\mu^-) \int_{s/(2\hat{q}\gamma)^2}^{(2\hat{q}\gamma)^2/s} \frac{dx}{x} \\ &\times \ln \frac{(2\hat{q}\gamma)^2}{sx} \ln \left[ \frac{(2\hat{q}\gamma)^2}{s} \cdot x \right], \end{aligned}$$

$$\sigma(pp(\gamma\gamma) \rightarrow pp\mu^+\mu^-) = \frac{16\alpha^2}{3\pi^2} \int_{(2m_\mu)^2}^{(2\hat{q}\gamma)^2} \frac{ds}{s} \sigma(\gamma\gamma \rightarrow \mu^+\mu^-) \ln^3 \frac{2\hat{q}\gamma}{\sqrt{s}}.$$

Because  $\sigma(\gamma\gamma \rightarrow \mu^+\mu^-)$  decreases as  $1/s$  when  $s \gg 4m_\mu^2$ , in the leading logarithmic approximation the logarithm should be taken at  $s = 4m_\mu^2$ .

Substituting

$$\sigma(\gamma\gamma \rightarrow \mu^+\mu^-) = \frac{4\pi\alpha^2}{s} \left[ \left(1 + \frac{4m_\mu^2}{s} - \frac{8m_\mu^4}{s^2}\right) \ln \frac{1 + \sqrt{1 - \frac{4m_\mu^2}{s}}}{1 - \sqrt{1 - \frac{4m_\mu^2}{s}}} - \left(1 + \frac{4m_\mu^2}{s}\right) \sqrt{1 - \frac{4m_\mu^2}{s}} \right]$$

and performing integration we obtain

$$\sigma(pp(\gamma\gamma) \rightarrow pp\mu^+\mu^-) = 8 \cdot \frac{28}{27} \frac{\alpha^4}{\pi m_\mu^2} \ln^3 \frac{\hat{q}\gamma}{m_\mu},$$

the famous result of Landau and Lifshitz which demonstrates that cross section of muon pair production in proton collision grows as the  $\log^3$  of the proton energy. Here  $\gamma$  is taken in the protons center of mass system.

Why is it interesting to study lepton pair production at LHC? The point is that the result of the measurement of muon anomalous magnetic moment (the so called muon anomaly) deviates by  $4.5 \sigma$  from the result of SM calculations. If confirmed it will signal New Physics. NP contribution in muon  $g - 2$  should be of the order of  $(m_\mu/\Lambda)^2$ , and New Physics scale  $\Lambda \sim 1$  TeV will explain the deviation.  $(W/\Lambda)^2$  contribution in the cross section of lepton pair production, where  $W$  is the invariant mass of the lepton pair, can be noticeable at the LHC.

Fiducial cross section for the reaction  $pp(\gamma\gamma) \rightarrow pp\mu^+\mu^-$  at the center of mass energy 13 TeV should take into account experimental cuts: that on invariant mass of lepton pair, on transverse momenta of muons and that on muon pseudorapidities. These cuts are imposed on the experimental data in order to suppress background and to take into account detector geometry.

Cuts	Cross section, pb	
No cuts	$1.7 \cdot 10^5$	
$12 \text{ GeV} < \sqrt{s} < 30 \text{ GeV}$	54.1	59.7
$30 \text{ GeV} < \sqrt{s} < 70 \text{ GeV}$	5.66	
$12 \text{ GeV} < \sqrt{s} < 30 \text{ GeV}, p_T > 6 \text{ GeV}$	5.38	6.29
$30 \text{ GeV} < \sqrt{s} < 70 \text{ GeV}, p_T > 10 \text{ GeV}$	0.91	
$12 \text{ GeV} < \sqrt{s} < 30 \text{ GeV}, p_T > 6 \text{ GeV},  \eta  < 2.4$	3.07	3.63
$30 \text{ GeV} < \sqrt{s} < 70 \text{ GeV}, p_T > 10 \text{ GeV},  \eta  < 2.4$	0.54	

The inaccuracy of EPA originating from virtuality (deviation from reality) of the photons equals

$$\Delta \sim \left( \frac{\hat{q}^2}{\sqrt{s_{\min}} m_\mu} \right)^2 \left( \ln \frac{4E^2}{s_{\min}} \right)^{-1},$$

where  $E$  is the energy of the colliding particles. The accuracy is very high for muon-antimuon pair production, as far as  $\sqrt{s} \gg \hat{q}$ .

The spectrum of equivalent photons of a proton with the Lorentz factor  $\gamma$  is

$$n(b, \omega) = \frac{\alpha}{\pi^2 \omega} \left[ \int_0^\infty \frac{F(q_\perp^2 + \omega^2/\gamma^2)}{q_\perp^2 + \omega^2/\gamma^2} J_1(bq_\perp) q_\perp^2 dq_\perp \right]^2,$$

where  $n(b, \omega) d^2b d\omega$  is the number of photons with the energy  $\omega$  moving through a point of space with the impact parameter  $\vec{b}$ ,  $\alpha$  is the fine structure constant,  $q_\perp$  is the transverse photon momentum,  $q_\perp^2 + \omega^2/\gamma^2 \equiv Q^2$  is the photon virtuality,  $F(Q^2)$  is the Dirac form factor of the proton,  $J_1(z)$  is the Bessel function of the first kind.

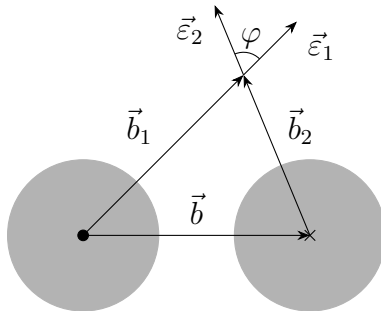


Figure 1: An ultraperipheral collision of two protons moving perpendicular to the figure plane.  $\vec{b}_1$  and  $\vec{b}_2$  are impact parameters of a point in space at which photons collide relative to the corresponding protons.  $b = |\vec{b}_1 - \vec{b}_2|$  is the impact parameter of the collision.  $\vec{\epsilon}_1$  and  $\vec{\epsilon}_2$  are the photon polarization vectors.

$$\sigma(pp \rightarrow ppX) = \int_0^\infty d\omega_1 \int_0^\infty d\omega_2 \int_0^\infty d^2b_1 \int_0^\infty d^2b_2 \sigma(\gamma\gamma \rightarrow X) n(b_1, \omega_1) n(b_2, \omega_2) P(b),$$

where  $P(b)$  takes into account protons desintegration:

$$P(b) = \left(1 - e^{-\frac{b^2}{2B}}\right)^2.$$

The ATLAS Collaboration published results of the measurements in the following paper: “Measurement of the exclusive  $\gamma\gamma \rightarrow \mu^+\mu^-$  process in proton-proton collisions at  $\sqrt{s} = 13$  TeV with the ATLAS detector.” Phys.Lett. B 777, 303 (2018), arXiv 1708.04053.

- experimental value:  $3.12 \pm 0.07$  (stat.)  $\pm 0.10$  (syst.) pb ;
- theory with proton disintegration neglected: 3.63 pb;
- theory with proton disintegration taken into account: 3.49 pb.

EPA predictions made with Monte Carlo simulations:

- HERWIG:  $3.56 \pm 0.05$  pb;

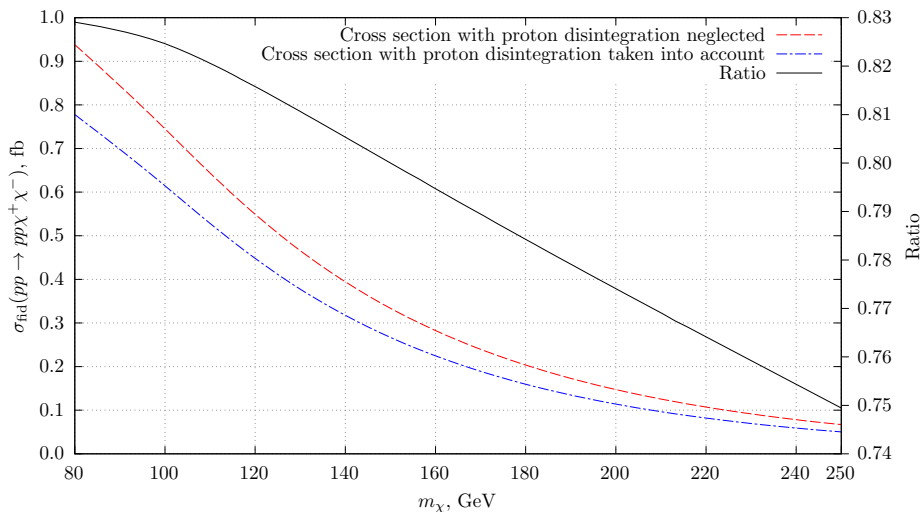


Figure 2: Fiducial cross section of the production of the chargino pair with proton desintegration taken into account. To produce heavy particles photons with larger energies are needed. Such photons are situated closer to parent protons which enhance proton desintegration probability.

- HERWIG with corrections:  $3.06 \pm 0.05$  pb;
- SUPERCHIC2:  $3.45 \pm 0.05$  pb.

Results of the new analysis was published in: “Observation and measurement of forward proton scattering in association with lepton pairs produced via the photon fusion mechanism at ATLAS.” Phys. Rev. Lett. 125, 261801 (2020), arXiv 2009.14537.

Lepton pairs produced in ultraperipheral collisions (UPC) of protons at the LHC are accompanied by forward scattering of the protons. Previous measurements of this process were performed by the ATLAS collaboration without proton tagging.

In the events selected for this new analysis, one of the scattered protons is detected by the ATLAS Forward Proton Spectrometer. The other proton could remain intact, or it could disintegrate. The transversal momentum of the lepton pair was required to be less than 5 GeV. This momentum equals to the sum of transversal momenta of the photons emitted by the protons. The transversal momentum of the photon that was emitted by the proton that survived the collision cannot be much higher than  $\hat{q} = 0.2$  GeV. Therefore, the

transversal momentum of the second photon has to be less than 5 GeV.

We derive analytical formulas which describe the measured fiducial cross sections. These formulas allow for simple numerical integration instead of the usual Monte Carlo approach and thus can provide intuitive insights into the process targeted by the experiment.

To hit the forward detector the proton must lose a fraction of its energy  $\xi$ :  $\xi_{\min} < \xi < \xi_{\max}$ , where  $\xi_{\min} = 0.035$ ,  $\xi_{\max} = 0.08$ . This translates to limits on the energy of the photon emitted by this proton:

$$227 \text{ GeV} \equiv \omega_{\min} < \omega_1 < \omega_{\max} \equiv 520 \text{ GeV} .$$

The following cuts were imposed on the experimental data:

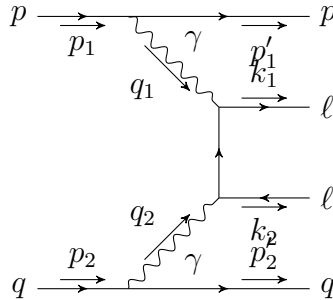
- $20 \text{ GeV} < W < 70 \text{ GeV}$  or  $W > 105 \text{ GeV}$ , where  $W$  is an invariant mass of the lepton pair.
- $0.035 < \xi < 0.08$  which is equivalent to  $227 \text{ GeV} < \omega < 520 \text{ GeV}$ .

For muons:

- $\hat{p}_T = 15 \text{ GeV}$ ,  $\hat{\eta} = 2.4$ .
- $\sigma_{\text{fid}}(pp \rightarrow p + \mu^+ \mu^- + p) = 8.6 \text{ fb}$ .

For electrons:

- $\hat{p}_T = 18 \text{ GeV}$ ,  $\hat{\eta} = 2.47$ .
- $\sigma_{\text{fid}}(pp \rightarrow p + e^+ e^- + p) = 0.1 \text{ fb}$ .



$$d\sigma(pq \rightarrow p + \ell^+ \ell^- + q) = \frac{Q_q^2 (4\pi\alpha)^2}{q_1^2 q_2^2} \rho_1^{\mu\nu} \rho_2^{\alpha\beta} M_{\mu\alpha} M_{\nu\beta}^* \times$$

$$\times \frac{(2\pi)^4 \delta^{(4)}(q_1 + q_2 - k_1 - k_2) d\Gamma}{4\sqrt{(p_1 p_2)^2 - p_1^2 p_2^2}} \frac{d^3 p'_1}{(2\pi)^3 2E'_1} \frac{d^3 p'_2}{(2\pi)^3 2E'_2} f_q(x, Q_2^2) dx$$

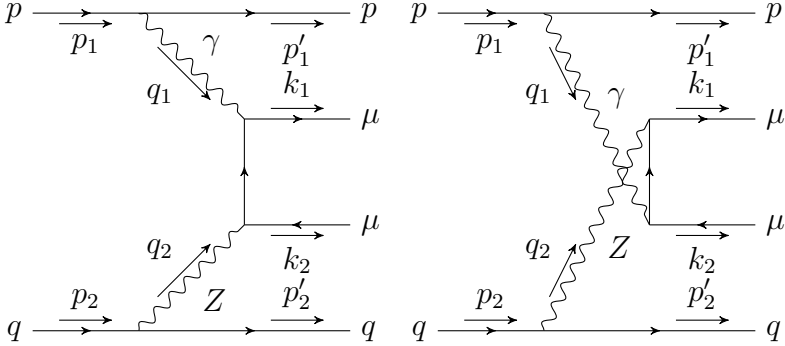
$$\sigma_{\mu\mu+p}^{\text{exp.}} = 7.2 \pm 1.6 \text{ (stat.)} \pm 0.9 \text{ (syst.)} \pm 0.2 \text{ (lumi.) fb,}$$

$$\sigma_{ee+p}^{\text{exp.}} = 11.0 \pm 2.6 \text{ (stat.)} \pm 1.2 \text{ (syst.)} \pm 0.3 \text{ (lumi.) fb.}$$

$$\tilde{\sigma}_{\mu\mu+p}^{\text{theor.}} = 18 \pm 3 \text{ fb,}$$

$$\tilde{\sigma}_{ee+p}^{\text{theor.}} = 22 \pm 3 \text{ fb.}$$

Survival factor diminishes cross section due to breaking of both protons. It equals  $\approx 0.9$  for elastic scattering and  $0.6 - 0.7$  for semi-exclusive reaction.



Here are main conclusions:

- analytical formulas for fiducial cross section of lepton pair production in UPC at the LHC are written and compared with the data;
- analogous formulas for the case when one of the protons is measured in forward detector and the second proton dissociates are derived and compared with the data as well;

- accounting for protons inelasticity (survival factor) is important;
- Z-boson exchange contribution should be accounted for;
- looking forward for New Physics in lepton interactions.

I am grateful to the organizers of the 55 PNPI Winter School for the invitation and to E. K. Karkaryan for the help in preparing the manuscript. We are supported by RSF grant No 19-12-00123II.

Our calculations were performed with the help of `libepa`: library for calculations of cross sections of ultraperipheral collisions of high energy particles under the equivalent photons approximation (E. V. Zhemchugov).  
<https://github.com/jini-zh/libepa>

## References

- [1] V. M. Budnev, I. F. Ginzburg, G. V. Meledin, and V. G. Serbo, *Phys. Rep.* **15**, 181 (1975).
- [2] M. I. Vysotsky and E. V. Zhemchugov, *Physics-Uspekhi.* **62**, 910 (2019).
- [3] S. I. Godunov, V. A. Novikov, A. N. Rozanov, M. I. Vysotsky, and E. V. Zhemchugov, *JHEP.* **2020**, 143 (2020).
- [4] S. I. Godunov, V. A. Novikov, A. N. Rozanov, M. I. Vysotsky, and E. V. Zhemchugov, *JHEP.* **2021**, 234 (2021).
- [5] S. I. Godunov *et al.*, *JETP Lett.* **115**, 59–62 (2022).
- [6] S. I. Godunov *et al.*, *Eur. Phys. J. C.* **82**, 1055 (2022).

# DEEP INELASTIC SCATTERING IN DOUBLE-LOGARITHMIC APPROXIMATION

Boris I. Ermolaev<sup>1</sup>, Sergei I. Troyan<sup>2</sup>

<sup>1</sup> Ioffe Physico-Technical Institute, St. Petersburg

<sup>2</sup> Petersburg Nuclear Physics Institute of NRC “KI”, Gatchina

Abstract

Unpolarized lepton-hadron Deep Inelastic Scattering (DIS) is parameterized by structure functions  $F_1(x, Q^2)$  and  $F_2(x, Q^2)$ , with the both arguments being made of the hadron momentum  $p$  and the virtual photon momentum  $q$ :  $Q^2 = -q^2$  and  $x = Q^2/(2pq)$ . The combination  $F_L(x, Q^2) = F_2(x, Q^2) - 2xF_1(x, Q^2)$  is called the longitudinal structure function. In order to calculate  $F_{1,2,L}$  at small  $x$  and  $Q^2 \geq \text{few GeV}^2$ , the Perturbative QCD is used. Fixed-order calculations predict too weak dependence of  $F_{1,2,L}$  on  $x$ , so conventionally BFKL-based approaches are used for description of the  $x$ -dependence and then the result is combined in a model way with DGLAP to describe the  $Q^2$ -dependence.

We suggest an alternative strategy: namely, to calculate  $F_{1,2,L}$  in the Double-logarithmic Approximation. As a result, we obtain the model-independent and unified description of the unpolarized DIS at small  $x$ . This DL result and the conventional approaches predict practically the same  $x$ -behavior but quite different  $Q^2$  dependence. Comparing the latter with experimental data can determine which of the approaches is more adequate.

# ГЛУБОКОНЕУПРУГОЕ РАССЕЙЕНИЕ В ДВАЖДЫ ЛОГАРИФМИЧЕСКОМ ПРИБЛИЖЕНИИ

Борис И. Ермолаев<sup>1</sup>, Сергей И. Троян<sup>2</sup>

<sup>1</sup> Физико-технический институт им. А.Ф. Иоффе, РАН,  
Санкт-Петербург

<sup>2</sup> Петербургский институт ядерной физики НИЦ «КИ», Гатчина

## Аннотация

Глубоконеупругое рассеяние неполяризованных лептонов на адронах описывается структурными функциями DIS:  $F_1(x, Q^2)$  и  $F_2(x, Q^2)$ , в которых оба аргумента выражаются через импульс адрона  $p$  и виртуального фотона  $q$ :  $Q^2 = -q^2$  and  $x = Q^2/(2pq)$ . Комбинация  $F_L(x, Q^2) = F_2(x, Q^2) - 2xF_1(x, Q^2)$  называется продольной структурной функцией. Для вычисления  $F_{1,2,L}$  при малых  $x$  и  $Q^2 \geq$  несколько  $\text{GeV}^2$  используется теория возмущений в КХД. Первых порядков теории возмущений недостаточно для адекватного описания зависимости  $F_{1,2,L}$  от  $x$  и  $Q^2$ . Поэтому, обычно используют подход БФКЛ для описания  $x$ -зависимости и объединяют его модельным образом с подходом ДГЛАП, чтобы описать зависимость от  $Q^2$ .

Мы предлагаем альтернативную стратегию: вычислить  $F_{1,2,L}$  в Дважды Логарифмическом Приближении. В итоге получается модельно-независимое описание неполяризованных DIS при малых  $x$ . Оно приводит практически к такому же поведению по  $x$ , как и в общепринятом подходе, но к отличному поведению по  $Q^2$ . Сравнение с экспериментом может показать, какой из подходов более адекватен.

# 1 Introduction

Deep-Inelastic Scattering (DIS) of lepton off hadrons is one of basic experiments to investigate the structure of the hadrons. Its essence is that leptons collide with hadrons at high energy and interact with them by exchanging virtual photons<sup>1</sup>, producing other hadrons. They however are not detected, so the only registered particle is the outgoing lepton. Its energy and the scattering angle is the only information supplied by DIS. Nevertheless, obtaining such comparatively poor information makes possible to draw important conclusions on the hadron structure. In the present lecture we consider the case when the leptons and hadrons are unpolarized. The most important element in theoretical description of the DIS cross-section is hadronic tensor  $W_{\mu\nu}(p, q)$ , where the Lorentz subscripts  $\mu, \nu$  denote polarizations of the virtual photons,  $p$  stands for the hadron momentum and  $q$  is the virtual photon momentum. Conventionally,  $W_{\mu\nu}$  is represented through the sum of simpler tensors, each multiplied by an invariant function. These tensors are called the projection operators, they are made of  $p$  and  $q$ . Arguments of the invariant functions (called the structure functions) are scalars made of  $p$  and  $q$ . Respecting the Bose statistics for the virtual photons makes  $W_{\mu\nu}$  be symmetrical in  $\mu, \nu$ . Respecting the electromagnetic current conservation leaves only two independent structure functions  $F_1$  and  $F_2$ . Conventionally,  $W_{\mu\nu}$  is written in the following form:

$$W_{\mu\nu}(p, q) = \left( -g_{\mu\nu} + \frac{q_\mu q_\nu}{q^2} \right) F_1 + \frac{1}{pq} \left( p_\mu - q_\mu \frac{pq}{q^2} \right) \left( p_\nu - q_\nu \frac{pq}{q^2} \right) F_2. \quad (1)$$

Each of  $F_1, F_2$  depends on  $Q^2$  and  $x = Q^2/w$ , with  $Q^2 = -q^2$  and  $w = 2pq$ . Besides  $F_1, F_2$ , the longitudinal structure function  $F_L$  is frequently used in the literature. It is defined as follows:

$$F_L = F_2 - 2xF_1. \quad (2)$$

Theoretical tools to calculate  $F_{1,2,L}$  is QCD. However, the problem is that each structure function contains both perturbative and non-perturbative contributions. The latter cannot be accounted for in the straightforward way. The conventional means to circumvent this obstacle is the use of QCD factorization. According to this concept, any structure function can be represented throughout convolutions of perturbative and non-perturbative contributions. Assuming scenario of the single-parton collision, we can write down Factorization in the following way:

$$F_1 = F_1^{(q)} \otimes \Phi_{(q)} + F_1^{(g)} \otimes \Phi_{(g)}, \quad F_2 = F_2^{(q)} \otimes \Phi_{(q)} + F_2^{(g)} \otimes \Phi_{(g)}, \quad (3)$$

---

<sup>1</sup>Exchange of  $Z$  and  $W$  bosons is also possible but we skip it here.

where  $\Phi_{1,2}^{(q,g)}$  stand for initial parton distributions whereas  $F_1^{(q,g)}, F_2^{(q,g)}$  are perturbative components of the structure functions  $F$  and  $F_2$  respectively. The superscripts  $q(g)$  in Eq. (3) mean that the initial partons are quarks (gluons). In order to define  $F_{1,2}^{(q,g)}$  and relate them with  $F_{1,2}$ , DIS off the partons is parameterized by the same way as Eq. (1):

$$W_{\mu\nu}^{(q,g)}(p, q) = \left( -g_{\mu\nu} + \frac{q_\mu q_\nu}{q^2} \right) F_1^{(q,g)} + \frac{1}{pq} \left( p_\mu - q_\mu \frac{pq}{q^2} \right) \left( p_\nu - q_\nu \frac{pq}{q^2} \right) F_2^{(q,g)}, \quad (4)$$

with  $p$  denoting the initial parton momentum. Throughout the paper we will neglect virtualities  $p^2$ , presuming the initial partons to be nearly on-shell. In the present lecture we focus on the perturbative components of the structure functions. Firstly they were calculated in fixed orders in  $\alpha_s$ , see Refs. [1]– [15]. However, it turned out that  $F_{1,2}$  calculated in fixed orders at small  $x$  grew too slowly and  $F_L$  even decreased. Similarly, too weak small- $x$  rise was obtained, when DGLAP [16] was applied. The way out was the use of BFKL [17] and the methods based on it. However, the problem was that BFKL did not account for the  $Q^2$  dependence. In contrast, tracing the  $Q^2$  dependence has nothing to do with BFKL, it is the domain of DGLAP. Because of that it there appeared models combining DGLAP and BFKL, see Refs. [18]– [26]. They provided  $F_{1,2,L}$  with sufficiently fast rise at small  $x$  and reasonable  $Q^2$  behavior at large  $Q^2$ . At the same time, they could not describe experimental data at small  $Q^2$ , which sounds reasonable because DGLAP is not intended to work well in that kinematics.

In what follows we show that  $F_{1,2,L}$  description of  $F_{1,2,L}$  in the framework of Double-Logarithmic Approximation (DLA) works well at small  $x$  and at any  $Q^2$ . The difference between BFKL and our approach is that.

(i) In order to account for the  $x$  dependence, the BFKL equation sums to all orders in  $\alpha_s$  the leading logarithmic (LL) contributions, i.e. it sums single-logarithmic contributions accompanied by the “Born” factor  $1/x$

$$(1/x) \left[ 1 + c_1 \alpha_s \ln(1/x) + c_2 (\alpha_s \ln(1/x))^2 + \dots \right]. \quad (5)$$

In contrast, DLA sums such contributions:

$$1 + c'_1 \alpha_s \ln^2(1/x) + c'_2 (\alpha_s \ln^2(1/x))^2 + \dots, \quad (6)$$

where the overall factor  $1/x$  is absent. As  $1/x$  is huge at small  $x$ , DL contributions to the structure functions a priori were considered as negligibly small

compared to the BFKL ones but actually they are of the same scale as the BFKL contributions.

(ii) As for the  $Q^2$  dependence, BFKL do not account for that, it deals with the  $x$ -dependence only while we account for DL of both  $x$  and  $Q^2$ .

The instrument for calculations is method of Infra-Red Evolution Equations (IREE) suggested by L.N. Lipatov [27]. The key point of the IREE method is the exceptionally useful result [28] known as the Gribov's bremsstrahlung theorem. It was obtained by V.N. Gribov.

In what follows we calculate  $F_{1,2,L}$  in DLA, obtain their small- $x$  asymptotics and discuss them.

## 2 Invariant amplitudes $A$ and $B$

It is convenient to calculate  $F_1^{(q,g)}$  and  $F_2^{(q,g)}$  through invariant amplitudes  $A^{(q,g)}$  and  $B^{(q,g)}$ . They are defined as follows:

$$-A^{(q)} = g_{\mu\nu} W_{\mu\nu}^{(q)} = 3F_1^{(q)} + \frac{F_2^{(q)}}{2x}, \quad (7)$$

$$-A^{(g)} \equiv g_{\mu\nu} W_{\mu\nu}^{(g)} = 3F_1^{(g)} + \frac{F_2^{(g)}}{2x},$$

$$B^{(q)} = \frac{p_\mu p_\nu}{pq} W_{\mu\nu}^{(q)} = -\frac{1}{2x} F_1^{(q)} + \frac{1}{4x^2} F_2^{(q)}, \quad (8)$$

$$B^{(g)} = \frac{p_\mu p_\nu}{pq} W_{\mu\nu}^{(g)} = -\frac{1}{2x} F_1^{(g)} + \frac{1}{4x^2} F_2^{(g)},$$

where we have neglected terms  $\sim p^2$ . We use Eqs. (7,8) to express  $A^{(q,g)}$  and  $B^{(q,g)}$  through  $F_{1,2}^{(q,g)}$ :

$$F_1^{(q,g)} = \frac{A^{(q,g)}}{2} + xB^{(q,g)}, \quad (9)$$

$$F_2^{(q,g)} = 2xF_1^{(q,g)} + 4x^2B^{(q,g)}.$$

Using Eq. (2) we represent  $F_L^{(q,g)}$  through  $B^{(q,g)}$

$$F_L^{(q,g)} = F_2^{(q,g)} - 2xF_1^{(q,g)} = 4x^2B^{(q,g)}. \quad (10)$$

### 3 Constructing and solving IREEs for amplitudes $A^{(q,g)}$ and $B^{(q,g)}$

In what follows we will use the Feynman gauge for virtual gluons and use the Sudakov representation for momenta  $k_i$  of virtual partons:

$$k_i = \alpha_i q' + \beta_i p' + k_{i\perp}, \quad (11)$$

where  $q'$  and  $p'$  are the massless (light-cone) momenta made of momenta  $p$  and  $q$

$$p' = p - q(p^2/w) \approx p, \quad q' = q - p(q^2/w) = q + xp. \quad (12)$$

IREEs for amplitudes  $A^{(q,g)}$  and  $B^{(q,g)}$  look much simpler when the Mellin transform is applied

$$\begin{aligned} A_{q,g}(w/\mu^2, Q^2/\mu^2) &= \int_{-i\infty}^{i\infty} \frac{d\omega}{2\pi i}, (w/\mu^2)^\omega f_{q,g}^{(A)}(\omega, Q^2/\mu^2), \\ B_{q,g}(w/\mu^2, Q^2/\mu^2) &= \int_{-i\infty}^{i\infty} \frac{d\omega}{2\pi i} (w/\mu^2)^\omega f_{q,g}^{(B)}(\omega, Q^2/\mu^2). \end{aligned} \quad (13)$$

Throughout the paper we will address  $f_{q,g}^{(A)}$  as the Mellin amplitudes. It is convenient to use the logarithmic variables  $\rho$  and  $y$ :

$$\rho = \ln(w/\mu^2), \quad \xi = \ln(w/Q^2) = \ln(1/x), \quad y = \ln(Q^2/\mu^2). \quad (14)$$

It allows us to bring Eq. (13) to a simpler form:

$$\begin{aligned} A_{q,g}(\rho, y) &= \int_{-i\infty}^{i\infty} \frac{d\omega}{2\pi i} \rho^\omega f_{q,g}^{(A)}(\omega, y), \\ B_{q,g}(\rho, y) &= \int_{-i\infty}^{i\infty} \frac{d\omega}{2\pi i} \rho^\omega f_{q,g}^{(B)}(\omega, y). \end{aligned} \quad (15)$$

$$f_{q,g}^{(A)}\left(\frac{\omega, Q^2}{\mu^2}\right) = \int_{\mu^2}^{\infty} \frac{dw}{w} (w/\mu^2)^{-\omega} A_{q,g}(w/\mu^2, Q^2/\mu^2) = \int_1^{\infty} d\rho e^{-\omega\rho} A_{q,g}(\rho, y). \quad (16)$$

The same form of transform (16) we will use for amplitudes  $B_{q,g}$ , denoting their Mellin amplitudes  $f_{q,g}^{(B)}$ .

### 3.1 Details of constructing IREEs for amplitudes $A^{(q,g)}$ and $B^{(q,g)}$

Technology of constructing and solving IREEs was reported in many publications, so we expound below the most important steps. All necessary details can be found e.g. in Ref. [27] and the overviews [31]. Because of that we focus below on the most essential points. IREEs for amplitudes  $A^{(q,g)}$  and  $B^{(q,g)}$  are quite similar, so we start with discussing amplitudes  $A^{(q,g)}$ . The l.h.s of each IREE is obtained with differentiation of  $A_{q,g}$  over  $\mu$ . It follows from Eq. (13) that

$$-\mu^2 dA_{q,g}/d\mu^2 = \partial A_{q,g}/\partial\rho + \partial A_{q,g}/\partial y = \int_{-\infty}^{\infty} \frac{d\omega}{2\pi i} (w/\mu^2)^\omega [\omega + \partial f_{q,g}^{(A)}/\partial y]. \quad (17)$$

The guiding principle to obtain the r.h.s. is to look for a  $t$ -channel parton with minimal transverse momentum  $\equiv k_\perp$ , so  $\mu$  is the lowest limit of integration over  $k_\perp$ . Integration over  $k_\perp$  yields a DL contribution only when there is a two-parton intermediate state in the  $t$  channel. Such pairs can consist of quarks or gluons. They factorize  $A_{q,g}$  into two amplitudes. Applying to them the operator  $-\mu^2\partial/\partial\mu^2$  leads to the following IREEs

$$\begin{aligned} \left[ \frac{\partial}{\partial y} + \omega \right] f_q^{(A)}(\omega, y) &= \frac{1}{(8\pi^2)} f_q^{(A)}(\omega, y) f_{qq}(\omega) + \frac{1}{(8\pi^2)} f_g^{(A)}(\omega, y) f_{gq}(\omega), \quad (18) \\ \left[ \frac{\partial}{\partial y} + \omega \right] f_g^{(A)}(\omega, y) &= \frac{1}{(8\pi^2)} f_q^{(A)}(\omega, y) f_{qg}(\omega) + \frac{1}{(8\pi^2)} f_g^{(A)}(\omega, y) f_{gg}(\omega), \end{aligned}$$

where amplitudes  $f_{rr'}$  ( $r, r' = q, g$ ) are the parton-parton amplitudes. In order to get rid of the factors  $1/(8\pi^2)$  in Eq. (18) we replace  $f_{rr'}$  by

$$h_{rr'} = f_{rr'}/(8\pi^2) \quad (19)$$

and rewrite (18) in the following way

$$\begin{aligned} \partial f_q^{(A)}(\omega, y)/\partial y &= [-\omega + h_{qq}(\omega)] f_q^{(A)}(\omega, y) + f_g^{(A)}(\omega, y) h_{gq}(\omega), \quad (20) \\ \partial f_g^{(A)}(\omega, y)/\partial y &= f_q^{(A)}(\omega, y) h_{qg}(\omega) + [-\omega + h_{gg}(\omega)] f_g^{(A)}(\omega, y). \end{aligned}$$

Eq. (20) looks quite similarly to the DGLAP equations [16], with  $h_{rr'}$  playing the role of new anomalous dimensions. They accommodate double-logarithmic (DL) contributions to all orders in  $\alpha_s$  and can be calculated in DLA with applying the same method: constructing and solving appropriate IREEs for

them. The DL contributions in the  $n^{\text{th}}$  order are  $\sim \alpha_s^n \ln^{2n} w$ , i.e. in the Mellin space they are  $\sim \alpha_s^n / \omega^{1+2n}$ . They are the most singular terms at  $\omega = 0$ , i.e. at small  $x$ , so total resummation of them is important for generalizing DGLAP to the small- $x$  region. In order to specify a general solution to Eq. (20) we use the matching

$$A_q(\rho, y)|_{y=0} = \tilde{A}_q(\rho), \quad A_g(\rho, y)|_{y=0} = \tilde{A}_g(\rho), \quad (21)$$

where  $\tilde{A}_q$  and  $\tilde{A}_g$  are the amplitudes of the same process at  $Q^2 \sim \mu^2$ . We denote  $\tilde{f}_q^{(A)}$  and  $\tilde{f}_g^{(A)}$  the Mellin amplitudes conjugated to them. Amplitudes  $\tilde{f}_{q,g}^{(A)}$  should be found independently. The IREEs for them do not contain derivatives because  $Q^2 = \mu^2$ , so they are algebraic equations but in contrast to Eqs. (18,20) they are inhomogeneous:

$$\begin{aligned} \omega \tilde{f}_q^{(A)}(\omega) &= \phi_q^{(A)} + \tilde{f}_q^{(A)}(\omega) h_{qq}(\omega) + \tilde{f}_g^{(A)}(\omega) h_{gq}(\omega), \\ \omega \tilde{f}_g^{(A)}(\omega) &= \phi_g^{(A)} + \tilde{f}_q^{(A)}(\omega) h_{qg}(\omega) + \tilde{f}_g^{(A)}(\omega) h_{gg}(\omega), \end{aligned} \quad (22)$$

with inhomogeneous terms  $\phi_q^{(A)}$  and  $\phi_g^{(A)}$ . We will call  $\phi_{q,g}^{(A)}$  inputs. We will specify them later. The technology of composing IREEs for amplitudes  $B_q$  and  $B_g$  is absolutely the same. As a result, the equations for  $f_q^{(B)}$  and  $f_g^{(B)}$  in the region  $Q^2 \gg \mu^2$  are

$$\begin{aligned} \partial f_q^{(B)}(\omega, y) / \partial y &= [-\omega + h_{qq}(\omega)] f_q^{(B)}(\omega, y) + f_g^{(B)}(\omega, y) h_{gq}(\omega), \\ \partial f_g^{(B)}(\omega, y) / \partial y &= f_q^{(B)}(\omega, y) h_{qg}(\omega) + [-\omega + h_{gg}(\omega)] f_g^{(B)}(\omega, y) \end{aligned} \quad (23)$$

while  $f_{q,g}^{(B)}$  at  $Q^2 \sim \mu^2$  obey the following IREEs:

$$\begin{aligned} \omega \tilde{f}_q^{(B)}(\omega) &= \phi_q^{(B)} + \tilde{f}_q^{(B)}(\omega) h_{qq}(\omega) + \tilde{f}_g^{(B)}(\omega) h_{gq}(\omega), \\ \omega \tilde{f}_g^{(B)}(\omega) &= \phi_g^{(B)} + \tilde{f}_q^{(B)}(\omega) h_{qg}(\omega) + \tilde{f}_g^{(B)}(\omega) h_{gg}(\omega), \end{aligned} \quad (24)$$

where  $\phi_q^{(B)}$  and  $\phi_g^{(B)}$  are the inputs. They differ from the inputs  $\phi_{q,g}^{(A)}$  for amplitudes  $A_{q,g}$ . We will specify them later.

### 3.2 Solution to IREEs for amplitudes $A_q$ and $A_g$

By obtaining first general solutions to differential equations in Eqs. (20), then solving algebraic equations (22) and using the matching (21) to specify the

general solutions, we arrive<sup>2</sup> at the following expressions for  $A_q$  and  $A_g$ :

$$A_q = \int_{-\infty}^{\infty} \frac{d\omega}{2\pi i} x^{-\omega} [\phi_q^{(A)} (C_q^{(+)} e^{\Omega_{(+)} y} + C_q^{(-)} e^{\Omega_{(-)} y}) + \phi_g^{(A)} (C_g^{(+)} e^{\Omega_{(+)} y} + C_g^{(-)} e^{\Omega_{(-)} y})], \quad (25)$$

$$A_g = \int_{-\infty}^{\infty} \frac{d\omega}{2\pi i} x^{-\omega} [\phi_q^{(A)} (\tilde{C}_q^{(+)} e^{\Omega_{(+)} y} + \tilde{C}_q^{(-)} e^{\Omega_{(-)} y}) + \phi_g^{(A)} (\tilde{C}_g^{(+)} e^{\Omega_{(+)} y} + \tilde{C}_g^{(-)} e^{\Omega_{(-)} y})],$$

where the anomalous dimensions  $\Omega_{(\pm)}$  are made of  $h_{rr'}$

$$\Omega_{(\pm)} = \frac{1}{2} [h_{gg} + h_{qq} \pm \sqrt{R}], \quad (26)$$

with

$$R = (h_{gg} + h_{qq})^2 - 4(h_{qq}h_{gg} - h_{qg}h_{gq}) = (h_{gg} - h_{qq})^2 + 4h_{qg}h_{gq}. \quad (27)$$

Coefficient functions  $C_{q,g}^{(\pm)}(\omega)$  and  $\tilde{C}_{q,g}^{(\pm)}(\omega)$  are also made of  $h_{rr'}$ . However, explicit expressions for them are rather bulky, so we put them in Appendix. The IREEs for amplitudes  $B_{q,g}$  are quite similar to the ones for  $A_{q,g}$ . As a result, the expressions for them are alike Eq. (25)

$$B_q = \int_{-\infty}^{\infty} \frac{d\omega}{2\pi i} x^{-\omega} \phi_q^{(B)} (C_q^{(+)} e^{\Omega_{(+)} y} + C_q^{(-)} e^{\Omega_{(-)} y}) \quad (28)$$

$$B_g = \int_{-\infty}^{\infty} \frac{d\omega}{2\pi i} x^{-\omega} \phi_g^{(B)} (\tilde{C}_g^{(+)} e^{\Omega_{(+)} y} + \tilde{C}_g^{(-)} e^{\Omega_{(-)} y}).$$

Eqs. (25) and 28) involve the same coefficient functions and anomalous dimensions. The only difference between Eqs. (25) and (28) is different inputs. Now we are going to specify them.

## 4 Specifying the inputs

By definition, inputs in evolution equations stand for the starting points of the evolution. They are considered elementary and cannot be obtained through evolution.

---

<sup>2</sup>Details can be found in Ref. [29].

## 4.1 Inputs for amplitudes $A_{q,g}$

Evolution of amplitude  $A_q$  starts from the Born contribution which is given by the following expression

$$A_q^{(Born)} = \frac{1}{\pi} g_{\mu\nu} \Im \left[ -\frac{1}{2} \frac{\bar{u}(p)\gamma_\nu(\hat{p} + \hat{q})\gamma_\mu u(p)}{w(1-x) - \mu^2 + i\epsilon} \right] = -2 \delta(1-x-\lambda), \quad (29)$$

where we have denoted  $\lambda = \mu^2/w$ . In Eq. (29), we dropped the quark electric charge and introduced the IR cut-off  $\mu$ . It is clear that  $\lambda$  can be neglected compared to  $x$  in the kinematics  $Q^2 \gg \mu^2$ , so  $A_q^{(Born)}$  is  $\mu$ -independent in this region and vanishes after differentiation over  $\mu$ . It explains why the quark inhomogeneous term is absent in Eqs. (18),(20). In contrast,  $A_q^{(Born)}$  depends on  $\mu$  in the region  $Q^2 \sim \mu^2$ . and appears in Eq. (22). Dropping  $x$  in Eq. (29) compared to  $\lambda$  in this region and applying the transform of Eq. (16), we obtain the input  $\phi_q^{(A)}$ . Remembering that there is no Born contribution to  $A_g$  at any  $Q^2$ , we arrive at the following expressions for the inputs

$$\begin{aligned} \phi_q^{(A)} &= -2, \\ \phi_g^{(A)} &= 0. \end{aligned} \quad (30)$$

## 4.2 Inputs for amplitudes $B_{q,g}$

The situation with specifying inputs  $\phi_{q,g}^{(B)}$  is more involved. In the Born approximation we have

$$B_q^{(Born)} = \frac{1}{\pi} \frac{p_\mu p_\nu}{pq} \Im \left[ -\frac{1}{2} \frac{\bar{u}(p)\gamma_\nu(\hat{p} + \hat{q})\gamma_\mu u(p)}{w(1-x) - \mu^2 + i\epsilon} \right] \sim p^2 \approx 0. \quad (31)$$

In addition,  $B_g^{(Born)} = 0$ . Thus, the both Born amplitudes are zeros, which excludes using the Born approximation as the starting point of the IR evolution in contrast to the standard technology. Calculations of  $F_{1,2}$  in the first and second loops can be found in Refs. [1]– [13]. The first loop contributions to  $B_{q,g}$  are

$$B_q^{(1)} = \frac{\alpha_s}{2\pi} C_F, \quad B_g^{(1)} = \frac{\alpha_s}{\pi} n_f (1-x), \quad (32)$$

where we have used the standard notations  $C_F = (N^2 - 1)/2N = 4/3$  and  $n_f$  is the number of flavours.

Straightforward calculations of  $F_L$  in the  $\alpha_s^2$  order (see Refs. [10]– [13]) demonstrate that the most important contributions to  $B_{q,g}$  at small  $x$  are

$\sim 1/x$ . The factor  $1/x$  cannot be obtained with IR evolution of the first-loop contributions (32) as well as with using any evolution equation available in the literature. Moreover, there is not any physical reason to predict existence of  $1/x$  in the second loop because amplitudes  $B_{q,g}$  are artificial while physical amplitudes involve  $xB_{q,g}$  and  $x^2B_{q,g}$  which are free of  $1/x$ . Fortunately, the higher loops yield logarithms instead of power contributions  $\sim 1/x^n$  as was shown in Refs. [14, 15]. These logarithms can be accounted for to all orders in  $\alpha_s$  with evolution equations. Our strategy is to account for DL contributions to  $B_{q,g}$ , evolving onwards the second-loop amplitudes  $B_{q,g}^{(2)}$ , so it is necessary to know which Feynman graphs contributing to  $B_{q,g}^{(2)}$  are most important at small  $x$ , what are the most essential kinematics of virtual partons in those graphs and why new power factors  $\sim 1/x^n$  do not appear in higher orders in  $\alpha_s$ . In order to clarify these issues we calculated  $B_{q,g}^{(2)}$  anew (see Ref. [30]), focusing on the small- $x$  kinematics and accounting for the leading contributions only. The results are given by the following expressions

$$\begin{aligned} B_q^{(2)} &= C_q^{(2)} \gamma^{(2)} \rho x^{-1}, \\ B_g^{(2)} &= C_g^{(2)} \gamma^{(2)} \rho x^{-1} \end{aligned} \tag{33}$$

with

$$\gamma^{(2)} = \alpha_s^2 \ln 2/2\pi \tag{34}$$

and the color factors

$$\begin{aligned} C_q^{(2)} &= C_F^2 - 2C_F n_f, \\ C_g^{(2)} &= C_F n_f - 2N n_f. \end{aligned} \tag{35}$$

The expressions of Eq. (33) come from the ladder Feynman graphs. The first terms in every expression of Eq. (35) come from the graphs where all intermediate  $t$ -channel partons are quarks whereas the second terms refer to the case where the upper rung contains quarks in the  $t$  channel and the lower rung involves  $t$ -channel gluons (see Ref. [30] for detail). Unfortunately, there were mistakes in Ref. [30]: the second terms in the both expressions for  $C_{q,g}^{(2)}$  were incorrect. For the simplicity sake, the QCD coupling in Eq. (34) was treated in Ref. [30] as fixed.

### 4.3 Remark on treatment of the QCD coupling in DLA

When calculations in DLA are combined with accounting the running  $\alpha_s$  effects, one can use the leading approximation for the  $\beta$ -function:  $\beta \approx \beta_0$ .

Implementation of the running  $\alpha_s$  in the IREEs was considered in Ref. [37], where it was shown that  $\alpha_s$  in the  $\omega$ -space is given by the expressions of Eq. (67). Alternatively, one can keep  $\alpha_s$  fixed in the DLA framework. Estimates of the numerical value of the fixed  $\alpha_s$  were obtained in Ref. [32]. Namely,  $\alpha_s \approx 0.24$  when the virtual gluons have time-like momenta and  $\alpha_s \approx 0.48$  when their momenta are space-like.

#### 4.4 Combining the inputs for $B_{q,g}$ with the DL contributions

We are going to treat  $B_{q,g}^{(2)}$  as the starting point of IR evolution and substitute them in Eq. (28) as the inputs, so they should be written in the  $\omega$  space. Remembering that  $\rho = \xi + y$  and applying the transform (16), we arrive at the following expressions for the inputs in the  $\omega$  space

$$\begin{aligned}\phi_q^{(B)} &= x^{-1} \gamma^{(2)} C_q^{(2)} \left( \frac{y}{\omega} + \frac{1}{\omega^2} \right), \\ \phi_g^{(B)} &= x^{-1} \gamma^{(2)} C_g^{(2)} \left( \frac{y}{\omega} + \frac{1}{\omega^2} \right).\end{aligned}\tag{36}$$

When  $x$  is small enough,  $\xi > y$ , so one can neglect the terms  $y/\omega$  compared to  $1/\omega^2$ . Substituting  $\phi_{q,g}^{(B)}$  of Eq. (36) in Eq. (28), we arrive at amplitudes  $B_{q,g}$  calculated in DLA

$$\begin{aligned}B_q &= \gamma^{(2)} x^{-1} \int_{-\infty}^{\infty} \frac{d\omega}{2\pi i} x^{-\omega} C_q^{(2)} \left( D_q^{(+)} e^{\Omega_{(+)} y} + D_q^{(-)} e^{\Omega_{(-)} y} \right) \\ B_g &= \gamma^{(2)} x^{-1} \int_{-\infty}^{\infty} \frac{d\omega}{2\pi i} x^{-\omega} C_g^{(2)} \left( \tilde{D}_g^{(+)} e^{\Omega_{(+)} y} + \tilde{D}_g^{(-)} e^{\Omega_{(-)} y} \right),\end{aligned}\tag{37}$$

where we have denoted

$$\begin{aligned}D_q^{(\pm)} &= \left( \frac{y}{\omega} + \frac{1}{\omega^2} \right) C_q^{(\pm)}, & D_g^{(\pm)} &= \left( \frac{y}{\omega} + \frac{1}{\omega^2} \right) C_g^{(\pm)}, \\ \tilde{D}_q^{(\pm)} &= \left( \frac{y}{\omega} + \frac{1}{\omega^2} \right) \tilde{C}_q^{(\pm)}, & \tilde{D}_g^{(\pm)} &= \left( \frac{y}{\omega} + \frac{1}{\omega^2} \right) \tilde{C}_g^{(\pm)}.\end{aligned}\tag{38}$$

## 5 Expressions for $F_1, F_2$ and $F_L$

Using Eqs. (30,25) and (37), we obtain explicit expressions for  $A_{q,g}$  and  $B_{q,g}$ . Using these results and Eq. (9), we arrive at explicit expressions for  $F_1^{(q,g)}$  and

$F_2^{(q,g)}$ 

$$\begin{aligned} F_1^{(q)} &= (I_q + \gamma^{(2)} C_q^{(2)} I'_q) + \gamma^{(2)} C_q^{(2)} I'_q, \\ F_1^{(g)} &= (\tilde{I}_g + \gamma^{(2)} C_g^{(2)} \tilde{I}'_g) + \gamma^{(2)} C_g^{(2)} \tilde{I}'_g, \end{aligned} \quad (39)$$

$$\begin{aligned} F_2^{(q)} &= 2x [(I_q + 3\gamma^{(2)} C_q^{(2)} I'_q) + 3\gamma^{(2)} C_q^{(2)} I'_q], \\ F_2^{(g)} &= 2x [(\tilde{I}_g + 3\gamma^{(2)} C_g^{(2)} \tilde{I}'_g) + 3\gamma^{(2)} C_g^{(2)} \tilde{I}'_g], \end{aligned} \quad (40)$$

$$\begin{aligned} F_L^{(q)} &= 4x\gamma^{(2)} C_q^{(2)} I'_q, \\ F_L^{(g)} &= 4x\gamma^{(2)} C_g^{(2)} \tilde{I}'_g. \end{aligned} \quad (41)$$

$I_{q,g}$ ,  $I'_{q,g}$  and  $\tilde{I}_{q,g}$ ,  $\tilde{I}'_{q,g}$  are defined as follows

$$\begin{aligned} I_q &= \int_{-i\infty}^{i\infty} \frac{d\omega}{2\pi i} x^{-\omega} (C_q^{(+)} e^{\Omega_{(+)} y} + C_q^{(-)} e^{\Omega_{(-)} y}), \\ I'_q &= \int_{-i\infty}^{i\infty} \frac{d\omega}{2\pi i} x^{-\omega} (D_q^{(+)} e^{\Omega_{(+)} y} + D_q^{(-)} e^{\Omega_{(-)} y}), \\ I_g &= \int_{-i\infty}^{i\infty} \frac{d\omega}{2\pi i} x^{-\omega} (C_g^{(+)} e^{\Omega_{(+)} y} + C_g^{(-)} e^{\Omega_{(-)} y}), \\ I'_g &= \int_{-i\infty}^{i\infty} \frac{d\omega}{2\pi i} x^{-\omega} (D_g^{(+)} e^{\Omega_{(+)} y} + D_g^{(-)} e^{\Omega_{(-)} y}), \\ \tilde{I}_q &= \int_{-i\infty}^{i\infty} \frac{d\omega}{2\pi i} x^{-\omega} (\tilde{C}_q^{(+)} e^{\Omega_{(+)} y} + \tilde{C}_q^{(-)} e^{\Omega_{(-)} y}), \\ \tilde{I}'_q &= \int_{-i\infty}^{i\infty} \frac{d\omega}{2\pi i} x^{-\omega} (\tilde{D}_q^{(+)} e^{\Omega_{(+)} y} + \tilde{D}_q^{(-)} e^{\Omega_{(-)} y}), \\ \tilde{I}_g &= \int_{-i\infty}^{i\infty} \frac{d\omega}{2\pi i} x^{-\omega} (\tilde{C}_g^{(+)} e^{\Omega_{(+)} y} + \tilde{C}_g^{(-)} e^{\Omega_{(-)} y}), \\ \tilde{I}'_g &= \int_{-i\infty}^{i\infty} \frac{d\omega}{2\pi i} x^{-\omega} (\tilde{D}_g^{(+)} e^{\Omega_{(+)} y} + \tilde{D}_g^{(-)} e^{\Omega_{(-)} y}). \end{aligned} \quad (42)$$

We remind that explicit expressions for  $C_q^{(\pm)}$ ,  $C_g^{(\pm)}$ ,  $\tilde{C}_q^{(\pm)}$  and  $\tilde{C}_g^{(\pm)}$  can be found in Appendix A. Eqs. (39,40) are valid at  $Q^2 > \mu^2$  ( $\mu \approx 1$  GeV, see Ref. [31] for detail) but it is easy to generalize them for small  $Q^2$ . The prescription is obtained in Ref. [38]: Eqs. (39,40,41) can be used at arbitrary

$Q^2$  providing that  $Q^2$  is replaced by  $\bar{Q}^2 = Q^2 + \mu^2$ . It leads to replacing  $x, y$  and  $\xi$  by  $\bar{x}, \bar{y}, \bar{\xi}$  respectively

$$\bar{x} = (Q^2 + \mu^2) / w, \quad \bar{y} = (Q^2 + \mu^2) / \mu^2, \quad \bar{\xi} = \ln [(Q^2 + \mu^2) / w]. \quad (43)$$

Now we use Eq. (3) and convolute Eqs. (39, 40,41) with the parton distributions  $\Phi_q$  and  $\Phi_g$ , By doing so we obtain the expressions for the structure functions  $F_1, F_2, F_L$  which can be used at small  $x$  and arbitrary  $Q^2$

$$\begin{aligned} F_1(\bar{x}, \bar{Q}^2) &= F_1^{(q)}(\bar{x}, \bar{Q}^2) \otimes \Phi_q + F_1^{(g)}(\bar{x}, \bar{Q}^2) \otimes \Phi_g, \\ F_2(\bar{x}, \bar{Q}^2) &= F_1^{(q)}(\bar{x}, \bar{Q}^2) \otimes \Phi_q + F_2^{(g)}(\bar{x}, \bar{Q}^2) \otimes \Phi_g, \\ F_L(\bar{x}, \bar{Q}^2) &= F_L^{(q)}(\bar{x}, \bar{Q}^2) \otimes \Phi_q + F_L^{(g)}(\bar{x}, \bar{Q}^2) \otimes \Phi_g. \end{aligned} \quad (44)$$

Technically, such convolution is convenient to make with multiplying all integrands in Eq. (42) by the factors  $\hat{\Phi}_q(\omega)$  and  $\hat{\Phi}_g(\omega)$  which denote the parton distributions in the  $\omega$  space.

## 6 Small- $x$ asymptotics of the unpolarized structure functions

In this Sect. we calculate small- $x$  asymptotics of  $F_{1,2,L}$ . To begin with, we notice that Eq. (26) reads that  $\Omega_{(+)} > \Omega_{(-)}$ . Because of that we can drop the terms comprising  $\Omega_{(-)}$ . Then, we represent all integrals in Eq. (42) in the exponential form. For instance,

$$\begin{aligned} I_{q,g} &\approx \int_{-i\infty}^{i\infty} \frac{d\omega}{2\pi i} e^{\omega \bar{\xi} + \Psi_{q,g}(\omega)}, \\ \tilde{I}_{q,g} &\approx \int_{-i\infty}^{i\infty} \frac{d\omega}{2\pi i} e^{\omega \bar{\xi} + \tilde{\Psi}_{q,g}(\omega)}, \end{aligned} \quad (45)$$

with

$$\begin{aligned} \Psi_{q,g} &= \Omega_{(+)} \bar{y} + \ln C_{q,g}^{(+)} + \ln \hat{\Phi}_{q,g}, \\ \tilde{\Psi}_{q,g} &= \Omega_{(+)} \bar{y} + \ln \tilde{C}_{q,g}^{(+)} + \ln \hat{\Phi}_{q,g}. \end{aligned} \quad (46)$$

Handling any of  $I_{q,g}, I'_{q,g}$  and  $\tilde{I}'_{q,g}, \tilde{I}_{q,g}$  is the same. Finally, we push  $x \rightarrow 0$  (i.e.  $\xi \rightarrow \infty$ ) and apply the Saddle-Point method to each expression in Eq. (44).

This method states that the small- $x$  asymptotics of the structure functions is given by the following expressions

$$\begin{aligned} F_1 &\sim \frac{\chi_1}{\xi^{3/2}} \bar{x}^{-\omega_0} (\bar{Q}^2/\mu^2)^{\omega_0/2}, \\ F_2 &\sim \frac{\chi_2}{\xi^{3/2}} \bar{x}^{-\omega_0+1} (\bar{Q}^2/\mu^2)^{\omega_0/2}, \\ F_L &\sim \frac{\chi_L}{\xi^{3/2}} \bar{x}^{-\omega_0+1} (\bar{Q}^2/\mu^2)^{\omega_0/2}, \end{aligned} \quad (47)$$

where  $\bar{x}$  and  $\bar{Q}^2$  are defined in Eq. (43), so Eq. (47) is valid for large and small  $Q^2$ , including  $Q^2 = 0$ . The notation  $\omega_0$  in Eq. (47) stands for the rightmost singularities of the perturbative factors  $\Psi_{q,g}$  and  $\tilde{\Psi}_{q,g}$  in Eq. (46)

$$\omega_0 = 1.07. \quad (48)$$

The factors  $\chi_{1,2,3}$  include as numerical factors of the perturbative origin as the parton distributions  $\hat{\Phi}_{q,g}(\omega)$  at  $\omega = \omega_0$ . Those factors are different for different structure functions. The asymptotics of  $F_{1,2,L}$  in Eq. (47) exhibit the almost identical  $Q^2$  dependence. It is generated by the term  $e^{\Omega_{(+)}(\omega)y}$  which participates in each  $\Psi_r$ . Using explicit expressions for  $h_{rr'}$  in Appendix B, it is easy to show that  $\Omega_{(+)}(\omega_0) = \omega_0/2$ .

Eq. (47) demonstrates that asymptotics of all structure functions are of the Regge type. The Saddle-Point method turns the total sum of the terms  $\sim (\alpha_s \ln^2(1/x))^n$  into the Regge power factor  $x^{-\omega_0}$ . It grows steeply at small  $x$ , which makes redundant factors  $x^{-a}$  in the parton distributions  $\Phi_{q,g}$ . The intercept of the Reggeon controlling  $F_1$  exceeds unity, so it is a new (soft) Pomeron. Although it has nothing in common with the BFKL Pomeron, its intercept is surprisingly close to the one of the BFKL Pomeron in NLO. This issue was considered in detail in Ref. [29]. In contrast, the intercepts of the other Reggeons in Eq. (47) are much smaller than unity but nevertheless they predict the slow growth of  $F_2$  and  $F_L$  when  $x$  decreases. Below we briefly consider some corollaries of Eq. (47).

## 6.1 Asymptotic scaling

The asymptotics in Eq. (47) at  $Q^2 \gg \mu^2$  can approximately be represented as follows

$$\begin{aligned} F_1 &\sim \zeta^{-1.07}, \\ F_2 &\sim x\zeta^{-1.07}, \\ F_L &\sim x\zeta^{-1.07}, \end{aligned} \quad (49)$$

with  $\zeta = x\sqrt{\mu^2/Q^2}$ , so that  $F_1$  as well as  $F_2/x$  and  $F_L/x$  at  $x \ll 1$  and  $Q^2 \gg \mu^2$  depend on the argument  $\zeta$  save the logarithmic factors dropped in Eq. (49). Such scaling of the asymptotics of the structure functions has not been predicted by any other approach.

## 6.2 Ratio $F_L/F_2$ at small $x$

It follows from Eq. (47) that the ratio  $F_L/F_2$  is given by the following expression

$$R_{2L} \equiv F_L/F_2 = \frac{2\gamma^{(2)}\rho \left( C_q^{(2)}C_q^{(+)}(\omega_0)\lambda_q(\omega_0) + C_g^{(2)}C_g^{(+)}(\omega_0)\lambda_g(\omega_0) \right)}{\left( 1+3\gamma^{(2)}\rho C_q^{(2)} \right) C_q^{(+)}(\omega_0)\lambda_q(\omega_0) + 3\gamma^{(2)}\rho C_g^{(2)}C_g^{(+)}(\omega_0)\lambda_g(\omega_0)}. \quad (50)$$

We remind that  $\gamma^{(2)}$  is defined in Eq. (34) and  $\rho = \xi + y \approx \xi$  at  $x \ll 1$ . Obviously,  $F_L/F_2 \approx \gamma^{(2)}\rho \approx 0.006\rho$  at  $\rho \ll 1/\gamma^{(2)}$  which corresponds to the energy scale presently available at experiment. In the opposite case, i.e. at  $\rho \gg 1/\gamma^{(2)}$ , the ratio  $F_L/F_2 \sim 2/3$ , though this limit can be achieved at really asymptotic energies.

## 6.3 Relations between logarithmic derivatives of the structure functions

Logarithmic derivatives, i.e.  $\partial \ln F_r / \partial \ln Q^2 = (1/F_r)\partial F_r / \partial \ln Q^2$ , with  $r = 1, 2, L$ , were already discussed in the literature in the context of DGLAP and the dipole model (see e.g. Refs. [11,35]). It motivates us to construct analogous relations for  $F_r$  in DLA at the small- $x$  by differentiating Eq. (47). First of all, there are relations for the  $Q^2$ -dependence of the structure functions

$$\frac{\partial \ln F_1}{\partial y} = \frac{\partial \ln F_2}{\partial y} \approx \frac{\partial \ln F_L}{\partial y}. \quad (51)$$

Then, the relations involving the  $x$ - and  $Q^2$ -dependence of  $F_r$

$$\begin{aligned} \frac{\partial \ln F_1}{\partial \xi} - 2\frac{\partial \ln F_1}{\partial y} &\sim 0, \\ \frac{\partial \ln F_2}{\partial \xi} - 2\frac{\partial \ln F_2}{\partial y} &\sim -1, \\ \frac{\partial \ln F_L}{\partial \xi} - 2\frac{\partial \ln F_L}{\partial y} &\sim -1 \end{aligned} \quad (52)$$

at  $x \ll 1$  and  $Q^2 > \mu^2 \approx 1 \text{ GeV}^2$ . We stress that the relations (52) differ a lot from the results in all approaches based on BFKL and DGLAP or on their modifications (see e.g. Refs. [11, 21]). The difference between our results and the results (see e.g. Ref. [36]) obtained in the Regge inspired models [25, 26] is even greater: the intercepts in our approach do not depend on  $Q^2$ .

## 6.4 Remark on Soft and Hard Pomerons

One of results obtained in Ref. [29] is the estimate of the region of applicability of the Regge asymptotics: the expressions for the small- $x$  asymptotics in Eq. (47) are reliable at  $x \leq 10^{-6}$ . The straightforward way to describe  $F_{1,2}$  and  $F_L$  at larger  $x$  is to apply the parent expressions of Eqs. (44) despite their complexity. The same should be done, when BFKL is applied. However, there is a tendency in the literature to use the Regge asymptotics at  $x \gg 10^{-6}$ , which inevitably leads to introducing phenomenological Pomerons with intercepts much greater than 1.07. In order to simplify our explanation we use the generic notation  $F$  for any of  $F_{1,2}, F_L$  and denote  $\Gamma$  their small- $x$  asymptotics. The ratio

$$R_{as} \equiv \Gamma/F \tag{53}$$

depends on both  $Q^2$  and  $x$ , i.e.  $R_{as} = R_{as}(x, Q^2)$ . To begin with, we put  $Q^2 = \mu^2$  and study dependence of  $R_{as}(x, \mu^2)$  on  $x$ . It turns out that  $R_{as}(x, \mu^2)$  decreases when  $x$  grows. In particular, the values of  $R_{as}(x, \mu^2)$  at  $x_0 = 10^{-6}, x_1 = 10^{-4}, x_2 = 10^{-3}$  are as follows

$$\begin{aligned} R_{as}(x_0, \mu^2) &= 0.9, \\ R_{as}(x_1, \mu^2) &= 0.67, \\ R_{as}(x_2, \mu^2) &= 0.5. \end{aligned} \tag{54}$$

Eq. (54) reads that  $R_{as} = 0.9$  at  $x = x_0$ . We interpret it as indication that the asymptotics at  $x = x_0$  rather reliably represent the parent structure functions while it becomes unreliable at greater  $x$ . This is the reason why  $x_0$  was chosen in Ref. [29] as the upper border of the applicability region of the asymptotics. Then, numerical estimates show that  $R_{as}$  decreases when  $Q^2$  grows, so the asymptotics should not be used at  $x > x_0$ . On the other hand, in practice the Regge asymptotics are used at  $x > x_0$ . In this case a new Reggeon is supposed to mimic the structure functions and as a result it should equate the Regge factor of Eq. (47)

$$x_0^{-\omega_0} = x^{-a}. \tag{55}$$

For example, if the asymptotics is used at  $x_1 = 10^{-4}$ , the intercept  $a_1$  of the phenomenological Reggeon is

$$a_1 = \omega_0 \frac{\ln x_0}{\ln x_1} = \frac{6}{4} \omega_0 = 1.6, \quad (56)$$

which corresponds to the new hard supercritical Pomeron. This estimate demonstrates that approximating the structure functions by their asymptotics beyond the applicability regions inevitably leads to introducing artificial phenomenological hard Pomerons. Moreover, using a similar argumentation, one can obtain spin-dependent hard Pomerons by applying the small- $x$  asymptotics of the structure function  $g_1$  outside its applicability region.

## 7 Summary

In the present paper, we have calculate the structure functions  $F_{1,2}$  and  $F_L$  in DLA. The instrument we used in order to sum DL contributions to all orders in  $\alpha_s$  was the IREE method. As a result, we obtained explicit expressions for  $F_1, F_2$  and  $F_L$ . Then we used the Saddle-Point Method to calculate the small- $x$  asymptotics of  $F_{1,2,L}$ . These asymptotics prove to be of the Regge type, but they are controlled by different Reggeons. The intercept of the Reggeon controlling the asymptotics of  $F_1$  is greater than unity, so it is a new contribution to Pomeron. In contrast, the intercept of the Reggeon controlling asymptotics of  $F_2$  and  $F_L$  is small but positive, which leads to the slow growth of  $F_{2,L}$  when  $x$  is decreasing. We demonstrated that DLA predicts identical  $Q^2$ -dependence of  $F_1$  and  $F_2$  and explained the reason to it. We have used the asymptotics  $F_{1,2}$  and  $F_L$  to obtain several differential relations between logarithms of  $F_1$  and  $F_2$ , which are absent in all other approaches available in the literature. The small- $x$  behavior of  $F_{1,2,L}$  in our approach almost coincides with the one obtained by the NLO BFKL. This makes impossible to find out which of those approaches is more adequate. However, the  $Q^2$ -dependence of the asymptotics obtained in DLA differs a lot from the one predicted by the conventional methods. This difference is especially great at small  $Q^2$ . Therefore, comparison of the  $Q^2$ -dependence with experimental data can select a more adequate approach.

## 8 Appendix

### 8.1 Expressions for $C_{q,g}^{(\pm)}(\omega)$ and $\tilde{C}_{q,g}^{(\pm)}(\omega)$

$$\begin{aligned}
 C_q^{(+)} &= \frac{(h_{qq} - \omega) \left( h_{gg} - h_{qq} - \sqrt{R} \right) + 2h_{qg}h_{gq}}{2\Delta\sqrt{R}}, \\
 C_q^{(-)} &= \frac{-(h_{qq} - \omega) \left( h_{gg} - h_{qq} + \sqrt{R} \right) - 2h_{qg}h_{gq}}{2\Delta\sqrt{R}}, \\
 C_g^{(+)} &= \frac{-h_{qg} \left( h_{gg} - h_{qq} - \sqrt{R} \right) - 2h_{qg}(h_{qq} - \omega)}{2\Delta\sqrt{R}}, \\
 C_g^{(-)} &= \frac{h_{qg} \left( h_{gg} - h_{qq} + \sqrt{R} \right) + 2h_{qg}(h_{qq} - \omega)}{2\Delta\sqrt{R}},
 \end{aligned} \tag{57}$$

where  $R$  is defined in Eq. (27),

$$\Delta = (\omega - h_{qq})(\omega - h_{gg}) - h_{qg}h_{gq} \tag{58}$$

and  $h_{ik}$  are defined below. Coefficient functions  $\tilde{C}_g^{(\pm)}$  and  $\tilde{C}_q^{(\pm)}$  are related with  $C_{q,g}^{(\pm)}$

$$\begin{aligned}
 \tilde{C}_q^{(+)} &= C_q^{(+)}X^{(+)}, & \tilde{C}_g^{(+)} &= C_g^{(+)}X^{(+)}, \\
 \tilde{C}_q^{(-)} &= C_q^{(-)}X^{(-)}, & \tilde{C}_g^{(-)} &= C_g^{(-)}X^{(-)},
 \end{aligned} \tag{59}$$

where

$$X^{(\pm)} = \frac{h_{gg} + h_{qq} \pm \sqrt{R}}{2h_{qg}}. \tag{60}$$

Thus we have expressed all coefficient functions in Eqs. (39 - 41) through  $h_{rr'}$ .

### 8.2 Expressions for $h_{ik}$

$$\begin{aligned}
 h_{qq} &= \frac{1}{2} \left[ \omega - Z - \frac{b_{gg} - b_{qq}}{Z} \right], & h_{qg} &= \frac{b_{qg}}{Z}, \\
 h_{gg} &= \frac{1}{2} \left[ \omega - Z + \frac{b_{gg} - b_{qq}}{Z} \right], & h_{gq} &= \frac{b_{gq}}{Z},
 \end{aligned} \tag{61}$$

where

$$Z = \frac{1}{\sqrt{2}} \sqrt{Y + W} , \quad (62)$$

with

$$Y = \omega^2 - 2(b_{qq} + b_{gg}) \quad (63)$$

and

$$W = \sqrt{(\omega^2 - 2(b_{qq} + b_{gg}))^2 - 4(b_{qq} - b_{gg})^2 - 16b_{qq}b_{gg}} , \quad (64)$$

where the terms  $b_{rr'}$  include the Born factors  $a_{rr'}$  and contributions of non-ladder graphs  $V_{rr'}$

$$b_{rr'} = a_{rr'} + V_{rr'} . \quad (65)$$

The Born factors are (see Ref. [31] for detail)

$$a_{qq} = \frac{A(\omega)C_F}{2\pi} , \quad a_{qg} = \frac{A'(\omega)C_F}{\pi} , \quad a_{gq} = -\frac{A'(\omega)n_f}{2\pi} . \quad a_{gg} = \frac{2NA(\omega)}{\pi} , \quad (66)$$

where  $A$  and  $A'$  stand for the running QCD couplings as shown in Ref. [37]

$$A = \frac{1}{b} \left[ \frac{\eta}{\eta^2 + \pi^2} - \int_0^\infty \frac{dze^{-\omega z}}{(z + \eta)^2 + \pi^2} \right] , \quad A' = \frac{1}{b} \left[ \frac{1}{\eta} - \int_0^\infty \frac{dze^{-\omega z}}{(z + \eta)^2} \right] , \quad (67)$$

with  $\eta = \ln(\mu^2/\Lambda_{QCD}^2)$ ,  $\mu \approx 1$  GeV and  $b$  being the first coefficient of the Gell-Mann–Low function. When the running effects for the QCD coupling are neglected,  $A(\omega)$  and  $A'(\omega)$  are replaced by  $\alpha_s$ . The terms  $V_{rr'}$  approximately represent the impact of non-ladder graphs on  $h_{rr'}$  (see Ref. [31] for detail)

$$V_{rr'} = \frac{m_{rr'}}{\pi^2} D(\omega) , \quad (68)$$

with

$$m_{qq} = \frac{C_F}{2N} , \quad m_{gg} = -2N^2 , \quad m_{gq} = n_f \frac{N}{2} , \quad m_{qg} = -NC_F , \quad (69)$$

and

$$D(\omega) = \frac{1}{2b^2} \int_0^\infty dze^{-\omega z} \ln((z + \eta)/\eta) \left[ \frac{z + \eta}{(z + \eta)^2 + \pi^2} - \frac{1}{z + \eta} \right] . \quad (70)$$

# References

- [1] E.G. Floratos, D.A. Ross, C.T. Sachrajda, Nucl. Phys. B**129** (1977) 66; [E B**139** (1978) 545]; Nucl. Phys. B**152** (1979) 493.
- [2] W.A. Bardeen, A.J. Buras, D.W. Duke, T.Muta, Phys. Rev. D**18** (1978) 3998.
- [3] G. Altarelli, R.K. Ellis, G. Martinelli, Nucl. Phys. B**143** (1978) 521; [E B**146** (1978) 544]; B**157** (1979) 461; **160** (1979) 301.
- [4] J. Kuhar-Andre, F.G. Paige, Phys. Rev. D**19** (1979) 221.
- [5] B. Humpert, W.L. Van Neerven, Phys. Lett. B**85** (1979) 293.
- [6] K. Harada, T. Kaneko, N. Sakai, Nucl. Phys. B**155** (1979) 169.
- [7] R. Baier, K.Fey: Z. Phys. C -Particles and Fields (1979) 339.
- [8] G. Curci, W. Furmanski, R. Petronzio, Nucl. Phys. B**175** (1980) 27; W. Furmanski, R. Petronzio, Z. Phys. C**11** (1982) 293.
- [9] A.A. Grigorian, N.Ya. Ivanov, A.B. Kaidalov, Sov. J. Nucl. Phys. **36** (1982) 867; Yad. Fiz. **36** (1982) 1490.
- [10] D.I. Kazakov, A.V. Kotikov, G. Parente, O.A. Sampayo, and J. Sanchez Guillen, Phys. Rev. Lett. **65** (1990) 1535.
- [11] L.P. Kaptari, A.V. Kotikov, N.Yu. Chernikova, Pengming Zhang, Phys. Rev. D**99** (2019) 096019.
- [12] W.L. van Neerven and E.B. Zijlstra, Phys. Lett. B**272** (1991) 127; E.B. Zijlstra and W.L. van Neerven, Phys. Lett. B**273** (1991) 476; Phys. Lett. B**297** (1992) 377; Nucl. Phys. B**383** (1992) 525.
- [13] S. Moch and J.A.M. Vermaseren, Nucl. Phys. B**573** (2000) 853.
- [14] S. Moch, J.A.M. Vermaseren, A. Vogt, Phys. Lett. B**606** (2005) 123.
- [15] J.A.M. Vermaseren, A. Vogt and S. Moch, Nucl. Phys. B**724** (2005) 3.
- [16] G. Altarelli and G. Parisi, Nucl. Phys. B**126** (1977) 297; V.N. Gribov and L.N. Lipatov, Sov. J. Nucl. Phys. **15** (1972) 438; L.N. Lipatov, Sov. J. Nucl. Phys. **20** (1972) 95; Yu.L. Dokshitzer, Sov. Phys. JETP **46** (1977) 641.

- [17] E.A. Kuraev, L.N. Lipatov and V.S. Fadin, Sov. Phys. JETP **44** (1976) 443; Sov. Phys. JETP **45**, 199 (1977);  
I.I. Balitsky and L.N. Lipatov, Sov. J. Nucl. Phys. **28** (1978) 822;  
V.S. Fadin and L.N. Lipatov. Phys. Lett. **B429** (1998) 127;  
G. Camici and M. Ciafaloni. Phys. Lett. **B430** (1998) 349.
- [18] J. Kwiecinski, A.D. Martin, A.M. Stasto. Phys. Rev. **D56** (1997) 3991
- [19] R.D. Ball, V. Bertone, M. Bonvini, S. Marzani, J. Rojo, L. Rottoli. Eur. Phys. J. **C78** (2018) 321.
- [20] A.H. Mueller, Nucl. Phys. **B415**, 373 (1994);  
A.H. Mueller and B. Patel, Nucl. Phys. **B425** (1994) 471; A.H. Mueller,  
Nucl. Phys. **B437** (1995) 107;  
Z. Chen, A.H. Mueller, Nucl. Phys. **B451** (1995) 579.
- [21] Yuri V. Kovchegov. Phys. Rev. **D60** (1999) 034008.
- [22] A. Luszczak, H. Kowalski. Phys. Rev. **D95** (2017) 1, 014030.
- [23] AAMQS: *A non-linear QCD analysis of new HERA data at small- $x$  including heavy quarks*. J.L. Albacete, N. Armesto, J. G. Milhano, P. Quiroga-Arias, C. A. Salgado. Eur. Phys. J. **C71** (2011) 1705.
- [24] xFitter Developer's Team. Eur. Phys. J. **C78** (2018) 621.
- [25] A. Capella *et al.* Phys. Lett. **B343**, 403 (1995);  
A. Capella *et al.* Phys. Rev. **D53** (1996) 2309.
- [26] J. Bartels, M. Wusthoff. J. Phys. G: Nucl. Part. Phys. **22** (1996) 929;  
Jochen Bartels, John R. Ellis, H. Kowalski, M. Wusthoff. Eur. Phys. J. **C7** (1999) 443 .
- [27] L.N. Lipatov. Zh. Eksp. Teor. Fiz. **82** (1982) 991; Phys. Lett. **B116** (1982) 411. R. Kirschner and L.N. Lipatov. ZhETP **83** (1982) 488; Nucl. Phys. **B213** (1983) 122.
- [28] V.N. Gribov. Yad. Fiz. **5** (1967) 399.
- [29] B.I. Ermolaev, S.I. Troyan. Eur. Phys. J. **C78** (2018) 204.
- [30] B.I. Ermolaev, S.I. Troyan. JHEP **03** (2021) 274.

- [31] B.I. Ermolaev, M. Greco, S.I. Troyan. Riv. Nuovo Cim. **33** (2010) 57; Acta Phys.Polon.B 38 (2007) 2243.
- [32] B.I. Ermolaev, S.I. Troyan. Eur. Phys. J. Plus **128** (2013) 34.
- [33] V.G. Gorshkov, L.N. Lipatov, M.M. Nesterov. Yad.Fiz. **9** (1969) 1221.
- [34] J. Bartels, B.I. Ermolaev, M.G. Ryskin. Z.Phys. **C70** (1996) 273; Z. Phys.**C72** (1996) 627.
- [35] G.R. Boroun. Phys. Lett. B (2021) 816; Phys. Rev. **C97** (2018) 015206.
- [36] M.B. Gay Ducati, V.P. Goncalves, M.V.T. Machado. Nucl. Phys. **A697** (2002) 767.
- [37] B.I. Ermolaev, M. Greco, S.I. Troyan. Phys. Lett. **B522** (2001) 57.
- [38] B.I. Ermolaev, S.I. Troyan. Eur. Phys. J. **C80** (2020) 98.
- [39] B.I. Ermolaev, M. Greco, S.I. Troyan. Phys. Lett. **B622** (2005) 93.

# BFKL EVOLUTION AND ENERGY FLOW FOR DIJET PRODUCTION WITH JET VETO AT LHC ENERGIES

Anatolii Iu. Egorov<sup>1,2</sup>, Victor T. Kim<sup>1,2</sup>

<sup>1</sup> Petersburg Nuclear Physics Institute of NRC “KI”, Gatchina

<sup>2</sup> Peter the Great St. Petersburg Polytechnic University,  
St. Petersburg

## Abstract

The calculations based on the next-to-leading logarithm approximation for the Balitsky–Fadin–Kuraev–Lipatov evolution are presented for the Mueller–Navelet dijet production cross section, as well as for their ratios to the dijet cross sections with a jet veto, as functions of the rapidity separation,  $\Delta y$ , between the two jets of a dijet. The veto on additional jet activity was accounted for in the Banfi–Marchesini–Smye approach. The results are compared to the measurements by the CMS experiment in proton-proton collisions at  $\sqrt{s} = 2.76$  and 7 TeV.

# БФКЛ ЭВОЛЮЦИЯ И ПОТОК ЭНЕРГИИ ПРИ ОБРАЗОВАНИИ ПАР АДРОННЫХ СТРУЙ С ВЕТО ПРИ ЭНЕРГИЯХ ЛНС

Анатолий Ю. Егоров<sup>1,2</sup>, Виктор Т. Ким<sup>1,2</sup>

<sup>1</sup> Петербургский институт ядерной физики НИЦ «КИ», Гатчина

<sup>2</sup> Санкт-Петербургский политехнический университет Петра Великого, Санкт-Петербург

## Аннотация

Представлены вычисления, основанные на следующем за главным логарифмическим приближении эволюции Балицкого–Фадина–Кураева–Липатова, для процессов рождения пар адронных струй Мюллера–Навелле, а также их отношений к двухструйным сечениям со струйным вето в зависимости от интервала быстроты,  $\Delta y$ , между струями в паре. Вето на дополнительную струйную активность учтено на основе подхода Банфи–Маркезини–Смая. Результаты сравниваются с измерениями эксперимента CMS в протон-протонных столкновениях при  $\sqrt{s} = 2.76$  и 7 ТэВ.

# 1 Introduction

To explore new physics at modern hadron colliders it is important to correctly take into account the effects of quantum chromodynamics (QCD). With the increase of the collision energy  $\sqrt{s}$ , the semihard QCD regime of high-energy also known as the Gribov-Regge limit is expected to become essential. In the Gribov-Regge limit, the energy tends to infinity ( $\sqrt{s} \rightarrow \infty$ ), while the momentum transfer,  $Q = \sqrt{-q^2} \simeq p_\perp$ , is kept finite, in such a way that  $p_\perp/\sqrt{s} \rightarrow 0$ , where  $p_\perp$  is the parton transverse momentum. As far as the momentum transfer is large enough, i.e.,  $Q \gg \Lambda_{\text{QCD}}$ , the perturbative QCD (pQCD) can be employed. With the pQCD approach and the Regge-Limit implied, the large logarithms of  $s$  need to be resummed, which is achieved with the Balitsky-Fadin-Kuraev-Lipatov (BFKL) approach [1–3]. This is in contrast to the hard QCD regime, for which  $Q \sim \sqrt{s} \rightarrow \infty$ , where the large logarithms required to resum are those of large  $Q$ . They are resummed within the Gribov-Lipatov-Altarelli-Parisi-Dokshitzer (DGLAP) formalism [4–8], which implies collinear factorization. While the DGLAP evolution is well established in the hard regime, the indications of the BFKL evolution in data still remain uncertain.

Hadron jets, produced at large rapidities,  $y$ , or dijets with a large rapidity separation,  $\Delta y$ , between the two jets of a dijet are considered to be good probes in the search for the BFKL effects at hadron colliders. Three main types of observables, that make use of hadronic jets as a probe, can be distinguished. The first type includes the ratios of the dijet production cross sections [9–12]. The main contribution to the dijet production cross section at large  $\Delta y$  in the BFKL approach comes from the Mueller-Navelet (MN) dijets, where the MN dijet is the pair of jets with the largest  $\Delta y$ , and jet pairs are combined from all the reconstructed jets with the transverse momentum,  $p_\perp$ , above some chosen transverse momentum threshold,  $p_{\perp\text{min}}$ . In fact, the MN dijets are a subset of inclusive dijets, a larger set consisting of all pairwise combinations (taken within a single event) of jets, that have  $p_\perp > p_{\perp\text{min}}$  [10].

The first type of observables can also be generalized by doing a different kind of experimental selections known as the jet veto. We also needed it to be introduced in the measurements. Hereafter, we define the *jet veto* as an event selection that prohibits (vetoes) the jets above some chosen jet  $p_\perp$  threshold,  $p_{\perp\text{veto}}$ . Also, the jet veto can be narrowed down to jets that appear only in some ranges of rapidity. For example, if the jet veto is introduced in the rapidity region between the two jets of a dijet, then it is referred to as the inter-jet veto.

The second type of observables includes the azimuthal decorrelations be-

tween the two jets in a dijet with large  $\Delta y$  [13–15]. Finally, the cross sections of the jet-gap-jet production via color singlet exchange [16–18] belong to the third type.

The aforementioned observables were measured at the Tevatron in the D0 [19–21] and CDF [22] experiments at  $\sqrt{s} = 0.63$  and 1.8 TeV, as well as at the Large Hadron Collider (LHC) by ATLAS [23, 24] and CMS [25–27] at  $\sqrt{s} = 7$  TeV. Exclusive dijet production via color singlet exchange was measured by CMS-TOTEM at  $\sqrt{s} = 13$  TeV [28]. Inclusive and MN dijet cross sections and the ratios with the jet veto were recently measured as functions of  $\Delta y$  by CMS at  $\sqrt{s} = 2.76$  TeV [29].

There are several problems that prevent us from drawing a firm conclusion in the BFKL evolution search. One of the problems is that the leading-logarithmic (LL) BFKL calculations provide us only with the qualitative results. The reason for that is that the LL BFKL calculations, designed for infinite energies in the first place, predict too high a value of the pomeron intercept, being equal to 1.54, which governs the rise of the cross sections with energy  $\sqrt{s}$  and  $\Delta y$ . Therefore, the LL BFKL predictions tend to overshoot the high-energy asymptotic effects. The other problem is that the DGLAP-based predictions, often given by the Monte Carlo (MC) simulations, contain corrections beyond the main approximation. For example, the LL DGLAP-based MC generators PYTHIA8 [30] and HERWIG [31] include some corrections accounting for the color coherence. For the parton shower, this leads to an angular ordering and, eventually, to a rapidity ordering, which mimics the BFKL dynamics. These corrections are small in the kinematic domain of the DGLAP evolution, but become unstable at large  $\Delta y$ . The problem is that there is no possibility to disentangle (exclude) the color coherence corrections from the all-order pQCD (shower) calculations in the modern DGLAP-based MC generators.

The next-to-leading logarithm (NLL) BFKL calculations became possible after the renormalization scheme and renormalization scale ambiguity [32, 33] was resolved by the generalization of the Brodsky–Lepage–Mackenzie optimal scale setting procedure [34] to the non-Abelian case by Brodsky–Fadin–Kim–Lipatov–Pivovarov (BFKLP) [35]. In the NLL BFKL calculations improved by the BFKLP approach the value of the pomeron intercept decreases to 1.13–1.18 in a wide range of  $Q$ , which agrees to the conventional Regge-Gribov theory.

The comparison of the theory to the data at the Tevatron and LHC shows that none of the DLGAP-based models are able to describe all the aspects of the observed data. On the other hand, the NLL BFKL calculations, when available, are in agreement to the data. However, rather complicated NLL BFKL calculation methods employing BFKLP scale setting [35] are developed

only for the azimuthal decorrelations and the Mueller-Navelet dijet production cross section [36, 37]. The jet-gap-jet production cross section ratios can be calculated in the LL BFKL approximation improved with the principal NLL BFKL contributions [17, 18]. The cross section ratios with the veto can only be calculated with the LL BFKL accuracy by an MC simulation with the generator HEJ [38]. Therefore, the important task is the development of the NLL BFKL-based calculations for all the measured observables.

The goal of this paper is to confront the calculation based on the NLL BFKL improved with BFKLP approach [35] to the MN cross section measured by CMS at  $\sqrt{s} = 2.76$  TeV, and the ratios with the inter-jet veto at 2.76 and 7 TeV [25, 29], as well as to make predictions for the MN cross section and ratios with the inter-jet veto for  $\sqrt{s} = 13$  TeV, which are possible to measure at the LHC.

To the best of our knowledge, there is no BFKL-based method to calculate the impact of the jet veto. For the purposes of the current paper, we calculate the veto impact with the Banfi–Marchesini–Smye (BMS) approach [39]. The BMS approach was elaborated to describe the physics of the energy flow away from jets. The approach was tested against the ATLAS [40] and CMS [41] inter-jet/jet veto measurements, and showed some level of agreement. In both papers, the Born level subprocess convoluted with the parton distribution functions (PDFs) was used in the inclusive cross section calculation. In the method, a probability of not breaking the veto is added to the calculation. This probability was governed by the BMS evolution equation. Even though such calculations have a decent agreement to the ratios of the cross sections with veto, the agreement to the absolute values of the cross sections is expected to be worse. A recent paper by CMS [29] provides a measurement of the absolute values of the cross sections and the cross section ratios with veto, which allows for a better testing of the models.

In Sec. 2 we briefly outline the BFKLP approach [35] to the MN cross section calculation. In Sec. 3 we describe the application of the BMS equation to the inter-jet veto, i.e., veto in rapidity region between the jets of dijets. In Sec. 4 the theoretical uncertainty of the calculation is discussed. In Sec. 5 we present the comparison of the calculations to the CMS measurements [25, 29] at  $\sqrt{s} = 7$  and 2.76 TeV, as well as our predictions for proton-proton ( $pp$ ) collisions at  $\sqrt{s} = 13$  TeV.

## 2 BFKLP approach to Mueller-Navelet cross section

In the semihard regime, the MN cross section can be written, assuming the factorization, as a convolution of a partonic subprocess cross section  $\hat{\sigma}$  and PDFs, as follows:

$$\frac{d\sigma}{dy_1 dy_2 d^2\vec{k}_1 d^2\vec{k}_2} = \sum_{ij} \int_0^1 dx_1 dx_2 f_i(x_1, \mu_F) f_j(x_2, \mu_F) \frac{d\hat{\sigma}_{ij}(x_1 x_2 s, \mu_F, \mu_R)}{dy_1 dy_2 d^2\vec{k}_1 d^2\vec{k}_2}, \quad (1)$$

where  $y_{1(2)}$  are the rapidities of the two jets in a dijet,  $\vec{k}_{1(2)}$  are the transverse momenta of the two jets,  $f_{i(j)}$  are the PDFs,  $x_{1(2)}$  are the longitudinal proton momentum fractions carried by partons before their scattering,  $\mu_R$  and  $\mu_F$  are the renormalization and factorization scales respectively. The summation in Eq. (1) goes through all the open parton flavors, and the integration performed is over  $x_{1(2)}$ .

Within the LL/NLL BFKL approach, the partonic cross section  $\hat{\sigma}$  itself factorizes into the process dependent vertices  $V$  and the universal Green's function  $G$ :

$$\begin{aligned} \frac{d\hat{\sigma}_{ij}(x_1 x_2 s, \mu_F, \mu_R)}{dy_1 dy_2 d^2\vec{k}_1 d^2\vec{k}_2} &= \frac{x_{J1} x_{J2}}{(2\pi)^2} \int \frac{d^2\vec{q}_1}{\vec{q}_1^2} V_i(\vec{q}_1, x_1, s_0, \vec{k}_1, x_{J1}, \mu_F, \mu_R) \\ &\times \int \frac{d^2\vec{q}_2}{\vec{q}_2^2} V_j(-\vec{q}_2, x_2, s_0, \vec{k}_2, x_{J2}, \mu_F, \mu_R) \int_C \frac{d\omega}{2\pi i} \left( \frac{x_1 x_2 s}{s_0} \right)^\omega G_\omega(\vec{q}_1, \vec{q}_2), \quad (2) \end{aligned}$$

where  $x_{J1(J2)}$  are the longitudinal momentum fractions carried by the jets  $J1$  and  $J2$  of the MN dijet,  $\vec{q}_{1(2)}$  are the transverse momenta of the Reggeized gluons, and  $s_0$  is an arbitrary energy scale introduced by the Mellin transform within the BFKL formalism. The vertex  $V(\vec{q}, x, \vec{k}, x_J)$  describes the transition of an incident parton with the longitudinal momentum fraction  $x$  to a jet with the longitudinal momentum fraction  $x_J$  and the transverse momentum  $\vec{k}$  by scattering off a Reggeized gluon with the transverse momentum  $\vec{q}$ . The integration contour  $C$  is a vertical line in the  $\omega$  complex plane such that all the poles of the Green's function  $G_\omega$  are to the left of the contour. The Green's function  $G_\omega$  obeys the BFKL equation

$$\omega G_\omega(\vec{q}_1, \vec{q}_2) = \delta^2(\vec{q}_1 - \vec{q}_2) \int d^2\vec{q} K(\vec{q}_1, \vec{q}) G_\omega(\vec{q}, \vec{q}_2), \quad (3)$$

where  $K(\vec{q}_1, \vec{q})$  is the BFKL kernel.

The vertices  $V$  are calculated at the NLL accuracy in the small-cone approximation in Ref. [42]. They are often combined with PDFs within the impact factors

$$\Phi(\vec{q}, \vec{k}, x_J, \omega, s_0, \mu_F, \mu_R) \equiv \sum_i \int_0^1 dx f_i(x, \mu_F) \left(\frac{x}{x_J}\right)^\omega V_i(\vec{q}, x, s_0, \vec{k}, x_J, \mu_F, \mu_R), \quad (4)$$

Using the impact factors  $\Phi$ , the differential cross section for dijet production can be rewritten as

$$\begin{aligned} \frac{d\sigma}{dy_1 dy_2 d^2\vec{k}_1 d^2\vec{k}_2} &= \frac{x_{J1} x_{J2}}{(2\pi)^2} \int_C \frac{d\omega}{2\pi i} e^{\omega(Y-Y_0)} G_\omega(\vec{q}_1, \vec{q}_2) \\ &\times \int \frac{d^2\vec{q}_1}{\vec{q}_1^2} \Phi_1(\vec{q}_1, \vec{k}_1, x_{J1}, \omega, s_0, \mu_F, \mu_R) \int \frac{d^2\vec{q}_2}{\vec{q}_2^2} \Phi_2(-\vec{q}_2, \vec{k}_2, x_{J2}, \omega, s_0, \mu_F, \mu_R), \end{aligned} \quad (5)$$

where  $Y = y_1 - y_2 = \ln \frac{x_{J1} x_{J2} s}{|\vec{k}_1| |\vec{k}_2|}$  and  $Y_0 = \ln \frac{s_0}{|\vec{k}_1| |\vec{k}_2|}$

To calculate the cross section at NLL accuracy, it is convenient to consider the impact factors and the Green's function in the basis of the LL BFKL kernel eigenfunctions, which are labeled with the conformal spin  $n$  and the conformal weights  $\nu$ . The projections of the impact factors are given by

$$\begin{aligned} \Phi_1(n, \nu, \vec{k}_1, x_{J1}, \omega, s_0, \mu_F, \mu_R) &= \int \frac{d^2\vec{q}_1}{\vec{q}_1^2} \Phi_1(\vec{q}_1, \vec{k}_1, x_{J1}, \omega, s_0, \mu_F, \mu_R) \frac{1}{\pi\sqrt{2}} (\vec{q}_1^2)^{i\nu-1/2} e^{in\phi_1}, \\ \Phi_2(n, \nu, \vec{k}_2, x_{J2}, \omega, s_0, \mu_F, \mu_R) &= \int \frac{d^2\vec{q}_2}{\vec{q}_2^2} \Phi_2(-\vec{q}_2, \vec{k}_2, x_{J2}, \omega, s_0, \mu_F, \mu_R) \frac{1}{\pi\sqrt{2}} (\vec{q}_2^2)^{-i\nu-1/2} e^{-in\phi_2}, \end{aligned} \quad (6)$$

where  $\phi_{1(2)}$  are the azimuthal angles of jets.

We employ the expansion of the impact factors in powers of strong coupling  $\alpha_s(\mu_R)$

$$\Phi_{1,2}(n, \nu, \vec{k}_{1,2}, x_{J1,2}, \omega, s_0, \mu_F, \mu_R) = \alpha_s(\mu_R) [c_{1,2}(n, \nu) + \bar{\alpha}_s(\mu_R) c_{1,2}^{(1)}(n, \nu)], \quad (7)$$

which can be found in Eqs. (34) and (36) of Ref. [43]. In this equations,  $\bar{\alpha}_s(\mu_R) = C_A \alpha_s(\mu_R) / \pi$  and  $C_A$  is the quadratic Casimir operator for the adjoint

representation of the SU(3) group. The variables  $\vec{k}_{1,2}$ ,  $x_{J1,2}$ ,  $\omega$ ,  $s_0$ ,  $\mu_F$ ,  $\mu_R$  are suppressed in Eq. (7) for  $c_{1,2}(n, \nu)$  and  $c_{1,2}^{(1)}(n, \nu)$  for shortness sake. The calculation of jet vertices at the NLL BFKL accuracy relies on the jet definition. In Ref. [43], the small cone approximation and end cone algorithm were used as jet reconstruction algorithms. The dependence on the jet algorithms was studied in Ref. [44]. In this work we present results for the  $k_t$  algorithm as described in Ref. [44].

The matrix elements of the NLL BFKL Green's function between the eigenfunctions of the LL BFKL kernel can be found in Eq. (24) of Ref. [36].

Making decomposition of the cross section Eq. (5) in cosines of the azimuthal angle  $\phi = \pi - (\phi_1 - \phi_2)$

$$\frac{d\sigma}{dy_1 dy_2 d|\vec{k}_1| d|\vec{k}_2| d\phi_1 d\phi_2} = \frac{1}{(2\pi)^2} \left[ \mathcal{C}_0 + \sum_{n=1}^{\infty} 2 \cos(n\phi) \mathcal{C}_n \right], \quad (8)$$

, transforming to the  $|n, \nu\rangle$  basis, and separating out the terms proportional  $\beta_0 = 11N_c/3 - 2n_f/3$  explicitly (as needed within the BFKLP approach [35]), one can get the expression for the  $\mathcal{C}_n$  coefficients of the expansion (8).

$$\begin{aligned} \mathcal{C}_n = & \frac{x_{J1} x_{J2}}{|\vec{k}_1| |\vec{k}_2|} \int_{-\infty}^{+\infty} d\nu e^{(Y-Y_0)\bar{\alpha}_s(\mu_R)\chi(n,\nu)} \alpha_s^2(\mu_R) c_1(n, \nu) c_2(n, \nu) \\ & \times \left[ 1 + \bar{\alpha}_s(\mu_R) \left( \frac{\bar{c}_1^{(1)}(n, \nu)}{c_1(n, \nu)} + \frac{\bar{c}_2^{(1)}(n, \nu)}{c_2(n, \nu)} + \frac{\beta_0}{2N_c} \left( \frac{5}{3} + \ln \frac{\mu_R^2}{|\vec{k}_1| |\vec{k}_2|} \right) \right) \right. \\ & \left. + \bar{\alpha}_s^2(\mu_R) \ln \frac{x_{J1} x_{J2} s}{s_0} \left\{ \bar{\chi}(n, \nu) + \frac{\beta_0}{4N_c} \chi(n, \nu) \left( -\frac{\chi(n, \nu)}{2} + \frac{5}{3} + \ln \frac{\mu_R^2}{|\vec{k}_1| |\vec{k}_2|} \right) \right\} \right], \quad (9) \end{aligned}$$

where  $\bar{c}_{1,2}^{(1)} \equiv c_{1,2}^{(1)} - \bar{c}_{1,2}^{(1)}$  and  $\bar{c}_{1,2}^{(1)}$  defined in Eq. (30) of Ref. [36].  $\bar{\alpha}_s \chi(n, \nu)$  is the eigenvalue of the LL BFKL kernel.  $\bar{\chi}(n, \nu)$  describes the diagonal part of the NLL BFKL kernel in the  $|n, \nu\rangle$  basis not proportional to  $\beta_0$ . It is defined by Eq. (19) of Ref. [36]. Within the BFKLP approach [35] one needs to change renormalization scheme from  $\overline{\text{MS}}$  to the physical momentum subtraction MOM

scheme. The  $\overline{\text{MS}}$  and MOM schemes are related by

$$\begin{aligned}\alpha_s^{\overline{\text{MS}}} &= \alpha_s^{\text{MOM}} \left( 1 + \frac{\alpha_s^{\text{MOM}}}{\pi} (T^\beta + T^{\text{conf}}) \right), \\ T^\beta &= -\frac{\beta_0}{2} \left( 1 + \frac{2}{3} I \right), \\ T^{\text{conf}} &= \frac{C_A}{8} \left[ \frac{17}{2} I + \frac{3}{2} (I-1) \xi + \left( 1 - \frac{1}{3} I \right) \xi^2 - \frac{1}{6} \xi^3 \right],\end{aligned}\quad (10)$$

where  $I \simeq 2.3439$  and  $\xi$  is a gauge parameter, which we fix to zero (that corresponds to the Landau gauge).

Then the optimal  $\mu_R^{\text{BFKLP}}$  scale is the value of  $\mu_R$  that makes the part of the integral in Eq. (9), proportional to  $\beta_0$ , vanish. This leads to the necessity to solve the integral equation, which can be done numerically. This can be impractical as far as the scale setting needs to be done under the integration. In Ref. [36] two approximate methods were suggested, which are referred to as the case (a) and the case (b).

In the case (a), the expression for the optimal scale

$$(\mu_{R,a}^{\text{BFKLP}})^2 = |\vec{k}_1| |\vec{k}_2| \exp \left[ 2 \left( 1 + \frac{2}{3} I \right) - \frac{5}{3} \right], \quad (11)$$

and in the case (b) it is

$$(\mu_{R,b}^{\text{BFKLP}})^2 = |\vec{k}_1| |\vec{k}_2| \exp \left[ 2 \left( 1 + \frac{2}{3} I \right) - \frac{5}{3} + \frac{1}{2} \chi(n, \nu) \right], \quad (12)$$

Only the  $\mathcal{C}_0$  term survive after the integration of Eq. (8) over the azimuthal angles.

$$\frac{d\sigma}{dy_1 dy_2 d|\vec{k}_1| d|\vec{k}_2|} = \mathcal{C}_0, \quad (13)$$

It is worth noting, that the results obtained in Ref. [45] show that the case (a) better reproduces the exact calculation for the optimal scale  $\mu_R^{\text{BFKLP}}$  for  $\mathcal{C}_0$ . Therefore we use the case (a), as an estimate of the MN cross section and the difference between the case (a) and the case (b) as an estimate of the theoretical uncertainty related to the choice of the renormalization and factorization scales.

In Sec. 5 we shall compare the results of the NLL BFKL calculations just described, the LL BFKL calculations performed according Eq. (12) from Ref. [46], as well as the leading order (LO)+LL DGLAP-based calculation provided by MC generator PYTHIA8. We confront the results to the recent CMS measurement at  $\sqrt{s} = 2.76$  TeV [29]. We will provide our predictions for the  $pp$  collisions at  $\sqrt{s} = 13$  TeV, which can be tested at the LHC.

### 3 The BMS equation for inter-jet veto

In the BMS approach the QCD cascade evolves due to soft gluon emission (ordered in  $p_{\perp}$ ) by color dipoles. Therefore, it accounts for the color coherence, which can partially reproduce the BFKL evolution. The BMS equation sums up the large logarithms of the transverse momenta of two types, namely the Sudakov one and the non-global one. The Sudakov logarithms come from the primarily emitted gluons, whereas the non-global ones are from the secondary gluons in the multiple gluon emission. It worth noting that, even though the BMS and BFKL equations have some similarity, the dominant contribution in both cases comes from different kinematic configurations. In the BMS case all angles are of the same order and the emission is  $p_{\perp}$ -ordered, whereas in the BFKL case all transverse momenta are of the same order and the emission is  $y$ -ordered.

The application of the BMS approach to the veto constraint imposed to the inclusive cross section calculated as the convolution of the PDFs with the Born level subprocess is described in Ref. [40]. As we shall show in the Sec. 5, the cross section calculations based on the Born level subprocess have poor agreement to the measurements. Therefore, we employ the NLL BFKL approach improved by the BFKLP prescription [35] for the MN cross section calculation. As far as the MN dijet is formed of the two jets maximally separated in rapidity (maximal  $\Delta y$ ), the main contribution to the veto comes from the inter-jet veto (a veto imposed on jets in the rapidity interval between the MN jets). In this section, we describe how to apply the procedure described in Ref. [40] to the cross section calculated by Eq. (13). Moreover, we discuss some modification which is needed to avoid the double counting of the emission from color octets.

First, let us recollect that the BMS approach allows the calculation of the probability,  $P$ , of not breaking the veto on emission above  $p_{\perp\text{veto}}$  from a color dipole. Consider a color dipole at the transverse momentum scale  $p_{\perp}$ , with the dipole ends moving in the directions  $\Omega_{\alpha}$  and  $\Omega_{\beta}$ . If the emission is vetoed in the  $\mathcal{C}_{\text{out}}$  direction region away from  $\Omega_{\alpha}$ ,  $\Omega_{\beta}$ , the probability  $P$  is obtained by

solving the equation:

$$\begin{aligned} \partial_\tau P_\tau(\Omega_\alpha, \Omega_\beta) &= - \int_{\mathcal{C}_{\text{out}}} \frac{d^2\Omega_\gamma}{4\pi} \frac{1 - \cos\theta_{\alpha\beta}}{(1 - \cos\theta_{\alpha\gamma})(1 - \cos\theta_{\gamma\beta})} \times P_\tau(\Omega_\alpha, \Omega_\beta) \\ &+ \int_{\mathcal{C}_{\text{in}}} \frac{d^2\Omega_\gamma}{4\pi} \frac{1 - \cos\theta_{\alpha\beta}}{(1 - \cos\theta_{\alpha\gamma})(1 - \cos\theta_{\gamma\beta})} (P_\tau(\Omega_\alpha, \Omega_\gamma)P_\tau(\Omega_\gamma, \Omega_\beta) - P_\tau(\Omega_\alpha, \Omega_\beta)), \end{aligned} \quad (14)$$

where  $\mathcal{C}_{\text{in}}$  is the region complementary to  $\mathcal{C}_{\text{out}}$ ,  $\theta_{ij}$  is the angle between the directions of  $\Omega_i$  and  $\Omega_j$ . The directions  $\Omega$  are defined by the polar and azimuthal angles. The evolution variable  $\tau$  is calculated by

$$\tau = \int_{p_{\perp\text{veto}}}^{p_{\perp}} \frac{dk_{\perp}}{k_{\perp}} \frac{\alpha_s(k_{\perp})C_A}{\pi}, \quad (15)$$

The initial and boundary conditions for the BMS equation Eq. (14) are set by the probability at  $\tau = 0$  equals 1, and  $P_\tau(\Omega_\alpha, \Omega_\alpha) = 1$  at all  $\tau$ .

Having the solutions of Eq. (14), one applies them as additional factors in Eq. (1) as described in Appendix A.3 of Ref. [39] to get the veto cross section  $\sigma^{\text{veto}}$ . Thus, one can calculate the ratios with veto as ratios of the cross sections calculated with and without the BMS factors. As mentioned in the introduction, this procedure described in Ref. [40] provides a decent agreement to the measured ratios. However, the agreement to the absolute values of the cross sections is expected to be worse, because the Born-level subprocess does not account for all the relevant QCD contributions.

The BFKL calculations employ the large  $\Delta y$  approximation for which  $|\hat{t}| \ll \hat{s}(|\hat{u}|)$ , where  $\hat{s}, \hat{t}, \hat{u}$  are the Mandelstam variables for the  $2 \rightarrow 2$  parton subprocess. In this approximation,  $\hat{\sigma}_{ij}$ , taken for all the combinations of flavors  $i$  and  $j$ , become proportional to each other, with the proportionality factors depending on the color summation. This allows us to restrict consideration to the gluon-gluon subprocess and the effective PDFs:

$$f^{\text{eff}}(x, \mu_F) = \frac{C_A}{C_F} f_g(x, \mu_F) + \sum_{i=q,\bar{q}} f_i(x, \mu_F), \quad (16)$$

Therefore it becomes possible to decouple the BMS probabilities from  $\hat{\sigma}_{ij}$  and to average them over the effective PDFs to get the effective BMS

probability:

$$\begin{aligned}
P^{\text{eff}} = & \frac{1}{f^{\text{eff}}(x_1)f^{\text{eff}}(x_2)} \times \left[ \left( \frac{C_A}{C_F} \right)^2 f_g(x_1)f_g(x_2)P_{gg} \right. \\
& + \frac{C_A}{C_F} \left( f_g(x_1) \sum_{i=q,\bar{q}} f_i(x_2) + f_g(x_2) \sum_{i=q,\bar{q}} f_i(x_1) \right) P_{gq} \\
& + \left( \sum_{\substack{i=q \\ j=q}} f_i(x_1)f_j(x_2) + \sum_{\substack{i=\bar{q} \\ j=\bar{q}}} f_i(x_1)f_j(x_2) \right) P_{qq} \\
& \left. + \left( \sum_{\substack{i=q \\ j=\bar{q}}} f_i(x_1)f_j(x_2) + \sum_{\substack{i=\bar{q} \\ j=q}} f_i(x_1)f_j(x_2) \right) P_{q\bar{q}} \right], \tag{17}
\end{aligned}$$

where the probabilities  $P_{gg}$ ,  $P_{gq}$ ,  $P_{qq}$  and  $P_{q\bar{q}}$  are calculated by:

$$\begin{aligned}
P_{gg} &= \frac{1}{2} (P_{12}P_{13}P_{24}P_{34} + P_{14}P_{24}P_{13}P_{23}), \\
P_{gq} &= \frac{1}{2} (P_{24}P_{12}P_{34} + P_{24}P_{14}P_{23}), \\
P_{qq} &= P_{14}P_{23}, \\
P_{q\bar{q}} &= P_{12}P_{34}, \tag{18}
\end{aligned}$$

where  $P_{ij}$ , the BMS probability for the color dipoles connecting partons  $i$  and  $j$ , is calculated as described in Ref. [40]. The ends of the dipole labeled by 1 and 2 are the remnants of the colliding protons 1 and 2 propagating to the pseudorapidities  $+\infty$  and  $-\infty$ , respectively. The ends 3 and 4 are the partons scattered from the protons 1 and 2, respectively. They propagate to the rapidities  $y_1$  and  $y_2$ , respectively.

The effective probability Eq. (17) can be used as an additional factor in the integrand for  $\mathcal{C}_0$  to get the veto cross section.

It should be noted that the color octet is exchanged in the  $t$ -channel in the large  $\Delta y$  approximation regardless of whether we use the Born level or the NLL BFKL  $\hat{\sigma}$  for the parton scattering. The emission rate of a gluon by the color octet is proportional to  $\alpha_s C_A$  as accounted originally in the BMS equation. However, in the approach described in Ref. [40] and adopted in the present paper, the exchanged color octet is represented by two dipoles. These two dipoles are stretched over the  $\Delta y$  interval. The ends of each dipole are in the color triplet-antitriplet state. Therefore each dipole should emit gluons proportionally  $\alpha_s C_F$ . Then, the gluon emission rate from the two

dipoles together is equivalent to the rate from a one color octet in the large  $N_c$  approximation, i.e.,  $2\alpha_s C_F = \alpha_s (C_A - 1/N_c)$ . As a result, the gluon emission leads to a splitting of a dipole to the two daughter dipoles. Each two daughter dipole has ends in the color triplet-antitriplet state again. Afterwards, they emit proportionally to  $\alpha_s C_F$ . Therefore, each successive emission is proportional to  $\alpha_s C_F$  during the whole BMS evolution. If, instead, we let each dipole to emit proportionally to  $\alpha_s C_A$ , the emission will be double counted. As we shall see in the Sec. 5, this is crucial for cases where  $p_{\perp\text{veto}}$  is much lower than  $p_{\perp\text{min}}$ . This is probably the reason why in Ref. [40] the calculations overshoot the veto impact in the “two leading” selection of the ATLAS measurements [24].

The replacement of  $C_A$  to  $C_F$  within the BMS approach can be easily done by replacing them in the  $\tau$  definition Eq. (15). We denote  $\tau$  calculated with  $C_F$  instead of  $C_A$  in Eq. (15) as  $\tau_F$  and  $\tau$  calculated by Eq. (15) as  $\tau_A$ . In the Sec. 5 we confront both variants of the calculation with  $\tau_A$  and  $\tau_F$  to the CMS measurements [25, 29].

## 4 Numerical calculation and theoretical uncertainty

The differential MN cross section  $d\sigma^{\text{MN}}/d\Delta y$  is calculated numerically with the NLL BFKL accuracy improved by the BFKLP approach [35] to the optimal scale setting for  $\sqrt{s} = 2.76$ , and 13 TeV, for jets with  $p_{\perp} > p_{\perp\text{min}} = 35$  GeV and  $y < 4.7$ . The ratios with veto  $R^{\text{MN}}$  and  $R_{\text{veto}}^{\text{MN}}$  are calculated as a ratio of  $d\sigma^{\text{MN}}/d\Delta y$  to the cross section calculated by the same expression, but with the multiplier  $P^{\text{eff}}$  provided with the numerical solution of the BMS equation Eq (14). The veto  $p_{\perp\text{veto}}$  is set at 35 and 20 GeV for  $R^{\text{MN}}$  and  $R_{\text{veto}}^{\text{MN}}$ , respectively. The ratio  $R^{\text{MN}}$  is calculated for  $\sqrt{s} = 2.76$ , 7 and 13 TeV, whereas  $R_{\text{veto}}^{\text{MN}}$  is calculated for 2.76 and 13 TeV. The jets in the calculations are defined with the  $k_t$  algorithm with the jet size parameter 0.5 for  $\sqrt{s} = 2.76$  and 7 TeV and 0.4 for 13 TeV. The calculations of  $R^{\text{MN}}$  and  $R_{\text{veto}}^{\text{MN}}$  are made for  $\tau_A$  and  $\tau_F$  in the BMS equation. The number of flavors  $n_f$  is kept 5. The strong coupling constant,  $\alpha_s$ , and PDFs are provided at the next-to-leading order (NLO) by the LHAPDF library [47] and MSTW2008nlo68cl [48] set.

The estimated theoretical uncertainty of the  $\sigma^{\text{MN}}$  calculation comes from three different sources. The first one is the renormalization and factorization scale uncertainty. It is estimated by the difference between case (a) Eq. (11) and case (b) Eq. (12). The second one is the uncertainty of  $s_0$ . The central value of  $s_0$  is chosen to be the  $|\vec{k}_1| \times |\vec{k}_2|$ . It is varied by factors 2 and 0.5 to

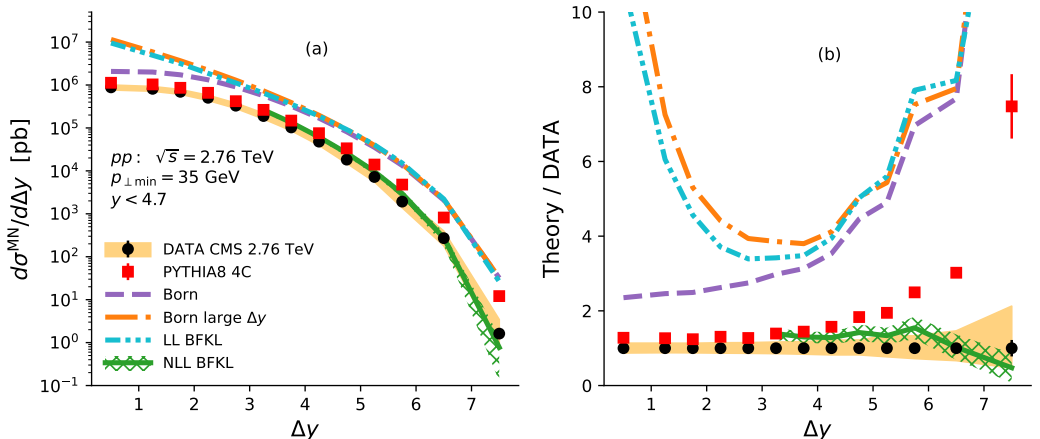


Figure 1: The MN  $\Delta y$ -differential cross section for  $pp$  collisions at  $\sqrt{s} = 2.76$  TeV. The cross section  $d\sigma^{\text{MN}}/d\Delta y$  (a) and the theory to data ratio (b). The CMS measurement [29] is represented by dots. Statistical uncertainty of the measurement and MC calculation by PYTHIA8 4C is represented by bars. Systematic uncertainty of the data is the shaded band and systematic uncertainty of the NLL BFKL calculation is the hatched band.

obtain the uncertainty. The third one is the uncertainty of the PDFs. This is estimated with MC replicas of PDF4LHC15\_NLO\_MC set [49]. These three sources provide a set of uncertainties which are approximately equal to each other in magnitude.

The cross sections with veto has one more sources of uncertainty, namely the BMS scale uncertainty. It is estimated by setting the upper limit  $p_{\perp}$  of the integral in Eq. (15) equal to  $\sqrt{|\vec{k}_1||\vec{k}_2|}$  for the central value, whereas it is set to  $\max(|\vec{k}_1|, |\vec{k}_2|)$  and  $\min(|\vec{k}_1|, |\vec{k}_2|)$  for the up and down variations. This is the largest uncertainty in the ratios with veto, because the deviations does not fully cancel out in the ratio.

The resulting uncertainty is the square root of the quadratic sum of uncertainty from different sources.

## 5 Results and discussion

The MN cross section calculated with the NLL BFKL approach improved by BFKLP scale setting [35] for  $pp$  collisions at  $\sqrt{s} = 2.76$  TeV is compared with

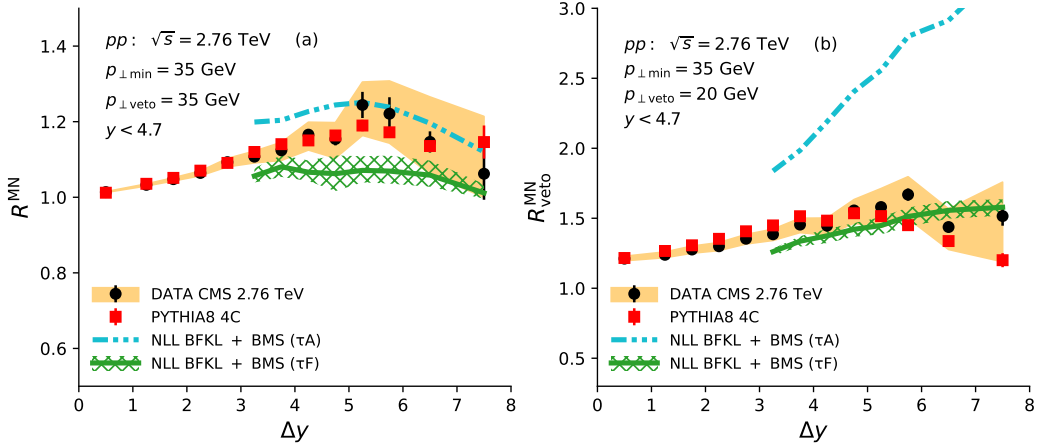


Figure 2: Ratios of cross sections with veto  $R^{\text{MN}}$  (a) and  $R_{\text{veto}}^{\text{MN}}$  (b) for  $pp$  collisions at  $\sqrt{s} = 2.76$  TeV. The CMS measurement [29] is represented by dots. Statistical uncertainty of the measurement and MC calculation by PYTHIA8 4C is represented by bars. Systematic uncertainty of the data is the shaded band and systematic uncertainty of the NLL BFKL+BMS ( $\tau_F$ ) calculation is the hatched band.

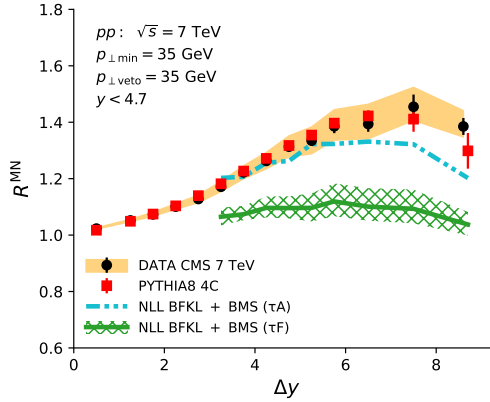


Figure 3: Ratio of cross sections  $R^{\text{MN}}$  for  $pp$  collisions at  $\sqrt{s} = 7$  TeV. The CMS measurement [25] is represented by dots. Statistical uncertainty of the measurement and MC calculation by PYTHIA8 4C is represented by bars. Systematic uncertainty of the data is the shaded band and systematic uncertainty of the NLL BFKL+BMS ( $\tau_F$ ) calculation is the hatched band.

the CMS measurements [29] in Fig. 1. The calculations with PYTHIA8 tune

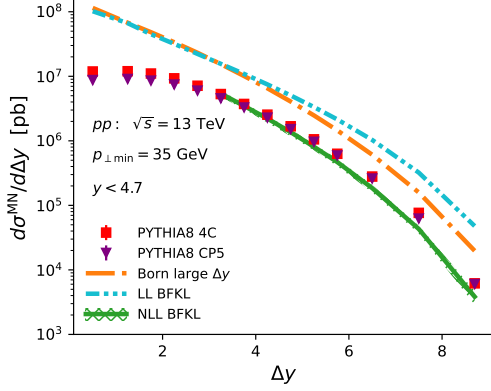


Figure 4: The MN  $\Delta y$ -differential cross section  $d\sigma^{\text{MN}}/d\Delta y$  for  $pp$  collisions at  $\sqrt{s} = 13$  TeV. Statistical uncertainty of the MC calculations by PYTHIA8 4C and CP5 is represented by bars. Systematic uncertainty of NLL BFKL calculation is represented by the hatched band.

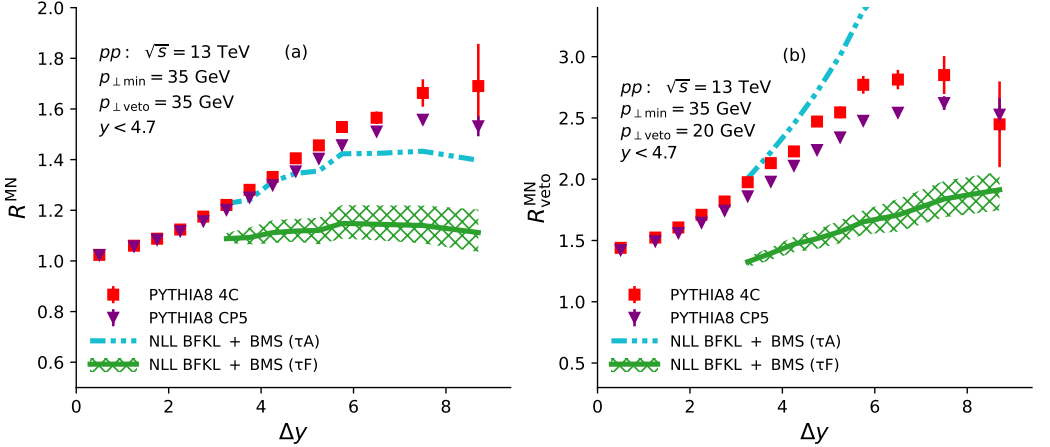


Figure 5: Ratios of cross sections with veto  $R^{\text{MN}}$  (a) and  $R^{\text{MN}}_{\text{veto}}$  (b) for  $pp$  collisions at  $\sqrt{s} = 13$  TeV. Statistical uncertainty of the MC calculations by PYTHIA8 4C and CP5 is represented by bars. Systematic uncertainty of NLL BFKL+BMS ( $\tau_F$ ) calculation is represented by the hatched band.

4C [50], as well as the Born level subprocess calculation with and without the large  $\Delta y$  approximation, and the LL BFKL calculation as described in [46] are also shown in Fig. 1 for the sake of comparison. As one can see from Fig. 1 the calculation with the NLL BFKL approach improved by BFKLP

prescription [35] agrees to data within the systematic uncertainty, whereas all other calculations significantly overestimate the measurements. Moreover, it is noticeable that the NLL corrections are of the major importance for the BFKL calculations. As can be seen by comparing the Born-subprocess calculations performed with and without (the use of) the large  $\Delta y$  approximation, the large  $\Delta y$  approximation becomes reliable for  $\Delta y > 4$ .

The comparison of calculations of cross section ratios  $R^{\text{MN}}$  and  $R_{\text{veto}}^{\text{MN}}$  in  $pp$  collisions at  $\sqrt{s} = 2.76$  TeV with the CMS measurements [29] is presented in Fig. 2. The calculations of the ratios are presented for  $\tau_A$  and  $\tau_F$ . As it can be seen from the panel (b) of Fig. 2 the  $\tau_A$  variant of calculation significantly overestimates the data, confirming the necessity of  $C_A$  to  $C_F$  replacement in the BMS equation. On the other hand the panel (a) of Fig. 2 shows that the BMS evolution does not provide with enough emission when  $p_{\perp\text{min}} = p_{\perp\text{veto}}$ , because of lack of the phase space for  $p_{\perp}$ -ordered emission cascade. This argues in favor of the necessity of the BFKL evolution, because of its  $p_{\perp}$  diffusion. The MC calculation by PYTHIA8 performed with the LO matrix element and the LL DGLAP-based shower is in agreement to data for  $R^{\text{MN}}$ , despite the fact that the DGLAP-based shower is also  $p_{\perp}$ -ordered. This is probably because of the color coherence which is implemented in PYTHIA8 differently than in the BMS equation. Slight difference in shape is observed between PYTHIA8 and the measurement for  $R_{\text{veto}}^{\text{MN}}$ . The calculation with the NLL BFKL+BMS ( $\tau_F$ ) approach is in good agreement to the measurement of  $R_{\text{veto}}^{\text{MN}}$ .

The comparison of calculation of the cross section ratio  $R^{\text{MN}}$  in  $pp$  collisions at  $\sqrt{s} = 7$  TeV with the CMS measurement [25] is presented in Fig. 3. The NLL BFKL+BMS calculations underestimates the ratio at large  $\Delta y$ , for both  $\tau_A$  and  $\tau_B$  variants of calculations. The comparison of the left plot in Fig. 2 and Fig. 3 shows that the BMS evolution has weaker  $\sqrt{s}$  dependence than observed in the data. This is not surprising because the BMS equation Eq. (14) has no explicit dependence on  $\sqrt{s}$ . The implicit  $\sqrt{s}$  dependence of the BMS approach comes from  $\sqrt{s}$  dependence of the shape of the jet  $p_{\perp}$ -spectrum. The BFKL-based methods for the veto calculation (if developed) will intrinsically include the  $\sqrt{s}$  dependence. The LO+LL DGLAP-based MC calculation by PYTHIA8 better reproduces the  $\sqrt{s}$  and  $\Delta y$  behavior of  $R^{\text{MN}}$ . So PYTHIA8 can serve as a reference point for  $R^{\text{MN}}$  and  $R_{\text{veto}}^{\text{MN}}$  predictions for  $\sqrt{s} = 13$  TeV.

The prediction for the MN cross section in  $pp$  collisions at  $\sqrt{s} = 13$  TeV is presented in Fig. 4. The NLL BFKL-based calculation (with BFKLP scale setting [35]) lies below all other predictions, as it is for  $\sqrt{s} = 2.76$  TeV. The predictions for the MC generator PYTHIA8 is given for two tunes, namely 4C, which is used for lower energies, and CP5 [51], which includes fit of the 13 TeV

measurements. Moreover the CP5 tune employs the next-to-next-to-leading order PDFs and  $\alpha_s$ , which effectively lowers the cross section. In addition this tune uses the rapidity ordering in the initial state radiation, which makes it even closer to the BFKL evolution as confirmed by Fig. 4. Therefore PYTHIA8 CP5 produces result far from pure DGLAP-based prediction.

The predictions for  $R^{\text{MN}}$  and  $R_{\text{veto}}^{\text{MN}}$  in  $pp$  collisions at  $\sqrt{s} = 13$  TeV are presented in Fig. 5. The prediction by PYTHIA8 is given for the 4C and CP5 tunes. As it can be seen, from the panel (b) of Fig. 5 the  $\tau_A$  variant of the NLL BFKL+BMS calculation predicts strongest emission, which is probably overestimation. On the other hand the  $\tau_F$  variant of the NLL BFKL+BMS calculation has weakest  $\sqrt{s}$  dependence. The measurements at 13 TeV can help to test for the correct  $\sqrt{s}$  and  $\Delta y$  behavior. Figure 5 shows that  $\tau_F$  variant of NLL BFKL+BMS calculation predicts the weakest emission which is probably underestimation.

## 6 Summary

The calculation of the set of observables intended for the search of the Balitsky–Fadin–Kuraev–Lipatov (BFKL) evolution is performed. The Mueller–Navelet (MN)  $\Delta y$ -differential cross section  $d\sigma^{\text{MN}}/d\Delta y$  is calculated in the next-to-leading logarithm (NLL) BFKL accuracy. The procedure of the optimal renormalization scale setting of Brodsky–Fadin–Kim–Lipatov–Pivovarov (BFKLP) [35] is applied to resum the large coupling constant effects. The ratios of the cross sections with a veto on additional jets between MN dijets  $R^{\text{MN}}$  and  $R_{\text{veto}}^{\text{MN}}$  are also calculated. The impact of the veto is calculated with the Banfi–Marchesini–Smye (BMS) approach [39], which resums the large-angle soft gluon emissions ordered in  $p_{\perp}$ .

The agreement of the NLL BFKL-based calculations of  $d\sigma^{\text{MN}}/d\Delta y$  to the CMS data at  $\sqrt{s} = 2.76$  (Ref. [29]) argues strongly in support of the BFKL evolution manifestation at LHC energies. The BMS evolution predicts weaker  $\sqrt{s}$  and  $\Delta y$  dependence of  $R^{\text{MN}}$  and  $R_{\text{veto}}^{\text{MN}}$  than observed in the CMS data at  $\sqrt{s} = 2.76$  and 7 TeV [25, 29], which also favors the BFKL evolution.

The predictions of  $d\sigma^{\text{MN}}/d\Delta y$ ,  $R^{\text{MN}}$  and  $R_{\text{veto}}^{\text{MN}}$  in the NLL BFKL approximation including the BFKLP optimal scale setting [35] and the BMS probabilities for inter-jet veto [39] are presented for  $\sqrt{s} = 13$  TeV. Therefore, our observations can be tested at a higher energy at the LHC.

# References

- [1] E. A. Kuraev, L. N. Lipatov, and V. S. Fadin, *Sov. Phys. JETP* **44**, 443 (1976).
- [2] E. A. Kuraev, L. N. Lipatov, and V. S. Fadin, *Sov. Phys. JETP* **45**, 199 (1977).
- [3] I. I. Balitsky and L. N. Lipatov, *Sov. J. Nucl. Phys.* **28**, 822 (1978).
- [4] V. N. Gribov and L. N. Lipatov, *Sov. J. Nucl. Phys.* **15**, 438 (1972).
- [5] V. N. Gribov and L. N. Lipatov, *Sov. J. Nucl. Phys.* **15**, 675 (1972).
- [6] L. N. Lipatov, *Sov. J. Nucl. Phys.* **20**, 94 (1975).
- [7] G. Altarelli and G. Parisi, *Nucl. Phys. B* **126**, 298 (1977).
- [8] Y. L. Dokshitzer, *Sov. Phys. JETP* **46**, 641 (1977).
- [9] A. H. Mueller and H. Navelet, *Nucl. Phys. B* **282**, 727 (1987).
- [10] V. T. Kim and G. B. Pivovarov, *Phys. Rev. D* **53**, 6 (1996), arXiv:hep-ph/9506381 [hep-ph].
- [11] V. B. Gavrilov *et al.*, *Nucl. Phys. B Proc. Suppl.* **245**, 153 (2013).
- [12] A. I. Egorov and Y. A. Berdnikov, *St. Petersburg Polytech. Univ. J. Phys. Math.* **12**, 118 (2019).
- [13] V. Del Duca and C. R. Schmidt, *Phys. Rev. D* **49**, 177 (1994), arXiv:hep-ph/9305346.
- [14] W. J. Stirling, *Nucl. Phys. B* **423**, 56 (1994), arXiv:hep-ph/9401266.
- [15] A. Sabio Vera and F. Schwennsen, *Nucl. Phys. B* **776**, 170 (2007), arXiv:hep-ph/0702158.
- [16] A. H. Mueller and W.-K. Tang, *Phys. Lett. B* **284**, 123 (1992).
- [17] R. Enberg, G. Ingelman, and L. Motyka, *Phys. Lett. B* **524**, 273 (2002), arXiv:hep-ph/0111090.
- [18] O. Kepka, C. Marquet, and C. Royon, *Phys. Rev. D* **83**, 034036 (2011), arXiv:1012.3849 [hep-ph].

- [19] S. Abachi *et al.*, (D0 Collaboration), Phys. Rev. Lett. **77**, 595 (1996), arXiv:hep-ex/9603010.
- [20] B. Abbott *et al.*, (D0 Collaboration), Phys. Lett. B **440**, 189 (1998), arXiv:hep-ex/9809016.
- [21] B. Abbott *et al.*, (D0 Collaboration), Phys. Rev. Lett. **84**, 5722 (2000), arXiv:hep-ex/9912032.
- [22] F. Abe *et al.*, (CDF Collaboration), Phys. Rev. Lett. **80**, 1156 (1998).
- [23] G. Aad *et al.*, (ATLAS Collaboration), JHEP **09**, 053 (2011), arXiv:1107.1641 [hep-ex].
- [24] G. Aad *et al.*, (ATLAS Collaboration), Eur. Phys. J. C **74**, 3117 (2014), arXiv:1407.5756 [hep-ex].
- [25] S. Chatrchyan *et al.*, (CMS Collaboration), Eur. Phys. J. C **72**, 2216 (2012), arXiv:1204.0696 [hep-ex].
- [26] V. Khachatryan *et al.*, (CMS Collaboration), JHEP **08**, 139 (2016), arXiv:1601.06713 [hep-ex].
- [27] A. M. Sirunyan *et al.*, (CMS Collaboration), Eur. Phys. J. C **78**, 242 (2018), arXiv:1710.02586 [hep-ex], [Erratum: Eur.Phys.J.C 80, 441 (2020)].
- [28] A. M. Sirunyan *et al.*, (TOTEM, CMS Collaboration), Phys. Rev. D **104**, 032009 (2021), arXiv:2102.06945 [hep-ex].
- [29] A. Tumasyan *et al.*, (CMS Collaboration), JHEP **03**, 189 (2022), arXiv:2111.04605 [hep-ex].
- [30] T. Sjostrand, S. Mrenna, and P. Z. Skands, Comput. Phys. Commun. **178**, 852 (2008), arXiv:0710.3820 [hep-ph].
- [31] J. Bellm *et al.*, Eur. Phys. J. C **76**, 196 (2016), arXiv:1512.01178 [hep-ph].
- [32] V. S. Fadin and L. N. Lipatov, Phys. Lett. B **429**, 127 (1998), arXiv:hep-ph/9802290.
- [33] M. Ciafaloni and G. Camici, Phys. Lett. B **430**, 349 (1998), arXiv:hep-ph/9803389.

- [34] S. J. Brodsky, G. P. Lepage, and P. B. Mackenzie, *Phys. Rev. D* **28**, 228 (1983).
- [35] S. J. Brodsky, V. S. Fadin, V. T. Kim, L. N. Lipatov, and G. B. Pivovarov, *JETP Lett.* **70**, 155 (1999), arXiv:hep-ph/9901229.
- [36] F. Caporale, D. Y. Ivanov, B. Murdaca, and A. Papa, *Phys. Rev. D* **91**, 114009 (2015), arXiv:1504.06471 [hep-ph].
- [37] B. Ducloue, L. Szymanowski, and S. Wallon, *JHEP* **05**, 096 (2013), arXiv:1302.7012 [hep-ph].
- [38] J. R. Andersen and J. M. Smillie, *JHEP* **06**, 010 (2011), arXiv:1101.5394 [hep-ph].
- [39] A. Banfi, G. Marchesini, and G. Smye, *JHEP* **08**, 006 (2002), arXiv:hep-ph/0206076.
- [40] Y. Hatta *et al.*, *Phys. Rev. D* **87**, 054016 (2013), arXiv:1301.1910 [hep-ph].
- [41] A. Y. Egorov and V. T. Kim, *J. Phys. Conf. Ser.* **1690**, 012158 (2020).
- [42] D. Y. Ivanov and A. Papa, *JHEP* **05**, 086 (2012), arXiv:1202.1082 [hep-ph].
- [43] F. Caporale, D. Y. Ivanov, B. Murdaca, and A. Papa, *Nucl. Phys. B* **877**, 73 (2013), arXiv:1211.7225 [hep-ph].
- [44] D. Colferai and A. Niccoli, *JHEP* **04**, 071 (2015), arXiv:1501.07442 [hep-ph].
- [45] F. G. Celiberto, D. Y. Ivanov, B. Murdaca, and A. Papa, *Eur. Phys. J. C* **76**, 224 (2016), arXiv:1601.07847 [hep-ph].
- [46] V. Del Duca and C. R. Schmidt, *Phys. Rev. D* **49**, 4510 (1994), arXiv:hep-ph/9311290.
- [47] A. Buckley *et al.*, *Eur. Phys. J. C* **75**, 132 (2015), arXiv:1412.7420 [hep-ph].
- [48] A. D. Martin, W. J. Stirling, R. S. Thorne, and G. Watt, *Eur. Phys. J. C* **63**, 189 (2009), arXiv:0901.0002 [hep-ph].
- [49] J. Butterworth *et al.*, *J. Phys. G* **43**, 023001 (2016), arXiv:1510.03865 [hep-ph].

- [50] R. Corke and T. Sjöstrand, JHEP **03**, 032 (2011), arXiv:1011.1759 [hep-ph].
- [51] A. M. Sirunyan *et al.*, (CMS Collaboration), Eur. Phys. J. C **80**, 4 (2020), arXiv:1903.12179 [hep-ex].

**FIRST MEASUREMENT OF THE CROSS SECTIONS OF THE  
LARGE RAPIDITY GAP PROCESSES IN pPb COLLISIONS AT  
 $\sqrt{s_{NN}} = 8.16$  TeV WITH THE CMS EXPERIMENT**

**Dmitry E. Sosnov**

**Petersburg Nuclear Physics Institute of NRC “KI”, Gatchina,  
on behalf of the CMS Collaboration**

Abstract

The forward rapidity gap spectra from proton-lead collisions for both pomeron-lead and pomeron-proton topologies are presented. The analysis was performed at a nucleon-nucleon center-of-mass energy of 8.16 TeV with the CMS detector at LHC. The previous measurements was done by HELIOS Collaboration at  $\sqrt{s_{NN}} = 29.1$  GeV i.e. almost 300 times lower. For the pomeron-lead topology the EPOS-LHC and QGSJET II generator predictions are a factor of two and four, respectively, below the CMS data, but the models give a reasonable description of the shape of the spectrum. For the pomeron-proton topology the EPOS-LHC, QGSJET II and HIJING generator predictions are all at least a factor of five below the data. This effect may be explained by a significant contribution of ultra-peripheral photoproduction events, not described by used generators. The obtained data may be of significant help in understanding the high energy limit of QCD and modeling cosmic ray air showers.

# ПЕРВОЕ ИЗМЕРЕНИЕ СОБЫТИЙ С БЫСТРОТНЫМИ ПРОВАЛАМИ ПРИ $\sqrt{s_{NN}} = 8.16$ ТэВ В СОУДАРЕНИЯХ ПРОТОНОВ С ЯДРАМИ СВИНЦА В ЭКСПЕРИМЕНТЕ CMS

Дмитрий Е. Соснов

Петербургский институт ядерной физики НИЦ «КИ», Гатчина,  
от коллаборации CMS

## Аннотация

Представлены распределения сечений по величине быстрого провала в столкновениях протонов с ионами свинца при энергии соударения  $\sqrt{s_{NN}} = 8.16$  ТэВ, измеренные детектором CMS БАК. Предыдущие измерения подобного рода были проведены коллаборацией HELIOS при энергии  $\sqrt{s_{NN}} = 29,1$  ГэВ, то есть при в 300 раз более низкой энергии в СЦМ. Для топологии соударения свинца с помероном, испущенным протоном, предсказания генераторов EPOS-LHC и QGSJET II в два и четыре раза, соответственно, ниже данных CMS, но при разумном описании формы спектра. Для топологии столкновения протонов с померонами или фотонами, испущенными ионом свинца предсказания всех трех использованных генераторов (EPOS-LHC, HIJING, QGSJET), в которых включены только обмены померонами, ниже как минимум в пять раз от данных, что может быть объяснено значительным вкладом фотон-протонных соударений, не описываемые использованными генераторами. Полученные данные могут оказать существенную помощь в понимании КХД и моделировании ливней от прохождения космических лучей через атмосферу.

# 1 Introduction

The large fraction of the collisions at the Large Hadron Collider are diffractive events [1–5], connected to the fundamental parts of QCD [6–11]. Such events are caused by pomeron ( $\mathbb{P}$ ) exchange. Pomeron exchange refers to  $t$ -channel exchanges of states that carry the quantum numbers of the vacuum [12, 13]. The diffractive one characterized by the large gaps in the pseudorapidity distribution of final-state particles, usually measured in the most forward region of detectors. For the hadron-nuclear diffraction processes the special Gribov inelastic screening contributions [14] can be involved. Also, diffraction is relevant for the modeling of cosmic ray showers [15].

The presented CMS analysis [16] was done with the forward rapidity gap studies at  $\sqrt{s_{NN}} = 8.16$  TeV with the CMS detector at the LHC at CERN. The previous forward rapidity gap cross section measurements at the LHC were performed in proton-proton collisions by the ATLAS [1] and CMS [2] Collaborations at a center-of-mass energy of 7 TeV, and the previous proton-nuclear diffraction studies was made at a center-of-mass energy of 29.1 GeV by HELIOS [17].

## 2 Data analysis

The cross section measurement of diffractive proton-lead collisions based on finding a rapidity gap forward detector region (FRG,  $\Delta\eta^F$ ) was done with  $6.4 \mu\text{b}^{-1}$  of data collected in 2016 [16] by the CMS detector [18]. Electromagnetic interactions in ultraperipheral collisions have a non-negligible contribution in events with forward rapidity gaps on the side of the outgoing nucleon [19–23] Figure 1 shows the Feynman diagrams and schematic topologies of single diffractive pomeron-lead ( $\mathbb{P}\text{Pb}$ ) and pomeron-proton ( $\mathbb{P}\text{p}$ ) processes.

In the analysis, the phase space within the pseudorapidity region  $|\eta| = 3.0$  is divided in 12 bins and the rapidity gap is calculated from  $|\eta| = 3.0$ . The obtained detector level forward rapidity gap cross section shown on Fig. 2. The CMS data are compared with EPOS-LHC [24] and HIJING v2.1 [25] predictions. All spectra fall at about 50 times at the first two FRG bins, due to high contribution of nondiffractive events, and becomes more flatten after  $\Delta\eta^F > 3$ . The discrepancy between Fig. 2 right panel and the left one suggests that the  $\mathbb{P}\text{p} + \gamma\text{p}$  CMS data contain large contribution of  $\gamma\text{p}$  events.

To increase sensitivity to the diffraction events the forward rapidity gap can be extended. For that, to select the events with the absence of signal in the region adjacent to the FRG region  $3.14 < |\eta| < 5.19$ , additional reweighting was

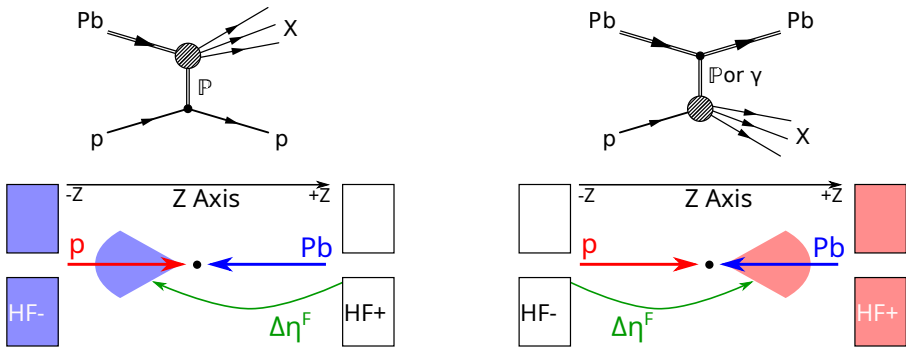


Figure 1: Top: schematic diagram of pPb events with large rapidity gaps for IPb (left) and IP or  $\gamma$ p (right). Bottom: topologies of the events. The blue and red cones indicate the products of diffractive dissociation for the lead ion and proton, respectively. The measured rapidity gaps are marked with green arrows. The figures taken from Ref. [16].

applied. Obtained distributions was unfolded to hadron level using EPOS-LHC Monte Carlo (MC) generator response matrices, are marked as “diffraction enhanced” distributions.

### 3 Results and conclusion

The resulting hadron level forward rapidity gap cross section shown in Fig. 3 is compared with EPOS-LHC [24], QGSJET II-04 [26] and HIJING v2.1 [25] predictions. The statistical and systematic uncertainties are added in quadrature. The full uncertainty is represented by the yellow band, and the uncertainty without the component associated to the correction for undetectable energy in the region  $3.14 < |\eta| < 5.19$  is represented by the grey band.

For both IPb and IP topologies the MC generator predictions of the FRG distribution differs from the CMS results. For the IPb case, the predictions by EPOS-LHC and QGSJET cross sections underestimate the data by factors ranging from two to four, respectively. The shapes are similar. The HIJING shape falls at large FRG sizes contrary to the trend in data. The large difference between the obtained data and the MC predictions for the IP case can be described by the  $\gamma$ p contribution, which is not present in the MC predictions, as shown in Refs. [27, 28].

In Fig. 4 the hadron level prediction from EPOS-LHC and QGSJET shown in Fig. 3 was splitted down to non-diffractive and single, central and double

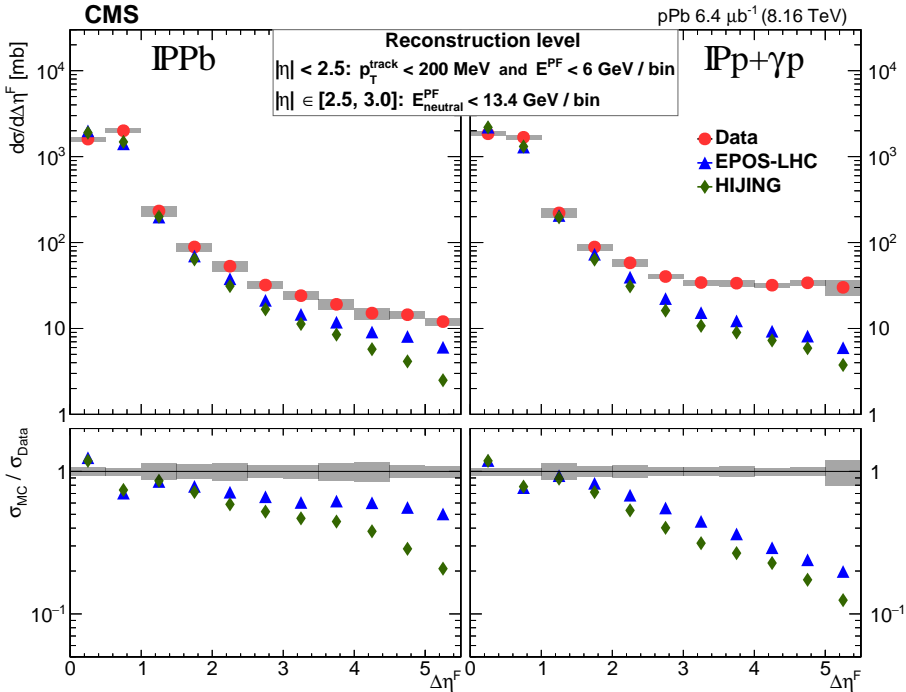


Figure 2: Top: the detector level cross section distribution for the CMS data [16] (red circles), and the predictions of the EPOS-LHC [24] (blue triangles), and HIJING [25] (green diamonds) MC generators. The distributions are shown for the IPPb (left) and IPp topologies. Bottom: the ratios between generator predictions and CMS data.

diffractive events. The prediction shows that the  $\frac{d\sigma}{d\Delta\eta^F}$  for the events with no energy deposition in the  $3.14 < |\eta| < 5.19$  region adjacent to FRG the contribution of the diffractive events become dominant after  $\Delta\eta^F = 1.0$ .

For the first time at the LHC, the forward rapidity gap cross section distribution for the proton-lead collisions were measured at the energy  $\sqrt{s_{NN}} = 8.16$  TeV with the CMS detector for IPPb and IPp+ $\gamma$ p topologies. Surprisingly, the dominant photon exchange processes contribution in IPp+ $\gamma$ p topology is found. This type of processes should be implemented into modern MC event generators to describe high energy proton-nuclear collisions with large rapidity gaps. The obtained distributions can provide significant information for diffractive processes on nuclei and for the cosmic ray showers modelling.

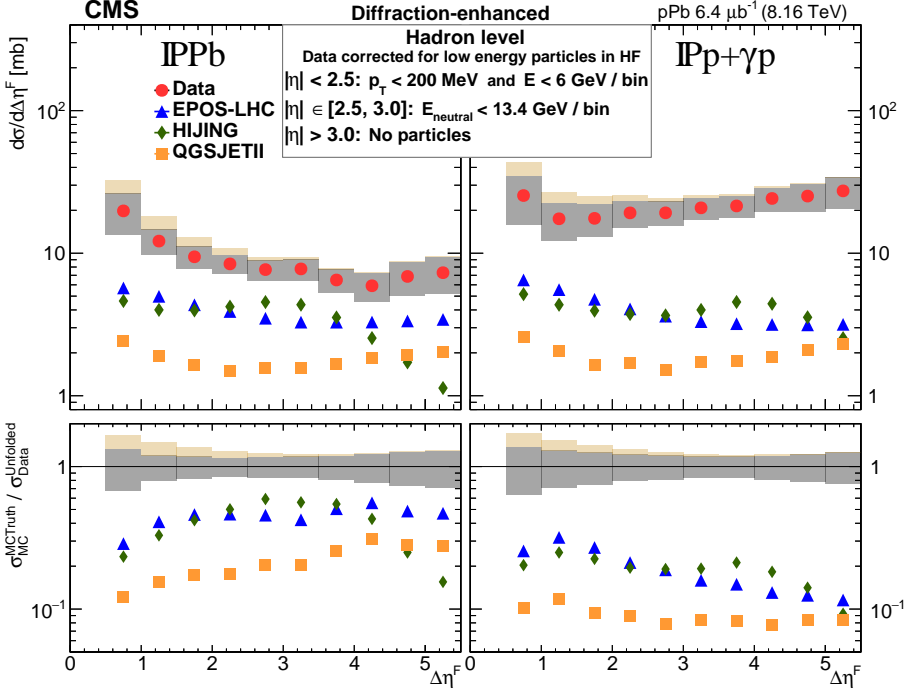


Figure 3: Top: the hadron level cross section distribution with no energy deposition in the  $3.14 < |\eta| < 5.19$  region adjacent to FRG for the CMS data [16] (red circles), and the predictions of the EPOS-LHC [24] (blue triangles), QGSJET II [26] (orange squares) and HIJING [25] (green diamonds) MC generators. The distributions are shown for the IPPb (left) and IPp topologies. Bottom: the ratios between generator predictions and CMS data.

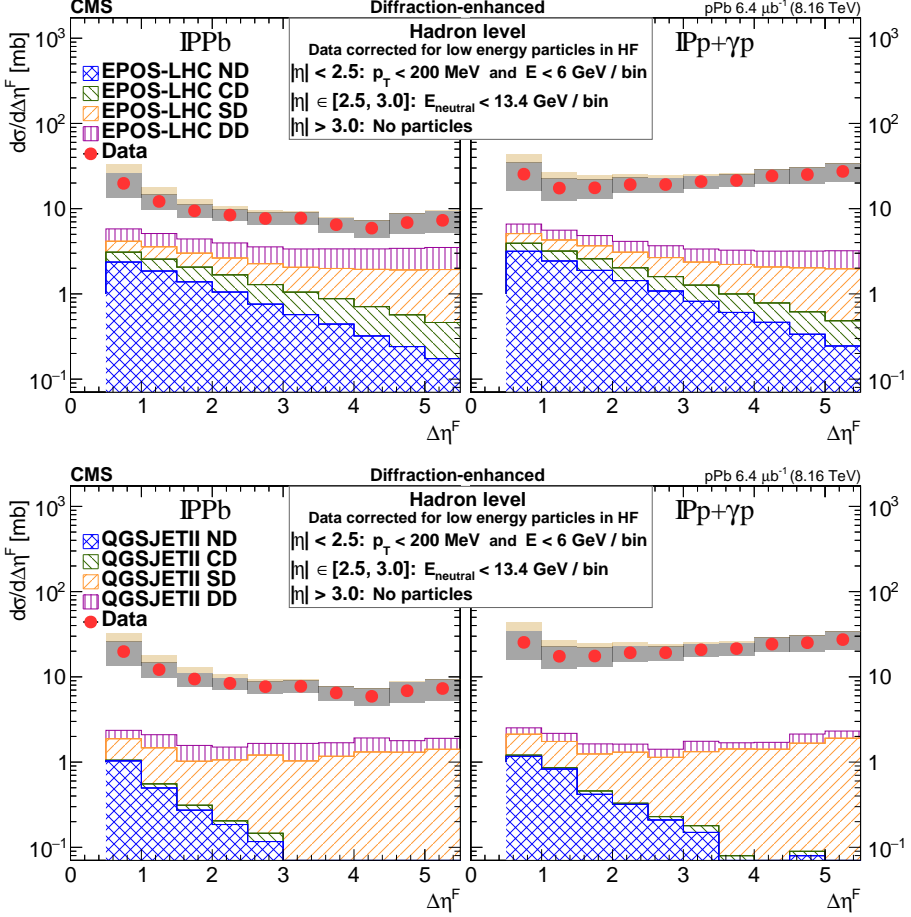


Figure 4: The hadron-level  $\frac{d\sigma}{d\Delta\eta^F}$  distribution for the events with no energy deposition in the  $3.14 < |\eta| < 5.19$  region adjacent to FRG for the EPOS-LHC [24] (top) and QGSJET [26] event generators, broken down to non-diffractive (blue), single (yellow), central (green) and double (magenta) diffractive events compared to CMS results [16] (red circles)

# References

- [1] G. Aad *et al.*, (ATLAS Collaboration), Eur. Phys. J. C **72**, 1926 (2012), arXiv:1201.2808 [hep-ex].
- [2] V. Khachatryan *et al.*, (CMS Collaboration), Phys. Rev. D **92**, 012003 (2015), arXiv:1503.08689 [hep-ex].
- [3] G. Antchev *et al.*, (TOTEM Collaboration), Eur. Phys. Lett. **96**, 21002 (2011), arXiv:1110.1395 [hep-ex].
- [4] G. Antchev *et al.*, (TOTEM Collaboration), Eur. Phys. Lett. **101**, 21002 (2013).
- [5] G. Antchev *et al.*, (TOTEM Collaboration), Eur. Phys. J. C **79**, 103 (2019), arXiv:1712.06153 [hep-ex].
- [6] F. E. Low, Phys. Rev. D **12**, 163 (1975).
- [7] S. Nussinov, Phys. Rev. Lett. **34**, 1286 (1975).
- [8] V. S. Fadin, E. A. Kuraev, and L. N. Lipatov, Phys. Lett. B **60**, 50 (1975).
- [9] A. B. Kaidalov, Phys. Rept. **50**, 157 (1979).
- [10] A. Donnachie and P. V. Landshoff, Nucl. Phys. B **244**, 322 (1984).
- [11] K. Akiba *et al.*, (LHC Forward Physics Working Group Collaboration), J. Phys. G **43**, 110201 (2016), arXiv:1611.05079 [hep-ph].
- [12] V. N. Gribov, JETP Lett. **41**, 667 (1961).
- [13] G. F. Chew and S. C. Frautschi, Phys. Rev. Lett. **7**, 394 (1961).
- [14] V. N. Gribov, Sov. Phys. JETP **29**, 483 (1969).
- [15] R. Luna, A. Zepeda, C. A. Garcia Canal, and S. J. Sciutto, Phys. Rev. D **70**, 114034 (2004), arXiv:hep-ph/0408303 [hep-ph].
- [16] A. Tumasyan *et al.*, (CMS Collaboration), Phys. Rev. D **108**, 092004 (2023), arXiv:2301.07630.
- [17] T. Akesson *et al.*, (HELIOS Collaboration), Z. Phys. C **49**, 355 (1991).
- [18] S. Chatrchyan *et al.*, (CMS Collaboration), JINST **3**, S08004 (2008).

- [19] A. J. Baltz *et al.*, Phys. Rept. **458**, 1 (2008), arXiv:0706.3356 [nucl-ex].
- [20] V. Khachatryan *et al.*, (CMS Collaboration), Phys. Lett. B **772**, 489 (2017), arXiv:1605.06966 [nucl-ex].
- [21] A. M. Sirunyan *et al.*, (CMS Collaboration), Eur. Phys. J. C **79**, 702 (2019), arXiv:1902.01339 [hep-ex].
- [22] A. M. Sirunyan *et al.*, (CMS Collaboration), Eur. Phys. J. C **79**, 277 (2019), arXiv:1809.11080 [hep-ex].
- [23] A. M. Sirunyan *et al.*, (CMS Collaboration), Phys. Lett. B **797**, 134826 (2019), arXiv:1810.04602 [hep-ex].
- [24] T. Pierog, I. Karpenko, J. M. Katzy, E. Yatsenko, and K. Werner, Phys. Rev. C **92**, 034906 (2015), arXiv:1306.0121 [hep-ph].
- [25] X.-N. Wang and M. Gyulassy, Phys. Rev. D **44**, 3501 (1991).
- [26] S. Ostapchenko, Phys. Rev. D **83**, 014018 (2011), arXiv:1010.1869 [hep-ph].
- [27] V. Guzey, M. Strikman, and M. Zhalov, Phys. Rev. C **106**, L021901 (2022), arXiv:2205.03861 [hep-ph].
- [28] V. A. Khoze and M. G. Ryskin, Eur. Phys. J. C **83**, 991 (2023), arXiv:2307.08625 [hep-ph].

# АНАЛИЗ ВКЛАДОВ БОЛЬШИХ РАССТОЯНИЙ В РАСПАДАХ $B^+ \rightarrow \pi^+ \ell^+ \ell^-$

Ирина М. Парнова<sup>1</sup>, Александр Я. Пархоменко<sup>1</sup>

<sup>1</sup> Ярославский государственный университет  
им. П. Г. Демидова, Ярославль

## Аннотация

Среди редких полулептонных распадов  $B$ -мезонов, идущих за счет нейтрального  $b \rightarrow d$  кваркового тока с изменением аромата, эксклюзивный распад  $B^+ \rightarrow \pi^+ \mu^+ \mu^-$  – один из немногих, обнаруженных экспериментально. Он достаточно хорошо изучен теоретически, а экспериментальные данные по этому распаду, полученные коллаборацией LHCb в 2015 г., хорошо согласуются с предсказаниями Стандартной Модели (СМ) практически во всей области допустимых значений  $q^2$  – квадрата импульса, уносимого лептонной парой. Поправки за счет вкладов аннигиляционных диаграмм, а также вкладов больших расстояний от векторных мезонов, улучшают согласие теории и эксперимента при  $q^2 \leq 1 \text{ ГэВ}^2$ , где экспериментальные данные существенно превосходят пертурбативный вклад. Более того, представляет интерес оценить влияние этих дополнительных вкладов на весь спектр по  $q^2$ . Такой анализ для распада  $B^+ \rightarrow \pi^+ \mu^+ \mu^-$ , а также для аналогичного распада  $B^+ \rightarrow \pi^+ \tau^+ \tau^-$ , представлен в настоящей работе.

# ANALYSIS OF LONG-DISTANCE CONTRIBUTIONS IN $B^+ \rightarrow \pi^+ \ell^+ \ell^-$ DECAYS

Irina M. Parnova<sup>1</sup>, Alexander Ya. Parkhomenko<sup>1</sup>  
<sup>1</sup>P. G. Demidov Yaroslavl State University, Yaroslavl

Abstract

Among the rare semileptonic  $B$  meson decays due to the  $b \rightarrow d$  flavor changing neutral current (FCNC), the exclusive  $B^+ \rightarrow \pi^+ \mu^+ \mu^-$  decay is the one of a few observed experimentally. It is well studied theoretically, and the experimental data on this decay obtained by the LHCb collaboration in 2015 are consistent with the Standard Model (SM) predictions in almost all regions of the  $q^2$  spectrum, where  $q^2$  is the momentum squared, transferred to the lepton pair. Accounting for subleading contributions, such as Weak Annihilation and Long Distance contributions, gives better agreement between theory and experiment at  $q^2 \lesssim 1 \text{ GeV}^2$ , where experimental data are substantially larger of the perturbative contribution. Moreover, it is of interest to evaluate an impact of subleading contributions on the entire  $q^2$  spectrum. Such an analysis for the  $B^+ \rightarrow \pi^+ \mu^+ \mu^-$  decay, as well as for the analogous  $B^+ \rightarrow \pi^+ \tau^+ \tau^-$  decay, is presented in this paper.

# 1 Введение

Редкие распады адронов, идущие за счет нейтральных кварковых  $b \rightarrow d$  и  $b \rightarrow s$  токов с изменением аромата, представляют особый интерес при проведении исследований по физике высоких энергий, поскольку, обладая малыми вероятностями распада, они особенно чувствительны к эффектам физики за рамками Стандартной модели (СМ). Эти процессы в СМ регулируются ГИМ механизмом [1], в рамках которого такие переходы определяются электрослабыми петлевыми диаграммами. В настоящее время интерес к физике редких распадов адронов в значительной степени стимулируется экспериментами LHCb, CMS и ATLAS на LHC, которые предоставляют большое количество новых и точных экспериментальных данных, касающихся рождений и распадов  $B$ -мезонов и прелестных барионов. Новые данные поступают также и от коллаборации Belle-II, проводящей исследования на фабрике  $B$ -мезонов SuperKEKB.

Редкие полулептонные распады, идущие за счет кваркового  $b \rightarrow s$  тока, такие, как  $B^\pm \rightarrow K^{(*)\pm} \mu^+ \mu^-$ ,  $B^0 \rightarrow K^{(*)0} \mu^+ \mu^-$  и  $B_s^0 \rightarrow \phi \mu^+ \mu^-$  и их аналоги в электронном секторе, достаточно хорошо изучены экспериментально и теоретически. Большинство данных по этим распадам, в частности вероятности распадов, распределения по инвариантной массе лептонной пары и угловые распределения, получены коллаборацией LHCb [2–8]. Было обнаружено, что некоторые из этих измерений не согласуются с предсказаниями СМ, что вызвало всплеск интереса к моделям, включающим новую физику, с целью объяснить обнаруженные расхождения между СМ и экспериментом [9–13].

Первое наблюдение редкого полулептонного  $B^+ \rightarrow \pi^+ \mu^+ \mu^-$  распада коллаборацией LHCb в 2012 году [14] стало началом исследований процессов, идущих за счет нейтрального  $b \rightarrow d$  тока с изменением аромата. Более того, в 2015 году этой же коллаборацией на большей статистике событий было получено распределение по инвариантной массе  $q^2$  мюонной пары в этом распаде [15]. Измеренное распределение хорошо согласуется с теоретическими предсказаниями в рамках СМ [16–18] во всех областях спектра за исключением области  $q^2 < 1 \text{ ГэВ}^2$ , в которой экспериментальные данные значительно превышают теоретические предсказания, основанные на вкладах коротких расстояний [15]. Однако учет аннигиляционных вкладов и вкладов больших расстояний, возникающих за счет распадов векторных мезонов на лептонную пару, позволяет согласовать теоретические предсказания с экспериментальными данными [19–21]. Интерференция между пертурбативным вкладом и непертурбативными вкладами больших рас-

стояний была исследована коллаборацией LHCb на основе данных 2011 и 2012 гг. по распаду  $B^+ \rightarrow K^+ \mu^+ \mu^-$  [22]. Из анализа следует, что фазы амплитуд, соответствующих  $J/\psi$ - и  $\psi(2S)$ -мезонам, важны, когда  $q^2 \sim m_{J/\psi}^2$  и  $q^2 \sim m_{\psi(2S)}^2$ , однако их влияние на распределение по  $q^2$  в других областях несущественно. Кроме того, были измерены вероятности распадов с рождением более тяжелых состояний чармония:  $\psi(3770)$ ,  $\psi(4040)$ ,  $\psi(4160)$  и  $\psi(4415)$ . Этот анализ представляется полезным для изучения других полулептонных распадов, в частности  $B^+ \rightarrow \pi^+ \ell^+ \ell^-$ . Более того, для распадов  $B \rightarrow \pi e^+ e^-$  и  $B \rightarrow \pi \mu^+ \mu^-$  легкие векторные  $\rho^0$ -,  $\omega$ - и  $\phi$ -мезоны дают значительный вклад в распределение по инвариантной массе дилептонной пары вблизи  $q^2 \sim 1 \text{ ГэВ}^2$ .

В настоящей работе представлен теоретический анализ редких полулептонных распадов  $B^+ \rightarrow \pi^+ \ell^+ \ell^-$ , где  $\ell = \mu, \tau$ , с учетом влияния вкладов больших расстояний. Получены предсказания для дифференциальной и полной вероятностей распада, а также распределения по инвариантной массе пары лептонов.

## 2 Теория редких полулептонных распадов $B$ -мезонов

Теоретический анализ был выполнен в рамках метода эффективных электрослабых гамильтонианов [23, 24], которые получаются после удаления из СМ тяжелых степеней свободы ( $t$ -кварк,  $W$ - и  $Z$ -бозоны). Эта эффективная теория также не содержит фотоны и глюоны с энергиями, превышающими массу  $b$ -кварка,  $m_b$ , которая выступает как наибольший энергетический масштаб теории. Фотоны и глюоны с более низкими энергиями описываются стандартными лагранжианами КЭД и КХД. В этом подходе обычно проводится расчет редких полулептонных распадов  $B$ -мезонов, идущих за счет кварковых  $b \rightarrow s$  и  $b \rightarrow d$  переходов. Эффективный гамильтониан, описывающий  $b \rightarrow d$  переход, имеет вид:

$$\begin{aligned} \mathcal{H}_{\text{weak}}^{b \rightarrow d} = & \frac{4G_F}{\sqrt{2}} \left\{ V_{ud}V_{ub}^* \left[ C_1(\mu) \mathcal{P}_1^{(u)}(\mu) + C_2(\mu) \mathcal{P}_2^{(u)}(\mu) \right] + \right. \\ & \left. + V_{cd}V_{cb}^* \left[ C_1(\mu) \mathcal{P}_1^{(c)}(\mu) + C_2(\mu) \mathcal{P}_2^{(c)}(\mu) \right] - V_{td}V_{tb}^* \sum_{j=3}^{10} C_j(\mu) \mathcal{P}_j(\mu) \right\} + \text{h. c.}, \end{aligned} \quad (1)$$

где  $G_F$  – постоянная Ферми,  $V_{q_1 q_2}$  – элементы матрицы ККМ, удовлетворяющее условию унитарности  $V_{ud}V_{ub}^* + V_{cd}V_{cb}^* + V_{td}V_{tb}^* = 0$ ,  $C_j(\mu)$  – коэффициенты

Вильсона, определяемые на масштабе  $\mu$  [25],  $\mathcal{P}_j(\mu)$  – локальные операторы  $b \rightarrow d$  перехода. Базис этих локальных операторов  $\mathcal{P}_j(\mu)$  включает в себя 10 операторов [24]. Лидирующий вклад в амплитуду  $B^+ \rightarrow \pi^+ \ell^+ \ell^-$  распада дают следующие три оператора:

$$\mathcal{P}_{7\gamma} = \frac{e}{16\pi^2} [\bar{d}\sigma^{\mu\nu}(m_b R + m_d L)b] F_{\mu\nu}, \quad (2)$$

$$\mathcal{P}_{9\ell} = \frac{\alpha}{2\pi} (\bar{d}\gamma_\mu L b) \sum_\ell (\bar{\ell}\gamma^\mu \ell), \quad \mathcal{P}_{10\ell} = \frac{\alpha}{2\pi} (\bar{d}\gamma_\mu L b) \sum_\ell (\bar{\ell}\gamma^\mu \gamma^5 \ell), \quad (3)$$

где  $L, R = (1 \mp \gamma_5)/2$  – операторы левой и правой проекции фермионов,  $F_{\mu\nu}$  – тензор электромагнитного поля,  $m_b$  и  $m_d$  – массы  $b$ - и  $d$ -кварков, причем массой  $d$ -кварка будем пренебрегать,  $\sigma^{\mu\nu} = i(\gamma_\mu \gamma_\nu - \gamma_\nu \gamma_\mu)/2$ , и  $\alpha = e^2/(4\pi)$  – постоянная тонкой структуры. Суммирование по  $\ell$  подразумевает суммирование по всем заряженным лептонам.

Матричные элементы  $B \rightarrow P$  перехода, где  $P$  – псевдоскалярный мезон, стандартным образом определяются тремя переходными формфакторами:  $f_+(q^2)$ ,  $f_0(q^2)$  и  $f_T(q^2)$  [26], где  $q^\mu = (p_B - k)^\mu$  – четырехмерный импульс, уносимый лептонной парой:

$$\langle P(k) | \bar{p}\gamma^\mu b | B(p_B) \rangle = f_+(q^2) \left[ p_B^\mu + k^\mu - \frac{m_B^2 - m_P^2}{q^2} q^\mu \right] + f_0(q^2) \frac{m_B^2 - m_P^2}{q^2} q^\mu, \quad (4)$$

$$\langle P(k) | \bar{p}\sigma^{\mu\nu} q_\nu b | B(p_B) \rangle = i \left[ (p_B^\mu + k^\mu) q^2 - q^\mu (m_B^2 - m_P^2) \right] \frac{f_T(q^2)}{m_B + m_P}, \quad (5)$$

$$\langle P(k) | \bar{p}\gamma^\mu \gamma_5 b | B(p_B) \rangle = 0, \quad \langle P(k) | \bar{p}\sigma^{\mu\nu} \gamma_5 q_\nu b | B(p_B) \rangle = 0, \quad (6)$$

где  $m_B$  и  $m_P$  – массы  $B$ - и псевдоскалярного мезона, соответственно. При нулевом передаваемом импульсе для векторных формфакторов выполняется соотношение:  $f_+(0) = f_0(0)$ .

Дифференциальную вероятность распада  $B \rightarrow P \ell^+ \ell^-$  с учетом вкладов больших расстояний и аннигиляционных диаграмм можно записать в виде [20]:

$$\frac{d\text{Br}(B \rightarrow P \ell^+ \ell^-)}{dq^2} = S_P \frac{2G_F^2 \alpha^2 \tau_B}{3(4\pi)^5 m_B^3} |V_{tp}^* V_{tb}|^2 \lambda^{3/2}(q^2) F^{BP}(q^2) \sqrt{1 - 4m_\ell^2/q^2}, \quad (7)$$

$$F^{BP}(q^2) = F_{97}^{BP}(q^2) + F_{10}^{BP}(q^2), \quad \lambda(q^2) = (m_B^2 + m_P^2 - q^2)^2 - 4m_B^2 m_P^2 \quad (8)$$

$$F_{97}^{BP}(q^2) = \left( 1 + \frac{2m_\ell^2}{q^2} \right) \left| C_9^{\text{eff}}(q^2) f_+^{BP}(q^2) + \frac{2m_b}{m_B + m_P} C_7^{\text{eff}}(q^2) f_T^{BP}(q^2) + L_A^{BP}(q^2) + \Delta C_V^{BP}(q^2) \right|^2, \quad (9)$$

$$F_{10}^{BP}(q^2) = \left( 1 - \frac{4m_\ell^2}{q^2} \right) \left| C_{10}^{\text{eff}} f_+^{BP}(q^2) \right|^2 + \frac{6m_\ell^2}{q^2} \frac{(m_B^2 - m_P^2)^2}{\lambda(q^2)} |C_{10}^{\text{eff}} f_0^{BP}(q^2)|^2, \quad (10)$$

где  $S_P$  – множитель, учитывающий кварковую структуру конечного мезона, в частности,  $S_{\pi^\pm} = 1$  и  $S_{\pi^0} = 1/2$  для  $\pi$ -мезонов,  $C_{7,9,10}^{\text{eff}}$  – эффективные коэффициенты Вильсона, включающие КХД поправки следующего за главным порядком теории возмущений [27],  $L_A^{BP}(q^2)$  – слагаемое, учитывающее вклад аннигиляционных диаграмм, и  $\Delta C_V^{BP}(q^2)$  – слагаемое, отвечающее за вклады больших расстояний.

Вклады аннигиляционных диаграмм вычисляются в рамках так называемой Эффективной теории больших энергий. Они существенны в начале спектра по  $q^2$ , и их учет имеет смысл только для распадов  $B^+ \rightarrow \pi^+ e^+ e^-$  и  $B^+ \rightarrow \pi^+ \mu^+ \mu^-$  [28]. Вклады больших расстояний получаются из двухчастичных  $B \rightarrow V\pi$  распадов, где  $V$  – нейтральный векторный мезон, а именно,  $\rho^0$ ,  $\omega$ ,  $\phi$ ,  $J/\psi$ ,  $\psi(2S)$  и более массивные векторные чармониевые резонансы, с последующим рождением мезоном лептонной пары  $V \rightarrow \ell^+ \ell^-$ . Они могут быть представлены следующим образом [19]:

$$\Delta C_V^{B\pi}(q^2) = -16\pi^2 \frac{V_{ud}^* V_{ub} H^{(u)}(q^2) + V_{cd}^* V_{cb} H^{(c)}(q^2)}{V_{td}^* V_{tb}}, \quad (11)$$

$$H^{(p)}(q^2) = (q^2 - q_0^2) \sum_V \frac{k_V f_V A_{BV\pi}^p}{(m_V^2 - q_0^2)(m_V^2 - q^2 - im_V \Gamma_V^{\text{tot}})}, \quad (12)$$

где  $f_V$ ,  $m_V$  и  $\Gamma_V^{\text{tot}}$  – постоянная распада, масса и полная ширина распада векторного мезона соответственно,  $k_V$  – коэффициент, определяемый кварковой структурой мезона,  $A_{BV\pi}^p$  ( $p = u, c$ ) – амплитуды распада, и свободный параметр  $q_0^2 = -1.0 \text{ ГэВ}^2$  выбран таким же, как и в [19]. Дифференциальная вероятность распада (7) содержит три формфактора  $B \rightarrow P$  перехода:  $f_+(q^2)$ ,  $f_0(q^2)$  и  $f_T(q^2)$ . Из известных в литературе параметризаций этих формфакторов в настоящей работе выбрана параметризация, предложенная Боррелеем, Каприни и Леллошем (БКЛ) [29].

### 3 Результаты и анализ вкладов больших расстояний

Распределения по инвариантной массе лептонной пары в распадах  $B^+ \rightarrow \pi^+ \mu^+ \mu^-$  и  $B^+ \rightarrow \pi^+ \tau^+ \tau^-$  с учетом вкладов аннигиляционных диаграмм и вкладов больших расстояний представлены на Рис. 1. Теоретические предсказания для полной вероятности распадов  $B^+ \rightarrow \pi^+ \mu^+ \mu^-$  и  $B^+ \rightarrow \pi^+ \tau^+ \tau^-$  в случае учета только пертурбативного вклада  $\text{Br}_{\text{pert}}$ , с учетом вкладов больших расстояний и вкладов аннигиляционных диаграмм (для

мюонного распада)  $\text{Br}_{\text{th}}$  в сравнении с имеющимися экспериментальными данными  $\text{Br}_{\text{exp}}$  представлены в Табл. 1.

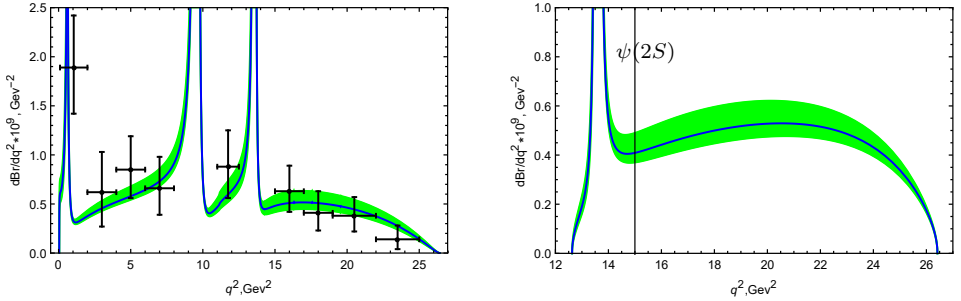


Рис. 1: Теоретические предсказания для распределений по инвариантной массе лептонной пары в распадах  $B^+ \rightarrow \pi^+ \mu^+ \mu^-$  (слева), где крестиками указаны экспериментальные данные [15], и  $B^+ \rightarrow \pi^+ \tau^+ \tau^-$  (справа). Области зеленого цвета показывают разброс значений, возникающий из неопределенностей в выборе масштаба факторизации и ошибки экспериментального определения элемента  $V_{td}$  матрицы Кабиббо–Кобаяши–Маскава.

Как можно видеть из Рис. 1, весомый вклад в распределение по инвариантной массе мюонной пары в распаде  $B^+ \rightarrow \pi^+ \mu^+ \mu^-$  дают вклады от легких векторных  $\rho^0$ -,  $\omega$ - и  $\phi$ -мезонов в области малых  $q^2$ , а также от  $J/\psi$ - и  $\psi(2S)$ -мезонов. Более массивные векторные чармонии не дают значительного вклада в распределение. Наши предсказания с учетом вкладов больших расстояний, как можно видеть, хорошо согласуются с экспериментальными данными, полученными коллаборацией LHCb по этому распаду [15] во всех областях спектра по  $q^2$ .

Таблица 1: Теоретические предсказания для полных вероятностей распадов  $B^+ \rightarrow \pi^+ \ell^+ \ell^-$ , где  $\ell = \mu, \tau$

	$B^+ \rightarrow \pi^+ \mu^+ \mu^-$	$B^+ \rightarrow \pi^+ \tau^+ \tau^-$
$\text{Br}_{\text{pert}} \times 10^8$	$1.72^{+0.27}_{-0.14}$	$0.60^{+0.08}_{-0.05}$
$\text{Br}_{\text{th}} \times 10^8$	$1.91^{+0.34}_{-0.17}$	$0.61^{+0.08}_{-0.05}$
$\text{Br}_{\text{exp}} \times 10^8$	$1.83 \pm 0.29$	–

Поскольку распределение по инвариантной массе тауонной пары в распаде  $B^+ \rightarrow \pi^+ \tau^+ \tau^-$  попадает в интервал  $q^2 \in [4m_\tau^2, (m_B - m_\pi)^2]$ ,

на него должны оказывать влияние  $\psi(2S)$ -мезон и следующие за ним чармониевые резонансы [30]. Из правого графика на Рис. 1 видно, что  $\psi(2S)$ -резонанс дает значительный вклад в распределение по инвариантной массе лептонной пары. Анализ возможности влияния на распределение по инвариантной массе лептонной пары более высоких чармониевых резонансов можно провести на примере  $\psi(3S)$ -мезона. Этот  $c\bar{c}$ -резонанс также известен как  $\psi(3770)$ . Вероятности распадов  $B^+ \rightarrow \pi^+\psi(3S)$  и  $\psi(3S) \rightarrow \tau^+\tau^-$  еще не измерены экспериментально, но можно оценить вероятность  $B^+ \rightarrow \pi^+\psi(3S)$ , используя каонные моды распада  $B$ -мезона, а именно  $B^+ \rightarrow K^+\psi(2S)$  и  $B^+ \rightarrow K^+\psi(3S)$ , относительные вероятности которых следующие:  $\text{Br}(B^+ \rightarrow K^+\psi(2S)) = (6.24 \pm 0.20) \times 10^{-4}$  и  $\text{Br}(B^+ \rightarrow K^+\psi(3S)) = (4.3 \pm 1.1) \times 10^{-4}$  [31]. Используя  $SU(3)_F$ -симметрию ароматов кварков, найдем полную вероятность  $B^+ \rightarrow \pi^+\psi(3S)$  распада из соотношения:

$$\frac{\text{Br}(B^+ \rightarrow \pi^+\psi(3S))}{\text{Br}(B^+ \rightarrow K^+\psi(3S))} \simeq \frac{\text{Br}(B^+ \rightarrow \pi^+\psi(2S))}{\text{Br}(B^+ \rightarrow K^+\psi(2S))}, \quad (13)$$

где  $\text{Br}(B^+ \rightarrow \pi^+\psi(2S)) = (2.44 \pm 0.30) \times 10^{-5}$  [31]. Считая (13) точным, получим:

$$\text{Br}(B^+ \rightarrow \pi^+\psi(3S)) = (1.7 \pm 0.5) \times 10^{-5}. \quad (14)$$

Поскольку  $\psi(3770)$  – широкий резонанс, основные каналы распада у которого на  $D^+D^-$  и  $D^0\bar{D}^0$  пары, то чисто лептонные каналы распада для него подавлены. Чтобы оценить величину этого подавления, можно использовать свойство лептонной универсальности, а также воспользоваться измеренной вероятностью распада  $\text{Br}(\psi(3S) \rightarrow e^+e^-) = (9.6 \pm 0.7) \times 10^{-6}$  [31]. Дифференциальные вероятности распадов  $\text{Br}(\psi(3S) \rightarrow e^+e^-)$  и  $\text{Br}(\psi(3S) \rightarrow \tau^+\tau^-)$  отличаются только фазовым объемом, и для их отношения следует:

$$\frac{\text{Br}(\psi(3S) \rightarrow \tau^+\tau^-)}{\text{Br}(\psi(3S) \rightarrow e^+e^-)} = \frac{\lambda(M_{\psi(3S)}, m_\tau, m_\tau)}{\lambda(M_{\psi(3S)}, m_e, m_e)}, \quad (15)$$

где  $\lambda(M, m, m) = M\sqrt{M^2 - 4m^2}$  [32]. Используя значения масс  $M_{\psi(3S)} = (3773.7 \pm 0.4)$  МэВ,  $m_e = 0.511$  МэВ и  $m_\tau = (1776.86 \pm 0.12)$  МэВ [31], получаем:

$$\text{Br}(\psi(3S) \rightarrow \tau^+\tau^-) = (3.2 \pm 0.2) \times 10^{-6}, \quad (16)$$

что, в свою очередь, дает следующую оценку вероятности распада:

$$\text{Br}(B^+ \rightarrow \pi^+\psi(3S) \rightarrow \pi^+\tau^+\tau^-) = (5.4 \pm 1.9) \times 10^{-11}. \quad (17)$$

Сравнивая с вероятностью  $B^+ \rightarrow \pi^+ \tau^+ \tau^-$  распада, учитывающей только пертурбативный вклад (Табл. 1) и по порядку величины равной  $\sim 10^{-9}$ , легко заметить, что вклад от  $\psi(3770)$ -резонанса (17) не оказывает существенного влияния на относительную вероятность, будучи порядка ошибки пертурбативного вклада.

Более тяжелые векторные чармонии, а именно  $\psi(4040)$ ,  $\psi(4160)$ ,  $\psi(4230)$ ,  $\psi(4360)$ , и  $\psi(4415)$ , также в основном распадаются на  $D\bar{D}$  пару, поэтому, как и для  $\psi(3S)$ -мезона, их электронные и мюонные моды подавлены [30]. Следовательно, их вкладами можно пренебречь и учесть вклады вплоть до узкого  $\psi(2S)$ -мезона включительно.

## 4 Заключение

В настоящей работе представлены теоретические предсказания для полной вероятности, а также распределений по инвариантной массе лептонной пары для распадов  $B^+ \rightarrow \pi^+ \mu^+ \mu^-$  и  $B^+ \rightarrow \pi^+ \tau^+ \tau^-$  с учетом аннигиляционных вкладов и вкладов больших расстояний. Проведен анализ вкладов больших расстояний и показано, что вклады от следующих за  $\psi(2S)$ -мезоном резонансов не превышают неопределенность теоретических расчетов, учитывающих только пертурбативный вклад. Предсказания, полученные для  $B^+ \rightarrow \pi^+ \mu^+ \mu^-$  распада, находятся в хорошем согласии с экспериментальными данными в пределах погрешностей. Что же касается экспериментальной проверки предсказаний для распада  $B^+ \rightarrow \pi^+ \tau^+ \tau^-$ , то обнаружение этого распада можно ожидать при наборе достаточной статистики распадов в последующих периодах работы ЛНС и Belle-II.

## Благодарности

Мы благодарим Ахмеда Али за совместную работу по данной тематике и обсуждение результатов. Работа выполнена при финансовой поддержке РФФ (проект № 22-22-00877).

# Литература

- [1] S. L. Glashow, J. Iliopoulos, and L. Maiani, *Phys. Rev. D* **2**, 1285 (1970).
- [2] R. Aaij *et al.*, (LHCb Collaboration), *JHEP* **06**, 133 (2014), arXiv:1403.8044 [hep-ex].
- [3] R. Aaij *et al.*, (LHCb Collaboration), *JHEP* **05**, 082 (2014), arXiv:1403.8045 [hep-ex].
- [4] R. Aaij *et al.*, (LHCb Collaboration), *JHEP* **09**, 179 (2015), arXiv:1506.08777 [hep-ex].
- [5] R. Aaij *et al.*, (LHCb Collaboration), *JHEP* **02**, 104 (2016), arXiv:1512.04442 [hep-ex].
- [6] R. Aaij *et al.*, (LHCb Collaboration), *JHEP* **11**, 047 (2016), arXiv:1606.04731 [hep-ex], [Erratum: *JHEP*, 04:142, 2017].
- [7] R. Aaij *et al.*, (LHCb Collaboration), *Phys. Rev. Lett.* **127**, 151801 (2021), arXiv:2105.14007 [hep-ex].
- [8] R. Aaij *et al.*, (LHCb Collaboration), *JHEP* **11**, 043 (2021), arXiv:2107.13428 [hep-ex].
- [9] A. Celis, J. Fuentes-Martin, A. Vicente, and J. Virto, *Phys. Rev. D* **96**, 035026 (2017).
- [10] D. Buttazzo, A. Greljo, G. Isidori, and D. Marzocca, *JHEP* **11**, 044 (2017).
- [11] J. Aebischer *et al.*, *Eur. Phys. J. C* **80**, 252 (2020).
- [12] L. Alasfar, A. Azatov, J. de Blas, A. Paul, and M. Valli, *JHEP* **12**, 016 (2020).
- [13] G. Isidori *et al.*, *Phys. Lett. B* **830**, 137151 (2022).
- [14] R. Aaij *et al.*, (LHCb Collaboration), *JHEP* **12**, 125 (2012), arXiv:1210.2645 [hep-ex].
- [15] R. Aaij *et al.*, (LHCb Collaboration), *JHEP* **10**, 034 (2015), arXiv:1509.00414 [hep-ex].
- [16] A. Ali, A. Y. Parkhomenko, and A. V. Rusov, *Phys. Rev. D* **89**, 094021 (2014), arXiv:1312.2523 [hep-ph].

- [17] R. N. Faustov and V. O. Galkin, Eur. Phys. J. C **74**, 2911 (2014), arXiv:1403.4466 [hep-ph].
- [18] W.-S. Hou, M. Kohda, and F. Xu, Phys. Rev. D **90**, 013002 (2014), arXiv:1403.7410 [hep-ph].
- [19] C. Hambroek, A. Khodjamirian, and A. Rusov, Phys. Rev. D **92**, 074020 (2015), arXiv:1506.07760 [hep-ph].
- [20] A. Ali, A. Parkhomenko, and I. Parnova, J. Phys.: Conf. Ser. **1690**, 012162 (2020).
- [21] I. Parnova, A. Ali, and A. Parkhomenko, PoS(PANIC2021) **380**, 158 (2022).
- [22] R. Aaij *et al.*, (LHCb Collaboration), Eur. Phys. J. C **77**, 161 (2017).
- [23] G. Buchalla, A. J. Buras, and M. E. Lautenbacher, Rev. Mod. Phys. **68**, 1125 (1996), arXiv:hep-ph/9512380.
- [24] K. G. Chetyrkin, M. Misiak, and M. Munz, Phys. Lett. B **400**, 206 (1997), [Erratum: *Phys. Lett. B*, 425:414, 1998].
- [25] C. Bobeth, M. Misiak, and U. Jorg, Nucl. Phys. B **574**, 291 (2000), arXiv:hep-ph/9910220.
- [26] M. Beneke and T. Feldmann, Nucl. Phys. B **592**, 3 (2001), arXiv:hep-ph/0008255.
- [27] H. M. Asatrian, K. Bieri, C. Greub, and M. Walker, Phys. Rev. D **69**, 074007 (2004), arXiv:hep-ph/0312063.
- [28] M. Beneke, T. Feldmann, and D. Seidel, Eur. Phys. J. C **41**, 173 (2005), arXiv:hep-ph/0412400.
- [29] C. Bourrely, I. Caprini, and L. Lellouch, Phys. Rev. D **79**, 013008 (2009), arXiv:0807.2722 [hep-ph], [Erratum: *Phys. Rev. D*, 82:099902, 2010].
- [30] A. Ali, A. Y. Parkhomenko, and I. M. Parnova, Phys. Lett. B **842**, 137961 (2023), arXiv:2303.15384 [hep-ph].
- [31] R. L. Workman *et al.*, (Particle Data Group Collaboration), PTEP **2022**, 083C01 (2022).
- [32] E. Bycking and K. Kajantie, *Particle Kinematics* (Wiley, London, 1973).

# CHARGED AND NEUTRAL PION POLARIZABILITY MEASUREMENT IN THE CPP/NPP EXPERIMENTS

Ilya F. Larin<sup>1,2</sup>, Victor V. Tarasov<sup>1</sup>

<sup>1</sup> National Research Centre “Kurchatov Institute”, Moscow

<sup>2</sup> University of Massachusetts, Amherst  
on behalf of the GlueX collaboration

## Abstract

Polarizability is a fundamental particle property. Measurement of pion polarizability values allows checking strict ChPT prediction. Charged and neutral  $\pi$ -mesons polarizability will be extracted from the CPP and NPP experimental data using Primakoff pair production cross section on nuclear target. The CPP/NPP experiment run at TJNAF Hall-D was conducted in the summer of 2022 and utilized a polarized photon beam with an energy range of 4.5–6.0 GeV and the lead-208 target on the upgraded GlueX experimental setup. The report considers existing experiments on measuring pion polarizability, theoretical predictions of polarizabilities, setting up CPP/NPP experiments at the GlueX facility, expected results in these experiments, and preliminary analysis of the collected data.

# ИЗМЕРЕНИЕ ПОЛЯРИЗУЕМОСТЕЙ ЗАРЯЖЕННОГО И НЕЙТРАЛЬНОГО ПИОНОВ В ЭКСПЕРИМЕНТАХ CPP/NPP

Илья Ф. Ларин<sup>1,2</sup>, Виктор В. Тарасов<sup>1</sup>

<sup>1</sup> НИЦ “Курчатовский институт”, Москва

<sup>2</sup> Массачусетский университет, Амхерст,  
от коллаборации GlueX

## Аннотация

Поляризуемость – фундаментальная характеристика частиц. Измерение величин поляризуемостей пионов позволяет осуществить проверку предсказаний киральной пертурбативной теории (ChPT). Поляризуемости  $\pi$ -мезонов будут определены в экспериментах CPP и NPP посредством измерения Примаковского сечения фоторождения заряженных и нейтральных пионных пар на ядерной мишени. С этой целью летом 2022 года на ускорителе TJNAF проведен набор экспериментальных данных по взаимодействиям поляризованного фотонного пучка с энергией 4.5–6.0 ГэВ с ядрами свинца-208 на модернизированной установке GlueX. В докладе рассмотрены существующие эксперименты по измерению поляризуемости пионов, теоретические предсказания поляризуемостей, постановка экспериментов CPP/NPP на установке GlueX, ожидаемые в этих экспериментах результаты и предварительный анализ набранных данных.

# 1 Introduction

Polarizability is a fundamental particle property. The pion is the lightest strongly interacting observed particle. The measurement of the  $\pi$ -meson polarizability is an important test of the fundamental symmetries in QCD at low energy. Among all hadronic polarizabilities, the pion polarizability is significant, since it provides a test of fundamental QCD symmetries in the leading order of perturbation theory. ChPT prediction at leading order  $O(p^4)$  for the electric  $\alpha$  and magnetic  $\beta$  charged  $\pi$  polarizabilities is given by formula

$$\alpha_{\pi^+} = -\beta_{\pi^+} = \frac{4\alpha}{m_\pi F_\pi^2} (L_9^r - L_{10}^r)$$

with  $O(p^6)$  corrections predicted to be relatively small [1–3]

$$\alpha_{\pi^+} - \beta_{\pi^+} = (5.7 \pm 1.0) \times 10^{-4} \text{fm}^3$$

and for neutral pion polarizability (one loop chiral contribution) [4]

$$\alpha_{\pi^0} = -\beta_{\pi^0} = -\frac{\alpha}{96\pi^2 m_\pi F_\pi^2} \simeq -0.55 \times 10^{-4} \text{fm}^3$$

with  $O(p^6)$  corrections [5]

$$\alpha_{\pi^0} - \beta_{\pi^0} = (-1.9 \pm 0.2) \times 10^{-4} \text{fm}^3,$$

where  $m_\pi$  – pion mass,  $F_\pi$  – pion decay constant,  $\alpha$  – fine-structure constant,  $L_9^r$  and  $L_{10}^r$  are low energy constants in Lagrangian [6]. The pion polarizability also plays an important role in the  $(g-2)_\mu$  anomaly [7], the interest in measuring which has grown since it was recently reported 4.2 standard deviations from the Standard Model prediction [8].

## 2 Previous measurements and theoretical predictions of the pion polarizability

The charged pion polarizability  $\alpha_{\pi^+} - \beta_{\pi^+}$  was measured by three different methods. These are (1) radiative pion Primakoff scattering in the nuclear Coulomb field  $\pi Z \rightarrow \pi Z \gamma$ , (2) two-photon fusion production of pion pairs  $\gamma\gamma \rightarrow \pi\pi$  via the  $e^+e^- \rightarrow e^+e^-\pi^+\pi^-$  reaction, (3) radiative pion photoproduction from the proton  $\gamma p \rightarrow \pi + n$ . The most up to date measurement in each type are COMPASS [9] where  $\alpha_\pi - \beta_\pi = (4.0 \pm 1.2_{stat} \pm 1.4_{syst}) \times 10^{-4} \text{fm}^3$ ,

MARK-II [10] where  $\alpha_\pi - \beta_\pi = (4.4 \pm 3.2_{stat+syst} \times 10^{-4} \text{fm}^3)$  and MAMI [11] where  $\alpha_\pi - \beta_\pi = (11.6 \pm 1.5_{stat} \pm 3.0_{syst} \pm 0.5_{model}) \times 10^{-4} \text{fm}^3$ . Until now only the COMPASS collaboration measurement has reasonably small uncertainties and coincides within the uncertainty with the theoretical calculations [3]. Previous measurements grouped by different experimental techniques and theoretical predictions of  $\alpha_{\pi^+} - \beta_{\pi^+}$  shown in Fig. 1.

The neutral pion polarizability was estimated by [12] as  $(0.8 \pm 2.0) \times 10^{-4} \text{fm}^3$  according to the only currently existing measurement of the cross section for the  $\gamma\gamma \rightarrow \pi^0\pi^0$  reaction in the mass region below 0.7 GeV in studies of the  $e^+e^- \rightarrow e^+e^-\pi^0\pi^0$  interactions in the Crystal Ball experiment at DESY [13]. A large uncertainty in the measurement of polarizability arises from the low statistics collected for the reaction  $\gamma\gamma \rightarrow \pi^0\pi^0$  at  $W_{\pi^0\pi^0} < 0.7 \text{ GeV}$  (about 300 events).

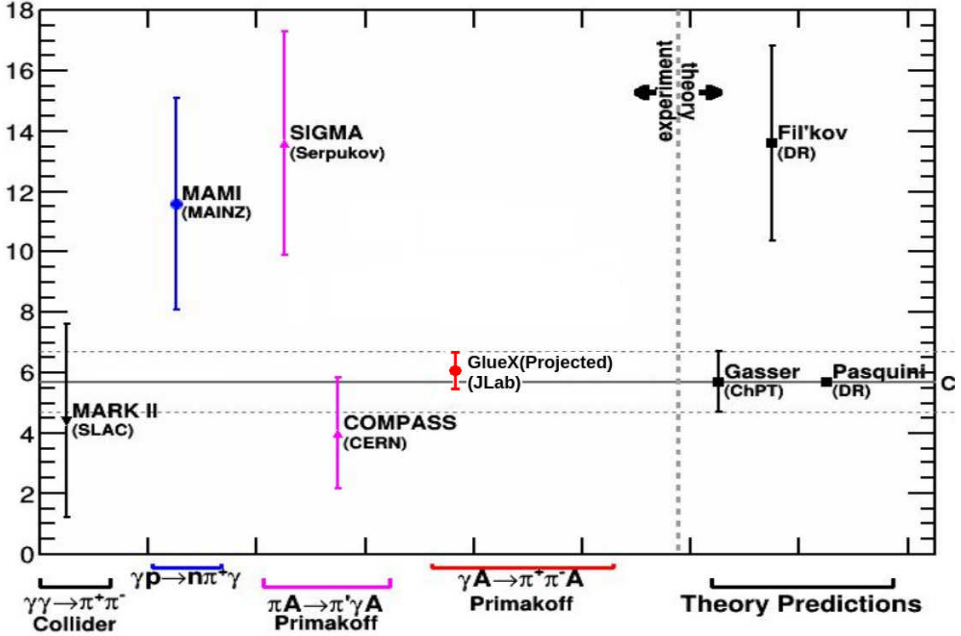


Figure 1: Experimental data for  $\alpha_{\pi^+} - \beta_{\pi^+}$  grouped by measurement type along with the theoretical predictions

### 3 CPP and NPP experiments at Jefferson Lab

The goal of the CPP and NPP experiments is to make a precision measurement of pion polarizabilities by collecting of a high statistical data set of the  $\gamma\gamma \rightarrow \pi^+\pi^-$  and  $\gamma\gamma \rightarrow p i^0 \pi^0$  reactions near the threshold through the Primakoff process (Fig. 2.). The cross section of this reaction can be accessed in a tagged-photon beam measurement of  $\gamma A \rightarrow \pi^+\pi^- A$  ( $\gamma A \rightarrow \pi^0 \pi^0 A$ ) at very low momentum transfer:

$$\frac{d^2\sigma_{Pr}}{d\Omega_{\pi\pi}dM_{\pi\pi}} = \frac{2\alpha Z^2 E_\gamma^4 \beta^2 \sin^2\theta}{\pi^2 M_{\pi\pi} Q^4} |F(Q^2)|^2 (1 + P_\gamma \cos 2\phi_{\pi\pi}) \sigma(\gamma\gamma \rightarrow \pi\pi),$$

where  $\sigma_{Pr}$  is the Primakoff cross section of two pions production,  $\Omega_{\pi\pi}$  is the solid angle in the laboratory frame for the emission of the  $2\pi$  system,  $M_{\pi\pi}$  is the invariant mass of the  $2\pi$  system,  $E_\gamma$  is the energy of the incident photon beam,  $Z$  is the target atomic number,  $\beta$  is the velocity of the  $2\pi$  system,  $F(Q)$  is the electromagnetic form factor for the target,  $\theta_{\pi\pi}$  is the lab angle for the  $2\pi$  system,  $P_\gamma$  is the linear polarization of the incident beam,  $\phi_{\pi\pi}$  is the azimuth angle of the  $2\pi$  system, and  $\sigma(\gamma\gamma \rightarrow \pi\pi)$  is total cross section which is sensitive for the pion polarizability. Existing theoretical calculations for the pion pair photoproduction at forward angles and near the threshold should provide opportunity for extracting  $\pi$ -meson polarizabilities [14].

Fig. 3 (left) presents calculated total cross sections for  $\gamma\gamma \rightarrow \pi^+\pi^-$  from Pasquini *et al.* [3] for the different  $\alpha_\pi - \beta_\pi$  values (with  $|\cos\theta_{\pi\pi}| < 0.6$ ). The black curve is a calculation with no polarizability effect. The blue dashed curve is subtracted dispersion relation (DR) calculation with  $\alpha_{\pi^+} - \beta_{\pi^+} = 5.7 \times 10^{-4} \text{fm}^3$ . The dotted curve is the subtracted DR calculation with the polarizabilities from [15] with  $\alpha_\pi - \beta_\pi = 13.0 \times 10^{-4} \text{fm}^3$ . Comparison of the curves with  $\alpha_{\pi^+} - \beta_{\pi^+}$  equal to  $5.7 \times 10^{-4} \text{fm}^3$  (blue dashed) and  $13.0 \times 10^{-4} \text{fm}^3$  (black dotted) shows a change in the cross section at  $W_{\pi\pi} = 0.4 \text{ GeV}$  of approximately 20%. The red data points are expected for the Jlab CPP experiment and black data points from the Mark II experiment for  $\gamma\gamma \rightarrow \pi^+\pi^-$  reaction. Simulation for the CPP measurement [16] predicts the total cross section uncertainty about 1% and  $\alpha_{\pi^+} - \beta_{\pi^+} \sim (6.0 \pm 0.6) \times 10^{-4} \text{fm}^3$  with an expected accuracy of about 10% which is few times more precise than best available. The main uncertainty components are the trigger efficiency,  $\mu^+\mu^-$  background, beam polarization.

Estimated cross section uncertainty for the NPP experiment – about 5% gives  $\alpha_{\pi^0} - \beta_{\pi^0}$  expected value about  $(-2.0 \pm 0.8) \times 10^{-4} \text{fm}^3$  (uncertainty about 40% in determination of the  $\pi^0$  polarizability [17]). Total uncertainty in NPP comes from available statistics, yield extraction, acceptance. Fig. 3

(right) shows predicted total cross section of  $\gamma\gamma \rightarrow \pi^0\pi^0$  reaction with estimated uncertainties for NPP experiment (assuming that about 2K pairs of neutral pions will be collected during the run). The data points from the single previous Crystal Ball measurement [13] are shown for the comparison.

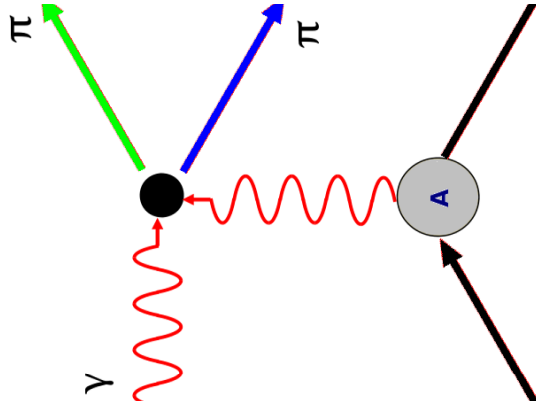


Figure 2: Diagram of the  $\gamma\gamma \rightarrow \pi\pi$  reaction

## 4 Experimental setup

The simplified layout of the GlueX detector is shown in Fig. 4. The spectrometer is based on a 4 meters long solenoidal magnet operated at the maximum field of 2T. The lead-208 target is located inside the upstream bore of the magnet and placed upstream of the nominal GlueX target by 64 cm. The central drift chambers(CDC), are cylindrical straw-tube detector, starts at a radius of 10 cm from the beam line. The CDC consists of 28 layers of straw tubes in axial and two stereo orientations. The forward drift chambers(FDC) are located downstream of the central tracker and consist of four packages, each containing 6 planar layers in alternating u-y-v orientations. The Time-of-Flight scintillator paddles(TOF) located downstream of the magnet. This system consists of two planes in a crossed pattern. Photons arising from  $\pi^0$  decays are detected by two calorimeter systems. The Barrel Calorimeter(BCAL), located inside the solenoid, consists of layers of scintillating fibers alternating with lead sheets. The Forward Calorimeter(FCAL) is located downstream of the Time-of-Flight planes, and consists of 2800 lead-glass blocks. Special muon detector was developed to distinguish charged pions from muons placed behind FCAL. Muon detector consists of one lead, four steel walls and 6 MWPC chambers. This detector was used only for the CPP experiment. NPP experiment doesn't need

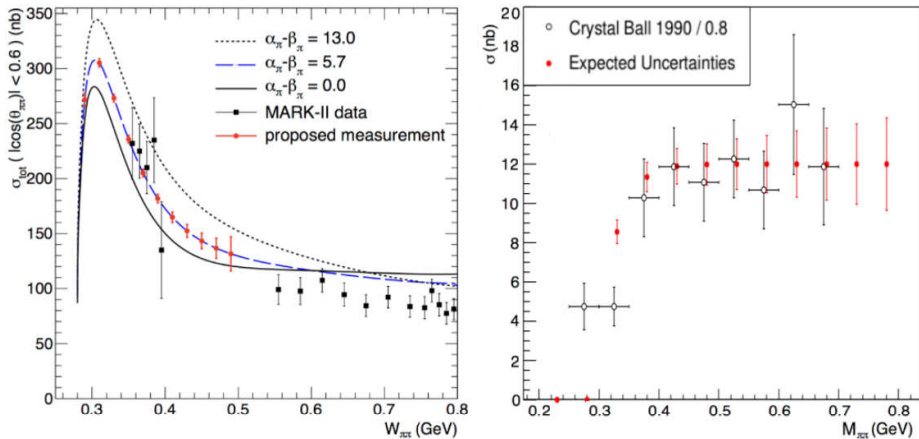


Figure 3: (Left):  $\gamma\gamma \rightarrow \pi^+\pi^-$  cross sections. The solid, dashed, dotted curves are subtracted dispersion model calculations with  $\alpha_\pi - \beta_\pi$  equal to 0.0,  $5.7 \times 10^{-4}\text{fm}^3$  (ChPT), and  $13.0 \times 10^{-4}\text{fm}^3$  respectively. The black data points are from the Mark II, the red data points are projected data points from the CPP experiment. (Right): Estimated total cross section for  $\gamma\gamma \rightarrow \pi^0\pi^0$  from NPP experiment and data points from the single previous Crystal Ball measurement

an additional equipment as all gammas from  $\pi^0$  decays were analyzed via FCAL and BCAL.

The diamond radiator (installed in the electron beam direction) sets the main coherent peak edge of the tagged photon beam near 6 GeV. This enhances the polarization significantly and also the tagging ratio compared to regular GlueX conditions. Also Diamond radiator was installed in two positions during run where beam polarization angle was 135 and 45 degrees respectively (positions where beam polarization is maximum – 72%). To reduce the systematic uncertainties beam polarization angle was changed every four hours. More detail information about GlueX setup can be found here [18].

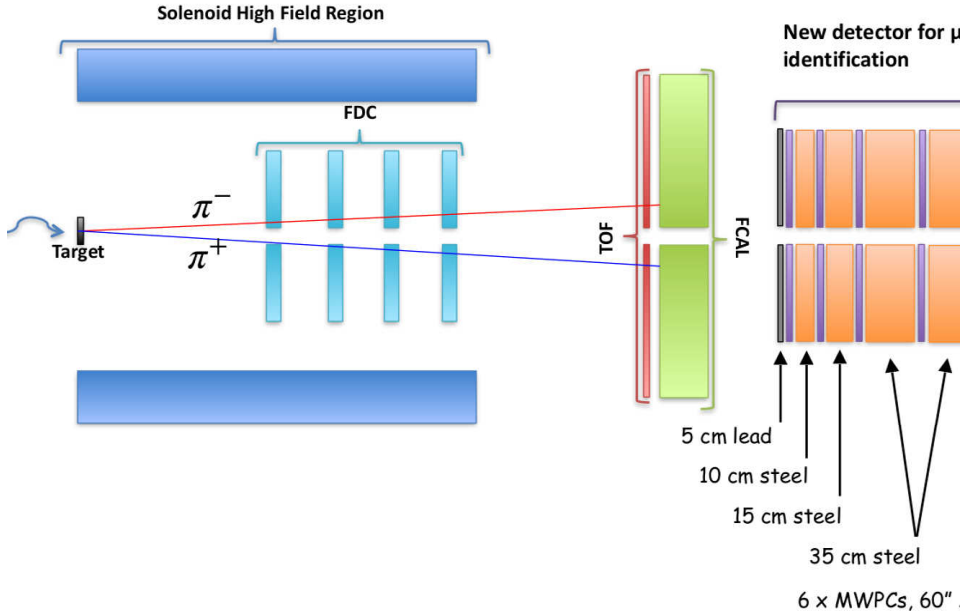


Figure 4: Experimental setup

## 5 Experimental conditions and preliminary data analysis

Simultaneously with the data collection for the experiment on measuring the polarizability of charged pions (CPP experiment), the data collection was carried out for measuring the polarizability of neutral pions (NPP experiment). For CPP the Time Of Flight detector based trigger has been used. The trigger is organized in such a way that makes it possible to select events with two charged particles reached the GlueX time-of-flight (TOF) system [19]. This is ideal for detecting pairs of charged tracks. In the further offline analysis muon pairs will be rejected by muon detector and electron pairs will be rejected via electromagnetic calorimeters. For NPP experiment FCAL/BCAL trigger has been used as the Primakoff reaction will convert almost all of the beam's energy into four photons. Most of the energy will be deposited in FCAL, with the exception of beampipe leakage and a small amount deposited in BCAL. This simple trigger with 1 GeV energy threshold has a very high efficiency for neutral pion production events.

Summer 2022 run was lasting from June 8 to August 17, used  $10^7$  photons

per second from a tagged, collimated coherent bremsstrahlung beam. 106B triggers have been recorded on lead-208 target and 23B triggers with no target for out of target background subtraction. During and after the run, a preliminary analysis of the data was performed, and important several distributions were produced to ensure the data quality. Examples of such distributions are present in figures 5,6,7. The MWPC performance has been tested on the  $\omega \rightarrow \pi^+\pi^-\pi^0$  decay (Fig. 5). Black points are showing the events with pion tracks with sufficient energy and correct trajectories to hit MWPCs beyond the 2nd chamber, without requiring those hits. Red points – the same selection criteria but with the requirement of hits beyond the 2nd chamber. It is clearly seen that this simple muon criterion does not reject charged pion events. In fig. 6, the invariant masses for the reactions  $\pi \rightarrow \gamma\gamma$  (on the left, around 250K events,  $\sigma \sim 7$  MeV) and  $\eta \rightarrow \gamma\gamma$  (on the right, around 2.5K events,  $\sigma \sim 23$  MeV) are shown for the beam energy ranges 4.5–6 GeV and 8–11 GeV, respectively. The thick red curve in the upper figures is the invariant mass without a target and bottom pictures are for invariant mass of two gammas with the background subtracted. Fig. 7. shows very preliminary plot of the invariant mass of two charged pions in the CPP experiment.

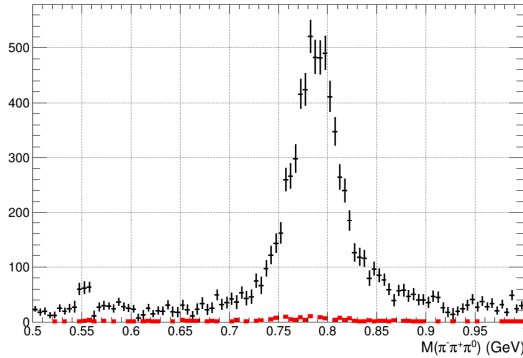


Figure 5: Invariant mass of  $\pi^+\pi^-\pi^0$  (see the text for the details)

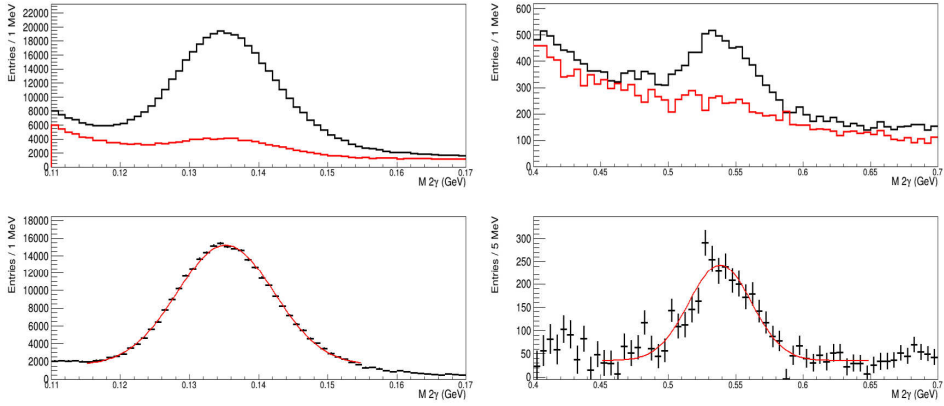


Figure 6: Invariant mass of two gammas. Left –  $\pi^0$  region and right –  $\eta$ -meson region

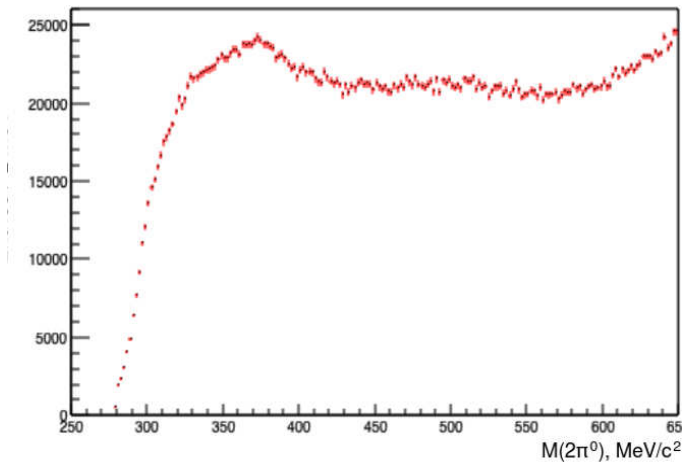


Figure 7: Very preliminary plot of invariant mass of two charged pions (by A. Schick)

## 6 Conclusion

In the summer of 2022 at Jefferson Lab in Hall D, the CPP experiment has been successfully conducted. Simultaneously the NPP experiment has been collecting the data. 106B triggers have been collected on lead-208 target, 23B triggers have been collected on empty target for out of target background subtraction. As a test of data quality, distributions for various kinematic variables (in particular, for the invariant mass of two photons) have been plotted. The collected distributions have the expected shape, indicating good quality of the data. The calibration and further analysis are currently ongoing.

## References

- [1] U. Burgi, Nucl. Phys. B. **479**, 392 (1996).
- [2] J. Gasser *et al.*, Nucl. Phys. B. **745**, 84 (2006).
- [3] B. Pasquini, D. Drechsel, and S. Scherer, Phys. Rev. C **77**, 065211 (2008).
- [4] B. Babusci *et al.*, Phys. Lett. B **277**, 158 (1992).
- [5] S. Belucci, J. Gasser, and M. Sainio, Nucl. Phys. B **423**, 80 (1994).
- [6] J. Gasser and H. Leutwyler, Ann. Phys. **158**, 142 (1984).
- [7] K. Engel, H. Patel, and M. Ramsey-Musolf, Phys. Rev. D **86**, 037502 (2012).
- [8] B. Abi *et al.*, Phys. Rev. Lett. **126**, 141801 (2021).
- [9] C. Adolph *et al.*, Phys. Rev. Lett. **114**, 1 (2015).
- [10] J. Boyer *et al.*, Phys. Rev. D **42**, 1350 (1990).
- [11] J. Ahrens *et al.*, Eur. Phys. J A **23**, 113 (2005).
- [12] A. Kaloshin and V. Serebryakov, Phys. Lett. B **278**, 198 (1992).
- [13] H. Marsiske *et al.*, Phys. Rev. D. **41**, 3324 (1990).
- [14] H. Gevorkyan *et al.*, Rhys. Rev. C **105**, 065202 (2022).
- [15] L. Fil'kov and V. Kashevarov, Phys. Rev. C. **73**, 035210 (2006).

- [16] A. Aleksejev *et al.*, [https://www.jlab.org/exp\\_prog/proposals/13/PR12-13-003.pdf](https://www.jlab.org/exp_prog/proposals/13/PR12-13-003.pdf) (2013).
- [17] L. Y. Dai and M. R. Pennington, *Phys. Rev. D* **94**, 1 (2016).
- [18] S. Adhikari *et al.*, *Nucl.Instrum. & Meth. A* **987**, 1 (2021).
- [19] P. M. Eugenio, Technical Report GlueX-doc-4023, Jefferson Lab (2019).

**INTRODUCTION TO PHYSICS OF ATOMIC NUCLEI.  
I. NUCLEUS AS A SYSTEM OF NONRELATIVISTIC  
NUCLEONS**

**Eugene G. Drukarev  
Petersburg Nuclear Physics Institute of NRC “KI”, Gatchina**

Abstract

We present the main points of the nowadays knowledge of physics of atomic nuclei without running for technical details. The lectures consist of three Parts. In Part I we consider the nucleus as a system of nonrelativistic nucleons. In Part II we consider the nucleus as a relativistic system. In Part III we discuss the approaches based on quantum chromodynamics.

*From editor:*

*Unfortunately, Eugene Grigorievich Drukarev passed away before preparation for publication of these lectures was completed. However the already existing Part I may be interesting for the readers. Therefore we decided to publish the text in the School Proceedings.*

# ВВЕДЕНИЕ В ФИЗИКУ ЯДРА. I. ЯДРО КАК СИСТЕМА НЕРЕЛЯТИВИСТСКИХ НУКЛОНОВ

Евгений Г. Друкарев

Петербургский институт ядерной физики НИЦ «КИ», Гатчина

## Аннотация

Мы изложим основные положения современных знаний по физике атомных ядер, не вдаваясь в технические подробности. Лекции состоят из трех частей. В Части I мы рассматриваем ядро как систему нерелятивистских нуклонов. В Части II мы рассматриваем ядро как релятивистскую систему. В Части III мы обсуждаем подходы, основанные на квантовой хромодинамике.

*От редактора:*

*К сожалению, Евгений Григорьевич Друкарев покинул нас до завершения подготовки публикации лекций. Однако уже существующая Часть I может быть интересна читателям. Поэтому мы решили опубликовать текст в Трудах Школы.*

# 1 Introduction

## 1.1 The contents of the lecture

The lecture is addressed to the people who know very little about the physics of atomic nuclei but want to have a general view. Thus we present the main points of the nowadays knowledge of the subject without running for technical details. We also say very little about the experimental methods, just reporting the main experimental data.

In early thirties of the XX century the people realized that the atomic nucleus consists of protons and neutrons. This was just several years after the equations of quantum mechanics were written down. The theory of nucleus developed together with the progress of theoretical physics. The nowadays knowledge consists of the results obtained in framework of nonrelativistic and relativistic quantum mechanics, combined with some aspects of the field theory and includes the results based on the quantum chromodynamics (QCD). We try to present the main points.

In Part I, we consider the nucleus as a nonrelativistic system. The  $R \sim A^{1/3}$  dependence of the nucleon radius  $R$  on the number of nucleons  $A$  lead to conclusion of that the nucleon density does not depend on  $A$  and is constant inside the nuclei. This provided a qualitative picture of the nucleons in nuclei. The observed structure of the energy levels analogous to that of an atom prompted the possibility of single-particle description of nucleon in the nucleus with the rest  $A - 1$  nucleons (the core) treated as a source of the field described by potential  $U(r)$ . The small values of the nucleon kinetic energies stimulated further analysis by employing the nonrelativistic wave equation. Calculations with simple well potential provided the shell structure of nuclear levels and explained the existence of most stable magic nuclei.

Much further progress was achieved in framework of the nonrelativistic approximation. The theory of the nonspherical nuclei was built. The quadrupole moments were calculated. The rotating spectrum was obtained.

In the next step interaction of the nucleon in nucleus was expressed in terms of NN interactions. The latter was extracted from experimental data on the NN interaction. It was understood that at large distances the NN interaction is determined by the one-pion exchange. However the self-consistent calculations for heavier nuclei contained uncertainties due to large role of small internucleon distances where the quark structure of the nucleons becomes important. Also, the phenomenological expression for the LS interaction was employed to obtain the quantitative results.

The attempt to find the lowest order relativistic corrections to the energies of nuclear levels, i.e. the spin-orbit (LS) splitting, in the way analogous the one used in atomic physics was unsuccessful. The calculations provided the wrong sign of the effect and undershoot the absolute value of the observed LS splitting by an order of magnitude. This stimulated to apply the relativistic approach.

In Part II, we present the relativistic view on the problem. Large progress was obtained by employing the Dirac wave equation for description of nucleon in nucleus. The nucleon can be considered as moving in superposition of vector and scalar fields  $V$  and  $S$ . These fields were found to be of about several hundred MeV (recall that the nucleon mass is  $m \approx 940$  MeV). The fields compensate each other to large extent leading to the potential energy of about -60 MeV. The operator of kinetic energy appeared to be more complicated than in nonrelativistic case. The relativistic approach provided proper value of the LS splitting.

In the Walecka model, the scalar and vector fields were considered as due to exchange by mesons with the corresponding quantum numbers. Equations of the model have been solved in the mean field approximation. The couplings of the vector and scalar mesons to the nucleons can be considered as free parameters. They can be fixed by fixing the observed values of saturation density and of the binding energies in nuclear matter. The saturation of nuclear matter is a relativistic effect in this approach. It is caused by the difference in values of densities of the vector and scalar fields.

The scalar-vector approach has its weak points. The observed vector mesons have the masses of the order 700 MeV which are close to the nucleon masses. Thus we expect the vector mesons to be of the same size as the nucleons and it does not look to be sufficient to calculate the meson exchanges between the nucleons. In other words, the radiative corrections to the lowest order contributions are expected to be important. On the other hand, the radiative corrections have ultraviolet divergences. Thus we face the problem of small distances between the nucleons. Also, the effective scalar interaction includes the two-pion exchanges between the nucleons. Here we again come to the problem of small distances.

In part III, we consider the QCD motivated approaches to the physics of nuclei. The consistent calculation of pion-nucleon interaction can be carried out by employing the chiral low energy pion-nucleon Lagrangian (ChL). The ideas of chirality come from the particle physics. The ChL enables to calculate the scalar part of the nucleon interaction. Another important point is that it enables to trace the density dependence of the scalar quark condensate

$\langle M|\bar{q}q|M\rangle$  which characterizes the chirality symmetry breaking effects. The evaluation of this condensate as well as that of the nucleon axial coupling constant confirms the tendency to restoration of the chiral symmetry at larger densities. Another approach, based on dispersion relations, known as the QCD sum rules is also discussed.

## 1.2 Parameters and structure of free nucleons

The QCD describes the nucleons as the lightest systems of three light quarks surrounded by the sea of quark–antiquark pairs [1]. The proton consists of two  $u$  quarks with the electric charges  $2e/3$  (the electron charge is  $-e$  with  $e = \alpha^{1/2}$  while  $\alpha \approx 1/137$  is the fine structure constant) and one  $d$  quark with the charge  $-e/3$ . The neutron has the structure (ddu). This insures the proton charge  $z_p = e$  while the neutron charge is  $z_n = 0$ .

Sixty years ago the nucleons were viewed as the structurless elementary particles. Large part of the knowledge about the atomic nuclei, described in Part I of our lecture is based on this picture. However we shall see that view provided by quantum chromodynamics (QCD) appears to be useful even in nonrelativistic physics of nuclei.

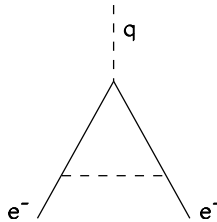


Figure 1: The Feynman diagram describing the leading order electron anomalous magnetic moment. The solid lines stand for electron. The dashed line denotes photon.

The proton radius can be found from experiments on the elastic  $ep$  scattering at fixed values of three dimensional momentum  $\mathbf{q}$  transferred to the proton – Fig. 1. The angular distribution is determined by the squared amplitude  $|M(q)|^2$

$$\frac{d\sigma}{d\Omega} \sim |M(q)|^2.$$

The amplitude can be written as  $M(q) = M_0(q)F(q)$  with  $M_0(q) = 4\pi\alpha/q^2$ ,

the amplitude of electron scattering on the point-like proton while

$$F(q) = \int d^3r \rho(\mathbf{r}) e^{-i\mathbf{q}\mathbf{r}}.$$

Here  $\rho(\mathbf{r}) = \rho(r)$  is the density of the charge distribution inside the proton,  $\int d^3r \rho(r) = 1$ . For the point proton  $\int d^3r \rho(\mathbf{r}) = 1$ , and  $M(q) = M_0(q)$ . At small values of  $qr \ll 1$  we find

$$F(q) = 1 - \frac{q^2 \langle p|r^2|p \rangle}{6},$$

with  $\langle p|r^2|p \rangle = \int d^3r \rho(r) r^2$ . The value

$$r_E = (\langle p|r^2|p \rangle)^{1/2} = 0.86 \text{ fm} \quad (1)$$

is called the proton charge radius. It is often assumed to be the size of the proton.

The values of the proton and neutron masses are very close. The mass of the neutron is  $m_n = 939.57 \text{ MeV}/c^2$  while that of the proton is  $m_p = 938.27 \text{ MeV}/c^2$ . The free neutron is unstable and transfers to the proton, positron and electron antineutrino via the beta decay



The neutron half-life is about 14.7 minutes. In the Standard model the proton is stable. However in some of the theories going beyond the Standard model the proton is also unstable. Anyway, the experimental data require that the proton half life is more than  $10^{31}$  years. Hence, we assume the proton to be stable.

The potential energy of the proton at rest in the time-independent magnetic field  $\mathbf{H}$  is (we employ the system of units with  $\hbar = 1$ )  $U_H = -\boldsymbol{\mu}_p \mathbf{H}$  (we omitted the terms of the order  $H^2$ ), with  $\boldsymbol{\mu}_p$  the proton magnetic moment. In nonrelativistic quantum mechanics this term is introduced “by hands” and one can attribute any value to  $\boldsymbol{\mu}_p$ . The proton and neutron are the fermions, carrying the spin  $s = 1/2$ . Thus one could expect that nucleon can be described by the relativistic (Dirac) equation which determines the operator of magnetic moment. The latter is related to the spin operator  $\mathbf{s}$ . The Dirac value for the proton magnetic moment is  $\boldsymbol{\mu}_p^D = (e/m_p)\mathbf{s}$  with  $\mathbf{s} = \boldsymbol{\sigma}/2$  while  $\boldsymbol{\sigma}$  are the Pauli matrices. For neutron, as for any neutral fermion  $\boldsymbol{\mu}_n^D = 0$  since the static magnetic field interacts only with moving charges.

However the experiments carried out in 1933 provided [2,3]

$$\mu_p = 2.79\mu_p^D. \quad (3)$$

The standard notation is  $\mu_p = \mu_p^D + \mu_p^{an}$  where  $\mu_p^{an} = 1.79\mu_p^D$  is called the anomalous part. This was a surprise result. However the data on the neutron magnetic moment obtained a year later [4,5] were still more surprising. The experiments provided

$$\mu_n = -1.91\mu_p^D, \quad (4)$$

with all magnetic momentum being its anomalous part.

The steps to solve the puzzle were made about 15 years later when it was found that the electron magnetic momentum also has an anomalous part [6]. The experiments provided  $\mu_e^{an} = 1.16 \cdot 10^{-3}\mu_e^D$ . The result was immediately explained in terms of recently formulated quantum electrodynamics. The Dirac part of the electron magnetic moment comes from direct interaction of the electron with the magnetic field. However the electron can radiate a photon before interacting with the field. The photon is absorbed after the interaction takes place – see Fig. 1. The mechanism is described by a nice formula

$$\mu_e^{an} = \alpha/(2\pi) \cdot \mu_e^D [7].$$

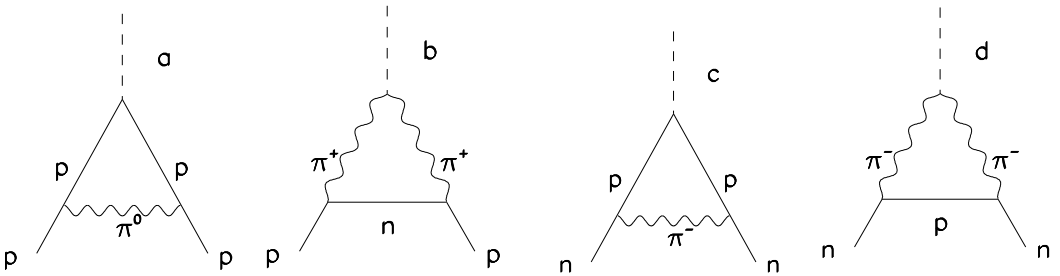


Figure 2: The Feynman diagrams describing leading order contributions anomalous magnetic moments of proton (a,b) and neutron (c,d). The solid lines stand for nucleons. The dashed line denotes photon. The wavy line is for pions. Only the nucleon intermediate states are shown.

In an attempt to explain the origin of the nucleon anomalous magnetic moments in similar way one can include the radiation and absorption of a  $\pi$  meson by the nucleon while interaction with the magnetic field takes place between these events – see Fig. 2. The neutron anomalous magnetic momentum is not a surprise any more due to the reaction  $n \rightarrow p + \pi^- \rightarrow n$ , with the intermediate state proton and pion interacting with the magnetic field. Direct calculations reproduced the nucleon magnetic moments with the errors of about

20 percent [8]. The role of the heavier hadron intermediate states is obscure. Thus the hadron language results are not reliable. The accurate values of the nucleon anomalous magnetic moments were obtained in framework of QCD.

There are the positive and negative charges inside the neutron. One can view the neutron as a system of the charges  $ez$  and  $-ez$  separated by distance  $x$  and the modulus of the dipole moment is  $|d_n| = e^2 z^2 x$ . Electric dipole moment can be written as  $\mathbf{d}_n = e\langle \mathbf{r} \rangle$  with the last factor being the expectation value of  $\mathbf{r}$  in neutron. One can see that  $d_n$  obtains a nonzero value only if the spacial parity ( $P$ ) is violated. A more detailed analysis demonstrates that the time reversal symmetry also should be violated. The latest experiments provide  $|d_n| < 3 \cdot 10^{-26} e \text{ cm}$ , i.e. very small on the nuclear scale.

### 1.3 Notations and definitions. Stability of nuclei

Usually the number of the protons in nuclei is denoted as  $Z$ . It is called also the atomic number. The number of neutrons is  $N$ . The total number of nucleons  $A = Z + N$  is called the mass number. The standard notation of the nuclei  $X$  is  ${}^A_Z X$  or just  ${}^A X$ . The nuclei with the same numbers of  $Z$  but with different values of  $N$  are called the isotopes. For example the nucleus  ${}^4_2 \text{He}$  is the main isotope of helium, while  ${}^3_2 \text{He}$  is helium-3. The nuclei with the same numbers of  $A$  but with different compositions of  $N$  and  $Z$  are called the isobars. Also, the nucleus with  $Z$  protons and  $N$  neutrons and that with  $Z$  neutrons and  $N$  protons are the mirror nuclei (making a special case of isobars). The nuclei of  ${}^3_2 \text{He}$  and that of tritium  ${}^3_1 \text{H}$  provide an example. There are about 3500 stable

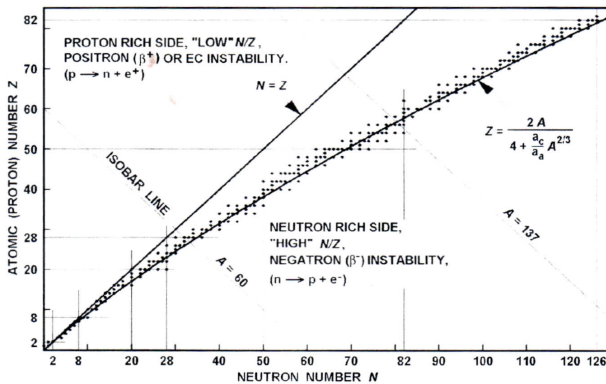


Figure 3: Region of stability of nucleons. The little squares denote the stable nucleons

nuclei. In the  $(N, Z)$  plane (see Fig. 3) they are grouped mostly a little bit below the line  $N = Z$ , having thus a small neutron excess. The symmetry parameter

$$\alpha_A = \frac{N - Z}{A} \quad (5)$$

is small enough in real nuclei,  $|\alpha_A| \ll 1$ . In neutron-rich nuclei with larger numbers of  $N$  the neutrons undergo  $\beta^-$  decay. In the proton-rich nuclei  $\beta^+$  decay of the proton takes place. Thus the  $\beta^+$  decay

$$p \rightarrow n + e^+ + \nu_e \quad (6)$$

becomes possible. Also, the heavy nuclei with large proton excess decay into a lighter nuclei and  $\alpha$  particle (the nuclei  ${}^4_2\text{He}$ ). For example,  ${}^{238}_{94}\text{Pu}$  decays to the nuclei  ${}^{234}_{92}\text{U}$  and  ${}^4_2\text{He}$ .

The nuclei with atomic number  $Z \leq 92$  ( $Z = 92$  corresponds to uranium) can be found in nature. Some of the nuclei with the larger atomic number can be created in laboratories (there were reports about some traces of the nuclei with  $Z = 93, 94$  in nature as well). The half life of these nuclei decreases with  $Z$  very fast. Being  $4.47 \cdot 10^9$  years for  $Z = 92$  it is 900 years for  $Z = 98$ . It is 100 days for  $Z = 100$ , 1 minute for  $Z = 107$  and  $10^{-3}$  seconds for  $Z = 118$ . There are also some theoretical speculations about the "islands of stability" – the values of large  $Z$  and  $N$  for which the half life can become larger. The most attention is devoted to the nuclei with  $Z = 114$ ,  $N = 184$ . These are the magic numbers of the shell model (see Chapter 2). The other possible islands of stability are at  $Z$  close to 126 and 164.

At  $Z \approx 170$  one finds new physics connected with quantum electrodynamics. In the limit of point-like nucleus the electron energy in the ground ( $1s$ ) state of the Dirac equation is  $\varepsilon(Z) = m_e(1 - \alpha^2 Z^2)^{1/2}$ , with  $m_e \approx 511$  keV the electron mass. Thus  $\varepsilon(Z) = 0$  at  $Z = 137$ . The nucleus containing 137 protons and the same nucleus binding two  $1s$  electrons (the interaction of the latter can be neglected up to the terms of the order  $1/Z$ ) have the same energy. There is no solution for the point-like nuclei at larger values of  $Z$ . The reason is that the effective Schrödinger equation for the large component of the wave function contains the term  $(3/4 - \alpha^2 Z^2)/2r^2$ . It describes attraction at  $\alpha^2 Z^2 > 3/4$  leading to the "fall on the center" situation at  $(\alpha^2 Z^2 - 3/4)/2 \geq 1/8$  [9], i.e. at  $\alpha^2 Z^2 \geq 1$ . Thus one should include the finite size of the nucleus. This changes the shape of the dependence  $\varepsilon(Z)$  [10]. Starting at  $\varepsilon(0) = m_e$ , the energy decreases with  $Z$ . Unlike the situation with the point nucleus, the curve  $\varepsilon(Z)$  passes smoothly the point where  $\varepsilon(Z) = 0$ . At certain  $Z = Z_c$   $\varepsilon(Z_c) = -m_e$ , and the ground state becomes degenerate. Except the nucleus containing  $Z_c$

protons, there can be two electrons bound in  $1s$  state with energies  $\varepsilon(Z_c) = -m_e$  and (due to the Dirac equation) two positrons at rest. At larger  $Z > Z_c$  the positrons obtain kinetic energies  $|\varepsilon(Z)| - m_e$  and go away being repulsed by the nucleus. Thus the nucleus containing  $Z > Z_c$  protons can exist only with the two bound  $1s$  electrons. It was found in that  $Z_c \approx 170$ .

The neutron stars is a special example of the system with many nucleons. The neutron stars emerge as one of possible scenario of what happens to the star [11] with the mass between 1.3 and 2 solar masses. The star consists of protons and electrons. It is compressed by gravitational forces. The work of these forces increases the kinetic energy of the electrons. When the latter exceed the neutron–proton mass splitting, the inverse beta decay



takes place. The compression is going on since the pressure of the classical nucleon gas cannot balance that of gravity. However that of the Fermi gas can. Finally we come to the equilibrium state of the system consisting mostly of neutrons. A small fraction of protons is needed to prevent the beta decay of neutrons. Thus

$$\alpha_A = \frac{N - Z}{A} \approx 1.$$

The density of the neutron star is close to that in heavy nuclei (see Ch. 2). However, the neutron star cannot be considered as a “giant nuclei” since the neutrons are kept together by gravitational forces but not by the strong interactions.

## 1.4 Isospin invariance

The isospin invariance known also as isotope invariance postulates that proton and neutron are the two states (charged and neutral) of the same particle called nucleon. Thus all strong interactions of proton and neutron are the same. Forgetting for some time about the proton charge, we can replace the states  $|p\rangle$  and  $|n\rangle$  by their linear combinations

$$|p\rangle = a|p'\rangle + b|n'\rangle; \quad |n\rangle = a'|n'\rangle + b'|p'\rangle. \quad (8)$$

Due to normalization condition  $a^2 + b^2 = 1$  and  $a'^2 + b'^2 = 1$ . Also, it is natural to assume that  $|\langle p'|p\rangle|^2 = |\langle n'|n\rangle|^2$  and  $|\langle p'|n\rangle|^2 = |\langle n'|p\rangle|^2$ . Thus  $|a'|^2 = |a|^2$  and  $|b'|^2 = |b|^2$ . The set of parameters, corresponding to rotation in a two-dimensional space  $a' = a^*$  and  $b' = -b^*$  satisfies these conditions.

Thus Eq. (8) can be written in the matrix form. Writing the nucleon wave function as

$$\Psi = \begin{pmatrix} p \\ n \end{pmatrix}, \quad (9)$$

we can present Eq. (8) as

$$\Psi' = U\Psi, \quad (10)$$

with

$$U = \begin{pmatrix} a & b \\ -b^* & a^* \end{pmatrix}. \quad (11)$$

One can see that  $U$  is a unitary matrix  $U = U^\dagger$  with the determinant equal to unity,  $\det U = 1$ . Such matrices form the  $SU(2)$  group.

The  $SU(2)$  transformation corresponding to rotation on the angle  $\omega$  with direction of the axis of rotation  $\mathbf{n}$  is

$$U = e^{ig\omega\boldsymbol{\tau}\cdot\mathbf{n}}, \quad (12)$$

with  $g$  a constant factor, while  $\tau$  are just the Pauli matrices

$$\tau_1 = \begin{pmatrix} 0 & 1 \\ 1 & 0 \end{pmatrix}; \quad \tau_2 = \begin{pmatrix} 0 & -i \\ i & 0 \end{pmatrix}; \quad \tau_3 = \begin{pmatrix} 1 & 0 \\ 0 & -1 \end{pmatrix}. \quad (13)$$

Following this analysis it looks reasonable to attribute a new quantum number  $T = 1/2$  called isospin to the nucleons. The protons have the projection  $T_z = 1/2$  while for neutrons  $T_z = -1/2$ . The notations  $I$  and  $I_z$  for the isospin and for its projection are used quite often.

To demonstrate how the isospin invariance works, consider interactions between nucleons and pions. Recall that there are three  $\pi$  mesons or pions  $\pi^0, \pi^+$  and  $\pi^-$  with very close values of masses. There are four pion-nucleon vertices corresponding to interactions  $p\pi^0p, p\pi^+n, n\pi^-p$  and  $n\pi^0n$ . Suppose, we know nothing about isotope invariance. The Lagrangian density of interaction contains four terms

$$L(x) = \bar{\psi}_p(x)\Gamma^{p\pi^0p}\psi_p(x)\varphi^0(x) + \bar{\psi}_n(x)\Gamma^{p\pi^+n}\psi_p(x)\varphi^+(x) + \\ + \bar{\psi}_p(x)\Gamma^{n\pi^-p}\psi_n(x)\varphi^-(x) + \bar{\psi}_n(x)\Gamma^{n\pi^0n}\psi_n(x)\varphi^0(x),$$

with  $\varphi^0(x)$  and  $\varphi^\pm(x)$  the fields of the neutral and charged pions correspondingly. The matrices  $\Gamma^{p\pi^0p}, \Gamma^{p\pi^+n}, \Gamma^{n\pi^-p}, \Gamma^{n\pi^0n}$  act on Lorentz indices of the proton and neutron bispinors. The second and third terms of the Lagrangian density are equal due to the time invariance. There are three terms of the Lagrangian

density which are quite independent. Even if somehow know, e.g. the first term, we can say nothing about the other ones. Thus one cannot make any predictions on the relative values of three independent vertices of the nucleon-pion interactions.

Assuming that there is the isotope invariance, we can treat the pions as the components of the isovector  $\varphi$  with  $\pi^+$ ,  $\pi^0$  and  $\pi^-$  corresponding to the isospin projections  $T_z = 1, 0, -1$  correspondingly. The Lagrangian density written in isospin invariant way is

$$L(x) = \bar{\Psi}(x)\Gamma(\boldsymbol{\tau} \cdot \boldsymbol{\varphi})\Psi(x), \quad (14)$$

with  $\Gamma$  acting on Lorenz indices of the nucleon bispinors. It is convenient to introduce matrices

$$\tau^+ = \frac{\tau_1 + i\tau_2}{2}; \quad \tau^- = \frac{\tau_1 - i\tau_2}{2}; \quad \tau^0 = \tau_3,$$

i. e.

$$\tau^+ = \begin{pmatrix} 0 & 1 \\ 0 & 0 \end{pmatrix}; \quad \tau^- = \begin{pmatrix} 0 & 0 \\ 1 & 0 \end{pmatrix}; \quad \tau^0 = \begin{pmatrix} 1 & 0 \\ 0 & -1 \end{pmatrix}. \quad (15)$$

In these notations

$$\begin{aligned} \tau^+|n\rangle &= |p\rangle; & \tau^+|p\rangle &= 0; & \tau^-|p\rangle &= |n\rangle; & \tau^-|n\rangle &= 0; \\ \tau^0|p\rangle &= |p\rangle; & \tau^0|n\rangle &= -|n\rangle. \end{aligned} \quad (16)$$

Thus

$$\begin{aligned} L(x) &= \bar{\psi}_p(x)\Gamma\psi_p(x)\varphi^0(x) + \sqrt{2}\bar{\psi}_n(x)\Gamma\psi_p(x)\varphi^+(x) + \\ &+ \sqrt{2}\bar{\psi}_p(x)\Gamma\psi_n(x)\varphi^-(x) - \bar{\psi}_n(x)\Gamma\psi_n(x)\varphi^0(x). \end{aligned} \quad (17)$$

Thus all vertices of the nucleon pion interactions  $\Gamma^{p\pi^0 p}$ ,  $\Gamma^{n\pi^+ p}$ ,  $\Gamma^{p\pi^- n}$  and  $\Gamma^{n\pi^0 n}$  can be expressed in terms of one of them, e.g

$$\Gamma^{n\pi^+ p} = \Gamma^{p\pi^- n} = \sqrt{2}\Gamma^{p\pi^0 p}, \quad \Gamma^{n\pi^0 n} = -\Gamma^{p\pi^0 p}. \quad (18)$$

The isospin invariance is one of the key ideas of particle and nuclear physics. It was introduced by Heizenberg in 1932.

During several decades there was a general belief that the isospin invariance is an exact symmetry and that the small neutron-proton mass splitting is caused by electromagnetic interactions. At least in framework of QCD this is not true. Electromagnetic interactions of the three valence quarks in nucleon make proton

heavier than neutron by 0.7 MeV [12]. Thus the strong interactions contribute 2 MeV to the neutron-proton mass splitting. In QCD, the isospin symmetry breaking effects manifest themselves in different values of the scalar condensates of light quarks with  $|(\langle 0|\bar{u}u|0\rangle - \langle 0|\bar{d}d|0\rangle)/(\langle 0|\bar{u}u|0\rangle + \langle 0|\bar{d}d|0\rangle)| \sim 2 \cdot 10^{-3}$ . Of course, large relative difference between the light quark current masses  $m_u \approx 4$  MeV,  $m_d \approx 7$  MeV, corresponds to isospin symmetry breaking by about 30 percent. However, since the current masses are small on the particle physics and nuclear physics scale, it is difficult to observe this 30 percent effect directly.

In physics of nuclei the isospin symmetry breaking manifests itself in difference between the masses of the mirror nuclei which remains after the electromagnetic effects are included. The difference increases with  $A$  reaching 0.9 keV for  $A = 208$ . This is known as the Nollen–Schiffer anomaly [13].

The invariance under transformation expressed by Eq. (12) is called the global invariance since it corresponds to the same rotations in  $(p, n)$  plane in all space-time points  $x$ . It can be generalized by allowing independent rotations at each point  $x$ , i.e. the invariance under transformations

$$U = e^{ig(x)\omega\mathbf{T}\cdot\mathbf{n}}. \quad (19)$$

Unlike Eq. (12)  $g$  is a function of  $x$  now. This is called the local isotope invariance. The consequence of the local isospin invariance for physics of nuclei is discussed in Part III.

## PART I

### NUCLEUS AS A NONRELATIVISTIC SYSTEM

## 2 Qualitative picture of a heavy nucleus

### 2.1 The $A$ dependence of the size of heavy nucleus

The scattering of high energy electrons on the nuclei provides the data on the size of the latter. The results combined with those obtained by other methods (see, e.g. [14]) give the dependence of nucleon size on the total number of nucleons  $A$ . Assuming that the nuclei have spherical shapes, one finds that for sufficiently large  $A > 20$  the radius of a nucleus is

$$R_0 = r_0 A^{1/3}, \quad (20)$$

with  $r_0 = 1.25$  fm. Here the lower index in notation  $R_0$  means that we assumed spherical shape of the nucleus. This equation provides a qualitative picture of a nuclei with  $A > 20$ . We shall call them the “heavy nuclei”.

Employing Eq. (20) we find that the volume of spherical nucleus containing  $A$  nucleons is

$$V(A) = V_0 A, \quad (21)$$

with

$$V_0 = \frac{4}{3}\pi r_0^3 \approx (2\text{fm})^3. \quad (22)$$

Thus the nucleon volume is proportional to the number of nucleons  $A$ . What happens to the nuclei with the mass number  $A$  when we add one nucleon? One can see that additional nucleon just adds its volume  $V_0$  to the total volume  $V(A)$ . The density

$$\rho_0 = \frac{A}{V(A)} = \left(\frac{4}{3}\pi r_0^3\right)^{-1} \quad (23)$$

remains the same. Numerically

$$\rho_0 = 0.17\text{fm}^{-3}. \quad (24)$$

Note also that the nucleons undergo the short range interaction. It becomes much weaker when the distance between the nucleons exceeds 2 fm.

This leads to several consequences. Since the distance between the nucleons is about 2 fm, each of them interacts only with several closest neighbors. Also, strictly speaking the nucleon density depends on the distance  $r$  from the center of mass of the nuclei. However all the nucleons except those at the surface are in similar position. Hence they are distributed with uniform density inside the nucleus, where  $\rho(r) = \rho_0$  with  $\rho_0$  expressed by Eq. (24).

The liquid drop model treats nucleus as incompressible system of high density. Such view enables to obtain several quantitative relations.

## 2.2 The Weizsäcker formula

The work which should be carried out for total disintegration of the nucleus consisting of  $Z$  protons and  $N$  neutrons is called its binding energy  $\varepsilon_B > 0$ . Thus the binding energy of such nucleus can be expressed as  $\varepsilon_B = m_p Z + m_n N - m(Z, N)$ , with  $m(Z, N)$  the mass of the nucleus. Now we try to express  $\varepsilon_B$  as a function of  $Z$  and the total number of nucleons  $A = Z + N$ . Recall that we deal with large number of nucleons  $A \gg 1$ .

We can predict at least four ingredients of the expression for  $\varepsilon_B$ . Each of the nucleons interacts only with several neighbors. In other words it interacts

with a constant number of nucleons independent of  $A$ . Thus the energy of each nucleon does not depend on  $A$ . Hence, the total energy is proportional to  $A$ . It is called the volume energy  $\varepsilon_V$  since the volume of a nucleus is proportional to  $A$ .

The nucleons on the surface of the nucleus have smaller number of nearest neighbors than those which are deep within the nucleus. This can manifest itself in a correction to the volume energy which is called the surface energy  $\varepsilon_{sur}$ . Since the square of the sphere is proportional to  $R^2 \sim A^{2/3}$ , we can guess that  $\varepsilon_{sur} \sim A^{2/3}$ .

Another contribution  $\varepsilon_C$  ( $C$  stands for Coulomb) is caused by the electrostatic interactions between the protons. Each of the protons interacts with all the other ones. There are  $Z(Z - 1)/2$  independent pairs of protons in the nucleus. Since the size of the nucleus is proportional to  $A^{1/3}$ ,  $\varepsilon_C$  is proportional to  $Z^2/A^{1/3}$ .

The fourth contribution reflects the phenomenological fact that the stable nuclei are located close to the line  $N = Z$  in the  $(N, Z)$  plane (see Sec. 2 of Introduction and Fig. 3 ). Thus the binding energy can be expanded in powers of  $(N - Z)/A$ . Due to isotope invariance only the even terms of the expansion contribute. Since  $|N - Z|/A \ll 1$  we include only the quadratic term of the expansion. The corresponding contribution is called the symmetry energy. It is denoted as  $\varepsilon_{sym}$ . One can see that  $\varepsilon_{sym} \sim (N - Z)^2/A^2$ .

Thus we can write

$$\varepsilon_B = \varepsilon_V + \varepsilon_{sur} + \varepsilon_C + \varepsilon_{sym}. \quad (25)$$

or

$$\varepsilon_B = a_1 A - a_2 A^{2/3} - a_3 Z^2/A^{1/3} - a_4 (N - Z)^2/A, \quad (26)$$

with the coefficients  $a_i > 0$  ( $i = 1, \dots, 4$ ). This expression is known as the Weizsäcker formula [15]. Now we explain the signs on the right-hand side of Eq. (26).

Due to definition of the binding energy the potential energies corresponding to the first three terms on the right-hand side of Eq. (26) are

$$U_i = -\varepsilon_i. \quad (27)$$

The volume potential energy corresponds to attractive forces. Thus  $U_V < 0$  and  $a_1 > 0$ . The surface energy diminishes the contribution of the volume energy. Hence  $a_2 > 0$ . Since  $U_C > 0$  we find  $a_3 > 0$ . Note that these results are obtained in framework of classical physics, without applying the quantum mechanics.

However, to predict the sign of  $a_4$  we must recall the Pauli principle of quantum mechanics. The nucleons occupy the states with momenta  $p_p$  and  $p_n$  limited by conditions  $p \leq p_{Fp}$  and  $p \leq p_{Fn}$  with  $p_{Fp,n}$  the values of the Fermi momenta. Thus the kinetic energy of the nucleons can be written as  $E_{\text{kin}} = 3/5(\rho_p p_{Fp}^2/2m + \rho_n p_{Fn}^2/2m)$ . As we shall see in next chapter,  $p_{Fi}^2 \sim \rho_i^{2/3}$  ( $i = p, n$ ). Thus  $E_{\text{kin}}$  is proportional to the sum  $\rho_p^{5/3} + \rho_n^{5/3}$ . Adding the potential energies  $U_i$  we find that  $-\varepsilon_B = E_{\text{kin}} + U_p + U_n$ . Presenting  $E_{\text{kin}}$  in terms of  $\rho_p + \rho_n$  and  $\rho_p - \rho_n$  we find that it reaches its minimal value at  $\rho_p = \rho_n$  for the fixed value of  $\rho_p + \rho_n$  (i.e. for fixed value of  $A$ ). As to the potential energy, note that the main contribution to wave function of two nucleons comes from configurations in which the space part is given by  $s$  wave. Otherwise the function is dominated by larger distances where the strong interaction becomes smaller. Thus the wave function of two nucleons is mostly space symmetric. In the case of two protons and two neutrons the wave function is isospin symmetric and only the single spin asymmetric state is available. The system consisting of proton and neutron ( $T_z = 0$ ) can be either in symmetric or asymmetric isospin states. We have just more possible states if the two nucleons are proton and neutron. Thus the nuclei with  $N = Z$  nuclei bound stronger. Hence, the contribution of  $\varepsilon_{\text{sym}}$  to the binding energy obtains its largest value at  $\rho_p = \rho_n$ , i.e. at  $N = Z$ .

The values of coefficients obtained by fitting the observable masses of heavy nuclei are [16]

$$a_1 = 15.78 \text{ MeV}; \quad a_2 = 17.90 \text{ MeV}; \quad a_3 = 0.724 \text{ MeV}; \quad a_4 = 23.72 \text{ MeV}. \quad (28)$$

The evaluation of the dependence  $\varepsilon_B(A)$  with successive inclusion of the terms on the right hand side of Eq. (26) is illustrated by Fig. 4.

The value of the Coulomb energy  $\varepsilon_C$  can be calculated assuming that the electric charge is carried by protons distributed uniformly in the nucleus. The density of the electric charge is thus

$$\rho^C(r) = \rho_0^C \cdot \theta(R - r), \quad (29)$$

with  $\rho_0^C = eZ/V$ , while  $V = 4\pi/3 \times R^3$  is the volume of the nucleus. The energy of the electrostatic field is

$$U_C^{(0)} = \frac{1}{8\pi} \int d^3x E^2(x),$$

with  $\mathbf{E}$  the strength of the electrostatic field. The upper index (0) denotes the energy related to the spherical nuclei (see next Subsection). One can write

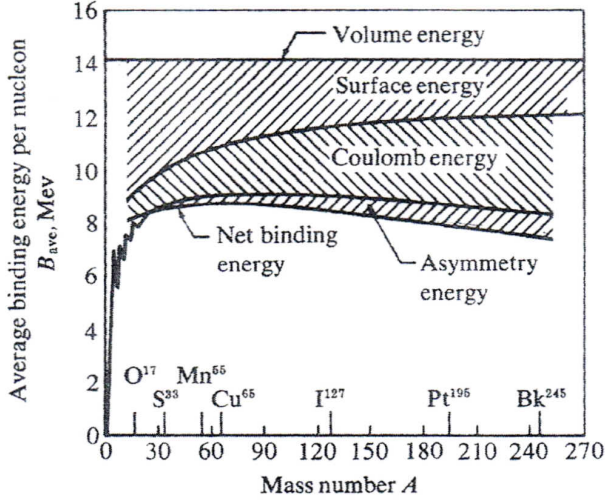


Figure 4: Evaluation of the dependence  $\varepsilon_B(A)$  with successive inclusion of the terms in the right-hand side of Eq. (26)

$\mathbf{E} = -\nabla\varphi$  with

$$\varphi(r) = \int d^3x \frac{\rho^C(x)}{|\mathbf{r} - \mathbf{x}|}, \quad (30)$$

the potential of the field. Calculating

$$\varphi(r) = \frac{eZ}{r}; \quad r \geq R, \quad (31)$$

$$\varphi(r) = \frac{eZ}{2R} \left( 3 - \frac{r^2}{R^2} \right); \quad r \leq R,$$

we find

$$U_C^{(0)} = \frac{3e^2 Z^2}{5R} = \frac{3e^2 Z^2}{5r_0 A^{1/3}}.$$

Thus in this approach

$$a_3 = \frac{3e^2}{5r_0}. \quad (32)$$

For  $r_0 = 1.25 \text{ fm}^{-1}$  we find  $a_3 = 0.692 \text{ MeV}$ . This is very close to the value provided by Eq. (28).

In theory of liquids the surface energy is usually presented as

$$U_{\text{sur}}^{(0)} = \sigma S, \quad (33)$$

with  $\sigma$  called the tension coefficient while  $S = 4\pi R^2$  is the surface of the drop. Thus the nuclear tension can be defined as

$$\sigma = a_2/(4\pi r_0^2). \quad (34)$$

The energy per nucleon provided by Eq. (26) is

$$B(A) \equiv \frac{\varepsilon_B}{A} = a_1 - a_2A^{-1/3} - a_3Z^2/A^{4/3} - a_4(N - Z)^2/A^2. \quad (35)$$

Neglecting the Coulomb energy presented by the third term we would find  $B \rightarrow a_1$  at  $A \rightarrow \infty$ . However, since  $Z \approx A/2$ , the Coulomb energy increases as  $A^{2/3}$  at large  $A$ . Thus the energy  $B(A)$  increases at small values of  $A$ , reaching the largest values at  $A \approx 56$ . It experience a slow drop for heavier nuclei – see Fig. 5. One can assume that for  $A > 60$  the binding energy per nucleon does not depend on  $A$  with  $B \approx 8.3$  MeV. The three mostly tied nuclei are

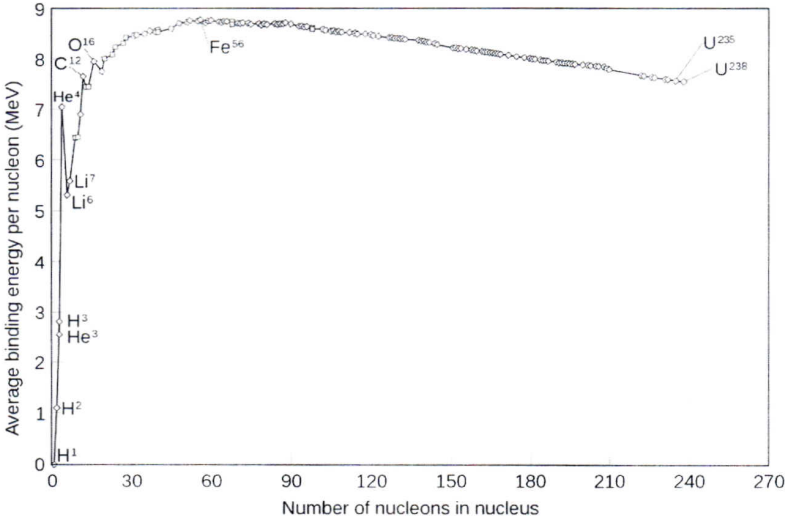
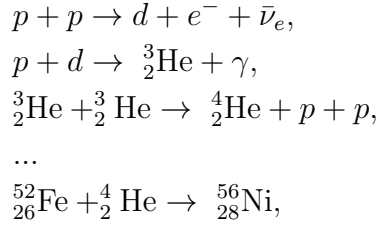


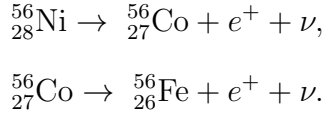
Figure 5: Binding energy per nucleon  $B(A)$  as a function of the atomic number  $A$

$^{56}\text{Fe}$  ( $Z = 26$ ),  $^{58}\text{Fe}$  ( $Z = 26$ ), and  $^{62}\text{Ni}$  ( $Z = 28$ ). Their binding energies per nucleon are  $B = 8790.35$  keV,  $B = 8792.25$  keV and  $B = 8794.53$  keV correspondingly [17,18]. The nuclei  $^{56}\text{Fe}$  are formed in the final step of stellar

nuclear fusion reactions



with the nucleus  ${}^{56}_{28}\text{Ni}$  unstable to  $\beta^+$  decay. Thus in the next chain [19]



The nuclei of nickel  ${}^{62}_{28}\text{Ni}$  cannot be produced in this chain since such process requires several additional neutrons. One cannot find them in the stars [20]. Hence  ${}^{56}_{26}\text{Fe}$  is the end product of the stellar nuclear burning process. This explains why the abundance of  ${}^{56}_{26}\text{Fe}$  is higher than that of  ${}^{62}_{28}\text{Ni}$  although the latter is bound more tightly. The iron fusion is the final step of evolution of the stars with the masses larger than about 10 solar masses [20].

Note that Eq. (35) for the binding energy per nucleon presents a smooth dependence of  $B$  on  $A$  resented by Fig. 5. However the experimental dependence  $\varepsilon_B(A)$  experience jumps. They can be described by inclusion of the fifth term on the right hand sides of Eqs. (25), (26) and (35) [21]. Unlike the other contributions it is of purely quantum mechanical origin, being based on the Pauli principle. The binding energy becomes larger if the number of protons or neutrons is even. We explained earlier that the main contribution to wave function of two nucleons comes from configurations in which the space part is given by  $s$  wave. Thus two nucleons with the same projection of isospin (two protons or two neutrons) have the largest energy of interaction if they form spin asymmetric state, with spin projections having the opposite directions. Thus we can assume that there is additional attractive interaction between two nucleons of the same type (in other words, with same projections of isospin). This causes additional contribution to the right hand side of Eq. (25) called the pairing term. Now we have

$$\varepsilon_B = \varepsilon_V + \varepsilon_{\text{sur}} + \varepsilon_C + \varepsilon_{\text{sym}} + \varepsilon_{\text{pair}}, \quad (36)$$

with

$$\varepsilon_{\text{pair}} = \delta \cdot \kappa; \quad \delta > 0; \quad \kappa = \left( (-1)^N + (-1)^Z \right) / 2 \quad (37)$$

In other words  $\varepsilon_{\text{pair}} = \delta$  if both  $Z$  and  $N$  are even (even–even nuclei),  $\varepsilon_{\text{pair}} = -\delta$  if both  $Z$  and  $N$  are odd (odd–odd nuclei),  $\varepsilon_{\text{pair}} = 0$  if  $A$  is odd. To fit the experimental data we must assume that  $\delta$  decreases slowly with  $A$ . The usual parametrization is

$$\delta = a_5/A^{1/2},$$

with the value  $a_5 = 11$  MeV provided in [16]. Sometimes the parametrization  $\delta = a_5/A^{3/4}$  with  $a_5 \approx 34$  is also employed [14]. Expression (36) for the binding energy is often called the Bethe–Weizsäcker formula.

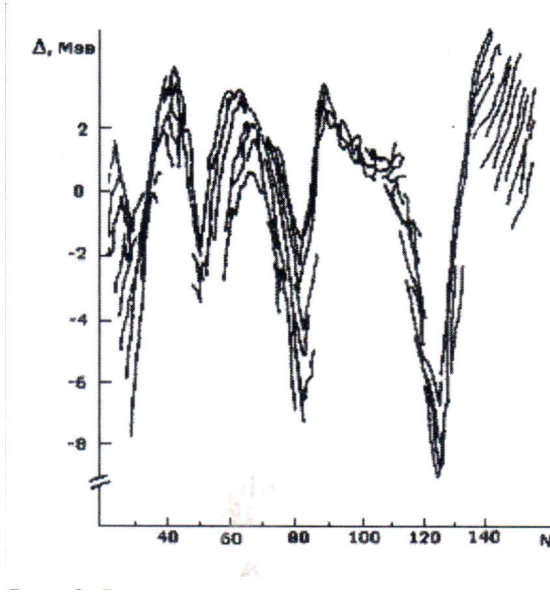


Figure 6: Deviations between the binding energy of nuclei provided by Eq. (36) and the observed value as a function of the number of neutrons in nucleus. Dependence on the number of protons has similar shape

Expression given by Eq. (36) reproduces the binding energy  $\varepsilon_B$  with the error which does not exceed 10 MeV – see Fig. 6. The largest deviations between the experimental data and predictions of Eq. (36) take place for magic number of neutrons. The average energy per nucleon is reproduced with the accuracy of about 1%.

### 2.3 Lines of stability

The Weizsäcker formula provides constraints on possible values of  $A$ ,  $N$  and  $Z$  for stable nuclei. We can find also the value of  $N$  to  $Z$  ratio for which the

binding energy reaches its largest value at fixed value of  $A$ . This determines the center of the region of stability. We replace  $N = A - Z$  in the last term on the right hand side of Eq. (26). Calculating the derivative with respect to  $Z$  and putting it to zero, we find the value of  $N$  to  $Z$  ratio for which the binding energy reaches its largest value at fixed value of  $A$  (one can see the second derivative to be negative). This provides

$$\frac{N}{Z} = 1 + b \frac{2A^{2/3} - A^{-1/3}}{1 + bA^{-1/3}}; \quad b = \frac{a_3}{4a_4}. \quad (38)$$

This is in good agreement with Fig. 3. At fixed value of  $A$  the largest value of the binding energy is reached at

$$Z = \frac{A}{2} \cdot \frac{1 + bA^{-1/3}}{1 + bA^{2/3}}. \quad (39)$$

Neglecting the second term in numerator of Eq. (39) we obtain

$$Z \approx \frac{A}{2} \cdot \frac{1}{1 + (A/1500)^{2/3}}. \quad (40)$$

Thus at  $A$  close to the lower limit  $A = 20$  the deviations from the line  $Z = A/2$ , or  $N = Z$  are small. They are about 7 percent at  $A = 30$ . However they become larger for large  $A$ , e.g. making 26 percent for  $A = 200$ .

To find the limiting possible values for the number of neutrons  $N$  at fixed  $Z$  introduce the neutron separation energy  $S_N(Z)$ . This is the work which is needed to move a neutron from the nucleus containing  $A$  nucleons  $N$  of which are neutrons.

$$S_n(Z) = \varepsilon_B(N, Z) - \varepsilon_B(N - 1, Z). \quad (41)$$

Also,  $-S_n(Z)$  is the binding energy of the neutron added to the nucleus  $(N - 1, Z)$ . The condition

$$S_n(Z) \leq 0$$

means that the nucleus  $(A - 1, Z)$  cannot join a neutron. There are no nuclei with  $N \geq N_{\text{lim}}$  where  $N_{\text{lim}}$  is solution of the equation

$$S_n(Z) = 0. \quad (42)$$

In similar way the proton separation energy is

$$S_p(N) = \varepsilon(N, Z) - \varepsilon(N, Z - 1),$$

and the condition

$$S_p(N) = 0 \quad (43)$$

determines the upper limit for the values of  $Z$  at fixed value of  $N$ . The curves determined by Eqs. (42) and (43) are called the drip lines.

Stability against the alpha decay is described by condition

$$\varepsilon_B(A, Z) < \varepsilon_B(A - 4, Z - 2) + \varepsilon_B(4, 2). \quad (44)$$

Since the binding energy of helium is not supposed to be described by the Weizsäcker formula, one should use the empirical value. In the same way one can find condition for stability with respect to fission of a nucleus to any other fragments.

To obtain the condition of stability with respect to beta decay  $n \rightarrow p + e^- + \bar{\nu}_e$  we consider the total energy of the nucleus

$$E(A, N) = m_n N + m_p (A - N) - \varepsilon_B(A, N) \quad (45)$$

with  $m_{n,p}$  the vacuum masses of neutron and proton. The condition of stability is

$$E(A, N) < E(A, N - 1). \quad (46)$$

Employing Eq. (36) we find that Eq. (46) is equivalent to

$$N - Z < \frac{m_p - m_n + a_3 A^{2/3} + 2a_5/A^{1/3}}{a_3/A^{1/3} + 4a_4/A}. \quad (47)$$

Due to the numerically small value of  $a_3$  denominator is dominated by the second term. Near the lower limit of applicability of the approach all three terms of numerator are important. For example, at  $A = 30$  we find  $N - Z \leq 4$  for even-even nuclei while  $N - Z \leq 1$  for odd-odd nuclei. At large  $A$  we obtain

$$N - Z \leq \frac{a_3}{4a_4} A^{5/3} \approx \left(\frac{A}{19}\right)^{5/3}. \quad (48)$$

This provides  $N - Z \leq 50$  for  $A = 200$ .

In similar way the condition of stability with respect to  $\beta^+$  decay  $p \rightarrow n + e^+ \nu_e$  is

$$E(A, Z) < E(A, Z - 1), \quad (49)$$

where

$$E(A, N) = m_n (A - Z) + m_p Z - \varepsilon(A, Z). \quad (50)$$

Similar to Eq. (48) we find

$$Z - N \leq \frac{m_p - m_n + a_3 A^{2/3} - 2a_5/A^{1/3}}{a_3/A^{1/3} + 4a_4/A}. \quad (51)$$

with  $Z - N \leq (A/19)^{5/3}$  at large  $A$ .

## 2.4 Stability against small perturbations

As we have seen, for nuclei heavier than nickel it is energy not prohibitive to disintegrate into lighter fragments. The process, called spontaneous fission should last for a typical nuclear time  $10^{-22} - 10^{-23}$ sec. However, usually this does not happen.

To understand why, note that the spherical nuclei should change its shape before the fission takes place. We assumed that the volume of the nucleus does not change. This leads to the change of two ingredients of the binding energy. The surface ( $S$  in Eq. (33)) changes leading to the change of the potential energy  $U_{\text{sur}}$ . Also does the energy of the proton electrostatic interaction  $U_C$ . External perturbations change the shape of the nucleus. The values corresponding to the nucleus with the changed shape (it is usually referred to as the “deformed nucleus”) are  $U_{\text{sur}} = U_{\text{sur}}^{(0)} + \delta U_{\text{sur}}$  and  $U_C = U_C^{(0)} + \delta U_C$  with  $U_{\text{sur}}^{(0)}$  and  $U_C^{(0)}$  corresponding to the spherical nuclei. The change of the potential energy is  $\delta U = \delta U_{\text{sur}} + \delta U_C$ .

The spontaneous fission can take place if  $\delta U \leq 0$  since under this condition the nucleus moves to a more bound deformed state. Thus the condition of stability is

$$\delta U > 0. \quad (52)$$

We consider the case of small deformations which do not alter the  $A$  and  $Z$  dependence of the surface and Coulomb energies. Since  $U_{\text{sur}}^{(0)} \sim A^{2/3}$  while  $U_C^{(0)} \sim Z^2/A^{1/3}$ , the condition of stability against the spontaneous fission is expected to provide be the upper limit for the ratio  $Z^2/A$ .

Each point on the surface of deformed nucleus is described by vector  $\mathbf{R}$ . Its length  $R = |\mathbf{R}|$  depends on the angle  $\theta$  between  $\mathbf{R}$  and  $z$  axis and on the angle  $\varphi$  in  $(x, y)$  plane. The distance between the origin and a point on the surface of the deformed nucleus can be presented as

$$R(\theta, \varphi) = R_0 + \lambda(\theta, \varphi); \quad \lambda(\theta, \varphi) = R_0 \sum \alpha_{\ell m} Y_{\ell m}(\theta, \varphi), \quad (53)$$

with  $Y_{\ell m}$  – the spherical harmonics. We shall use also notations  $R(\Omega)$  and  $\lambda(\Omega)$ . One can see that

$$\alpha_{\ell m} = \frac{1}{R_0} \int d\Omega R(\Omega) Y_{\ell m}^*(\Omega).$$

The term with  $\ell = 0$  on the right-hand side of Eq. (53) corresponds to modification of the value of  $R$  keeping the spherical shape of the nucleus. Perturbations with  $\ell = 1$  lead just to the shift of the center of mass without changing the shape of the nucleus.

If  $\alpha_{\ell m} = \alpha_{\ell 0} \delta_{m0}$  the nucleus is symmetric with respect to rotations in  $(xy)$  plane, thus having the axial symmetric shape with  $z$  the axis of symmetry. In this case  $R$  does not depend on  $\varphi$  and in the lowest order

$$R(\theta) = R_0 \left( 1 + \sum_{\ell} \epsilon_{\ell} P_{\ell}(t) \right); \quad t = \cos \theta; \quad \epsilon_{\ell} = \sqrt{\frac{2\ell + 1}{4\pi}} \alpha_{\ell 0}, \quad (54)$$

while  $P_{\ell}(t)$  are the Legendre polynomials. (In the second order we cannot neglect the term  $\alpha_{00}$  – see below).

For the quadruple deformations with  $\ell = 2$  we find  $R(\theta) = R_0 \left( 1 + \epsilon_2 P_2(t) \right)$  with  $P_2(t) = (3t^2 - 1)/2$ . At  $t = \pm 1$  the values of  $R$  reach the largest values  $R = R_0(1 + \epsilon)$ , while  $R = R_0(1 - \epsilon/2)$  in  $(xy)$  plane corresponding to  $t = 0$ . The nucleus has a shape of spheroid

$$\frac{x^2 + y^2}{a^2} + \frac{z^2}{b^2} = 1$$

with the minor axis  $a = R_0(1 - \epsilon/2)$  and the major axis  $b = R_0(1 + \epsilon)$ . The volume of the nucleus did not change being  $V = 4\pi/3 \cdot a^2 b = (4\pi/3) R_0^3 (1 + o(\epsilon))$ .

In this section we consider the small deformations

$$|\alpha_{\ell m}| \ll 1. \quad (55)$$

The volume of deformed nucleus is

$$V_d = \int d\Omega \int_0^{R(\Omega)} dr r^2 = \frac{1}{3} \int d\Omega R^3(\Omega).$$

Once we assumed that deformations do not change the volume of the nucleus,

$$\frac{1}{3} \int d\Omega R^3(\Omega) = \frac{1}{3} \int d\Omega R_0^3 = \frac{4\pi}{3} R_0^3. \quad (56)$$

Keeping only the terms linear in  $\alpha_{\ell m}$  we should put  $\alpha_{00} = 0$ . However, we shall see that the deformation leads to the second order effects. In this approximation  $\alpha_{00}$  is not an independent parameter since Eq. (56) provides

$$\alpha_{00} = -\frac{1}{\sqrt{4\pi}} \sum_{\ell m} \alpha_{\ell m}^2; \quad \ell \geq 1. \quad (57)$$

Now we are ready to calculate the shifts of the energies  $U_{sur}$  and  $U_C$  – [22–24]. Recall that we include the terms up to  $\alpha_{\ell m}^2$ . The surface energy of the deformed nucleus can be written as

$$U_{sur} = \sigma \int d\Omega \frac{R^2(\Omega)}{\cos \tau}, \quad (58)$$

with  $\tau = \nabla R(\Omega)$ . For small deformations  $\tau \ll 1$ ,  $\cos \tau = 1 - \tau^2/2$ . Thus we can write

$$\delta U_{sur} = \sigma \int d\Omega \left( R^2(\Omega) - R_0^2 + \frac{R_0^2}{2} (\nabla R)^2 \right).$$

Integrating the last term in the parenthesis by parts and doing simple algebra rearrangements we present

$$\delta U_{sur} = \sigma \int d\Omega \left( 2R_0 \lambda(\Omega) + \lambda^2(\Omega) - \frac{R_0^2}{2} R \nabla^2 R \right).$$

One immediately finds for the integral of the first term  $\int d\Omega \lambda(\Omega) = \alpha_{00}$  while the contributions of higher  $\ell$  vanish due to orthogonality of  $Y_{\ell m}$  and  $Y_{00}$ . We obtain  $\int d\Omega \lambda^2(\Omega) = \sum_{\ell m} \alpha_{\ell m}^2$ . The third term can be evaluated by noting that  $R^2 \nabla^2 Y_{\ell m} = \ell(\ell+1) Y_{\ell m}$  and by presenting  $1/R = 1/R_0(1 - \lambda/R_0)$ . Employing Eq. (57) we obtain

$$\delta U_{sur} = \frac{\sigma R_0^2}{2} \sum_{\ell m} (\ell-1)(\ell+2) \alpha_{\ell m}^2; \quad \ell \geq 1. \quad (59)$$

Thus the deformation of the nucleus increases its surface energy. The nucleus becomes more bound.

In the case of axial symmetric quadrupole perturbation mentioned earlier  $\delta U_{sur} = U_{sur}^{(0)} \cdot 2\epsilon_2^2/5$ . The surface energy does not change due to dipole perturbations ( $\ell = 1$ ). As we noted earlier, such perturbations just shift the center of mass of the nucleus.

Let us look how does the energy of the proton electrostatic interaction change. The electrostatic energy of the spherical nucleus can be presented as

$$U_C^{(0)} = \frac{1}{2} \int d^3r \rho^C(r) \varphi(r),$$

with the charge density  $\rho^C(r)$  and the potential  $\varphi(r)$  determined by Eq. (30). Writing similar expression for the deformed nucleus

$$U_C = \frac{1}{2} \int d^3r \rho^{Cdef}(r) \varphi^{def}(r)$$

with

$$\rho^{Cdef}(r, \Omega) = \rho_0^C \cdot \theta(R(\Omega) - r); \quad \varphi^{def}(r, \Omega) = \int d^3x \frac{\rho^{Cdef}(x, \Omega_x)}{|\mathbf{r} - \mathbf{x}|}, \quad (60)$$

(recall that  $\rho_0$  remains unchanged since the volume of the nucleus does not change), we present

$$\begin{aligned} \delta U_C = J_1 + J_2 + J_3; \quad J_1 = \frac{1}{2} \int d^3r \delta \rho^C(r) \cdot \varphi(r); \quad J_2 = \frac{1}{2} \int d^3r \rho^C(r) \delta \varphi(r); \\ J_3 = \frac{1}{2} \int d^3r \delta \rho(r) \cdot \delta \varphi(r), \end{aligned} \quad (61)$$

with  $\delta \rho^C(r) = \rho^{Cdef}(r) - \rho^C(r)$ ,  $\delta \varphi(r) = \varphi^{def}(r) - \varphi(r)$ .

Carrying out expansion in powers of  $\lambda$  on the right-hand side of the first equality of Eq. (60) we obtain

$$\delta \rho^C(r, \Omega) = \rho_0^C \lambda(\Omega) \left( \delta(r - R_0) - \frac{\lambda(\Omega)}{2} \delta'(r - R_0) \right). \quad (62)$$

Thus the change of the shape of the nucleus causes additional electric charge on the surface of the spherical nucleus. Employing Eq. (62) with the second term on the right hand side being integrated by parts, we find

$$J_1 = -eZ\rho_0^C R_0^2 \sum_{\ell m} \alpha_{\ell m}^2. \quad (63)$$

In the lowest order in  $\alpha_{\ell m}$  the change of the potential caused by the first term on the right-hand side of Eq. (62) is

$$\begin{aligned} \delta \varphi^{(1)} = \frac{eZ}{R_0} \sum \delta \varphi_{\ell m}^{(1)}; \quad \varphi_{\ell m}^{(1)} = \frac{3}{2\ell + 1} \alpha_{\ell m} Y(\Omega)_{\ell m} \times \\ \times \left( \left( \frac{r}{R_0} \right)^\ell \theta(R_0 - r) + \left( \frac{R_0}{r} \right)^{\ell+1} \theta(r - R_0) \right). \end{aligned} \quad (64)$$

Only the contribution of the term  $\delta \varphi_{00}^{(1)} = (R_0/r)\theta(r - R_0)$  survives after the angular integration in the integral  $J_2$  given by the third equality of Eq. (61). The

following radial integration provides for the first order contributions  $J_2^{(1)} = 0$ . In similar way we find that the second order contributions  $J_2^{(2)} = 0$ . Thus  $J_2 = 0$ .

Turning to  $J_3$ , we must include only the first order deformation terms in expressions for  $\delta\rho_C$  and  $\delta\varphi$ . Direct calculation provides

$$J_3 = 3eZ\rho_0^C R_0^2 \sum_{\ell m} \frac{\alpha_{\ell m}^2}{2\ell + 1}. \quad (65)$$

Thus  $U_C = J_1 + J_3$ , i.e

$$\delta U_C = -eZ\rho_0^C R_0^2 \sum_{\ell m} \frac{\ell - 1}{2\ell + 1} \alpha_{\ell m}^2. \quad (66)$$

Thus the deformation of the nucleus decreases the contribution of electrostatic interactions to its potential energy. For the axial symmetric quadrupole perturbation  $\delta U_C = U_C^{(0)} \cdot (-1/5)\epsilon_2^2$ .

Combining Eqs. (59) and (66) we find

$$\delta U_{\text{sur}} + \delta U_C = \sum_{\ell m} \frac{R_0^2(\ell - 1)}{2} \left( (\ell + 2)\sigma - \frac{eZ\rho_0^C}{2\ell + 1} \right) \alpha_{\ell m}^2. \quad (67)$$

In terms of the coefficients of the Weizsäcker formula

$$\delta U_{\text{sur}} + \delta U_C = \sum_{\ell m} \frac{\ell - 1}{4\pi} \left( \frac{(\ell + 2)a_2 A^{2/3}}{2} - \frac{5a_3}{2\ell + 1} \frac{Z^2}{A^{1/3}} \right) \alpha_{\ell m}^2. \quad (68)$$

The monopole perturbations do not contribute in the lowest order due to Eq. (57). The dipole contributions do not change the potential energy, providing only the shift of the center of mass. For  $\ell \geq 2$  the condition of stability expressed by Eq. (52) takes the form

$$\frac{Z^2}{A} < \frac{a_2(\ell + 2)(2\ell + 1)}{a_3 \cdot 10}. \quad (69)$$

Hence we have the strongest limitation for  $\ell = 2$ . The limitations become weaker while  $\ell$  increases. For  $\ell = 2$  we obtain

$$\frac{Z^2}{A} < \frac{2a_2}{a_3}. \quad (70)$$

This insures stability against the perturbations with larger  $\ell$  as well. Employing the values provided by Eq. (28) we find

$$\frac{Z^2}{A} < 49. \quad (71)$$

For example, for  $^{125}_{54}\text{Xe}$  we find  $Z^2/A = 23$ , for  $^{235}_{92}\text{U}$  we obtain  $Z^2/A = 36$ . For transuranium  $^{289}_{114}\text{Fl}$  (Flerovium)  $Z^2/A = 45$ .

Note that much earlier J. Rayleigh carried out similar analysis of stability for the charged liquid drop (not nuclear liquid drop) – see [25]. In this case the potential energy is composed by the surface tension energy and the energy of the electric field caused by the charge localized on the surface of the drop.

Recall that dipole perturbations ( $\ell = 1$ ) lead to the shift of the center of mass of the system. This is true if the coefficients  $\alpha_{1m}$  are the same for all nucleons. In interaction with electromagnetic field  $\alpha_{1m}$  for the protons are determined by their electric charges. They are much smaller for the neutrons being determined by their magnetic moments. This leads to bright consequences for interaction of photons with nuclei. The atomic physics teaches us that at the photon energies  $\omega \ll m$  the process can be treated in dipole approximation. The electromagnetic wave provides oscillations of the proton sphere of the nucleus while the neutron sphere remains at rest. This phenomena called the giant dipole resonance was first observed in photoionization of the nuclei of uranium and thorium at the photon energies 15–20 MeV [26]. It was explained in [27].

## 2.5 Fission of nuclei

A nucleus which is stable against small deformations may appear to be unstable against large ones. This happens because the distances between the nucleons increases in large deformations. Thus the surface tension energy which is due to short range interaction is less effected by the large deformation than the electrostatic energy which is due to the long range Coulomb repulsion. The short range attraction caused by the surface tension changes slower than the long range Coulomb repulsion, and the change of the potential energy runs negative.

The case of large deformations, for which  $|\epsilon_\ell|$  (see Eq. (54)) is of the order of unity was analyzed in [28]. It was demonstrated that in the decays of the nucleus  $(A, Z)$  into two fragments  $(A_1, Z_1)$  and  $(A_2, Z_2)$  ( $A_1 + A_2 = A$ ,  $Z_1 + Z_2 = Z$ ) the probability reaches its largest value for the symmetric fission  $A_1 = A_2 = A/2$ ,

$Z_1 = Z_2 = Z/2$ . The energy released in the symmetric decay is

$$\varepsilon_f = 2\varepsilon_B(A/2, Z/2) - \varepsilon_B(A, Z). \quad (72)$$

Employing Eq. (26) we find

$$\varepsilon_f = 2a_2A^{2/3}(2^{-1} - 2^{-2/3}) + a_3Z^2A^{-1/3}(1 - 2^{-2/3}). \quad (73)$$

The symmetry terms cancel on the right hand side of Eq. (72).

The condition of stability against fission is  $\varepsilon_f < 0$ , i.e.

$$\frac{Z^2}{A} < \frac{2a_2}{a_3}\nu; \quad \nu = \frac{1}{2^{1/3}(2^{1/3} + 1)} \approx 0.35. \quad (74)$$

This condition differs from the condition of stability against small deformations expressed by Eq. (71) by the numerical factor  $\nu$ . Numerically

$$\frac{Z^2}{A} < 17. \quad (75)$$

For example,  $Z^2/A = 12$  for  ${}^{56}_{26}\text{Fe}$  while  $Z^2/A = 17.6$  for  ${}^{91}_{40}\text{Zr}$ . Employing Eq. (40) we see that the nuclei with  $A > 87$  are unstable against spontaneous fission.

The analysis carried out in [24] provides the explicit picture for the symmetric decay of the nucleus  $(A, Z)$ . At the moment preceding the fragmentation into two nuclei  $(A/2, Z/2)$  it can be viewed as two spheres with the radii  $R_{A/2} = r_0(A/2)^{1/3}$  connected by a cylindrical isthmus of the length  $x$  and the radius of the cylinder base  $r_n$ . To estimate the value of  $r_n$  note that at the moment of fragmentation the repulsive Coulomb force between the nuclei  $(A/2, Z/2)$  which is  $F_C = (eZ/2)^2/(R_{A/2})^2$  is balanced by the surface tension force  $F_{sur} = -dU_{sur}/dx$  where  $U_{sur} = 2\pi r_n x \sigma$  is the potential energy of the surface tension. Thus  $F_C + F_{sur} = 0$ . Employing Eq. (32) and Eq. (34) we obtain

$$\frac{r_n}{R_{A/2}} = \frac{5}{6} \frac{Z^2/A}{(Z^2/A)_{\text{lim}}}. \quad (76)$$

Here

$$\left(\frac{Z^2}{A}\right)_{\text{lim}} = \frac{2a_2}{a_3} \approx 49,$$

(see Eq. (70)) is just the limiting value for the ratio  $Z^2/A$  consistent with stability against small deformations. We find  $r_n/R_{A/2} = 0.61$  for  ${}^{235}_{92}\text{U}$ . The ratio becomes smaller for lighter nuclei. We obtain  $r_n/R_{A/2} = 0.30$  for  ${}^{91}_{40}\text{Zr}$ .

Note that domination of the symmetric mode of the decay is a model result which contradicts the experimental data. The symmetric channel dominates in seldom cases. The number of nucleons in the fragments of fission is determined by the individual properties of the latter. We discuss the point in the next Chapter.

## 3. Interaction of nucleons inside the nucleus

### 3.1. Arguments in favor of nonrelativistic approach

In previous Chapter we considered the characteristics of nucleus as a whole. Now we try to describe the behavior of a nucleon in the nucleus. In this Chapter we discuss the nuclei with the number of nucleons  $A \geq 4$ . The nuclei with  $A = 2$  and  $A = 3$  will be studied in Chapter 6.

Note that the very idea that one can choose any nucleon is a very strong assumption. Anyway, once we have chosen a nucleon, it is reasonable to ask ourselves if its motion can be treated as nonrelativistic.

To answer the question we express the limiting values of nucleon momenta through the value of saturation density which we know to be  $\rho_0 = 0.17 \text{ fm}^{-3}$  – see Ch. 2. Start with the case of free nucleons, assuming them to be placed in a cube of volume  $V = L^3$ . The motion of the nucleon with momentum  $p$  corresponds to propagation of the wave with the wavelength  $\lambda = 2\pi/p$ . The quasiclassical boundary condition is  $L/\lambda = n$  with  $n$  being an integer number. Thus  $p_i = 2\pi n_i/L$  for each of the three components of the nucleon momentum  $\mathbf{p}$ . Hence the total number of states is  $A_0 = VV_p/(2\pi)^3$  with  $V_p = p_x p_y p_z$  the volume in momentum space. Since the nucleons are the fermions, there can be four of them in any state with momentum  $\mathbf{p}$ . This corresponds to two possible spin and isospin states. Thus the number of nucleons is  $A = 4A_0$  and in differential form

$$dA = 4V \cdot \frac{d^3p}{(2\pi)^3}. \quad (77)$$

The values of  $p$  are limited by condition  $p \leq p_F$  with the Fermi momentum  $p_F$  defined by the equation

$$d\rho \equiv \frac{dA}{V} = \frac{4\theta(p_F - p)d^3p}{(2\pi)^3}, \quad (78)$$

providing for the density

$$\rho_0 = \frac{2p_F^3}{3\pi^2}. \quad (79)$$

Employing the observed value of saturation density  $\rho_0$  we find that it corresponds to the Fermi momentum  $p_F = 268 \text{ MeV}/c$  ( $p_F = 268 \text{ MeV}$  in our units). It can be expressed also as  $p_F = 1.38 \text{ fm}^{-1}$ . The nucleon kinetic energy  $T(p)$  on the Fermi surface is  $T(p_F) = T_F = p_F^2/2m$ . Thus

$$T_F \approx 39 \text{ MeV}; \quad \frac{T_F}{m} \approx 0.04, \quad (80)$$

looks to be a good small parameter. For the ideal Fermi gas we can calculate also the averaged kinetic energy

$$T_{av} = \int \frac{\theta(p_F - p)T(p)d^3p}{\rho_0(2\pi)^3} \approx 24 \text{ MeV}.$$

In infinitely heavy nucleus<sup>1</sup> the potential energy is the same for all nucleons while the binding energy is  $\varepsilon_B = 16 \text{ MeV}$ . Thus we can estimate the nucleon potential energy in nuclear matter  $U = -\varepsilon_B - T_F \approx -55 \text{ MeV}$ . The binding energy in finite nuclei is  $\varepsilon_B = 8 \text{ MeV}$ . Thus in the interior (accept the vicinity of the surface)  $U \approx -50 \text{ MeV}$ .

Thus the ratios  $T_F/m$  and  $T_{av}/m$  in the Fermi gas are rather small. How will the nucleon interaction change these estimations? To answer the question note that in the system of  $A \gg 1$  interacting nucleons each of them can be viewed as a quasiparticle [29, 30]. This means that the motion of each nucleon causes virtual excitations of the other ones and is influenced by them. It can be demonstrated (employing the Fermi liquid theory) that integrated Eq. (79) holds for the interacting fermions as well [31]. Interactions shift the position of the pole of nucleon propagator. Thus the vacuum value  $m$  is shifted to certain effective value  $m^*$ . The experimental data are consistent with a small shift  $|m^* - m|/m \lesssim 0.1$ . Thus for interacting nucleons the ratio  $T_F/m^* \approx 0.05$  is still small.

This prompts that the nucleon motion can be considered in nonrelativistic approximation. We shall see in Part II the ratio (80) is not always a proper parameter and relativistic treatment becomes necessary. However, much of understanding was achieved in framework of nonrelativistic approach.

### 3.2. Effective potential

As the stating point we try to describe the motion of nucleon in nucleus as the elastic rescattering on the other nucleons. The distribution of the latter is

---

<sup>1</sup>The system of nucleons with  $A \rightarrow \infty$  and  $N = Z$  in which the electromagnetic interactions are removed is called the nuclear matter. We shall sometimes appeal to the results for such system.

not changed in such processes. In such approach a nucleon in the nucleus can be described by external field Schrödinger equation with the potential energy  $U(\mathbf{r})$  which depends on the position of the nucleon  $\mathbf{r}$  in the nucleus center mass frame.

In this Chapter we consider the spherical nuclei. Hence in the first step we assume that  $U$  depends only on  $r = |\mathbf{r}|$ .

The wave equation is

$$H\psi_\lambda(\mathbf{r}) = \varepsilon_\lambda\psi_\lambda(\mathbf{r}). \quad (81)$$

Here  $\varepsilon_\lambda$  is the energy of the nucleon in the state  $\lambda$  while

$$H = T + U(r); \quad T = -\frac{\Delta_r}{2m}. \quad (82)$$

The shape of the potential  $U(r)$  is chosen to reproduce the different experimental data: spectra of one-particle states, collective states, nuclear charge density, *et al.*

### 3.2.1. Light nuclei

In this case the density  $\rho(r)$  drops rapidly with increasing of  $r$ . Thus it is reasonable to try the harmonic oscillator potential

$$U(r) = -U_0 + \frac{m^2\omega^2r^2}{2}; \quad U_0 = -U(r=0) > 0, \quad (83)$$

since it provides the rapidly dropping wave functions (see, e.g. [32]). For the lowest state  $\psi(r) \sim \exp(-m\omega r^2/2)$ , providing the density  $\rho(r) \sim \exp(-m\omega r^2)$ . The wave function of the higher states have polynomial factors. The energies of the bound states are

$$\varepsilon_n = -U_0 + (n + 3/2)\omega, \quad (84)$$

with  $n = 0, 1, 2, \dots$ . There are several states with different values of the orbital momenta  $\ell \leq n$  corresponding to each value of  $n$ . For even values of  $n = 2k$  we find  $\ell = 2k_1$  with  $k_1 \leq k$ . For odd  $n = 2k + 1$  we obtain  $\ell = 2k_1 + 1$  with  $k_1 \leq k$ . Thus  $\ell$  is even if  $n$  is even and  $\ell$  is odd if  $n$  is odd.

One can trace the  $A$  dependence of the frequency  $\omega$ . Since in the oscillator  $\langle n|T|n \rangle = m^2\omega^2\langle n|r^2|n \rangle/4$  (see, e.g., [32]) and the total binding energy is proportional to  $A$ , we find that  $\omega^2 \sum_n \langle n|r^2|n \rangle$  is proportional to  $A$ . Thus  $\omega^2 R^2$  with  $R^2 = \sum_n \langle n|r^2|n \rangle/A$  does not depend on  $A$ . Since  $R \sim A^{1/3}$  we find that  $\omega \sim A^{-1/3}$ . To fit the observable values of  $R$  one can put (see, e.g., [33])

$$\omega \approx \frac{40 \text{ MeV}}{A^{1/3}}. \quad (85)$$

Following 3.1 we put  $U_0 = 50 \text{ MeV}$ . The potential (83) with these parameters provides reasonable description of the light nuclei.

### 3.2.2. Heavy nuclei

For heavy nuclei the shape of the central potential  $U(r)$  follows that of the nuclear density  $\rho(r)$ . This can be understood considering the potential to be caused by interaction with the nucleon of the nucleons located at the points  $\mathbf{r}_i$ . We present

$$U(r) = \int d^3r_i u(\mathbf{r} - \mathbf{r}_i) \rho(r_i), \quad (86)$$

with  $u(\mathbf{r} - \mathbf{r}_i)$  interaction between the nucleons (later we shall see that this is a rather rough approximation). Since the scale of the interaction  $u$  is much smaller than the size of heavy nucleon, we can put  $u(\mathbf{r} - \mathbf{r}_i) = -C\delta(\mathbf{r} - \mathbf{r}_i)$  with a constant factor  $C > 0$ . This provides

$$U(r) = -C\rho(r). \quad (87)$$

As we have seen earlier, at larger values of  $A$  the density  $\rho(r)$  actually depends on  $r$  only in the thin layer  $|R - r| \sim a \ll R$ . Here it drops from the value  $\rho_0 = \rho(0)$  to zero. The  $r$  dependence of density is usually approximated by the Fermi function

$$\rho(r) = \frac{\rho_0}{1 + e^{(r-R)/a}}.$$

Here

$$R = r_0 A^{1/3}, \quad (88)$$

with  $r_0 \approx 1.25 \text{ fm}$  is size of the nucleus, while  $a \approx 0.5 \text{ fm}$ . The field of the nucleus can be approximated by the Woods–Saxon potential

$$U(r) = -\frac{U_0}{1 + e^{(r-R)/a}}; \quad U_0 = -U(r = 0) > 0, \quad (89)$$

with  $U_0 \approx 50 \text{ MeV}$ ,  $a \approx 0.5 \text{ fm}$ . Such potential provides reasonable description of heavy nuclei. However the calculations should be carried out numerically.

To have a feeling of the level structure we consider the limiting case  $a \rightarrow 0$ . Now Eq. (89) turns to

$$U(r) = -U_0\theta(R - r). \quad (90)$$

Recall that  $\theta(x) = 1$  for  $x \geq 0$  while  $\theta(x) = 0$  for  $x < 0$ . This is the quadratic well potential.

Start with a simplified version the well potential has infinitely high wall

$$U(r) = -U_0 \quad (r \leq R); \quad U(r) = \infty \quad (r > R). \quad (91)$$

In this case the nucleon experience free motion at  $r \leq R$ . The nucleon wave function vanishes at  $r > R$ . The nucleon in the bound state with the quantum numbers  $\lambda$  carries the energy  $\varepsilon_\lambda$  and momentum  $k_\lambda = (2m(\varepsilon_\lambda + U_0))^{1/2}$ . Introducing the nucleon energy counted from the bottom of the well  $\tilde{\varepsilon}_\lambda = \varepsilon_\lambda + U_0$  we write  $k_\lambda = (2m\tilde{\varepsilon}_\lambda)^{1/2}$ .

Separating the angular variables in the wave equation we come to equation for the radial wave functions  $R_{n\ell}(r)$  with orbital angular momentum  $\ell$  while  $n$  numbers the states with fixed value of  $\ell$ . The lowest states with  $\ell = 0, 1$  are labelled as  $1s$  and  $1p$  correspondingly. Note that such notation differs from that accepted in atomic spectroscopy.

We find

$$R_{n\ell}(r) = C j_\ell(kr), \quad (92)$$

with  $C$  a normalization constant while  $j_\ell$  are the spherical Bessel functions of the first kind. Since the wave functions vanish at  $r > R$ , the values of the binding energies are determined by the border condition

$$j_\ell(kR) = 0. \quad (93)$$

The functions  $j_\ell(x)$  can be expressed in terms of the trigonometric functions

$$j_0(x) = \frac{\sin x}{x}; \quad j_1(x) = \frac{\sin x}{x^2} - \frac{\cos x}{x},$$

etc. Denoting the roots of Eq. (93) as  $x_{n\ell}$  we present

$$\tilde{\varepsilon}_\lambda = \frac{x_{n\ell}^2}{2mR^2}. \quad (94)$$

One finds  $x_{n0} = n\pi$  for  $\ell = 0$ . For  $\ell = 1$  the values  $x_{n1}$  are solution of the equation  $x = \tan x$ . The numerical values of  $x_{n\ell}$  for several values of  $n, \ell$  are given in Table 1.

In the case of finite square well with the potential  $U(r)$  determined by Eq. (90) the wave function drops as  $\psi_{n\ell}(r) = C e^{-k'_{n\ell} r}$  at  $r > R$  with  $k'_{n\ell} = (-2m|\varepsilon_{n\ell}|)^{1/2}$ . At  $r \geq R$  the solution of wave equation is

$$R_{n\ell}(r) = C_1 h_\ell^{(1)}(ik'_{n\ell} r), \quad (95)$$

with  $h^{(1)}$  the spherical Hankel function with the purely imaginary argument. One finds the spectrum of the wave equation with the potential determined by

Table 1: Values of  $x_{n\ell} = k_{n\ell}R$ . Second column – the infinite square well; third column – finite square well with  $(2mU_0)^{1/2}R = 10$ .

$n\ell$	$x_{n\ell}$	$x_{n\ell}$
1s	3.14	2.85
1p	4.49	4.07
1d	5.76	5.23
2s	6.28	5.70
2p	7.72	6.96

Eq. (91) matching the solutions (92) and (95) at  $r = R$ . After some algebra [34] we come to equation

$$\tan x = f_\ell(\eta, x/\eta); \quad x = kR; \quad k = (2m\tilde{\varepsilon})^{1/2}, \quad (96)$$

and denote

$$\eta = (2mU_0)^{1/2}R. \quad (97)$$

The functions  $f_\ell(\eta, x/\eta)$  for the lowest values  $\ell = 0, 1, 2$  are presented in [33]. For  $\ell = 0$  the function  $f_0 = \xi/\sqrt{1-\xi^2}$  depends only on  $x/\eta = \xi$ . The energy levels are determined by Eq. (94) but  $x_{n\ell}$  depends now on parameter  $\eta$ . The values of  $x_{n\ell}$  for several values of  $n, \ell$  at  $\eta = 10$  are given in Table 1. For  $U_0 = 50$  MeV and  $r_0 = 1.25$  fm (see Eq. (88)) the value  $\eta = 10$  corresponds to the nucleus with  $A \approx 140$  nucleons.

Equations for the bound state energies in the Woods–Saxon potential (89) can be obtained by some mathematical evaluations. For  $\ell = 0$  [34]

$$k = -k' \cdot \tan \left( kR - \sum_{n=1}^{\infty} \left( \arctan \frac{2ka}{n} - 2 \arctan \frac{ka}{n+k'a} \right) \right);$$

$$x = kR; \quad k' = (-2m|\varepsilon_{n0}|)^{1/2}. \quad (98)$$

For  $a = 0$  this provides Eq. (96) for the finite square well. In the lowest order of expansion in powers of  $a/R \ll 1$

$$k = -k'(1 - \frac{\pi^2}{3}kk'a^2) \tan kR. \quad (99)$$

The further calculations should be carried out numerically.

### 3.3. More complicated forms of effective potential

#### 3.3.1. Momentum dependent forces

In general the nucleon-nucleon interaction depends on the momentum of nucleon. Now we show that for a small momenta this dependence can be accounted for introducing the *effective* mass  $m^*$ .

The point is that the forces are resulted from the meson exchange. Since the meson is emitted by one nucleon and is absorbed by other one, the forces depend on the distance between the nucleons, that is they are not the local ones. So the nucleon interaction  $u(r_1 - r_2)$  (Eq. (86)) can be written in the momentum space in the form

$$\langle p|u|p' \rangle = \frac{1}{(2\pi)^3} \int d^3r u(r)e^{-i(p-p')r}. \quad (100)$$

Here  $\langle p|u|p' \rangle$  is a constant if  $u(r)$  is a  $\delta$  function but nonlocality of  $u(r)$  leads to the momentum dependence. Expanding the dependence in a powers of momenta at the lowest ( $p^2$ ) order we get

$$u(p, p') = u_0 + u_1 (p^2 + p'^2) + u_2 (p \cdot p'). \quad (101)$$

where  $p, p'$  are the relative wave vectors of two nucleons. In the coordinate space  $p$  denotes the operator  $(\nabla_1 - \nabla_2)/(2i)$  acting on the right and  $p'$  denotes the operator  $-(\nabla_1 - \nabla_2)/(2i)$  acting on the left.

The best is to construct the NN interactions inside the nuclei from the interactions of the free nucleons. This was done in the Brueckner theory [35] using a lot of suggestions and simplifications.

Another possibility is to study the nuclear properties using the phenomenological NN interactions. The most useful is the Skyrme interaction [36]. It depends on the momenta of interacting nucleons and the nuclear density and include 2-particle and 3-particle interaction. Two-particle part reads

$$\langle p|u|p' \rangle = t_0(1 + x_0 P_\sigma) + \frac{1}{2} t_1(p^2 + p'^2) + t_2 (p \cdot p') + iW_0 (\sigma_1 + \sigma_2) \cdot [p, p'], \quad (102)$$

The parameters  $x_0, t_0, t_1, t_2$  and  $W_0$  are obtained by fitting the binding energy of nuclear matter and radii of the finite nuclei.  $P_\sigma$  is a spin-exchange operator of two particles. The last term gives the spin-orbit contribution into the one-particle potential (see the next Subsection).

Turning  $\langle p|u|p' \rangle$  into the coordinate space and using Eqs.(86),(100) we obtain the one-particle potential. This is the effective potential that is included

in the Schrödinger equation Eq. (82) which now takes the form

$$\left[ -\nabla \left( \frac{1}{2m^*(r)} \nabla \right) + U(r) \right] \psi_\lambda(\mathbf{r}) = \varepsilon_\lambda \psi_\lambda(\mathbf{r}), \quad (103)$$

where  $m^*(r)$  we consider as an effective mass of nucleons in matter.

Indeed, adding the term  $t_i p^2/2$  to the kinetic energy  $p^2/2m$  we can write the result as  $p^2/2m^*$ . In symmetric nuclear matter ( $N=Z$ ) and without the Coulomb force taken into account we obtain the following view for the effective mass:

$$\frac{1}{2m^*(r)} = \frac{1}{2m} + (c_1 t_1 + c_2 t_2) \rho. \quad (104)$$

$c_1$  and  $c_2$  are the numerical factors.

We see that momentum dependent terms of the effective NN interaction lead to the effective mass of nucleon in nuclei and nuclear matter. Using the Skyrme interaction we get the effective mass considerably smaller than  $m$ :  $m^* \approx m/2$ . Besides this in the nuclei  $m^*(r)$  depends on the coordinate through the density  $\rho(r)$ .

### 3.3.2. Forces depending on angular momentum

In previous Subsection we discussed the forces proportional to the squared momentum  $p^2$ . There can be also a contribution linear in  $\mathbf{p}$ . Momentum  $\mathbf{p}$  can compose three combinations with the distance vector  $\mathbf{r}$  and with the nucleon spin  $\mathbf{S}$  which is a pseudovector. However the combination  $\mathbf{r} \cdot \mathbf{p}$  is impossible due to the time invariance of strong interactions while the product  $\mathbf{r} \cdot \mathbf{S}$  would violate the space parity. The only way to construct a scalar structure linear in  $\mathbf{p}$  is to write pseudovector  $[\mathbf{r}, \mathbf{p}]$  multiplying it by  $\mathbf{S}$ . One can see that  $[\mathbf{r}, \mathbf{p}]$  is just the operator of orbital angular momentum  $\mathbf{L}$ . Thus the contribution is proportional to the product  $\mathbf{L}\mathbf{S}$ . The corresponding term in the Hamiltonian is denoted as  $U_{LS}$  and the effective potential is

$$U_{eff}(\mathbf{r}) = U_c(r) + U_{LS}(\mathbf{r}), \quad (105)$$

with the first term on the right hand side being the central part of interaction. The interaction  $U_{LS}$  has analog in atomic physics where the moving electron magnetic moment interacts with electrostatic field of the nucleus. Thus it is called the spin-orbit interaction.

The dependence of the spin-orbit interaction on  $\mathbf{r}$  can manifest itself only as  $\nabla\rho(r)$ . Since  $\nabla\rho = \mathbf{r}/r \cdot d\rho/dr$ , we can write

$$U_{LS}(\mathbf{r}; \mathbf{p}) \sim \mathbf{S} \cdot [\mathbf{p}\nabla]\rho(r),$$

which can be written as

$$U_{LS}(\mathbf{r}; \mathbf{p}) \sim \frac{\mathbf{L}\mathbf{S}}{r} \cdot \frac{d\rho(r)}{dr}.$$

In heavy nuclei this interaction has noticeable values only in the surface region of the nuclei, where the  $\rho(r)$  changes rapidly.

Recall that in heavy nuclei the shape of the central potential is chosen to reproduce that of  $r$  dependence of density. Hence, we can write for heavy nuclei [33]

$$U(\mathbf{r}) = U_c(r) - 2\alpha(r)\mathbf{L}\mathbf{S}; \quad \mathbf{L} = [\mathbf{r}\mathbf{p}], \quad (106)$$

with

$$\alpha(r) = u_{\ell s} \frac{r_0^2}{r} \frac{dU(r)}{dr}, \quad (107)$$

where  $U(r)$  is the central potential, while  $u_{\ell s}$  is a certain coefficient. Employing the Woods–Saxon potential given by Eq. (89) one finds that the values  $u_{\ell s} \approx 17$  MeV fit the experimental data on the scattering of nucleons on nuclei [33].

The operator of total angular momentum of the nucleon  $\mathbf{J} = \mathbf{L} + \mathbf{S}$  and operators  $L$  and  $S$  compose a set of commuting operators. Hence,

$$\mathbf{L}\mathbf{S} = \frac{\mathbf{J}^2 - \mathbf{L}^2 - \mathbf{S}^2}{2}. \quad (108)$$

Thus in the action of the potential (106) on the function with fixed values of  $j$  and  $\ell$  the operator  $\mathbf{L}\mathbf{S}$  can be replaced by its eigen value

$$\ell_s = \frac{j(j+1) - \ell(\ell+1) - 3/4}{2}. \quad (109)$$

Hence for the potential defined by Eq. (106)

$$U(\mathbf{r})\psi_{j\ell} = U_{eff}(r)\psi_{j\ell} \quad (110)$$

with the effective central potential

$$U_{eff}(r) = U_c(r) + \alpha(r)\kappa_\ell. \quad (111)$$

Here  $\kappa_\ell = -\ell$  for  $j = \ell + 1/2$  while  $\kappa_\ell = (\ell + 1)$  for  $j = \ell - 1/2$  for  $\ell > 0$ . Certainly,  $\kappa_\ell = 0$  for  $\ell = 0$ .

The potential which include the terms  $U_{LL}$  proportional to  $L^2$  was suggested in [37]. Satisfactory description of all nuclei was obtained by employing

harmonic oscillator potential combined with the spin orbit term and the one proportional to  $L^2$

$$U(\mathbf{r}) = -U_0 + \frac{m^2\omega^2r^2}{2} - 2\alpha(r)\mathbf{LS} + DL^2; \quad U_0 = -U(r=0) > 0. \quad (112)$$

One can put  $D = 0$  for light nuclei. The values  $D = -(0.056 \pm 0.043)$  MeV provide description of single-particle states in the nucleus  $^{209}\text{Pb}$  [38]. The last term on the right hand side of Eq. (112) is of the order of hundreds keV. This is much smaller than the depth of the well  $U_0$ . However it becomes important for the energy splitting of nucleon levels.

### 3.4. Shell structure of nucleon levels

Consider first the light nuclei with the spectrum determined by Eq. (84). The energies do not depend on the orbital momentum  $\ell$  of the nucleon. There can be  $(2\ell + 1) \cdot 4$  nucleons in the state with fixed value of  $\ell$ . They correspond to  $2\ell + 1$  possible values of the orbital momentum projection  $m = -\ell, -\ell + 1 \dots \ell - 1, \ell$ , two possible values of the spin projection  $s_z = \pm 1/2$  and two possible values of the isospin projection  $T_z = \pm 1/2$ . In other words, there can be  $2(2\ell + 1)$  protons and  $2(2\ell + 1)$  neutrons in a state with orbital momentum  $\ell$ .

Only the value  $\ell = 0$  is possible for the lowest state with  $n = 0$ . There can be 2 protons and 2 neutrons in the state  $1s$ . Next comes the state with  $n = 1$ . Only the value  $\ell = 1$  is possible, and there can be 6 protons and 6 neutrons in the state  $1p$ . The values of  $n = 2$  are consistent with the values  $\ell = 0$  and  $\ell = 2$ . They form the  $2s$  and  $1d$  states with 2 and 10 nucleons of each kind correspondingly. The nucleons in the states with  $n = 3$  can carry orbital momenta  $\ell = 1$  or  $\ell = 3$ . There can be 6 nucleons in the former case and 14 nucleons in the latter case.

Thus in the light nuclei described by totally nonrelativistic potential given by Eq. (83) the nucleons occupy the strongly degenerate levels with  $n = 0, 1, 2, 3$ . There can be as much as 2 protons or neutrons at  $n = 0$ , and 6, 12 and 20 nucleons of each kind at  $n = 1, 2, 3$ . The sets of states with fixed values of  $n$  are called "the shells". Thus the nuclei with totally occupied shells contain 2, 8, 20 and 40 nucleons of each kind for  $n = 0, 1, 2, 3$  correspondingly. They are called "magic nuclei". In "double magic nuclei" both protons and neutrons form totally occupied shells. The single particle binding energies for the double magic nuclei are presented in Table 2.

A small perturbation can eliminate the degeneracy of the levels with different values of  $\ell$ . However the energy splitting remains much smaller than the energy interval between the shells.

Table 2: Single particle binding energies in the field given by Eq. (83). The quantum numbers  $n$  and  $\ell$  are presented in two first colons. The number of protons and neutrons are given in the third colon. Single particle binding energies are given for double magic nuclei ( $N=Z$ ) in MeV units.

$n$	$\ell$	N and Z	$\varepsilon_B$
0	0	2	12.5
1	1	6	10.3
2	0;2	12	9.1
3	1;3	20	8.1

It follows from analysis carried out in Ch.2 that the nucleon separation energies reach their largest values for the closed shells, i.e. for the magic number of nucleons. The purely nonrelativistic Hamiltonian (83) reproduces three lowest magic numbers 2, 8 and 20 with the corresponding double magic nuclei  ${}^4_2\text{He}$ ,  ${}^{16}_8\text{O}$  and  ${}^{40}_{20}\text{Ca}$ . The binding energy per nucleon is 7.1 MeV  ${}^4_2\text{He}$ , while for neighboring nuclei it makes 2.8 MeV for tritium  ${}^3_1\text{H}$  and 2.6 MeV for  ${}^3_2\text{He}$ . Also, there are no stable nuclei with 5 nucleons.

However, the approach predicts magic structure of nuclei with  $N = 40$ . This is not confirmed by experimental data. Also, the experiments show the nuclei with the number of protons  $Z = 28$ , i.e. the isotopes of nickel to be very tightly bound. This is missed by the Hamiltonian (83). Similar situation took place for heavy nuclei. The well-type potentials predicted a set of magic numbers. It did not coincide with those where the separation energies obtained from experiments experienced jumps.

The problem was solved by inclusion of the spin-orbit interaction. Considering the light nuclei we combine the harmonic oscillator potential given by Eq. (83) with the spin-orbit one presented by (106)

$$U(\mathbf{r}) = -U_0 + \frac{m^2\omega^2r^2}{2} - 2\alpha(r)\mathbf{L}\mathbf{s}; \quad U_0 = -U(r=0) > 0. \quad (113)$$

We consider the states with definite values of orbital momentum  $\ell$ . This enables to present

$$U_{eff}(r) = -U_0 + \frac{m^2\omega^2r^2}{2} + \alpha(r)\kappa_\ell. \quad (114)$$

Recall that  $\kappa_\ell$  is defined after Eq. (115). Now let us trace what happens when we add nucleons to the nuclei with totally occupied shells with  $n = 0, 1, 2$ . Now

we are adding nucleons which have definite values of total angular momentum  $\mathbf{j} = \ell + \mathbf{s}$  and its projection  $j_z$ . Two states with orbital momenta  $j = \ell \pm 1/2$  correspond to each value of  $j$ . Since  $\alpha(r) \sim dU(r)/dr > 0$ , the lowest laying states with  $n = 3$  correspond to  $j = 3 + 1/2 = 7/2$ . There are 8 such states corresponding to the values  $j_z = 7/2, 5/2, \dots, -5/2, -7/2$ . They form new closed shell containing 8 nucleons.

To trace the  $A$  dependence of the energy shift caused by the  $LS$  interaction  $\delta\varepsilon = \langle \psi | U_{LS} | \psi \rangle$  we employ Eqs. (106) and (107) and use the square well central potential (90). We find  $\langle \psi | U_{LS} | \psi \rangle \sim r_0^2/R^2 \cdot R^3 \psi^2(R)$ . Since the normalization integral  $\int d^3r \psi^2(r) \sim R^3 \psi^2(R)$  does not depend on  $A$  we find  $\delta\varepsilon \sim A^{-2/3}$  (see Eq. (88)). The  $\ell$  dependence of the shift is determined by the factor  $\kappa_\ell$  defined in the line below Eq. (116). Finally, [33]

$$\delta\varepsilon = \frac{10\kappa_\ell}{A^{2/3}} \text{MeV}. \quad (115)$$

For  $N = Z = 28$  we find  $|\delta\varepsilon| \approx 2 \text{MeV}$ . This is of the same order as the energy splitting between the shells with  $n = 3$  and  $n = 4$ . Thus 28 becomes a magic number.

We face similar situation with heavier nuclei described by the well-type central potentials. The wave equation predicts the shell structure of the levels. However the magic numbers differ from the observed ones. Inclusion of the  $LS$  interaction removes the discrepancy. This adds 50, 82 and 126 to the sequence of the magic numbers. The approach predicts the "islands of stability" for the heavy transuranium nuclei which were not observed yet.

This picture is sometimes called the shell model. Note that the very shell structure of levels is a direct consequence of the wave equation. The model assumption is the large value of spin-orbit interaction.

The explanation of the magic numbers was obtained mainly due to the studies of Maria Goeppert-Mayer and Hans D. Jensen. They worked on the subject separately in USA and in Germany correspondingly. In their Nobel lectures (they shared the prize in 1963) the two scientists recalled that it was not easy to get the physical community to accept the key role of the spin-orbit interactions [39].

Goepert Mayer told the people about her discussion of nuclear levels with Enrico Fermi. "One day as Fermi was leaving the office he asked me: "Is there any indication of spin-orbit coupling? ...Only if one had lived with the data as long as I could one immediately answer: "Yes, of course and that will explain everything." Fermi was sceptical and left me with my numerology... After a week when I had written up all the consequence carefully, Fermi was no longer sceptical. He even taught this in his classes in nuclear physics."

Also Hans Jensen recalled how Robert Openheimer told him that “Maria [Goeppert-Mayer] and you are trying to explain magic be miracles... ” and also “...Wigner ”said something quite similar...in his careful way of choosing his words”. Jensen told also that “a serious journal refused to publish our first letter [on the magic numbers], stating ‘it is not really physics but rather playing with numbers’ ”.

## References

- [1] B. L. Ioffe, V. S. Fadin, and L. N. Lipatov, *Quantum Chromodynamics. Perturbative and Nonperturbative Aspects* (Cambridge University Press, 2010).
- [2] R. Frisch and O. Stern, *Zeitschrift für Physik* **85**, 4 (1933).
- [3] I. Estermann and O. Stern, *Zeitschrift für Physik* **85**, 17 (1933).
- [4] R. F. Bacher, *Phys. Rev.* **43**, 1001 (1933).
- [5] L. W. Alvarez and F. Bloch, *Phys. Rev.* **57**, 111 (1940).
- [6] P. Kusch and H. M. Foley, *Phys. Rev.* **72**, 1256 (1947).
- [7] J. Schwinger, *Phys. Rev.* **73**, 416 (1948).
- [8] B. D. Serot and J. D. Walecka, *Relativistic Nuclear Many-Body Theory* (Springer US, Boston, MA, 1992), pp. 49–92.
- [9] L. Landau and E. Lifshitz, *Quantum Mechanics* (Pergamon, 1977).
- [10] Y. B. Zeldovich and V. S. Popov, *Usp. Fiz. Nauk* **105**, 403 (1971).
- [11] S. L. Shapiro and S. A. Teukolsky, *Black Holes, White Dwarfs, and Neutron Stars* (John Wiley & Sons, Ltd, 1983).
- [12] G. Miller, B. Nefkens, and I. Šlaus, *Physics Reports* **194**, 1 (1990).
- [13] J. A. Nolen and J. P. Schiffer, *Annual Review of Nuclear Science* **19**, 471 (1969).
- [14] H. Bethe and P. Morrison, *Elementary Nuclear Theory* (Dover Books on Physics Series (Dover Publications, 2006)).

- [15] C. F. v. Weizsäcker, *Zeitschrift für Physik* **96**, 431 (1935).
- [16] G. Royer and C. Gautier, *Phys. Rev. C* **73**, 067302 (2006).
- [17] M. Wang, W. J. Huang, F. G. Kondev, G. Audi, and S. Naimi, *Chin. Phys. C* **45**, 030003 (2021).
- [18] R. Shurtleff and E. Derrin, *American Journal of Physics* **57**, 552 (1989).
- [19] N. R. S. Harsha, *European Journal of Physics* **39**, 035802 (2018).
- [20] K. Heyde, *Basic Ideas and Concepts in Nuclear Physics* (Inst. of Phys. Publishing, 2004).
- [21] H. A. Bethe and R. F. Bacher, *Rev. Mod. Phys.* **8**, 82 (1936).
- [22] Y. I. Frenkel, *Sov. Phys. ZhETP* **9**, 641 (1939).
- [23] J. Frenkel, *Phys. Rev.* **55**, 987 (1939).
- [24] N. Bohr and J. A. Wheeler, *Phys. Rev.* **56**, 426 (1939).
- [25] L. Landau and E. Lifshitz, *Electrodynamics of Continuous Media* (Pergamon Press, 1960).
- [26] G. C. Baldwin and G. S. Klaiber, *Phys. Rev.* **71**, 3 (1947).
- [27] M. Goldhaber and E. Teller, *Phys. Rev.* **74**, 1046 (1948).
- [28] S. Frankel and N. Metropolis, *Phys. Rev.* **72**, 914 (1947).
- [29] L. Landau, *Sov. Phys. J. Exptl. Theoret. Phys.* **35**, 97 (1958).
- [30] A. B. Migdal and S. A. Moszkowski, *American Journal of Physics* **36**, 855 (1968).
- [31] L. Landau and E. Lifshitz, *Theory of condensed state* (Oxford, 1980).
- [32] L. I. Schiff, *Quantum Mechanics* (McGraw-Hill, New York–Toronto–London, 1955).
- [33] A. Bohr and B. Mottelson, *Nuclear structure* (W.A. Benjamin, Inc, NY, New York, 1969).
- [34] S. Flugge, *Practical Quantum Mechanics I* (Springer-Verlag, Berlin–New York, 1971).

- [35] K. A. Brueckner, *Phys. Rev.* **97**, 1353 (1955).
- [36] D. Vautherin and D. M. Brink, *Phys. Rev. C* **5**, 626 (1972).
- [37] S. G. Nilsson, *Mat. Fys. Medd. Dan. Vid. Selsk* **29** (1955).
- [38] J. Aisenberg and W. Greiner, *Nuclear Theory* (North Holland Pub. Co., Amsterdam, 1970).
- [39] *Nobel Lectures, Physics 1963-1970* (Elsevier Publishing Company, Amsterdam–London–New York, 1972).

# НЕРАВНОВЕСНЫЙ ГИДРОДИНАМИЧЕСКИЙ ПОДХОД ДЛЯ ОПИСАНИЯ ЭМИССИИ ВЫСОКОЭНЕРГЕТИЧЕСКИХ ВТОРИЧНЫХ ЧАСТИЦ В СТОЛКНОВЕНИЯХ ТЯЖЕЛЫХ ИОНОВ ПРОМЕЖУТОЧНЫХ ЭНЕРГИЙ

Александр Т. Дьяченко<sup>1,2</sup>

<sup>1</sup> Петербургский институт ядерной физики НИЦ «КИ», Гатчина

<sup>2</sup> Петербургский государственный университет путей сообщения

## Аннотация

С целью развития гидродинамического подхода для описания столкновений тяжелых ионов промежуточных энергий в работе предложено совместно с решением уравнений гидродинамики решать кинетическое уравнение. Это позволило включить в рассмотрение неравновесную компоненту и успешно описать двойные дифференциальные сечения испускания кумулятивных протонов, пионов и фотонов при столкновениях тяжелых ядер углерода с бериллиевой мишенью в области энергий 0.3–3.2 ГэВ/нуклон, полученные в экспериментах ИТЭФ. При описании этих спектров были учтены поправка на микроканоническое распределение и вклад процесса фрагментации для выходов протонов. Полученное описание экспериментальных данных оказалось лучше, чем в каскадных моделях и моделях квантовой молекулярной динамики. Проведено сравнение с другими реакциями и подходами. Оказалось, что эффекты короткодействующих корреляций включены в предложенном подходе, поскольку в нем успешно описываются экспериментальные данные по спектрам жестких фотонов, которые в молекулярной динамике согласуются с экспериментом только при добавлении высокоимпульсной компоненты. В термодинамической модели предложена интерпретация спектров мягких фотонов по поперечному импульсу в  $pp$ -столкновениях с учетом бозона  $X_{17}$  с массой 17 МэВ – новой частицы, возможного кандидата на роль частиц темной материи. На основе объединения двумерных квантовой хромодинамики и квантовой электродинамики в модели трубки найдена масса частиц.

# NON-EQUILIBRIUM HYDRODYNAMIC APPROACH FOR DESCRIPTION OF THE EMISSION OF HIGH ENERGY OF SECONDARY PARTICLES IN HEAVY ION COLLISIONS INTERMEDIATE ENERGIES

Alexandr T. D'yachenko<sup>1,2</sup>

<sup>1</sup> Petersburg Nuclear Physics Institute of NRC "KI", Gatchina

<sup>2</sup> Emperor Alexander I Petersburg State Transport University, St. Petersburg

Abstract

In order to develop a hydrodynamic approach for describing collisions of heavy ions of intermediate energies, it is proposed in this paper to solve the kinetic equation together with the solution of the equations of hydrodynamics. This made it possible to include the nonequilibrium component in the consideration and successfully describe the double differential cross sections for the emission of cumulative protons, pions, and photons in collisions of heavy carbon nuclei with a beryllium target in the energy range 0.3–3.2 GeV/nucleon obtained in the ITEP experiments. When describing these spectra, the correction for the microcanonical distribution and the contribution of the fragmentation process for proton yields were taken into account. The obtained description of the experimental data turned out to be better than in cascade models and models of quantum molecular dynamics. A comparison with other reactions and approaches was made. It turned out that the effects of short-range correlations are included in the proposed approach, since it successfully describes the experimental data on the spectra of hard photons, which in molecular dynamics agree with the experiment only when a high-momentum component is added. In a thermodynamic model, an interpretation of the transverse momentum spectra of soft photons in  $pp$  collisions is proposed, taking into account the X17 boson with a mass of 17 MeV, a new particle, a possible candidate for the role of dark matter particles. Based on the combination of two-dimensional quantum chromodynamics and quantum electrodynamics in the tube model, the mass of particles is found.

# 1 Введение

Успех применения гидродинамики к столкновениям элементарных частиц высокой энергии начался с работы Л.Д. Ландау по множественному рождению вторичных частиц [1]. В [2] впервые использовано равновесное уравнение состояния, предполагающее установление в системе локального термодинамического равновесия для описания столкновений тяжелых ионов. В [3, 4] для энергий строящегося в ОИЯИ (Дубна) ускорительного комплекса «НИСА» предложено использовать гибридную модель, которая включает в себя быструю неравновесную кинетическую стадию на основе кода HSD (адронная струнная динамика) и последующее описание динамики ядро-ядерного столкновения на основе равновесной релятивистской гидродинамики (см. также [5, 6]). В [5] гибридная модель была усовершенствована включением вязкости в релятивистскую гидродинамику и заменой кода HSD на PHSD (партон-адронная струнная динамика). Это дополняет описание процесса столкновения тяжелых ионов, проведенное как в рамках одножидкостной [7], так и двухжидкостной [8] и трехжидкостной [9] релятивистских гидродинамических моделей, поскольку существенную роль в процессе столкновения ядер играет его неравновесный характер.

С другой стороны, начатый А.М. Балдиным поиск объяснения механизма ядерных кумулятивных процессов [10, 11], кинематически запрещенных во взаимодействиях свободных нуклонов, до сих пор является нерешенной проблемой. Было предложено большое количество теоретических подходов, варьирующихся от образования многокварковых кластеров в ядерной материи [12, 13] до эффектов многократного рассеяния при прохождении частиц через ядро [14, 15]. Исследование этого явления в случае столкновения тяжелых ионов представляет интерес с целью выяснения коллективного многочастичного механизма кумулятивных процессов и проверки различных моделей ядро-ядерного взаимодействия при промежуточных и высоких энергиях. Это отмечается в обзоре Г.А. Лексина [16], сделанном на XXXV Зимней школе ПИЯФ.

В [17–22] нами было показано, что локальное термодинамическое равновесие в процессе столкновений тяжелых ионов устанавливается не сразу, поскольку на стадии сжатия важна неравновесная компонента функции распределения, приводящая к формированию бесстолкновительной ударной волны, аналогично бесстолкновительным ударным волнам в расчетах по зависящему от времени методу Хартри–Фока (TDHF) [23]. Для учета неравновесной компоненты было предложено совместно с уравнениями гидродинамики решать кинетическое уравнение. В [21] нами была усовершен-

ствована модель ударной волны с изменяющимся фронтом, предложенная в пионерской работе W. Scheid, H. Muller, W. Greiner [24], которая затем применена к процессу сжатия образующегося горячего пятна – hot spot.

В настоящей работе рассмотрено необходимое развитие гидродинамического подхода при описании столкновений тяжелых ионов промежуточных энергий, с одной стороны, и его применение к описанию спектров кумулятивных вторичных частиц, с другой. В предыдущих работах [17–22] в рамках неравновесного гидродинамического подхода рассчитаны дифференциальные сечения образования протонов, пионов и легких фрагментов при относительно низких энергиях ( $E < 1-2$  ГэВ на нуклон). В процессе развития гидродинамического подхода с неравновесным уравнением состояния [17–20] нами рассмотрены столкновения ядер  $^{12}\text{C}$  с бериллиевой мишенью при энергиях налетающих ядер углерода 2.0 и 3.2 ГэВ/нуклон [25], экспериментально исследованные на ускорителе ИТЭФ, с испусканием протонов [26, 27], пионов [27] и фотонов [28]. Данные недавней работы [27] группы ИТЭФ были предоставлены нам В.В. Куликовым.

Решение гидродинамических уравнений здесь найдено численно, но нами показано [29], что, в принципе, можно получить аналитическое решение уравнений с помощью солитонов. Также уравнения квантовой релятивистской гидродинамики могут быть связаны с уравнением Клейна–Гордона [30] аналогично представлению Маделунга для временного уравнения Шредингера.

Анализируя вслед [31] экспериментальные данные [32] по спектрам мягких фотонов в зависимости от поперечного импульса, в данной работе предлагается интерпретировать ужесточение спектра [32] как проявление вклада новой частицы бозона X17, массой около 17 МэВ, являющуюся кандидатом на роль частиц темной материи. Предложен алгоритм нахождения массы бозона X17 на основе модели трубки [33].

Настоящая работа является естественным продолжением лекции, прочитанной автором на XXXV Зимней школе ПИЯФ и посвященной подпороговым тяжелым мезонам и антипротонам в столкновениях тяжелых ионов [34]. Далее изложение построено следующим образом. В разделе 2 описан неравновесный гидродинамический подход. В разделе 3 описана схема наших гидродинамических расчетов с учетом микроканонической поправки. В разделе 4 приведены формулы для учета статистического механизма фрагментации, предложенного [35, 36]. В разделах 5–7 приведено сравнение с экспериментальными данными и другими моделями и кодами. Показан успех нашего гидродинамического подхода при описании экспериментальных данных коллаборации HADES (GSI) [37] и преимущество

нашего подхода в описании спектров кумулятивных частиц (протонов, пионов и фотонов) по сравнению с кодами, использованными в работах [26, 27], а также с кодом HSD [38], использованном нами. Используемые в [26, 27] коды являются вполне современными, и они встроены в пакет GEANT4, также востребованным является и код HSD, созданный в институте теоретической физики в Гессене (Германия). В разделе 7 также показано, что наш подход описывает спектры жестких фотонов, которые в работе [39] описывались только за счет эффекта короткодействующих корреляций (SRC). В разделе 8 найдены формулы для фотонов от распада новых частиц и проведено сравнение с экспериментальными данными, обосновываются массы бозонов X17 и X38 В Заключении, раздел 9, приведены основные результаты работы.

## 2 Неравновесный гидродинамический подход

Для описания системы нуклонов воспользуемся одночастичной функцией распределения  $f(\mathbf{r}, \mathbf{p}, t)$  ( $\mathbf{r}$  – пространственная координата,  $\mathbf{p}$  – импульс,  $t$  – время), для которой при промежуточных энергиях сталкивающихся тяжелых ионов мы используем кинетическое уравнение [17–20]:

$$\frac{df}{dt} = \frac{f_0 - f}{\tau}, \quad (1)$$

где  $f_0(\mathbf{r}, \mathbf{p}, t)$  – локально равновесная функция распределения,  $\tau$  – время релаксации. Уравнение (1) должно решаться совместно с уравнениями гидродинамики, следующими из (1) взятием моментов с весом  $1$ ,  $\mathbf{p}$ ,  $\mathbf{p}^2$  в импульсном пространстве для нахождения функции распределения. Входящий в члены взаимодействия самосогласованный потенциал  $W(\rho)$  задается так же, как это делается в случае зависящих от плотности эффективных сил типа сил Скирма. Время релаксации здесь выбрано в традиционной форме  $\tau = \lambda/v_T$  [17–20], где длина свободного пробега нуклонов  $\lambda = 1/\sigma\rho$ ,  $\sigma \approx 40$  мбн – элементарное полное нуклон-нуклонное сечение,  $\rho$  – нуклонная плотность,  $v_T$  – средняя скорость теплового движения нуклонов. При низких энергиях для выбранной формы  $\tau$  его численное значение близко к значению, полученному для ферми-жидкости. При высоких энергиях нужно вместо сечения  $\sigma$ , вообще говоря, подставлять транспортное сечение  $\sigma_T$ , что увеличивает величину  $\tau$ . При больших временах релаксации можно использовать уравнения неравновесной длиннопробежной гидродинамики в приближении локальной плотности [21].

Решение уравнения (1) ищется в виде

$$f(\mathbf{r}, \mathbf{p}, t) = f_1 q + f_0(1 - q), \quad (2)$$

где функция  $f_1(\mathbf{r}, \mathbf{p}, t)$  соответствует состоянию с деформированной ферми-поверхностью,  $q(\mathbf{r}, t)$  ( $0 \leq q \leq 1$ ) – релаксационный фактор, находящийся из кинетического уравнения с помощью взятия момента с весом  $p_{\parallel}^2 - p_{\perp}^2$ , определяющего степень анизотропии функции распределения в импульсном пространстве [17–20] ( $p_{\parallel}$  и  $p_{\perp}$  – соответственно, продольная и поперечная составляющие импульса). При  $q = 0$  получаем уравнения равновесной гидродинамики, а при  $q = 1$  получаем уравнения неравновесной длиннопробежной гидродинамики. В результате, имеем замкнутую систему уравнений для нахождения плотности  $\rho(\mathbf{r}, \mathbf{t})$ , поля скоростей  $\mathbf{v}(\mathbf{r}, \mathbf{t})$ , поля температур  $T(\mathbf{r}, \mathbf{t})$  и релаксационного фактора  $q(\mathbf{r}, \mathbf{t})$ , позволяющую найти функцию распределения  $f(\mathbf{r}, \mathbf{p}, \mathbf{t})$ .

### 3 Инклюзивное дифференциальное сечение процесса

После выделения области локального нагрева hot spot – области перекрытия сталкивающихся ядер – мы проанализировали стадии сжатия, расширения и разлета вещества в процессе столкновений тяжелых ионов. На стадии сжатия формируются бесстолкновительные ударные волны с изменяющимся фронтом [20, 21].

На стадии расширения [17–20] по достижении ударной волной границ hot spot происходит расширение первоначально сжатой системы, которое описывается с учетом ядерной вязкости, найденной нами в релаксационном  $\tau$ -приближении. В рассматриваемом диапазоне энергий на этой стадии коэффициент вязкости  $\eta$  достаточно велик (число Рейнольдса  $Re = \frac{m\rho v}{\eta} < 1$ ). Это уменьшает скорость разлета hot spot и увеличивает его температуру. По достижении расширяющейся ядерной системой критической плотности (плотности замораживания)  $\rho^*$ , определяемой из условия  $\frac{dW}{d\rho} = 0$ , происходит формирование вторичных частиц (нуклонов, фрагментов, пионов) и их разлет. Инвариантное двойное дифференциальное сечение испускания протонов в реакции  $A + B \rightarrow p + X$  имеет вид ( $b$  – параметр удара):

$$E \frac{d^2\sigma}{p^2 dp d\Omega} = \frac{2\pi}{(2\pi\hbar)^3} \int G(b) b db \int d\mathbf{r} \gamma(E - \mathbf{p}\mathbf{v}) f(\mathbf{r}, \mathbf{p}, t), \quad (3)$$

где  $G(b) = \sigma_t/\sigma_g$  – фактор, учитывающий, что сечение образования hot spot  $\sigma_t = \pi < R_b >^2$  всегда больше геометрического  $\sigma_g$ -сечения перекрывающихся частей,  $E = \sqrt{p^2 + m^2}$ ,  $\gamma = 1/\sqrt{1 - v^2}$  и  $\mathbf{p}$  – соответственно, полная энергия, Лоренц-фактор и импульс протонов,  $\Omega$  – телесный угол,  $\mathbf{v}(\mathbf{r}, \mathbf{t})$  – поле скоростей,  $f(\mathbf{r}, \mathbf{p}, \mathbf{t})$  – функция распределения испускаемых протонов в пренебрежении неравновесной компонентой на стадии замораживания

$$f(\mathbf{r}, \mathbf{p}, t) = g \left[ \exp \left( \frac{\gamma(E - \mathbf{p}\mathbf{v} - \mu) + T\delta}{T} \right) \pm 1 \right]^{-1}. \quad (4)$$

В (4) спиновый фактор  $g = 2$ ,  $\mu(\mu = \mu_T + m)$  – химический потенциал, который находится из условия сохранения в среднем числа частиц для большого канонического ансамбля,  $T$  – температура,  $\delta$  – поправка на микроканоническое распределение [17]. Знак « $\pm$ » означает, соответственно, «+» для фермионов и «-» для бозонов. Для описания испускания пионов можно использовать выражения (3) и (4), где в качестве функции распределения пионов можно использовать функцию (4), положив везде массу пионов равной  $m_\pi$ , а химический потенциал равным нулю, поскольку число пионов не задано. Для фотонов масса и химический потенциал равны нулю с учетом двух поляризаций. Для бозонов в (4) выбираем знак «-» перед 1. Кроме вклада (3) в сечение от испускания протонов из hot spot нами учитывался также вклад от слияния неперекрывающихся частей сталкивающихся ядер – «спектаторов», как в модели «корона-кор» при высоких энергиях [40]. Временная эволюция hot spot, сжатие и последующее его разрежение напоминают флуктуации в ядерной системе, подобные флуктону Д.И. Блохинцева [41], введенному для объяснения кумулятивного эффекта.

## 4 Статистический механизм фрагментации

Для описания мягкой части спектра испускаемых протонов нами использована статистическая модель фрагментации сталкивающихся тяжелых ионов, предложенная в [35, 36]. Согласно этой модели, вероятность выхода фрагментов из составного ядра пропорциональна  $\exp(-p^2/2\sigma_K^2)$ , где  $\mathbf{p}$  – импульс фрагмента в системе покоя ядра, дисперсия  $\sigma_K^2$

$$\sigma_K^2 = \sigma_0^2 \frac{K(A - K)}{A - 1}, \quad (5)$$

где  $A$  – массовое число фрагментирующего ядра, а  $K$  – число нуклонов во фрагменте,

$$\sigma_0^2 = \frac{\langle p^2 \rangle}{3} = \frac{1}{3} \frac{3}{5} p_F^2, \quad (6)$$

$p_F$  – импульс Ферми. Ограничимся испусканием протонов с  $K = 1$ , а нормировочный множитель  $C$  для определения выхода протонов найдем из условия [36]:

$$C4\pi \int \frac{p^2 dp}{(2\pi\hbar)^3} \exp\left(-\frac{p^2}{2\sigma_0^2}\right) = A/4/V. \quad (7)$$

В результате,  $C = \frac{A(2\pi\hbar)^3}{4\pi\sqrt{\pi}(2\sigma_0^2)^{3/2}V}$ , где  $V$  – объем системы. Используя (7), определяем, [18], вклад в сечение при фрагментации протонов ( $b$  – параметр удара):

$$E \frac{d^2\sigma}{p^2 dp d\Omega} = \frac{2\pi}{(2\pi\hbar)^3} \int b db \int C dr \gamma(E - \mathbf{p}\mathbf{v}) \exp\left(-\frac{(\mathbf{p} - \mathbf{p}_0)^2}{2\sigma_0^2}\right), \quad (8)$$

где  $E$  – полная энергия испускаемого протона,  $\mathbf{p}$  ( $p = \sqrt{E^2 - m^2}$ ) – импульс протона с учетом движущейся со скоростью  $\mathbf{v}(\mathbf{r}, t)$  системы отсчета ( $r$  – радиус-вектор,  $t$  – момент времени начала фрагментации),  $\mathbf{p}_0 = \gamma\mathbf{m}\mathbf{v}$ . Отметим, что сечение (8) относится к неперекрывающимся частям сталкивающихся тяжелых ионов – периферическая фрагментация. В (8) учтено, что при вылете протоны могут запираются средним полем за счет энергии связи, от которой надо отсчитывать энергию  $E$ . Вклад от фрагментации составного ядра, образующегося из перекрывающихся частей, получен аналогичным образом. В этом случае можно использовать (8) с  $\sigma_0^2 = mT$  при температуре  $T$  образующегося составного ядра – hot spot, временная эволюция которого рассматривается нами в гидродинамическом подходе [17–21].

## 5 Сравнение с экспериментальными данными

В качестве иллюстрации успеха гидродинамического подхода на рис. 1 (левая панель) приведены распределения  $\frac{dN}{p_T dp_T}$  испускаемых  $N$ -протонов по поперечному импульсу  $p_T$  в реакции  $^{197}\text{Au} + ^{197}\text{Au} \rightarrow p + X$  на фиксированной мишени при энергии налетающих ядер золота 1.48 ГэВ/нуклон. Можно видеть, что наш расчет (сплошная линия) находится в согласии с другими расчетами, проведенными в рамках решения кинетического уравнения Больцмана–Улинга–Уленбека (BUU) [38, 42] и модели квантовой молекулярной динамики [43, 44]. Эти расчеты приведены для сравнения различных кодов в [45].

Наш подход применим не только к данной реакции. Например, нам удалось воспроизвести (см. рис. 1, правая панель) экспериментальные данные коллаборации HADES [37] по энергетическим спектрам протонов в реакции  $\text{Ar} + \text{K} \rightarrow p + \text{X}$  при энергии ядер  $\text{Ar}$ , равной 1.76 ГэВ/нуклон. В расчетах выходов протонов учитывался вклад от фрагментации в области как перекрывающихся, так и неперекрывающихся областей сталкивающихся ядер. На рис. 1 (правая панель) приведены инвариантные двойные дифференциальные распределения протонов в зависимости от поперечной массы. Наши расчеты изображены сплошными линиями, экспериментальные точки взяты из [37]. Выходы протонов были нормированы на число участников  $N_0 = 38.5$  [37]. Как видно из рисунка, получено хорошее согласие расчетных распределений с экспериментальными во всех интервалах быстрот  $y$ , где  $y = \ln \left( \frac{p_{\parallel}}{m_T} + \sqrt{1 + \left( \frac{p_{\parallel}}{m_T} \right)^2} \right)$ ,  $p_{\parallel}$  – продольный импульс,  $m_T = \sqrt{m_0^2 + p_T^2}$  – поперечная масса. Другими словами, наш расчет оказался ничем не хуже более детального расчета, проведенного ранее в [46]. Рассмотренные реакции представляют интерес для экспериментов, проводимых на ускорителе SIS/GSI (Германия) и могут быть перенесены на область энергий строящегося в ОИЯИ (Дубна) ускорительного комплекса NICA.

## 6 Описание спектров кумулятивных протонов и пионов в экспериментах ИТЭФ

На рис. 2 приведены импульсные спектры протонов, испускаемых в реакции  $^{12}\text{C} + ^9\text{Be} \rightarrow p + \text{X}$  под углом  $3.5^0$  при энергии ионов  $^{12}\text{C}$ , равной 2.0 ГэВ/нуклон (рис. 2 (левая панель)) и 3.2 ГэВ/нуклон (рис. 2 (правая панель)). Экспериментальные данные, полученные в эксперименте FRAGM (ИТЭФ) [26, 27], показаны точками. Кривыми 1, 2 представлены результаты наших расчетов в рамках гидродинамического подхода для всей области импульсного спектра, при этом параметры расчета –  $\langle T_h \rangle$  – средняя температура hot spot,  $\langle \mu_T \rangle$  – средний химический потенциал,  $\langle R_h \rangle$  – средний радиус hot spot – зависят от энергии. Кривые 3, 4, 5 – результаты расчетов по транспортным кодам [26]: 3 – каскадная модель [47], 4 – транспортная модель кварк-глюонных струн [48], 5 – модель квантовой молекулярной динамики (QMD), встроенной в монте-карловский пакет GEANT4 [49]. Кривая 6 – наш расчет по коду адронной струнной динамики (HSD) [38].

Как видно из этих рисунков, в кумулятивной области спектров при им-

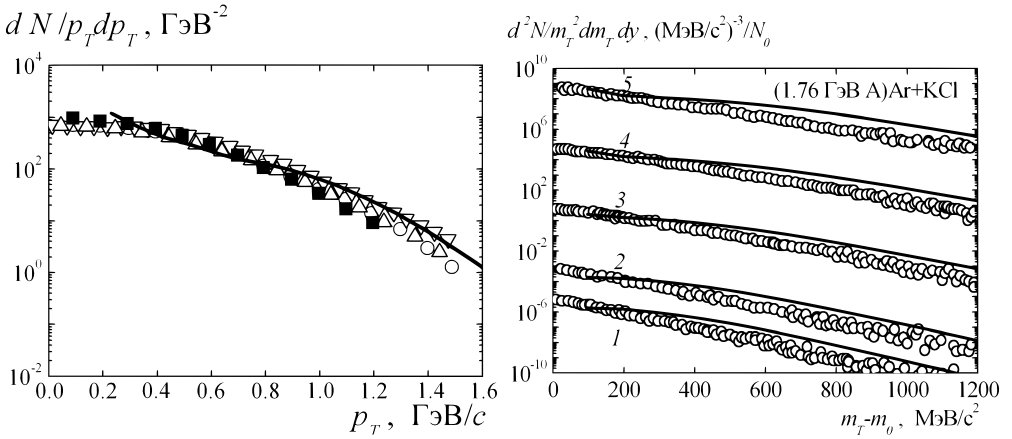


Рис. 1: Левая панель. Распределения протонов по поперечному импульсу  $p_T$  реакции  $\text{Au}+\text{Au} \rightarrow p+X$  при энергии ионов золота 1.48 ГэВ/нуклон с параметром удара  $b=1$  Фм. Сплошная кривая – наш расчет при температуре hot spot  $\langle T_h \rangle \approx 84.8$  МэВ. Значками показаны результаты расчетов по транспортным кодам [45]:  $\circ$  – [38],  $\Delta$  – [42],  $\nabla$  – [43],  $\blacksquare$  – [44]. Правая панель. Инвариантные распределения протонов в зависимости от поперечной массы  $m_T$  в реакции  $\text{Ar}+\text{KCl} \rightarrow p+X$ , испускаемых в интервале быстрот  $y$  при энергии ионов Ar 1.76 ГэВ/нуклон кривые: 1 –  $\times 10^2$  ( $0.1 < y < 0.15$ ), 2 –  $\times 10^4$  ( $0.2 < y < 0.25$ ), 3 –  $\times 10^8$  ( $0.4 < y < 0.45$ ), 4 –  $\times 10^{12}$  ( $0.6 < y < 0.65$ ), 5 –  $\times 10^{16}$  ( $0.8 < y < 0.85$ ) при  $\langle T_h \rangle \approx 91$  МэВ, средний химический потенциал  $\mu_T \approx 155$  МэВ,  $\langle R_h \rangle \approx 3.5$  фм точки – экспериментальные данные коллаборации NA49 из [37].

пульсе протонов  $p > 2$  ГэВ/с, когда кумулятивное число  $X = \frac{E - p \cos \theta}{m} > 1$ , наш расчет согласуется с экспериментальными данными [26, 27]. Спад величины сечений на 5 порядков воспроизводится в нашем подходе не хуже монте-карловских транспортных кодов. Причем, некоторые каскадные расчеты заметно недооценивают экспериментальные спектры в высокоимпульсной области. В области малых импульсов при всех энергиях наш расчет также воспроизводит экспериментальные спектры, что обусловлено вкладом от протонов, образующихся в результате фрагментации (согласно выражению (8)) для перекрывающихся и неперекрывающихся частей сталкивающихся ядер. Поправка на микроканоническое распределение проявляется в высокоимпульсной области распределений протонов.

Если не учитывать вклад от фрагментации и не вводить поправку на микроканоническое распределение (штриховые кривые 2), то в мягкой

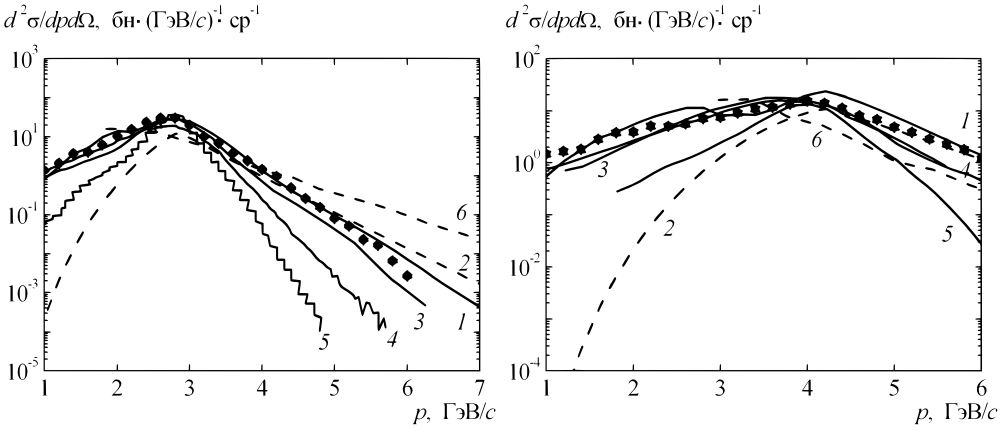


Рис. 2: Левая панель. Распределения протонов по лабораторному импульсу в реакции  $^{12}\text{C}+^9\text{Be} \rightarrow p+X$ , испускаемых под углом  $3.5^\circ$  при энергии  $^{12}\text{C}$  2.0 ГэВ/нуклон. Кривая 1 – наш расчет с значениями  $\langle T_h \rangle \approx 99$  МэВ,  $\langle \mu_T \rangle \approx -180$  МэВ,  $\langle R_h \rangle \approx 2$  Фм, штриховая кривая 2 – наш расчет без учета поправки на микроканоническое распределение и вклада от фрагментации; точки – экспериментальные данные из [26]. Кривые 3, 4, 5 – результаты расчетов по транспортным кодам [26]. Кривая 6 – результат проведенного нами расчета в модели HSD [38]. Правая панель. То же, что на левой панели при энергии ионов  $^{12}\text{C}$  3.2 ГэВ/нуклон и  $\langle T_h \rangle \approx 122$  МэВ,  $\langle \mu_T \rangle \approx -263$  МэВ, точки – экспериментальные данные из [27].

области спектра расчеты недооценивают эксперимент, а в кумулятивной области дают завышенные по сравнению с ним значения. Расчет на основе модели HSD (кривые 6 на рис. 2) также не описывает экспериментальные данные. На рис. 2 (левая панель) вычисленный в этой модели высокоимпульсный спектр оказался более пологим, чем экспериментальный, а на рис. 2 (правая панель) он недооценивает величину сечения. Форма спектра и в мягкой области не совпадает с экспериментальной, потому что в этом коде не учитывается механизм фрагментации.

Наш подход применим и к испусканию кумулятивных пионов, полученных в реакции  $^{12}\text{C}+^9\text{Be} \rightarrow \pi^-+X$  на ускорителе ИТЭФ при энергиях ядер  $^{12}\text{C}$  3.2 ГэВ/нуклон [27]. Нам удалось воспроизвести экспериментальные данные [27] по энергетическим спектрам отрицательных пионов (рис. 3 (левая панель)). В сечение рождения  $\pi^-$ -мезонов помимо тепловых  $\pi^-$  также вносит вклад канал от распада  $\Delta \rightarrow N+\pi^-$ , который мы включили в рассмотрение аналогично [50, 51]. В качестве иллюстрации на рис. 3 (левая панель) приведены инвариантные двойные дифференциальные сече-

ния испускания отрицательных пионов в реакциях  $^{12}\text{C}+^9\text{Be}\rightarrow\pi^-+X$  при энергии ядер углерода 3.2 ГэВ/нуклон, экспериментальные точки взяты из [27]. Сплошные кривые 1 – наш расчет, штриховые кривые 2 – наш расчет без учета поправки на микроканоническое распределение. Кривые 3, 4, 5 – результаты расчетов по транспортным кодам [27] в современных теоретических моделях, которые были использованы для расчета спектров протонов. Наш расчет в рамках гидродинамического подхода показывает хорошее согласие с экспериментальными спектрами [27]. Рассчитанный нами спектр (кривая 6) по модели HSD показывает более быстрый спад, чем экспериментальный.

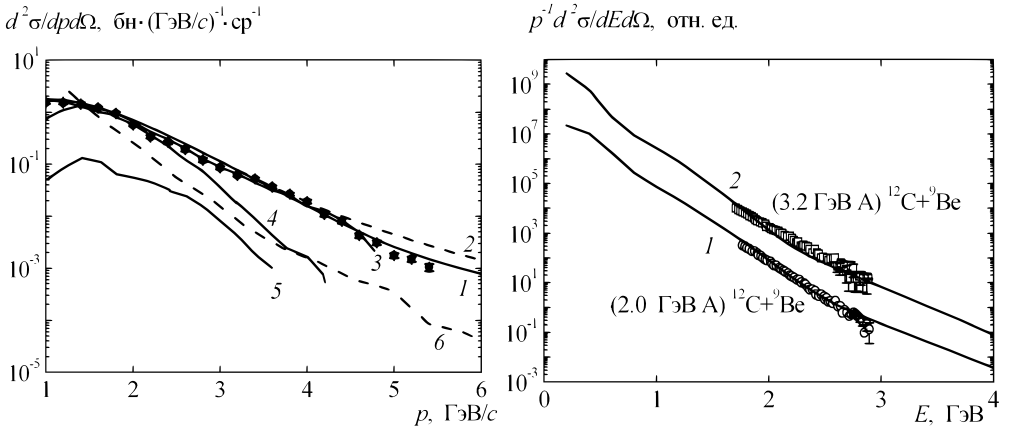


Рис. 3: Левая панель. То же, что на рис. 2, но для распределения  $\pi^-$ -мезонов в реакции  $^{12}\text{C}+^9\text{Be}\rightarrow\pi^-+X$ , при энергии ионов  $^{12}\text{C}$  3.2 ГэВ/нуклон и  $\langle T_h \rangle \approx 122$  МэВ, точки – экспериментальные данные из [27]. Правая панель. Инвариантные распределения фотонов по энергии в реакции  $^{12}\text{C}+^9\text{Be}\rightarrow\gamma+X$ , испускаемых под углом  $38^\circ$  при энергии ионов  $^{12}\text{C}$  2.0 ГэВ/нуклон (кривая 1 – расчет с  $\langle T_h \rangle \approx 99$  МэВ) и 3.2 ГэВ/нуклон (кривая 2 – расчет с  $\langle T_h \rangle \approx 122$  МэВ), точки – экспериментальные данные из [28] (кружки при энергии  $^{12}\text{C}$  2.0 ГэВ/нуклон и квадраты – 3.2 ГэВ/нуклон).

## 7 Спектры жестких фотонов

На рис. 3 (правая панель) приведены инвариантные двойные дифференциальные сечения жестких фотонов, образующихся в реакции  $^{12}\text{C}+^9\text{Be}\rightarrow\gamma+X$  при энергиях ядер  $^{12}\text{C}$  2.0 и 3.2 ГэВ/нуклон под углом испускания фотонов  $38^\circ$ . Здесь сплошные линии – наш расчет. Экспериментальные

точки из [28] в эксперименте FLINT (ИТЭФ). Для испускания прямых фотонов можно использовать выражения (3) и (4). Полученные таким способом прямые фотоны преобладают над фотонами от распада  $\pi^0$ -мезонов, вклад которых мы также учли и добавили к вкладу прямых фотонов. Поскольку экспериментальные данные приведены в относительных единицах, расчетные кривые также нормированы.

Нам представляется, что в гидродинамическом подходе учитывается эффект короткодействующих корреляций (SRC), которому уделяется большое внимание (см., например, [13]). На рис. 4 (левая панель) приведены рассчитанные нами двойные дифференциальные сечения фотонов, испускаемых в реакции  $^{14}\text{N} + ^{12}\text{C} + \gamma + \text{X}$  при энергиях ядер азота 20 (кривая 1), 30 (кривая 2) и 40 (кривая 3) МэВ/нуклон под углом испускания фотонов  $90^\circ$ . Экспериментальные точки взяты из [52]. Как видно из рисунка, наш расчет находится в согласии с экспериментальными данными в отличие от расчетов по квантовой молекулярной динамике [39]. Для достижения согласия с экспериментом в [39] дополнительно вводятся высокоимпульсные «хвосты» для протонов, что свидетельствует об учете эффекта короткодействующих корреляций SRC. Согласие наших расчетов с экспериментом без дополнительной коррекции показывает, что эффект SRC учитывается в развиваемом нами гидродинамическом подходе.

## 8 Распределения по поперечному импульсу для мягких фотонов

В эксперименте [32] изучались мягкие фотоны, испускаемые в  $pp$ -столкновениях при начальном импульсе 450 ГэВ/с на фиксированной мишени. Интерпретация эксперимента на основе механизма *bremsstrahlung* не воспроизводит наклон спектра [32].

Вонг в работах [31, 53] предложил интерпретировать эти данные на основе температурного спектра, подбирая соответствующую температуру и вводя вклад от распада бозона X17 на фотоны. Существование новой частицы – бозона X17 с массой, примерно равной 17 МэВ, впервые экспериментально было предсказано в работах [54, 55] группы АТОМКИ.

Наша интерпретация импульсных спектров фотонов заключается в использовании формулы для черного тела при  $m = 0$  с соответствующей температурой для фотонов согласно [56],  $T = \left( \frac{E_0}{g_Q V_R} 10^9 \right)^{1/4}$ , где  $E_0$  – кинетическая энергия в системе центра масс в ГэВ,  $g_Q = (2 \times 8 + \frac{7}{8} 2 \times 2 \times 3 \times 3) = 47$ ,

$V_R = (1.2)^3$ . Здесь за счет малости константы связи для электромагнитного взаимодействия энергия была уменьшена в соответствующее число раз, т.е. в  $137 \times 14.7$  раз. Соответствующая температура  $T = 5.9$  МэВ. Вклад от распада бозона X17 с массой 17 МэВ с испусканием фотона можно учесть аналогично работе [56].

Все распределения пропорциональны температуре  $T$ , чтобы воспроизвести пропорциональность  $N \sim T^3$ . Для вклада испускания фотонов при распаде бозона X17 можно учесть, что при распаде частицы X17 в 2 фотона их угловое распределение в системе покоя частицы изотропно по углам. Это распределение можно представить в инвариантной форме [50]

$$dw = \frac{m}{2\pi p_1^*} \delta(2(p_X p_1) - 2mE_1^*) \frac{d^3 p_1}{E_1}, \quad (9)$$

где  $p_1$  – импульс одного из фотонов,  $p_X$  – импульс X-бозона,  $p_1^*$  и  $E_1^*$  – импульс и энергия фотона в системе покоя X-бозона. В результате инвариантное сечение для испускания фотонов

$$E_1 f_\gamma = \frac{m}{2\pi p_1^*} \int d^3 p_X f_X \delta(2(p_X p_1) - 2mE_1^*), \quad (10)$$

где  $f_X$  – функция распределения для X-бозона. В результате интегрирования в (10), с учетом допустимых значений углов

$$|\cos \theta| = |E_X^* E_1 - mE_1^*| / p_X^* p_1 \leq 1. \quad (11)$$

После разрешения этого неравенства получаем

$$E_1 f_\gamma = \frac{m}{2p_1} \int_{E_+}^{E_-} E dE f_X, \quad (12)$$

где следующие из (11) пределы интегрирования в (12)  $E_\pm = \pm p_1 + m$ . Из (12) находим вклад в фотоны от распада X-бозона

$$\frac{dN}{dp_T} = CT \left( (E_- + T) \exp\left(\frac{\mu - E_-}{T}\right) - (E_+ + T) \exp\left(\frac{\mu - E_+}{T}\right) \right), \quad (13)$$

где коэффициент  $C$  и температура  $T$  – такие же, как в формуле для черного тела; химический потенциал  $\mu = 0$  и энергии должны быть пересчитаны в лаб. систему.

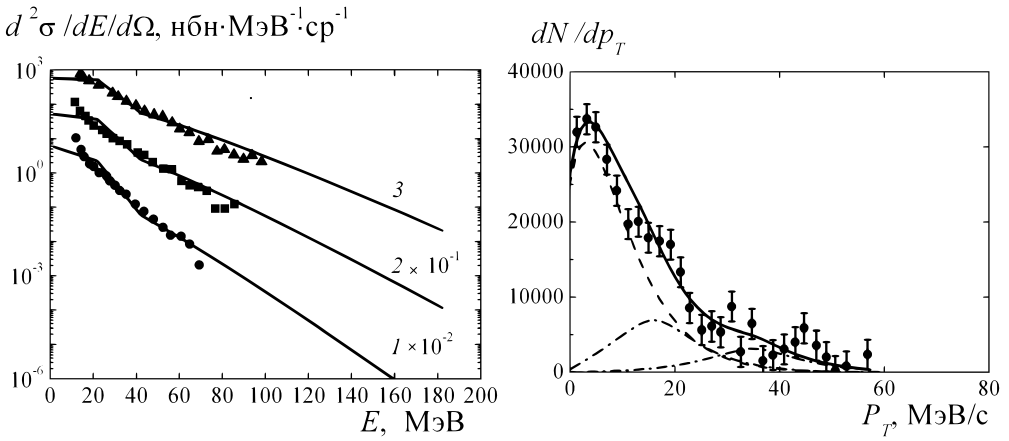


Рис. 4: Левая панель. Двойные дифференциальные сечения испускания фотонов в реакции  $^{14}\text{N}+^{12}\text{C}\rightarrow\gamma+X$  под углом  $90^\circ$  при энергиях  $^{14}\text{N}$  20(1), 30(2) и 40(3) МэВ/нуклон. Сплошные линии – наш расчет при  $\langle T_h \rangle$  равных 9.3 МэВ, 11.7 МэВ и 13.5 МэВ, соответственно. Точки – экспериментальные данные из [52] (кружки при 20, квадраты – 30 и треугольники – 40 МэВ/нуклон). Правая панель. Спектры мягких фотонов, испускаемых в столкновениях протонов на фиксированной мишени при импульсе 450 ГэВ/с, в зависимости от поперечного импульса фотонов  $p_T$ . Сплошная линия – наш расчет в соответствии с формулами черного тела и с учетом вклада испускания фотонов от распада бозона X17, штриховая линия – наш расчет без учета вклада бозона X17, штрихпунктирная линия – вклад от испускания фотонов при распаде X17 согласно формуле (13), точки – экспериментальные данные из работ [31, 32]

В отличие от работ Вонга, мы не фитировали экспериментальные данные, а вычислили температуру по формуле. Однако мы не претендуем на абсолютную величину распределения. Поэтому наши расчеты были нормированы на экспериментальные данные [31, 32]. На рис. 4 (правая панель) приведен экспериментальный спектр мягких фотонов – точки [32], а также расчет с учетом бозона X17 (сплошная линия) и без него (штриховая линия), штрихпунктирная линия – вклад от бозона X17. Из рисунка видно, что без учета вклада от бозона X17 расчет недооценивает экспериментальные данные, а с учетом этого вклада воспроизводит их. То есть такая интерпретация спектра мягких фотонов (его ужесточение) может служить еще одним свидетельством в пользу существования новой частицы – бозона X17. На том же рис. 4 (правая панель) приведен еще в соответ-

ствии с формулой (13) вклад фотонов от распада другой новой частицы – бозона X38 с массой 38 МэВ (штрихпунктирная линия), предсказанного в проведенных в Дубне экспериментах [57]. Однако его вклад проявляется только на хвосте спектра и слабо виден на рисунке.

Заметим, что такое ужесточение спектра фотонов не получается за счет вклада фотонов из hot spot, рассматривавшемся в предыдущем разделе. Поскольку в этом случае его вклад в 10 раз меньше полного сечения, а масса фотонов равна нулю, и ужесточение спектра фотонов в области энергий 20 МэВ за счет большей температуры hot spot все равно пренебрежимо мало. Предсказанный в работах [54, 55] бозон X17, возможно, проявляется в спектре мягких фотонов. Это было рассмотрено в наших работах [33, 56, 58, 59]. В работе Вонга [31] предложена интерпретация этого бозона как результат объединения КХД и КЭД. При этом объединение производится для двумерных  $KХД_2 \times КЭД_2$  в модели трубки.

В [56] мы предложили видоизмененную модель трубки. При этом, так же, как и Вонг [31], рассматриваем и адронную при константе связи  $\alpha = \alpha_s$  и электромагнитную при  $\alpha = \alpha_e = 1/137$  трубки. Радиусы трубок определяются из минимума энергии, приходящейся на единицу длины, а константа сильного взаимодействия  $\alpha_s \approx 0.5$ . Согласно модели трубки, натянутой между двумя кварками [56], можно найти массы образующихся адронов, а в случае электромагнитной трубки массу бозона X17. При этом, согласно [60, 61], плотность энергии трубки складывается из двух членов:

$$\rho = A + G. \quad (14)$$

Первый член  $A$  определяется напряженностью поля  $E$ . Если бы поле было распределено равномерно, то в полусферу распределена была бы энергия на единицу длины трубки радиуса  $r$ , равная

$$A = E^2 \frac{2\pi}{4\pi} \pi r^2 = \frac{1}{2} E^2 \pi r^2. \quad (15)$$

Но, поскольку в направлении длины трубки надо суммировать только телесные углы, умноженные на  $\cos \theta$ , проекции единичного вектора на направление трубки, то телесный угол

$$\Omega = \int_0^{\pi/2} \cos \theta \sin \theta d\theta \int_0^{2\pi} d\phi = \pi, \quad (16)$$

а не  $2\pi$ . Поэтому

$$A = E^2 \frac{\Omega}{4\pi} \pi r^2 = \frac{1}{4} E^2 \pi r^2, \quad (17)$$

где поток вектора напряженности  $E$  равен  $\Phi = \int_0^{\pi/2} E \cos \theta d\theta \int_0^r 2\pi r dr = E\pi r^2$ , и напряженность  $E = \frac{\Phi}{\pi r^2} = \frac{g}{\pi r^2}$ , а константа связи  $\alpha = \frac{g^2}{4\pi}$ ,  $r$  – радиус трубки. Следовательно,

$$A = \frac{\alpha}{r^2}. \quad (18)$$

Второй член выражается через мешковую константу  $B=0.17 \text{ ГэВ}/\text{Фм}^3$  [62]

$$G = B\pi r^2 \frac{\alpha}{\alpha_s}, \quad (19)$$

где нами введено отношение  $\alpha/\alpha_s$  константы  $\alpha$  к константе сильного взаимодействия  $\alpha_s$ . Здесь при  $\hbar = c = k = 1$   $\text{Фм}=5 \text{ ГэВ}^{-1}$ . Для колеблющейся прямолинейной струны-трубки получаем [60] массу  $M$ :

$$M^2 = 2\pi \rho n, \quad (20)$$

где  $n$  – квантовое число. Для адронной трубки при  $n = 1$  получаем  $M \approx 152 \text{ МэВ}$  для  $\pi^0$ -мезона. Но если мешковую константу  $B$  выбрать равной  $0.13 \text{ ГэВ}/\text{Фм}^3$ , то для  $\pi^0$ -мезона получаем более близкое к экспериментальному значение  $M \approx 140 \text{ МэВ}$ . Для электромагнитной трубки при том же радиусе трубки получаем массу нейтрального бозона  $X17$   $M \approx 17 \text{ МэВ}$ . По формуле  $M^2 = 2\pi \rho t$  можно получить и резонансы, где  $t$  – кратно сложенная струна с вращением. Так можно получить массу  $\rho$ -мезона, а для электромагнитной струны получаем массу бозона  $34 \text{ МэВ}$  при  $t = 4$ , полученную в работе Вонга другим путем.

Отметим, что эти результаты получены в нашем подходе по формулам, отличным от работы Вонга. В своей работе [31] Вонг предлагает интерпретировать бозон  $X17$  как частицу темной материи, поскольку он нейтрален, не барион, и может быть составной частицей астрофизических объектов большой массы.

## 9 Заключение

В лекции в рамках модифицированной гидродинамической модели с фиксированными параметрами уравнения состояния описаны экспериментальные высокоимпульсные спектры протонов, пионов и фотонов, испускаемых в столкновениях тяжелых ионов при  $E = 0.3 - 3 \text{ ГэВ}/\text{нуклон}$ , включая кумулятивную область спектра.

Весьма важным моментом явилось включение в рассмотрение эффектов ядерной вязкости, найденной нами в релаксационном  $\tau$ -приближении для кинетического уравнения, а также поправки на микроканоническое

распределение, проявляющейся в области высокоэнергетических «хвостов» спектров протонов. При промежуточных энергиях в кумулятивной области импульсных спектров протонов важен учет испускания протонов из образующегося горячего пятна – hot spot – и их испускания в результате слияния неперекрывающихся областей сталкивающихся ядер. То есть, в развиваемой модели представлен механизм «корона-кор», получивший распространение при высоких энергиях. Это может объяснить аппроксимацию экспериментальных данных двумя экспонентами со своими температурами, проведенную в [26]. В области малых импульсов протонов определяющий вклад в сечение дает учет фрагментации, проведенный нами в статистической модели фрагментации. Проведенные расчеты воспроизводят экспериментальные данные по выходам протонов и пионов как для средних, так и тяжелых ядер в области промежуточных и высоких энергий сталкивающихся ядер и могут быть применены к области энергий строящегося в Дубне ускорительного комплекса NICA. Описание спектров жестких фотонов указывает на то, что в нашем подходе могут быть учтены эффекты короткодействующих корреляций (SRC).

Правомерность использования макроскопических параметров для легких систем можно объяснить. В нашем случае среднее число частиц в hot spot  $N \approx 10$ , и дисперсия  $\sim 1/\sqrt{N}$  не столь велика. Поправка на микроканоническое распределение улучшает описание эксперимента. Плечо в кумулятивной области спектра протонов воспроизводится в нашем подходе и, как видно, иногда оно воспроизводится в транспортных каскадных кодах. Возможно, что это обусловлено перерассеянием пионов [63].

В термодинамической модели дана интерпретация экспериментальных данных по спектрам мягких фотонов с помощью новой частицы – бозона X17, который нейтрален и не является барионом. Он может образовывать массивные объекты темной материи в астрофизике. Обосновывается наличие массы бозона X17, равной 17 МэВ, исходя из электромагнитной трубки при объединении двумерных  $KX D_2 \times K\bar{X} D_2$ . А также дана интерпретация экспериментальных данных по обнаружению еще новой частицы бозона – X38 с массой 38 МэВ, открытого в Дубне на ускорителе в Лаборатории физики высоких энергий Объединенного института ядерных исследований.

Автор благодарен В.В. Вечернину, М.Б. Жалову, В.Т. Киму, И.А. Митропольскому, О.Л. Федину, А.В. Ставинскому, В.В. Куликову и С.С. Шиманскому за полезные обсуждения.

# Литература

- [1] L. Landau, *Izv. Akad. Nauk SSSR, Ser. fiz* **17**, 51 (1953).
- [2] H. Stoecker and W. Greiner, *Phys. Rept* **137**, 277 (1986).
- [3] A. Khvorostukhin and V. Toneev, *Phys. Part. Nucl. Lett.* **14**, 9 (2017).
- [4] A. Khvorostukhin and V. Toneev, *Phys. Atom. Nucl.* **80**, 285 (2017).
- [5] A.S. Khvorostukhin, E.E.Kolomeitsev, and V.D.Toneev, *Eur. Phys. J. A* **57**, 294 (2021).
- [6] H. et al., *Phys. Rev. C* **78**, 044901(20) (2008).
- [7] A.V. Merdeev, L.M. Satarov, and I.N. Mishustin, *Phys. Rev. C.* **84**, 014907 (2011).
- [8] I.N. Mishustin, V.N. Russkikh, and L.M. Satarov, *Sov. J. Nucl.Phys* **54**, 260 (1991).
- [9] Yu.B. Ivanov, V.N. Russkikh, and V.D. Toneev, *Phys. Rev. C* **73**, 044904(30) (2006).
- [10] A. et al., *Sov. J. Nucl. Phys.* **18**, 41 (1974).
- [11] Y. et al., *Sov. J. Nucl. Phys.* **18**, 639 (1974).
- [12] A.V. Efremov, A.B. Kaidalov, V.T. Kim, and et al, *Sov. J. Nucl. Phys.* **47**, 1364 (1988).
- [13] L. Frankfurt and M. Strikman, *Phys. Rept.* **76**, 215 (1981).
- [14] M. Braun and V. Vechernin, *J. Phys. G: Nucl. Part. Phys.* **19**, 517 (1993).
- [15] V. Toneev and K. Gudima, *Nucl. Phys. A* **400**, 173 (1983).
- [16] G. Leksin, *Phys. Atom. Nucl.* **65**, 1985 (2002).
- [17] A. D'yachenko and I. Mitropolsky, *Phys. Atom. Nucl.* **83**, 558 (2020).
- [18] A. D'yachenko and I. Mitropolsky, *Phys. Part. Nucl.* **53**, 505 (2022).
- [19] A. D'yachenko and I. Mitropolsky, *EPJ Web of Conf.* **204**, 03018(8) (2019).
- [20] A. D'yachenko and I. Mitropolsky, *Phys. Atom. Nucl.* **82**, 1641 (2019).

- [21] A.T. D'yachenko, K.A. Gridnev, and W. Greiner, J. Phys. G: Nucl. Part. Phys. **40**, 085101(9) (2013).
- [22] A. D'yachenko, Phys. Atom. Nucl. **57**, 1930 (1994).
- [23] P. Bonche, S. Koonin, and J.W. Negele, Phys. Rev. C **13**, 1226 (1976).
- [24] W. Scheid, H. Muller, and W. Greiner, Phys. Rev. Lett. **32**, 741 (1974).
- [25] A. D'yachenko and I. Mitropolsky, Phys. Atom. Nucl. **85**, 1053 (2022).
- [26] B. et al., Phys. Atom. Nucl. **78**, 373 (2015).
- [27] B. et al., Phys. Atom. Nucl. **84**, 467 (2021).
- [28] I. et al., Phys. Atom. Nucl. **78**, 936 (2015).
- [29] A. D'yachenko and I. Mitropolsky, Bull. Russ. Acad. Sci.: Phys. **86**, 1162 (2022).
- [30] A. D'yachenko, Phys. Atom. Nucl. **86**, 289 (2023).
- [31] C. Wong, JHEP **08**, 08165 (2020).
- [32] A. et al, Phys. Lett. B **548**, 129 (2002).
- [33] A. D'yachenko, Phys. Atom. Nucl. **85**, 1028 (2022).
- [34] A. D'yachenko and O. Lozhkin, Subthreshold heavy meson and antiproton production in nucleus-nucleus collisions, in *Материалы XXXV зимней школы ПИЯФ им. Б.П. Константинова.*, pp. 129–141, Gatchina, 2001, PNPI.
- [35] A. Goldhaber, Phys. Lett. B **53**, 306 (1974).
- [36] H. Feshbach and K. Huang, Phys. Lett. B **47**, 300 (1973).
- [37] H.Schuldes *et al.*, (HADES Collaboration), J. Phys.: Conf. Series **599**, 012028. (2015).
- [38] W. Cassing and E. Bratkovskaya, Phys.Rept. **308**, 65 (1999).
- [39] W.M. Guo, B.A. Li, and G.C.Yong, Phys.Rev. C **104**, 034603 (2021).
- [40] Y.Kanakubo, Y. Tachibana, and T. Hirano, Phys.Rev. C **101**, 024912 (2020).

- [41] D. I. Blokhintsev, Sov. Phys. JETP **6**, 995 (1958).
- [42] A.B. Larionov, W. Cassing, M. Effenberger, and U. Mosel., Eur.Phys.J.A **7**, 507 (2000).
- [43] C.Hartnack *et al.*, Nucl. Phys. A **495**, 303 (1989).
- [44] H. Barz and L. Naumann, Phys. Rev. C **68**, 041901 (2003).
- [45] E.E. Kolomeitsev *et al.*, J. Phys. G: Nucl. Part. Phys. **31**, 741 (2005).
- [46] J. Weil, V. Steinberg, J. Staudenmaier, and et al., Phys. Rev. C **94**, 054905 (2016).
- [47] A. Dementev and N. Sobolevsky, Nucl. Tracks Radiat. Meas **30**, 553 (1999).
- [48] S. et al, FERMILAB-CONF-08-322-APC, LA-UR-08-2931 **Los Alamos** (2008).
- [49] T. et al., AIP Conf.Proc **896**, 21 (2007).
- [50] V.I. Goldansky, Yu.I.Nikitin, and I.L. Rosenthal, *Kinematic methods in high energy physics*. (Nauka, Moscow, 1987).
- [51] V. D'yachenko, A.T.and Baryshnikov, Proc. of Baldin ISHEPP XIX **2**, 234 (2008).
- [52] J. Stevenson *et al.*, Phys. Rev. Lett. **57**, 555 (1986).
- [53] C. Wong, Phys. Rev. C **81**, 064903 (2010).
- [54] A.J. Krasznahorkay *et al.*, Phys. Rev.Lett. **116**, 042501 (2016).
- [55] A.J.Krasznahorkay *et al.*, Phys. Rev.C **104**, 044003 (2021).
- [56] A. D'yachenko, Phys. Atom. Nucl. **83**, 1597 (2020).
- [57] K.Abraamyan, C. Austin, M. Baznat, and et al, EPJ Web of Conf. **204**, 08004 (2019).
- [58] A. D'yachenko and E. Gromova, J. Phys.: Conf. Ser. **2131**, 022054 (2021).
- [59] A.T.D'yachenko, A.A. Verisokina, and M.A. Verisokina, Acta Phys. Polonica. B Proc. Suppl. **14**, 761 (2021).

- [60] V. et al., *Inelastic interactions at high energies and the chromodynamics* (Metsniereba, Tbilisi, 1986).
- [61] B. Barbashov and V. Nesterenko, *Relativistic string model in hadron physics* (Energoatomizdat, Moscow, 1987).
- [62] V.M. Emelyanov and S.L. Timoshenko and M.N. Strikhanov, *Introduction to relativistic nuclear physics* (Fizmatlit, Moscow, 2004).
- [63] M. Braun and V. V. Vechernin, *Sov. J. Nucl. Phys.* **44**, 1016 (1986).

# КОНЦЕПЦИЯ НОВОГО НЕЙТРИННОГО ДЕТЕКТОРА СВЕРХБОЛЬШОГО ОБЪЕМА В АНТАРКТИДЕ

Аркадий А. Захаров

Петербургский институт ядерной физики НИЦ «КИ», Гатчина

## Аннотация

Для создания нового нейтринного детектора сверхбольшого объема предлагается использовать подледниковое озеро Восток. Эта локация имеет определенные преимущества в сравнении с локациями существующих детекторов глобальной нейтринной сети и позволяет создать детектор объемом в десятки кубических километров в условиях низких фонов. Для бурения скважин к озеру Восток предложен новый способ быстрого и экологически чистого бурения и вскрытия озера, который может быть также применен для изучения подледниковых озер Антарктиды. В качестве детектора для нового нейтринного телескопа используется озерная вода и ледник толщиной около 4-х километров, при этом верхний слой льда будет служить экраном для атмосферных нейтрино и заряженных частиц высоких энергий. В прозрачной озерной воде и внутри ледника могут располагаться оптические и акустические датчики, а на поверхности размещаться антенны радиочастотного диапазона. Таким образом, предлагаемая локация дает возможность одновременно задействовать несколько методов детектирования, охватывающих широкий энергетический спектр нейтрино. Применение акустического метода с датчиками небольшого размера позволит создать детектор сверхбольшого объема, ориентированный на изучение источников высокоэнергетических нейтрино.

# CONCEPT OF A NEW ULTRA-LARGE-VOLUME NEUTRINO DETECTOR IN ANTARCTICA

Arcady A. Zakharov

Petersburg Nuclear Physics Institute of NRC “KI”, Gatchina

## Abstract

A proposal to create a new ultra-large-volume neutrino detector with the use of the Antarctic subglacial Lake Vostok is presented. This location has certain advantages in comparison with the locations of existing detectors of the global neutrino network and it makes possible to build a detector with a volume of tens of cubic kilometers with low background conditions. For wells drilling to the Lake Vostok, a new method for fast and environmentally friendly ice drilling and entrance opening of the lake has been proposed. This drilling method can also be used to study subglacial lakes in Antarctica. Lake water and a glacier about 4 kilometers thick are used as a detector for the new neutrino telescope, while the top layer of ice will serve as a screen for atmospheric neutrinos and high-energy charged particles. Optical and acoustic sensors can be located in clear lake water and inside a glacier, and radio frequency antennas can be placed on the surface. Thus, the proposed location makes provides opportunity to use simultaneously several detection methods covering a wide neutrino energy spectrum. The use of the acoustic method with small sensors will make it possible to create an ultra-large volume detector aimed at studying the sources of high-energy neutrinos.

Нейтринный телескоп на озере Восток в Антарктиде будет иметь параметры, превосходящие характеристики телескопов глобальной нейтринной сети GNN [1] даже по завершению работ по увеличению объемов их детекторов. При этом конструкция детектора в озере Восток позволит во много раз сократить расходы и время на его создание в сравнении с существующими аналогами. Прежде чем перейти к концепции нового нейтринного телескопа, кратко рассмотрим научные задачи, локации и устройство нейтринных детекторов сети GNN, которая объединяет телескопы со сверхбольшими объемами детекторов: KM3NeT, Baikal-GVD и IceCube.

В исследовательскую инфраструктуру KM3NeT [2] входит детектор ORCA [3] для исследования осцилляций нейтрино и детектор ARCA [4] для регистрации нейтрино высоких энергий. Предшественник KM3NeT нейтринный телескоп ANTARES [5] был выведен из эксплуатации в феврале 2022 года.

Глубоководная локация нейтринного детектора ORCA находится в Средиземном море в 40 км от Тулона и имеет глубину 2450 метров. Пространственная решетка детектора, состоящая из оптических модулей для фиксации вторичного черенковского излучения в воде, имеет плотность, которая обеспечивает угловое и энергетическое разрешение для детектирования атмосферных нейтрино. Атмосферные нейтрино являются ключом к решению фундаментального вопроса физики частиц: вопроса об относительном упорядочении масс нейтрино [6, 7]. После завершения строительства детектор ORCA будет состоять из гирлянд в количестве 115 штук, которые располагаются на расстоянии 20 м друг от друга в окружности радиусом 106 метров. Каждая гирлянда имеет высоту 150 м вдоль которой с дистанцией 9 м установлены оптические модули. Пространственный массив детектора объемом  $5.5 \times 10^6 \text{ м}^3$  будет содержать 2070 оптических модулей.

Локация нейтринного детектора ARCA расположена примерно в 100 км от Сицилии и имеет глубину около 3500 метров. Детектор предназначен для регистрации нейтрино высоких энергий от дальних астрофизических источников, таких как сверхновые или сталкивающиеся звезды [8, 9]. В завершающей фазе проекта предполагается иметь два блока детекторов высотой около 700 м по 115 гирлянд в каждом блоке. Расстояние между соседними гирляндами равняется  $\sim 90$  м. Гирлянда содержит 18 оптических модулей, установленных на расстоянии 36 м друг от друга. Полный объем нейтринного детектора из двух расположенных рядом блоков будет равен примерно  $1 \text{ км}^3$ . Пространственная сеть оптических модулей детектора ARCA постепенно расширяется и уже дает первые научные результаты [10, 11]. Совершенствуются также методы и подходы к обработке

экспериментальных данных [12, 13].

Детектор нейтринного телескопа Baikal-GVD [14] расположен в южной части озера Байкал в 4 км от берега. Глубина озера в этом месте составляет  $1366 \div 1367$  метров. Детектор предназначен для поиска нейтрино с энергией выше 100 ТэВ, источники которых еще не идентифицированы. По состоянию на 2021 год он включает 2304 оптических модуля, расположенных на 64 гирляндах. Глубоководные кластеры в количестве 8 штук расположены друг от друга на удалении 300 м. Каждый кластер объединяет 8 вертикальных тросов-гирлянд, которые находятся на расстоянии 60 м друг от друга [15]. Гирлянда включает в себя 36 оптических модулей, установленных с дистанцией 15 метров между ними. Сигналы от оптических модулей передаются по проложенным по дну кабелям на берег для сбора и обработки полученных данных. Эффективный объем детектора составляет  $0.4 \text{ км}^3$ .

Нейтринный телескоп IceCube [16] располагается внутри ледника, который находится над Южным полюсом Земли. С его помощью можно производить измерения потока нейтрино в диапазоне от 100 ТэВ до уровня ниже 10 ГэВ, на котором наблюдаются осцилляции атмосферных нейтрино и производится поиск стерильных нейтрино. Телескоп IceCube позволяет выполнять непрямой поиск темной материи по нейтринным сигнатурам аннигиляции темной материи в галактическом гало, в скоплениях галактик и в центре Земли.

Для создания нейтринного детектора IceCube на станции Amundsen–Scott в течение 6 лет (2004–2010 гг.) горячей водой в леднике было пробурено 86 скважин глубиной 2500 м и диаметром 60 см. На создание одной скважины требовалось порядка 30 часов и 21000 л топлива [17, 18]. В скважины были опущены гирлянды с оптическими модулями, после чего они вмерзли в лед.

Гирлянды детектора *IceCube* располагаются по гексагональной решётке в скважинах с расстоянием 125 м между ними на глубине от 1450 до 2450 м. Каждая гирлянда состоит из 60 оптических модулей для регистрации черенковского излучения. Детектор нейтринного телескопа IceCube имеет объем  $1 \text{ км}^3$  и содержит 5160 оптических модулей [19]. Восемь гирлянд в центре массива расположены более компактно на расстоянии 70 метров друг от друга, а оптические детекторы установлены по вертикали с дистанцией 7 метров. Такая более плотная конфигурация образует поддетектор *DeepCore*, который снижает энергетический порог регистрации нейтрино примерно до 10 ГэВ, создавая возможность для изучения осцилляций нейтрино. Дополнительные 324 модуля образуют поверхностный

детектор *IceTop* площадью  $1 \text{ км}^2$ . Детектор состоит из 81 станции, каждая из которых оборудована 4 оптическими детекторами, ориентированными вниз. Станции располагаются на поверхности над основными гирляндами. *IceTop*, созданный в качестве вето-детектора и калибровочного детектора для *IceCube*, также обнаруживает воздушные ливни от первичных космических лучей в диапазоне энергий от 300 ТэВ до 1 ЭэВ. Наземный массив измеряет направления прихода космических лучей в южном полушарии, а также поток и состав космических лучей.

В настоящее время началось осуществление проекта *IceCube-Gen2* [20], в котором планируется дополнительно разместить в леднике 120 гирлянд с оптическими модулями и увеличить объём детектора до  $7.9 \text{ км}^3$ . Детектор будет отличаться увеличенным расстоянием между гирляндами. Проект *IceCube-Gen2* позволит повысить чувствительность к нейтринным источникам в пять раз по отношению к существующей и улучшить угловое разрешение.

На поверхности предполагается установить радиочастотную решетку сверхвысоких энергий для расширения доступного энергетического диапазона космических нейтрино. Радиодетекторная станция *Gen2* сочетает в себе неглубокие антенны (лучшее усиление, чувствительность к частоте и поляризации, а также вето на атмосферные явления для улучшения идентификации космических нейтрино в оптическом массиве) с глубокими антеннами и триггерной цепью с фазированной антенной решеткой, что дает более эффективный объём и лучший охват неба. Радиорешетка будет охватывать около  $500 \text{ км}^2$ . В концептуальном проекте предполагается 200 станций, что обеспечивает беспрецедентную чувствительность при энергиях выше 10 ПэВ.

Рассмотрим особенности описанных выше детекторов, обусловленные их локацией. К основным негативным сторонам морской локации нейтринного детектора можно отнести распад изотопа  $^{40}\text{K}$ , который содержится в морской воде и производит до 150 черенковских фотонов на распад [21] и совместно с хемилюминесценцией создает световые помехи при регистрации черенковского излучения, изменения температуры и солености воды, значение которых влияют на расчет времени и определение позиции оптических модулей в момент фиксации событий, а также морские течения, воздействующие на пространственную решетку из оптических модулей. Для снижения негативного влияния среды на точность измерений установлены дополнительные лазерные и гидроакустические модули. Большой акустический шум от морских судов и обитателей моря оставляет под вопросом возможность использования акустического метода регистрации

нейтрино, о котором речь пойдет ниже. Регистрации нейтрино высоких энергий мешает фон атмосферных мюонов [22, 23].

В случае озерной локации Baikal-GVD отсутствует световой фон от распада изотопа  $^{40}\text{K}$ , однако на глубине проявляется хемилюминесценция, которая создает помехи для работы оптических модулей. Прозрачность озерной воды представлена в работе [24]. Из-за небольшой глубины расположения детектора присутствует фон атмосферных мюонов, который мешает регистрации нейтрино высоких энергий. Существующие в озере течения и сезонные штормы производят смещение гирлянд с оптическими модулями, которое может достигать десятков метров в зависимости от глубины. Для позиционирования оптических модулей во время измерений используется гидроакустическая система, которая представляет собой набор акустических модемов, установленных вдоль гирлянд. В течение кратковременного периода очень высокой гидродинамической активности точность позиционирования падает до  $20 \pm 10$  см [25]. Некоторые проблемы возникают также из-за хозяйственной деятельности на озере. Наличие ледового покрытия в течение двух месяцев в году позволяет проводить монтаж и обслуживание гирлянд с оптическими модулями с поверхности льда.

Локация нейтринного детектора внутри ледника (IceCube) связана с необходимостью бурения большого количества глубоких скважин для размещения гирлянд с оптическими модулями. Данные о местоположении в процессе бурения показывают, что гирлянда не является идеально вертикальной, хотя отклонения от вертикали составляет менее 1 м. Расположение гирлянд в леднике не позволяет менять пространственную решетку детектора, проводить ремонт и замену оптических модулей. Оптический модуль заключен в прозрачную сферу, которая рассчитана на давление 690 атм [26]. В верхних слоях лед содержит пузырьки воздуха, которые в нижних слоях превращаются в каверны, что приводит к снижению прозрачности льда. Замерзший в скважине лед состоит из внешнего слоя и центрального ядра диаметром около 16 см, которое имеет гораздо меньшую длину рассеяния света, чем у сплошного льда окружающего скважину. Внутри льда было выявлено преимущественное распространение света в направлении движения ледника [27].

Рассмотрим преимущества локации детектора в подледниковом озере, но для начала немного общей информации об озере Восток [28–30]. Подледниковое озеро Восток имеет слегка изогнутую форму, и его размеры превышают 275 км в длину и 50 км в ширину. Максимальное значение толщины ледника над озером составляет 4350 м, а максимальная зарегистри-

рованная толщина водного слоя достигает 1200 м. По уточненным оценкам ледник движется с запада на восток практически перпендикулярно продольной оси озера со скоростью  $2.0 \pm 0.01$  м/год [31]. В месте расположения антарктической станции Восток ледник имеет толщину 3758 м. Изучение ледяных кернов, извлеченных из скважины, показало, что слой аккреционного льда имеет толщину 230 м [32]. В районе полярной станции водный слой равен 680 м, а слой осадочных пород достигает 330 м [33]. Циркуляция воды в озере обусловлена геотермальным потоком, который оценивается в  $46 \text{ мВт/м}^2$ , плавлением нижней поверхности льда в северной части озера и приращением льда в его южной части со скоростью 4.5 мм/год [34].

Условия озера Восток позволяют применить одновременно нескольких методов детектирования нейтрино. Для детектирования нейтрино в прозрачной воде озера может использоваться оптический метод регистрации черенковского излучения от каскада заряженных частиц, как результата взаимодействия нейтрино со средой. В качестве оптических детекторов для нейтринного телескопа можно рассматривать используемый для этого тип ФЭУ или кремниевые ФЭУ. Важным моментом в выборе типа детекторов, помимо характеристик, будет являться геометрический размер для погружения в озеро через скважину и способность выдерживать давление на большой глубине ( $\sim 450$  атм).

Для детектирования редких космических высокоэнергетических нейтрино в озере может быть использован акустический детектор сверхбольшого объема. Акустический метод позволяет изучать спектр космических нейтрино от ГЗК взаимодействия, который может располагаться выше 100 ПэВ [35, 36]. Адронные каскады, образованные в результате взаимодействия высокоэнергетических нейтрино со средой, выделяют в ней тепловую энергию, что приводит к почти мгновенному расширению объема, которое сопровождается генерацией биполярного акустического импульса [37, 38]. Теоретически и экспериментально установлено, что амплитуда акустического давления прямо пропорциональна мощности каскада частиц. Важным преимуществом использования акустических датчиков в озерной воде является то, что длина затухания звукового сигнала может достигать 100 км [39]. Это позволит использовать огромные объемы воды с акустическими датчиками, расположенными на большом расстоянии друг от друга, что увеличит количество регистрируемых частиц. Другой полезной особенностью акустического сигнала является то, что его энергия сконцентрирована в небольшом угловом секторе перпендикулярно к направлению распространения каскада. Пространственная решетка акустических датчиков может регистрировать сигналы со всех сторон для последующего

реконструирования расположения каскада и его направления. Примерами использования акустического метода для детектирования высокоэнергетических нейтрино могут служить проекты DUMAND [40], SADC0 [41], SAUND [42], AMADEUS [43], SPATS [44, 45].

Отрицательным моментом для применения акустического метода в пресной воде будет сравнительно небольшая амплитуда акустического сигнала, что отчасти компенсируется очень низким затуханием сигнала и отсутствием акустических помех в озере. В качестве акустических датчиков могут применяться пьезоэлектрические гидрофоны или оптоволоконные деформационные детекторы, использующие метод когерентной рефлектометрии. Вопрос выбора типа акустических датчиков для нейтринного детектора в озере Восток подлежит более детальному изучению.

Дополнительно к нейтринному детектору, расположенному в озере, в поверхностном фирне могут быть установлены антенны для радиоволнового детектирования нейтрино, что расширит энергетический диапазон регистрируемых нейтрино до десятков ПэВ.

Перечислим основные преимущества размещения нейтринного детектора в озере Восток в сравнении с другими локациями нейтринных телескопов со сверхбольшими объемами детекторов. К этим преимуществам относятся:

- возможность применения одновременно нескольких методов регистрации нейтрино: оптического, акустического и с помощью радиосигналов, что расширяет экспериментальные возможности;
- большая толщина ледника позволит эффективно экранировать нейтринный детектор от потоков солнечного и атмосферного излучения;
- отсутствие течений, способных смещать датчики, обеспечит их устойчивое положение в детекторе;
- высокая прозрачность воды в озере будет способствовать регистрации черенковского излучения;
- в пресной воде озера отсутствует световой фон от распада изотопа  $^{40}\text{K}$ , который содержится в морской воде;
- ожидаемое сравнительно небольшое содержание микроорганизмов в воде озера обеспечит низкий световой фон (вплоть до полного его отсутствия) от возможной биолуминесценции, что важно для работы оптических модулей;

- в подледниковом озере отсутствует какая-либо деятельность, которая может влиять на работу нейтринного детектора;
- крайне низкий акустический фон в удаленном подледниковом озере позволит использовать акустический метод регистрации нейтрино;
- длина затухания звукового сигнала в пресной воде в десятки раз больше, чем длина затухания в морской воде, что будет способствовать созданию нейтринного детектора сверхбольшого объема;
- размещение нейтринного детектора в воде подо льдом потребует бурения в леднике только двух скважин. Одна скважина будет использоваться для монтажа и обслуживания гирлянд с датчиками с помощью автономного подводного дрона, а вторая для вывода измерительных и питающих кабелей. Необходимость бурения всего двух скважин значительно сократит расходы и время на создание детектора сверхбольшого объема. Закрепление гирлянд с датчиками возможно либо на нижней поверхности льда, либо на дне озера с применением поплавков;
- использование скоростного метода бурения ледника позволит пробурить скважины к озеру в течение одного полярного сезона;
- определяющим моментом создания нейтринного детектора в озере Восток является скорое завершение строительства нового полярного комплекса, в котором может быть размещено оборудование для нейтринного телескопа, что в значительной степени поднимет научную значимость внутриконтинентальной полярной станции Восток;
- отработанная при строительстве полярного комплекса логистическая схема позволит организовать доставку бурового оборудования и приборной базы нейтринного телескопа на полярную станцию.

К отрицательным моментам, относящимся к размещению нейтринного телескопа в подледниковом озере, можно отнести необходимость бурения глубоких скважин в леднике, высокие экологические требования к работе в озерной среде, использование автономного глубоководного дрона для монтажа гирлянд с датчиками подо льдом, географическую удаленность и суровые климатические условия.

Для создания нейтринного детектора в озере Восток возможен также вариант сквозного размещения гирлянд с датчиками в слое льда и в

озерной воде. Это позволит создать нейтринный детектор высотой до четырех километров (3 км льда + 1 км воды) со слоем экранирующего льда около одного километра, что увеличит экспериментальные возможности телескопа и расширит энергетический диапазон регистрируемых нейтрино. Этот вариант потребует бурения большого числа скважин, но одновременно значительно упростит установку гирлянд с датчиками в скважинах.

Принципиальным вопросом при создании нейтринного детектора в озере Восток является применение такого способа бурения и вскрытия подледникового озера, который соответствует кодексу поведения научного комитета по антарктическим исследованиям для разведки и исследования подледниковой водной среды [46]. Для соблюдения экологических норм скважина к подледниковому озеру должна быть заполнена водой из расплавленного над ним льда или чистой незамерзающей гидрофобной заливочной жидкостью. Для решения этой задачи разработан экологически чистый способ скоростного бурения скважины и вскрытия подледникового озера, который заключается в том, что бурение льда и вскрытие озера производятся тепловым буровым снарядом, который состоит из герметичного гибкого трубопровода типа труба-в-трубе и тепловой буровой коронки, закрепленной на его конце. Внутри трубопровода циркулирует нагретый теплоноситель с целью поддержания образовавшейся талой воды в скважине в жидком состоянии в условиях окружающего льда с низкой температурой. Таким образом, в отличие от других способов бурения льда, буровая жидкость течет в герметичном трубопроводе и не контактирует с водой и стенками скважины. Роль заливочной жидкости, удерживающей стенки скважины от смыкания под воздействием горного давления в условиях глубокого бурения, выполняет вода, образовавшаяся в результате плавления льда тепловой буровой коронкой с установленным в ней электронагревателем. Талая вода вытесняется тепловым буровым снарядом из скважины на поверхность в подготовленное в снегу углубление. Перед погружением в скважину наружная поверхность теплового бурового снаряда проходит механическую и бактериологическую очистку. Проходка тепловым буровым снарядом скважины глубиной 4 километра займет несколько суток.

В момент вскрытия озера часть воды, образовавшаяся из расплавленного над озером аккреционного льда, уйдет в озеро и уровень воды в скважине установится в положении, когда гидростатическое давление столба воды в скважине равно давлению в озере на границе со льдом. После вскрытия озера тепловой буровой снаряд извлекается из скважины, и в нее поступает вода из озера. По окончании процесса бурения и вскрытия озера скважина остается заполненной озерной водой до высоты гидрологического уровня.

Сразу после этого через скважину до дна озера может быть опущена гирлянда с датчиками, нижняя часть которой будет находиться в озерной воде, а верхняя окажется внутри льда после того, как вода в скважине замерзнет. Как было отмечено выше, построенный таким образом нейтринный детектор будет обладать большим объемом и широкими экспериментальными возможностями, но потребует бурения большого количества скважин.

При необходимости длительного использования скважины она заполняется сверху незамерзающей гидрофобной силиконовой жидкостью с диметилполисилоксановой структурой таким образом, чтобы граница раздела жидкостей находилась в нижней части скважины. Это позволит многократно опускать в озеро различное оборудование, прошедшее предварительную очистку. Экологически чистая заливочная силиконовая жидкость предотвратит смыкание стенок скважины под воздействием давления окружающего льда и обеспечит длительную эксплуатацию скважины.

Созданию нейтринного детектора в озере должны предшествовать геофизические и биологические исследования. Проект создания нейтринного телескопа сопрягается с фундаментальным научным проектом, задача которого состоит в получении новых знаний о жизни и процессе эволюции в экстремальных условиях. Лабораторные исследования аккреционного льда указывают на присутствие термофильных хемоавтотрофных микроорганизмов, что предполагает наличие в озере микробной популяции, изолированной от биоты Земли на протяжении миллионов лет [47–52]. Биологические исследования изолированного подледникового озера Восток могут дать информацию о существовании жизни на спутниках Европа и Энцелад и на других подобных космических объектах, которые содержат воду под многокилометровым слоем льда.

Использование уникальных условий локации нейтринного детектора в подледниковом озере Восток позволит создать детектор объемом в десятки кубических километров в условиях низких фонов. Для реализации концепции предлагается экологически чистый способ скоростного бурения скважин и вскрытия подледникового озера с помощью специально разработанного теплового бурового снаряда для глубинного бурения льда. Предложенная локация имеет условия для одновременного использования радиочастотного, оптического и акустического методов детектирования. Применение акустического метода с датчиками небольшого размера, расположенными в озерной воде и внутри ледника, позволит создать детектор сверхбольшого объема, ориентированный на изучение источников высокоэнергетических нейтрино.

# Литература

- [1] URL: <https://www.globalneutrino.org/>.
- [2] URL: <https://www.km3net.org/>.
- [3] URL: <https://www.km3net.org/research/physics/particle-physics-with-orca/>.
- [4] URL: <https://www.km3net.org/research/physics/astronomy-with-arca/>.
- [5] URL: <https://antares.in2p3.fr/>.
- [6] S. Adrián-Martínez *et al.*, J. High Energ. Phys **2017**, 8 (2017).
- [7] S. Aiello *et al.*, Eur. Phys. J. C **82**, 26 (2022).
- [8] S. Aiello *et al.*, Astroparticle Physics **111**, 100 (2019).
- [9] W. I. Ibnsalih *et al.*, Expectations for the high-energy neutrino detection from starburst galaxies with km3net/arca, in *Proceedings of the 37th International Cosmic Ray Conference – ICRC2021*, p. 1168, Proceedings of Science, 2021.
- [10] S. Aiello *et al.*, Eur Phys. J. C **82**, 317 (2022).
- [11] S. Aiello *et al.*, Eur. Phys. J. C **81**, 445 (2021).
- [12] T. Eeden, J. Seneca, and A. Heijboer, High-energy reconstruction for single and doublecascades using the km3net detector, in *Proceedings of the 37th International Cosmic Ray Conference – ICRC2021*, p. 1089, Proceedings of Science, 2021.
- [13] J. P. Gonzalez *et al.*, Km3net/arca sensitivity to transient neutrino sources, in *Proceedings of the 37th International Cosmic Ray Conference – ICRC2021*, p. 1162, Proceedings of Science, 2021.
- [14] URL: <https://baikalgvd.jinr.ru/>.
- [15] V. A. Allakhverdyan *et al.*, Observations of track-like neutrino events with baikal-gvd, in *Proceedings of the 37th International Cosmic Ray Conference – ICRC2021*, p. 1177, Proceedings of Science, 2021.
- [16] URL: <https://icecube.wisc.edu/science/icecube/>.

- [17] T. Benson *et al.*, *Annals of Glaciology* **55**, 68 (2014).
- [18] L. Greenler *et al.*, *Annals of Glaciology* **55**, 115 (2014).
- [19] J. A. Aguilar *et al.*, *The IceCube Neutrino Observatory: Instrumentation and Online Systems* (Journal of Instrumentation, 2016).
- [20] M. G. Aartsenq *et al.*, Neutrino astronomy with the next generation icecube neutrino observatory, 2019, arXiv:1911.02561v1 [astro-ph.HE].
- [21] J. A. Aguilar *et al.*, (ANTARES Collaboration), *Astroparticle Physics* **33**, 86 (2010).
- [22] Y. Becherini, A. Margiotta, M. Sioli, and M. Spurio, *Astroparticle Physics* **25**, 1 (2006), arXiv:hep-ph/0507228v1.
- [23] S. Biagi *et al.*, (KM3NeT Collaboration), *Proceedings of the 36th International Cosmic Ray Conference - ICRC2019*, 943 (2019).
- [24] E. Ryabov and B. Tarashansky, Monitoring of optical properties of deep lake water, in *Proceedings of the 37th International Cosmic Ray Conference - ICRC2021*, p. 1034, *Proceedings of Science*, 2021.
- [25] A. D. Avrorin *et al.*, *EPJ Web of Conferences* **207**, 07004 (2019).
- [26] M. G. Aartsenq, M. Ackermannbk, J. Adamsq, J. A. Aguilarl, and others (IceCube Collab.), *Journal of Instrumentation* (2016), arXiv:1612.05093 [astro-ph.IM].
- [27] URL: <https://icecube.wisc.edu/science/research/>.
- [28] V. N. Masolov, S. V. Popov, V. V. Lukin, and A. M. Popkov, *East Antarctica Doklady Earth Sciences* **433**, 1092 (2010).
- [29] В. Н. Масолов, В. В. Лукин, А. Н. Шереметьев, and С. В. Попов, *Доклады Академии Наук* **379**, 680 (2001).
- [30] Г. Л. Лейченков, Б. В. Беляцкий, А. М. Попков, and С. В. Попов, *Материалы гляциологических исследований* **98**, 81 (2005).
- [31] A. A. Tikku *et al.*, *Earth and Planetary Science Letters* **227**, 249 (2004).
- [32] V. Lipenkov *et al.*, *Phil. Trans. R. Soc. A* **374**, 20140303 (2016).

- [33] В. Н. Масолов *et al.*, Доклады Академии Наук **379**, 680 (2001).
- [34] J. Petit, I. Alekhina, and S. Bulat, Lectures in Astrobiology , 227 (2005).
- [35] G. T. Zatsepin and V. A. Kuzmin, JETP Lett **4**, 78 (1966).
- [36] K. Greisen, Phys. Rev. Lett **16** (1966).
- [37] Г. А. Аскарьян, Атомная энергия **3**, 152 (1957).
- [38] G. A. Askarijan, B. A. Dolgoshein, A. N. Kalinovsky, and N. V. Mokhov, Nucl. Instrum, and Meth **164**, 267 (1979).
- [39] Г. А. Аскарьян and Б. А. Долгошеин, Академия наук СССР. Физический институт им. П.Н. Лебедева Report No. 160, 1976 (unpublished).
- [40] H. Bradner, Dumand – deep underwater muon and neutrino detection; in *Proc. La Jolla workshop on acoustic detection of neutrinos*, San Diego, 1977, Institute of Geophysics and Planetary Physics, Scripps Institution of Oceanography, University of California.
- [41] L. G. Dedenko *et al.*, (1997), arXiv:astro-ph/9705189v1.
- [42] J. Vandenbroucke, G. Gratta, and N. Lehtinen, The Astrophysical Journal **621**, 301 (2005).
- [43] J. A. Aguilar *et al.*, (2012), arXiv:1009.4179v3 [astro-ph.IM].
- [44] R. Abbasi *et al.*, (2011), arXiv:1103.1216v2 [astro-ph.IM].
- [45] J. Vandenbroucke, (2011), arXiv:1201.0072v1 [astro-ph.IM].
- [46] Scar’s code of conduct for the exploration and research of subglacial aquatic environments.
- [47] J. Priscu *et al.*, Science **286**, 2141 (1999).
- [48] C. Lavire *et al.*, Environmental Microbiology **8**, 2106 (2006).
- [49] S. Bulat, Phil. Trans. R. Soc. A **374**, 20140292 (2016).
- [50] S. Rogers *et al.*, Biology **2**, 629 (2013).
- [51] M. Siegert *et al.*, Nature **414** (2001).
- [52] A. Rinaldi, European Molecular Biology Organization reports **7**, 759 (2006).

## СОДЕРЖАНИЕ

• ПРЕДИСЛОВИЕ .....	3
• Анатолий В. Котиков О ПРЕОБРАЗОВАНИИ ЛАНДАУ–ХАЛАТНИКОВА–ФРАДКИНА В КЭД .....	5
• Виктор Т. Ким, Григорий Б. Пивоваров ОБОБЩЕНИЕ СУДАКОВСКОГО ФОРМФАКТОРА НА АСИММЕТРИЧНЫЙ РЕЖИМ .....	25
• Михаил И. Высоцкий ДВУХФОТОННАЯ ФИЗИКА НА ЛНС .....	43
• Борис И. Ермолаев, Сергей И. Троян ГЛУБОКОНЕУПРУГОЕ РАССЕЙЯНИЕ В ДВАЖДЫ ЛОГАРИФМИЧЕСКОМ ПРИБЛИЖЕНИИ ...	52
• Анатолий Ю. Егоров, Виктор Т. Ким БФКЛ ЭВОЛЮЦИЯ И ПОТОК ЭНЕРГИИ ПРИ ОБРАЗОВАНИИ ПАР АДРОННЫХ СТРУЙ С ВЕТО ПРИ ЭНЕРГИЯХ ЛНС .....	75
• Дмитрий Е. Соснов ПЕРВОЕ ИЗМЕРЕНИЕ СОБЫТИЙ С ВЫСКОТНЫМИ ПРОВАЛАМИ ПРИ $\sqrt{S_{NN}} = 8.16$ ТэВ В СОУДАРЕНИЯХ ПРОТОНОВ С ЯДРАМИ СВИНЦА В ЭКСПЕРИМЕНТЕ CMS .....	96
• Ирина М. Парнова, Александр Я. Пархоменко АНАЛИЗ ВКЛАДОВ БОЛЬШИХ РАССТОЯНИЙ В РАСПАДАХ $B^+ \rightarrow \pi^+ \ell^+ \ell^-$ .....	105
• Илья Ф. Ларин, Виктор В. Тарасов ИЗМЕРЕНИЕ ПОЛЯРИЗУЕМОСТЕЙ ЗАРЯЖЕННОГО И НЕЙТРАЛЬНОГО ПИОНОВ В ЭКСПЕРИМЕНТАХ CPP/NPP .....	116

- Евгений Г. Друкарев  
ВВЕДЕНИЕ В ФИЗИКУ ЯДРА.  
I. ЯДРО КАК СИСТЕМА  
НЕРЕЛЯТИВИСТСКИХ НУКЛОНОВ ..... 128
  
- Александр Т. Дьяченко  
НЕРАВНОВЕСНЫЙ ГИДРОДИНАМИЧЕСКИЙ ПОДХОД  
ДЛЯ ОПИСАНИЯ ЭМИССИИ ВЫСОКОЭНЕРГЕТИЧЕСКИХ  
ВТОРИЧНЫХ ЧАСТИЦ В СТОЛКНОВЕНИЯХ  
ТЯЖЕЛЫХ ИОНОВ ПРОМЕЖУТОЧНЫХ ЭНЕРГИЙ .... 172
  
- Аркадий А. Захаров  
КОНЦЕПЦИЯ НОВОГО НЕЙТРИННОГО ДЕТЕКТОРА  
СВЕРХБОЛЬШОГО ОБЪЕМА В АНТАРКТИДЕ ..... 194

## CONTENTS

• FOREWORD .....	3
• Anatoly V. Kotikov ON LANDAU–KHALATNIKOV–FRADKIN TRANSFORMATION IN QED .....	5
• Victor T. Kim, Grigorii B. Pivovarov GENERALIZATION OF SUDAKOV FORM FACTOR FOR SKEWED REGIME .....	25
• Mikhail I. Vysotsky TWO PHOTON PHYSICS AT THE LHC .....	43
• Boris I. Ermolaev, Sergei I. Troyan DEEP INELASTIC SCATTERING IN DOUBLE-LOGARITHMIC APPROXIMATION .....	52
• Anatolii Iu. Egorov, Victor T. Kim BFKL EVOLUTION AND ENERGY FLOW FOR DIJET PRODUCTION WITH JET VETO AT LHC ENERGIES .....	75
• Dmitry E. Sosnov FIRST MEASUREMENT OF THE CROSS SECTIONS OF THE LARGE RAPIDITY GAP PROCESSES IN pPb COLLISIONS AT $\sqrt{s_{NN}} = 8.16$ TeV WITH THE CMS EXPERIMENT .....	96
• Irina M. Parnova, Alexander Ya. Parkhomenko ANALYSIS OF LONG-DISTANCE CONTRIBUTIONS IN $B^+ \rightarrow \pi^+ \ell^+ \ell^-$ DECAYS .....	105
• Ilya F. Larin, Victor V. Tarasov CHARGED AND NEUTRAL PION POLARIZABILITY MEASUREMENT IN THE CPP/NPP EXPERIMENTS .....	116
• Eugene G. Drukarev INTRODUCTION TO PHYSICS OF ATOMIC NUCLEI. I. NUCLEUS AS A SYSTEM OF NONRELATIVISTIC NUCLEONS .....	128

- Alexandr T. D'yachenko  
NON-EQUILIBRIUM HYDRODYNAMIC APPROACH  
FOR DESCRIPTION OF THE EMISSION OF HIGH ENERGY  
OF SECONDARY PARTICLES IN HEAVY ION COLLISIONS  
INTERMEDIATE ENERGIES ..... 172
- Arcady A. Zakharov  
CONCEPT OF A NEW ULTRA-LARGE-VOLUME  
NEUTRINO DETECTOR IN ANTARCTICA ..... 194

ФИЗИКА АТОМНОГО ЯДРА  
И ЭЛЕМЕНТАРНЫХ ЧАСТИЦ  
ТЕОРЕТИЧЕСКАЯ ФИЗИКА

NUCLEAR  
AND PARTICLE  
PHYSICS  
THEORETICAL PHYSICS

---

МАТЕРИАЛЫ  
LIV И LV  
ЗИМНИХ ШКОЛ ПИЯФ  
10–15 МАРТА 2020  
13–18 МАРТА 2023

PROCEEDINGS OF THE  
LIV AND LV  
WINTER SCHOOLS OF PNPI  
MARCH 10–15, 2020  
MARCH 13–18, 2023

Научный редактор **В. Т. Ким**      Editor **V. T. Kim**

Ответственный за выпуск *В. Т. Ким*  
Техническое редактирование *Т. А. Парфеевой*  
Компьютерная обработка и верстка: *Г. В. Степанова, Д. Е. Соснов*

Отпечатано с готового оригинал-макета  
в Издательско-полиграфическом отделе НИЦ «Курчатовский институт» – ПИЯФ  
188300, Гатчина Ленинградской обл., мкр. Орлова роша, д. 1  
Зак. 130, тир. 40, уч.-изд. л. 13,6; 12.03.2024.  
Формат 70 × 100 1/16